



HAL
open science

Structural and functional studies of a human potassium channel, Kir2.1. Mechanism and consequences of mutations

Dania Zuniga

► **To cite this version:**

Dania Zuniga. Structural and functional studies of a human potassium channel, Kir2.1. Mechanism and consequences of mutations. Structural Biology [q-bio.BM]. Sorbonne Université, 2022. English. NNT : 2022SORUS336 . tel-04090654

HAL Id: tel-04090654

<https://theses.hal.science/tel-04090654>

Submitted on 5 May 2023

HAL is a multi-disciplinary open access archive for the deposit and dissemination of scientific research documents, whether they are published or not. The documents may come from teaching and research institutions in France or abroad, or from public or private research centers.

L'archive ouverte pluridisciplinaire **HAL**, est destinée au dépôt et à la diffusion de documents scientifiques de niveau recherche, publiés ou non, émanant des établissements d'enseignement et de recherche français ou étrangers, des laboratoires publics ou privés.

SORBONNE UNIVERSITÉ

École doctorale 515 : Complexité du vivant

Institut de Minéralogie, Physique des Matériaux et Cosmochimie / Équipe BIBIP

Études structurale et fonctionnelle d'un canal à potassium humain, Kir2.1 :

Mécanisme et conséquences des mutations

Par DANIA ZUNIGA

Thèse de doctorat de
Biochimie et Biologie Structurale

Dirigée par Professeur Catherine Vénien-Bryan

Devant le jury composé de :

Nazzareno D'Avanzo	Professeur des Universités (Associate)	Rapporteur
Delphine Bichet	Chargée de Recherches	Rapporteur
Gildas Loussouarn	Directeur de Recherches, DR2	Examineur
Chahrazade El-Amri	Professeur, Sorbonne Université	Examinatrice
Catherine Vénien-Bryan	Professeur, Sorbonne Université	Thesis Director
Renaud Wagner	Chercheur CNRS	Invité

Résumé de thèse

La capacité d'une cellule à faciliter le mouvement sélectif et rapide des ions et des petites molécules à travers la membrane plasmique est un processus biologique indispensable. Les canaux potassiques à rectification entrante (Kir) sont des protéines membranaires intégrales qui fournissent des voies sélectives aux ions K^+ à travers la membrane cellulaire autrement imperméable, le long des gradients électrochimiques. Les canaux Kir permettent le passage des ions K^+ dans les deux sens et régulent diverses fonctions chez les humains, notamment la fréquence cardiaque, le tonus vasculaire, la sécrétion d'insuline et l'équilibre salin et hydrique.

L'importance physiologique des canaux Kir est mise en évidence par le fait que des défauts génétiquement héréditaires de ces gènes entraînent des maladies humaines (canalopathies). Nous nous intéressons particulièrement au syndrome d'Andersen, pour lequel des mutations du gène *KCNJ2* codant pour la protéine Kir2.1 sont directement impliquées. Le syndrome d'Andersen (AS) est une maladie rare caractérisée par des arythmies cardiaques, des dysmorphies multiples et des paralysies périodiques. Le traitement disponible pour les patients atteints d'AS est empirique plutôt que rationnel en raison du manque de connaissance de ce canal Kir2.1.

Cette thèse visait à identifier les différences entre le canal Kir2.1 de type sauvage et deux canaux mutants causant l'AS afin de trouver des liens entre la structure et la fonction du Kir2.1 humain en utilisant une combinaison d'approches biochimiques, structurales et fonctionnelles. Dans cette étude, nous avons exprimé le canal Kir2.1 humain dans la levure et l'avons purifié dans un détergent. Nous avons caractérisé l'interaction entre Kir2.1 et l'activateur essentiel PIP_2 , résolu la première structure de canal Kir humain par Cryo-MET et exploré la reconstitution dans des systèmes sans détergent comme les amphipoles et les nanodisques. Les résultats de cette étude fourniront une base structurale et fonctionnelle pour mieux comprendre les mécanismes impliqués dans les canaux Kir et les effets de leurs mutations.

Ce manuscrit est divisé en trois parties. La première partie présente les canaux Kir et l'état de l'art. La deuxième partie porte sur la caractérisation du canal potassique humain Kir2.1 et l'impact des mutations sur sa structure et sa fonction. La troisième partie présente deux mutations dans l'homologue bactérien KirBac3.1, qui partage des caractéristiques structurales avec Kir2.1, pour donner un aperçu du mécanisme d'ouverture et fermeture des canaux Kir.

SORBONNE UNIVERSITY

“Complexité du vivant” doctoral school (ED515)

Institut de Minéralogie, Physique des Matériaux et Cosmochimie / BIBIP team

Structural and functional studies of a human potassium channel, Kir2.1: *Mechanism and consequences of mutations.*

by **DANIA ZUNIGA**

A thesis submitted for the degree of
Doctor of Philosophy in Biochemistry and Structural Biology

Directed by Professor Catherine Vénien-Bryan

The jury is composed of :

Nazzareno D’Avanzo	Professor (Associate), University of Montreal	Reviewer
Delphine Bichet	CNRS Researcher, University of Nice	Reviewer
Gildas Loussouarn	CNRS Research Director, Dr2, Thorax Institute	Examiner
Chahrazade El-Amri	Professor, Sorbonne University	Examiner
Catherine Vénien-Bryan	Professor, Sorbonne University	Thesis Director
Renaud Wagner	Senior Researcher, University of Strasbourg	Guest

Esta tesis está dedicada a:

Mi Amor

Mamita

Papi

Mis hermanas

Abuelitos

Tías y tíos

Y mi preciosa Esperanza

Los amo tanto <3

Abstract

The ability of a cell to facilitate the selective and rapid movement of ions and small molecules across the plasma membrane is one of the most fundamental biological processes. Inward rectifier potassium (Kir) channels are integral membrane proteins that provide K⁺-selective pathways across the otherwise impermeable cell membrane along the electrochemical gradients. Kir channels support the flow of K⁺ ions into and out of the cell and regulate various functions in the human body, including heart rate, vascular tone, insulin secretion, and salt and fluid balance.

The physiological significance of Kir channels is highlighted by the fact that genetically-inherited defects in these genes result in human diseases (channelopathies). We are particularly interested in Andersen's syndrome, where mutations in the KCNJ2 gene coding for the Kir2.1 protein are directly involved. Andersen's syndrome (AS) is a rare disease characterized by cardiac arrhythmias, dysmorphic features, and periodic paralysis. The available treatment for AS patients is empirical rather than rational due to the lack of knowledge of this Kir2.1 channel.

This thesis aimed to identify the differences between the wild-type Kir2.1 channel and two mutant AS-causing channels to find links between the structure and the function of human Kir2.1 using a combination of biochemical, structural, and functional approaches. In this study, we recombinantly expressed the human Kir2.1 channel in yeast and purified it in detergent. We characterized the interaction between Kir2.1 and the essential activator PIP₂, solved the first human Kir channel structure by cryo-EM, and explored reconstitution in detergent-free systems like amphipols and nanodiscs. The findings of this study will provide a structural and functional base to understand better the mechanisms involved in Kir channels and the effects of their mutations.

This manuscript is divided into three parts. The first part introduces Kir channels and state-of-the-art. The second part focuses on the characterization of the human potassium channel Kir2.1 and the impact of mutations on its structure and function. The third part presents two mutations in the bacterial homolog KirBac3.1, which shares structural features with Kir2.1, to provide insight into the gating mechanism of Kir channels.

Acknowledgments

I want to thank my supervisor, Dr. Catherine Vénien-Bryan, for embarking me on this amazing journey of membrane proteins, potassium channels, and cryo-EM. *Catherine, I particularly thank you for your kindness and enormous support. You helped me get out of my comfort zone and create paths where there weren't any before. I deeply appreciated our conversations, scientific and personal ones.* And thank you CVB team, Andreas, Carlos, Charles, and Charline for all your help.

I want to thank Sorbonne Université, IMPMC, and Ecole doctorale CDV for allowing me to pursue this Ph.D.

I would like to thank Dr. Renaud Wagner for teaching me so much about protein expression. *Renaud, merci de toujours être là pour répondre à mes incessantes questions toujours de façon si bienveillante et honnête. Je ne t'ai jamais senti loin malgré les kilomètres qui nous séparent. Merci pour tes conseils pour le manuscrit. Merci aussi à Lucile, Lina, Dorothee, Valérie et Gabrielle pour leur aide avec la production cellulaire quand nous avons eu des soucis, vous avez super bien géré, comme d'habitude.*

I thank Drs. Delphine Bichet and Nazzareno D'Avanzo for accepting to be reviewers for this manuscript, and for their valuable feedback. I thank also Drs. Chahrazade El Amri, and Gildas Loussouarn for accepting to be part of my examiners on my Ph.D. defense thesis jury.

I would like to thank Drs. Françoise Bonneté, Riccardo Pellarin, and Beatrice Gollinelli for being my thesis committee. Thank you for your valuable advice.

I want to thank collaborators Drs. Said Bendahhou, David Perahia, and Gérard Pehaut-Arnaudet for their contributions. I also want to thank Drs. Jean-Michel Guigner, Alexandre Pozza, Stéphanie Finet, and Tahar Bouceba for forming me to use techniques that I exploited during this thesis and will continue to use throughout my career.

I want to thank all the people who participated in this project, but particularly the interns that I was lucky to mentor: Madeleine Ying, Xavier Gallien, Aphirami Manoharan, Banuyaa Jeyarah, Jessica Alam, Clairia Gomes, and Andreas Zoumpoulakis (who is now a Ph.D. student in the lab). *It was a very special experience to help you grow in your careers, I hope I wasn't too strict with you 😊.*

I want to thank the following scientists for their help and advice on techniques or equipment use: Drs. Manuela Zoonens, Jean-Jacques Lacapere, Valérie Biou, and Fériel Skouri-Panet, as well as Ms. Mélanie Poinot and Cynthia Travert.

I want to thank my colleagues who have grown to be cherished friends for their support but also for filling their drawers with food so that I could have brain fuel during the late hours writing (*je pense à toi Cynthia, merci*) and the much-needed coffee/tea breaks

talking about anything under the sun, and the great escape games: Sigrid, Juliette, Juliette, Apolline, Amrita, Haneen, Léon, Jaysen, Cécile, Neha, Hortense, Mélanie, Baptiste, Lucie, Laura, Geoffroy, Yoann, Jeanne (and those whose names have escaped me, know that I'm grateful to you).

Lastly, I am incredibly grateful for my amazing support system. My fiancé, Thierry, who's been absolutely incredible, especially these past few months. *Sans ton amour, ta patience, ta bienveillance, je n'aurais pas pu garder ma santé mentale.* Our lovely daughter, Esperanza, who is sleeping through the night just so I can rest and is extra sweet 😊. My supportive parents that helped me develop my curiosity without limits and made me the person I am today. *Gracias por siempre esta allí para mi, y dejarme explorar el mundo y forjar mi propio camino.* To my sisters, thank you for your surprise visits that would just light up my week, I really appreciated them. To my family at large, thank you for being there for me. Et à ma belle-famille, merci de votre soutien et des bons weekends ensemble.

TABLE OF CONTENTS

1	Introduction and Background	13
1.1	POTASSIUM CHANNELS, AN OVERVIEW	14
1.1.1	Generalities and classification	14
1.1.2	Voltage-gated K ⁺ (K _v) channels	15
1.1.3	Calcium-activated K ⁺ (K _{Ca}) channels	16
1.1.4	Two-pore domain K ⁺ (K _{2p}) channels	16
1.2	INWARD RECTIFIER K ⁺ (K _{IR}) CHANNELS: FUNCTION AND RECTIFICATION	17
1.3	KIR CHANNELS' STATE-OF-THE-ART: STRUCTURAL FEATURES, SELECTIVITY, GATING, AND REGULATION.....	22
1.3.1	K ⁺ selectivity and conductivity	27
1.3.2	Blockade by endogenous polyamines and Mg ²⁺	29
1.3.3	Regulation of Kir Channels and gating	30
1.4	DYSFUNCTIONS IN THE HUMAN KIR2.1 CHANNEL LEAD TO ANDERSEN'S SYNDROME	32
1.5	THESIS PROJECT OBJECTIVES	33
1.6	BIBLIOGRAPHY	34
2	Materials and Methods	41
2.1	EXPRESSION AND PURIFICATION OF HUMAN KIR2.1 CHANNEL IN <i>PICHIA PASTORIS</i>	42
2.1.1	Production	42
2.1.2	Cell lysis	44
2.1.3	Membrane Preparation	45
2.1.4	Quantification of membranes.....	46
2.1.5	Solubilization of membranes	46
2.1.6	Direct extraction by the formation of protoplasts.....	46
2.1.7	Affinity chromatography	47
2.1.8	Size exclusion chromatography	47
2.2	IDENTIFICATION OF KIR2.1 FRACTIONS AND POST-TRANSLATIONAL MODIFICATIONS	48
2.2.1	Identification of Kir2.1 fractions	48
2.2.2	Mass Spectrometry and Post-Translational Modifications	49
2.3	BIOPHYSICAL CHARACTERIZATION OF KIR2.1	50
2.3.1	Dynamic Light Scattering	50
2.3.2	SEC-MALLS: a triple detection method to characterize membrane proteins in solution	53
2.4	FUNCTIONAL ASSAY AND LIGAND-PROTEIN INTERACTION.....	59
2.4.1	Electrophysiology	59
2.4.2	Surface Plasmon Resonance (SPR).....	60
2.5	TRANSMISSION ELECTRON MICROSCOPY AND STRUCTURE DETERMINATION	63
2.5.1	Introduction to electron microscopy.....	63
2.5.2	Image formation and contrast transfer.....	66
2.5.3	Single-particle analysis	70
2.5.4	Preparation of the specimen using Negative Staining	73
2.5.5	Cryo-EM	75
2.6	EXPRESSION AND PURIFICATION OF BACTERIAL HOMOLOG MUTANTS: KIRBAC3.1 W46R AND S129R	78
2.6.1	Production	78
2.6.2	Culture medium and growth conditions	78
2.6.3	Purification of KirBac 3.1 W46R and S129R.....	79
2.7	SUPPLEMENTARY MATERIAL	80
2.7.1	Transmission Electron Microscope	80
2.8	BIBLIOGRAPHY	82
3	Biochemical and Biophysical characterization of kir2.1 and mutants	85
3.1	INTRODUCTION.....	86
3.1.1	Recombinant expression of membrane proteins	86
3.1.2	Detergents	87
3.2	MATERIALS AND METHODS	88
3.3	RESULTS.....	88
3.3.1	Heterologous expression of human Kir2.1 in <i>Pichia pastoris</i>	89
3.3.2	Extracting human Kir2.1 from <i>Pichia pastoris</i> cell membranes.....	90

3.3.3	Two-step purification, identification of Kir2.1, and analysis of post-translational modifications by mass spectrometry	94
3.3.4	Evaluating the hydrodynamic radius of Kir2.1	96
3.3.5	SEC-MALLS – a triple detection method to characterize membrane proteins in solution	98
3.3.6	Analysis of Kir2.1 solubilized in FC14	101
3.3.7	Analysis of Kir2.1 mutants: R312H and C154Y	108
3.4	DISCUSSION	113
3.5	BIBLIOGRAPHY	114
3.6	SUPPLEMENTARY MATERIAL	116
3.6.1	Solubilization of membrane proteins	116
3.6.2	Cell culture optimization	117
3.6.3	Optimizing cellular lysis	119
3.6.4	Conclusion	126
4	Cryo-EM Structure of human Kir2.1 channel	127
4.1	INTRODUCTION TO CHAPTER	128
4.2	ABSTRACT	129
4.3	INTRODUCTION	130
4.4	RESULTS	131
4.4.1	Protein expression and purification of human Kir2.1 WT and R312H	131
4.4.2	Overall cryo-EM structure of the human Kir2.1 channel	131
4.4.3	Ions' location in the pore channel	132
4.4.4	Four constriction points (gates) in the Kir2.1 channel	133
4.4.5	Structural comparison between Kir2.1 and Kir2.2 structures	133
4.4.6	PIP ₂ binding interaction with Kir2.1 WT and mutant R312H	134
4.4.7	Functional studies on Kir2.1 WT and mutant R312H	134
4.4.8	Interaction network between R312, H221, and E303 residues	134
4.4.9	Investigation of global motions of the Kir2.1 channel by normal mode analysis	135
4.4.10	Investigation by MD simulations of local motions of residues K64 and R67	137
4.5	DISCUSSION	137
4.5.1	Conducting ions and blocking ions compete for sites in the pore	137
4.5.2	Inherent local and large-amplitude motions of the human Kir2.1 channel structure may describe the mechanism of CTD tethering to TMD	138
4.5.3	Central role of the G-loop in the gating and mechanism for releasing the constriction point	139
4.6	MATERIALS AND METHODS	140
4.6.1	Protein expression	140
4.6.2	Protein purification	140
4.6.3	Surface plasmon resonance (SPR)	141
4.6.4	Functional reconstitution of Kir2.1 WT and R312H mutant in lipid bilayer	141
4.6.5	Sample preparation and cryo-EM data collection	142
4.6.6	Cryo-EM data processing	142
4.6.7	Model building and refinement	142
4.6.8	R312H mutation modeling	143
4.6.9	Normal mode analysis	143
4.6.10	Molecular dynamics (MD) simulations	143
4.7	REFERENCES	144
4.8	FIGURES	148
1.1.1	Surface Plasmon Resonance controls and supplementary experiments	167
5	Reconstitution of Kir2.1 in model systems: Amphipols and Nanodiscs	173
5.1	INTRODUCTION	174
5.2	PART I: CHARACTERIZATION OF KIR2.1 IN AMPHIPOLS	175
5.2.1	Materials and Methods	175
5.2.2	Results	177
5.3	PART II: RECONSTITUTION KIR2.1 IN NANODISCS: INITIAL EXPERIMENTS	183
5.3.1	Materials and Methods	183
5.3.2	Results	187
5.4	DISCUSSION	190
5.4.1	Amphipols	190
5.4.2	Nanodiscs	190
5.5	REFERENCES	192
6	Side Projects: a bacterial homolog KirBac3.1 and mutants W46R and S129R	193

6.1	INTRODUCTION	194
1.	Introduction.....	196
2.	Results.....	197
2.1.	<i>Crystal Structure of KirBac3.1 W46R.....</i>	197
2.2.	<i>HDX-MS measurements</i>	199
2.3.	<i>Theoretical Results on KirBac3.1 W46R.....</i>	200
2.3.1.	Interaction Networks	200
2.3.2.	Contacts between residues	202
•	Accessible surface of the residues W46 and R46	202
•	Accessible surface of the residues R134 and F135 and contacts with I131	203
2.3.3.	Impact of the mutation on the gating.....	204
•	Upward movement of the slide helix.....	204
•	Movement of the cytoplasmic domain.....	205
•	Movement of the transmembrane helices.....	206
2.3.4.	Population of open and closed states corresponding to the MDeNM relaxed structures.....	207
2.4.	<i>Functional studies of the W46R protein</i>	208
3.	Discussion	209
3.1.	<i>Characteristics of mammalian Kir6.2 channel.....</i>	209
3.2.	<i>KirBac3.1 W46R: a good model for studying analogous W68R mutation in mammalian Kir6.2</i>	210
3.3.	<i>Suggestions to Kir6.2 by analogy</i>	211
4.	Materials and Methods.....	211
4.1	<i>Experimental Data</i>	212
4.1.1	Protein expression and purification	212
4.1.2	Protein Crystallization.....	212
•	Data collection and structure determination	212
4.1.3	Pepsin Digestion, Hydrogen/Deuterium exchange approach coupled to mass spectrometry (HDX-MS) and HPLC	212
4.1.4	Functional studies of the KirBac W46R protein in black lipid membrane	213
4.2	<i>Theoretical data.....</i>	213
4.2.1	Modeling and Dynamics.....	213
4.2.2	Normal Modes	214
4.2.3	Molecular Dynamics using excited Normal Modes	214
•	Relaxation of the excited MDeNM structures	214
4.2.4	Interaction networks	214
4.2.5	Structural determinants	215
•	Upward angle of the slide-helices.....	215
•	Tilt angle of the transmembrane helices	215
References		216
7	Conclusion and Perspectives.....	235
7.1	Conclusion.....	236
7.2	Perspectives.....	239

ABBREVIATIONS

AC: Amplitude contrast	FEG: Field emission (electron) gun	OGP: n-octyl- β -D glucopyranoside
Apix: Å/pixel	Ft: Flowthrough	PAGE: polyacrylamide gel electrophoresis
Apol: Amphipol	FT: Fourier transform	PBS: Phosphate-buffered saline
BCA: Bicinchoninic acid	GIRK: G-protein regulated K ⁺ channels	PCC-Malt: 4-trans-(4-trans-Propylcyclohexyl)-cyclohexyl α -maltoside
BCIP: 5-Bromo-4-chloro-3'-indolyphosphate	HS: High salt	PES: Polyethersulfone
BMGY: Buffered medium, glycerol, yeast	IMAC:	PIP ₂ : Phosphatidylinositol 4,5-bisphosphate
BMMY: Buffered medium, methanol, yeast	IPTG: Isopropyl β -D-1-thiogalactopyranoside	P-loop: extracellular pore-forming loop containing the selectivity filter
BSA: Bovine serum albumin	K _{2P} : mechano-sensitive, two-pore K ⁺ channels	PMSF: Phenylmethylsulfonyl fluoride
Cam: Chloramphenicol	Kan: Kanamycin	POPC: 1-Palmitoyl-2-oleoyl-sn-glycero-3-phosphocholine
Cc: Chromatic aberrations	K _{ATP} : ATP-sensitive Kir channels	PVDF: Polyvinylidene fluoride
CC: Cross-correlation	K _{Ca} : calcium-activated K ⁺ channels	QF: Quantifoil
CCD: Charge-couple device	K _{ir} /Kir: inwardly rectifying K ⁺ channels	RI: Refractive index
Cell D: Cell Disruptor	Kv: voltage-gated K ⁺ channels	RT: Room temperature
CHAPSa: 3-((3-cholamidopropyl)dimethylammonio)-1-propanesulfonate	L1: Lipophilic chip	RU: Response unit
CM5: Carboxymethylated dextran	LaB ₆ : Lanthanum hexaboride	S/N: Signal-to-noise ratio
CMC: Critical micellar concentration	LB: Luria broth	S200: Superdex 200 10/300 GL Increase
Cryo-EM: Transmission electron microscopy in cryogenic conditions	LMNG: Lauryl maltose neopentyl glycol	SDS: Sodium dodecyl sulfate
C _s : Spherical aberrations	LS: Static light scattering	SEC: Size exclusion chromatography
CTD: Cytoplasmic domain	MALDI: Matrix-assisted laser desorption ionization	SOC: Super optimal broth with catabolite repression
C-ter: Carboxy terminus	MALLS: Multiple-angle light scattering	SPR: Surface plasmon resonance
CTF: Contrast transfer function	MAPS: Monolithic active pixel sensors	SUR: Sulfonylurea receptor
DDM: n-Dodecyl- β -D-maltoside	MP: Membrane protein	TB: Terrific broth
DLS: Dynamic light scattering	MPD: Membrane protein-detergent complex	TCA: Trichloroacetic acid
DM: n-Decyl- β -D-maltoside	MS/MS: Mass spectrometry in tandem	TEM: Transmission electron microscopy/microscope
DMSO: Dimethyl sulfoxide	MS: Mass spectrometry	TM: Transmembrane
DOPC: 1,2-Dioleoyl-sn-glycero-3-phosphocholine	MSP: Membrane scaffolding protein	TMD: Transmembrane domain
DPhPC: 1,2-Diphytanoyl-sn-glycero-3-phosphocholine	MW: Molecular weight	TOF: Time of flight
DQE: Detection quantum efficiency	MWCO: Molecular weight cut-off	TriDM: N-Tridecyl- β -D-Maltoside
dRI: Differential refractive index	NanoLC: nanoflow liquid chromatography	UV: Ultraviolet
DTT: Dithiothreitol	NBT: Nitro-blue tetrazolium	VLM: visible light microscopy/microscope
EDC: N-ethyl-N'-(3-dimethylaminopropyl)carbodiimide	NHS: N-hydroxysuccinimide	WB: Western blot
EDTA: Ethylenediamine-N,N,N',N'-tetraacetic acid	NTA: Nitrilotriacetic acid	YDP: Yeast dextrose peptone
EM: Electron microscopy/microscope	N-ter: Amino terminus	YNB: Yeast nitrogen base
FC: Flow cell	OD _{600nm} : Optical density at 600 nm	β ME: β -mercaptoethanol
FC14: Foscholine 14		

1 INTRODUCTION AND BACKGROUND

1.1 POTASSIUM CHANNELS, AN OVERVIEW

Electrical signals control our bodies' most fundamental biological processes, from thinking and breathing to the beating of our hearts. All the intricate interactions that make our day-to-day start with an ion finding its way through an impermeable membrane and effecting change to establish the electrochemical equilibrium or modify it transiently. This thesis focuses on the biochemical and structural characterization of Kir2.1, a human inwardly rectifying potassium channel recombinantly expressed in *Pichia pastoris*, with functional implications. Before we delve into it, this chapter will briefly describe and compare potassium channels, look a little closer at the regulation and gating of Kir channels, and finally address the structures known to date.

1.1.1 Generalities and classification

K⁺ channels facilitate the selective and rapid movement of K⁺ ions through the cell membrane, establishing an electrical gradient and an electric field that helps orient membrane proteins within the membrane (Cardozo 2016). Like a switch, tightly-regulated K⁺ channels open and close in response to stimuli, like voltage change, calcium levels, temperature, pH, and cellular modulators (Luckey 2008).

K⁺ channels are ubiquitous and incredibly diverse. There are more than 80 genes that code for K⁺ channels in the human genome alone (Doupnik, Davidson, et Lester 1995). The differences in structure allow them to be regulated by various auxiliary subunits, interact with different agonists, and intervene at different stages of the action potential with different effects. These channels' functional and structural diversity surpasses that of any other channels (Luckey 2008).

K⁺ channels can be divided into four families (Taura et al. 2021):

1. Voltage-gated K⁺ channels: K_V,
2. Calcium-activated K⁺ channels: K_{Ca},
3. Two-pore domain K⁺ channels: K_{2P}, and
4. Inward rectifier K⁺ channels: K_{ir}

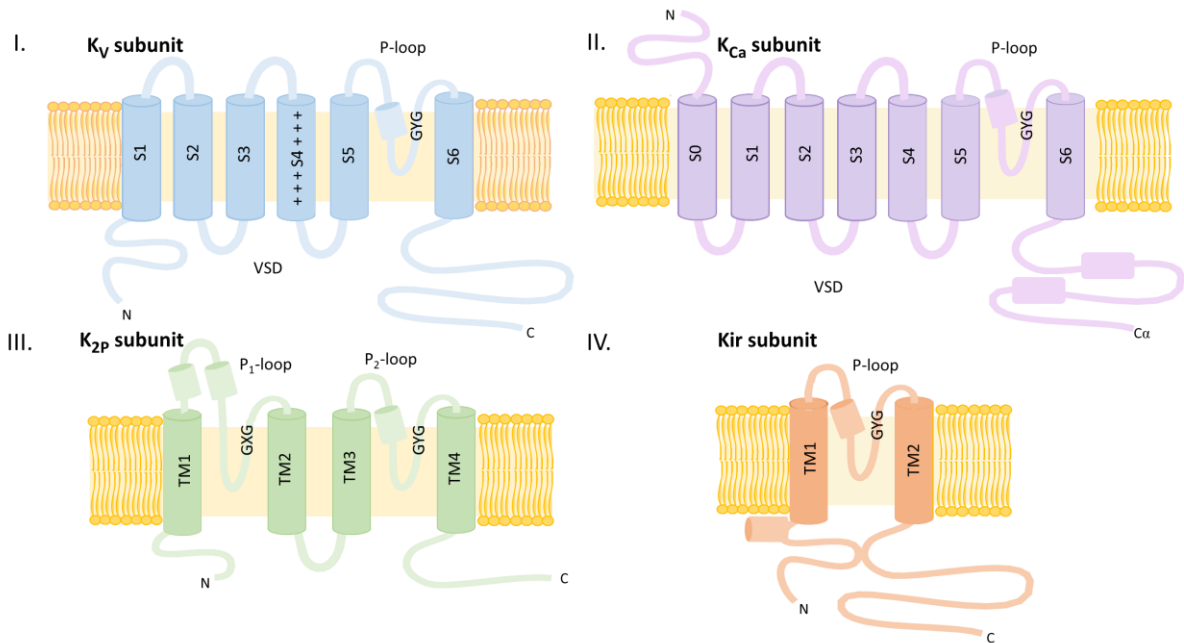


Figure 1-1. Topology of the four K^+ channel families.

1.1.2 Voltage-gated K^+ (K_V) channels

First described by Hodgkin and Huxley in 1945 (Hodgkin et Huxley 1945), voltage-gated K^+ channels (K_V) are the most prominent K^+ channel family. In mammals only, 40 genes code for K_V channels and their α subunits. K_V channels are traditional K^+ channels; they open to let K^+ ions out of the cell, helping to repolarize excitable cells during the action potential (Hille 1986). They are divided into 12 subfamilies.

K_V channels are multiunit channels (tetramers) consisting of α subunits containing the main transmembrane complex and accessory β subunits. $K_{V\alpha}$ subunits share a basic structure consisting of an amino- (N-) terminus, six transmembrane helices named S1–S6 connected by five loops, and a carboxy-(C-) terminus. The loop separating S5 and S6 contains the pore-forming loop (P-loop) and the K^+ -selective filter (SF) present in all K^+ channels. Pore opening is controlled through the intracellular loop between S4 and S5. S1–S4 form the voltage-sensing domain (VSD), which functions as an independent domain. Like most K^+ channels, the α subunits arrange as homo- or heterotetramers to form a K^+ selective pore (Abbott et al. 2001; Pongs et Schwarz 2010; A-González et Castrillo 2011; Kuang, Purhonen, et Hebert 2015).

The α subunits are in charge of voltage sensing, gating, and regulation. The biological role played by the β -subunits is the subject of ongoing research; they play roles in

altering expression, trafficking, and gating. The importance of the $Kv\alpha\text{-}\beta$ complex is undeniable as defects in either the α -subunit or the accessory subunits can lead to diseases like hypertension (Abbott et al. 2001), hypothyroidism, and epilepsy.

1.1.3 Calcium-activated K^+ (K_{Ca}) channels

In 1958, G. Gardos first described the activation of K^+ channel conductance by intracellular Ca^{2+} ions in red blood cells (Gardos 1958). The sensitivity to Ca^{2+} ions allows K_{Ca} channels to regulate the action potential. They can activate the afterhyperpolarization during high Ca^{2+} concentrations coupled to membrane potential changes during the action potential (Taura et al. 2021).

These K_{Ca} channels can be divided into three classes depending on their conductance: small conductance (SK_{Ca} , 4–14 pS) (Köhler et al. 1996), intermediate conductance (IK_{Ca} , 32–39 pS) (Ishii et al. 1997), and big conductance (BK_{Ca} , 200–300 pS) (Butler et al. 1993) (kshatri et al. 2018).

K_{Ca} channels have a similar basic structure as Kv channels with α and β subunits, with notable differences. $K_{(Ca)}$ channels are tetramers; the $K_{ca2.1}$ - $K_{ca2.3}$ and $K_{ca3.1}$ channels have six TM domains but lack voltage sensitivity. The SK_{Ca} and BK_{Ca} channels have an additional first TM domain (S0), making their N-terminus extracellular. BK_{Ca} have a vast intracellular C-terminal domain containing two regulating-conductance of K^+ domains (RCK, (Yuan et al. 2010)). SK_{Ca} channels lack this RCK domain for Ca^{2+} modulation. Instead, calmodulin (CaM) provides SK channels with their Ca^{2+} sensitivity.

The K_{Ca} channels have implications in diseases and are therapeutic targets in disorders including schizophrenia (Grube et al. 2011), atrial fibrillation (Diness et al. 2010), and even breast cancer (Potier et al. 2006).

1.1.4 Two-pore domain K^+ (K_{2P}) channels

In 1995, Ketchum et al. described the first two-pore domain K^+ channel (K_{2P}) in *Saccharomyces cerevisiae* (Ketchum et al. 1995). However, their effects, K^+ -selective leakage from the cell, were detected as early as 1952 (Hodgkin et Huxley 1952). These channels are distinguished from other members of the K^+ channel families by having

two pore-loops and four transmembrane domains (TM1–TM4) per subunit. Unlike the other K^+ channels, which are tetramers, the subunits assemble as a dimer to form one K^+ -selective pore. Their overall functional structure is similar to the other K^+ channels.

The K_{2P} family is encoded by 18 KCNK genes and comprises 15 different subunits. Three genes, KCNK8, KCNK11, and KCNK14, have no (detectable) expression levels. K_{2P} channels can be separated into six subfamilies according to their function and structure similarities: two-pore acid-sensitive K^+ channels (TASK 1–2,3,5), two-pore alkaline-activated K^+ channels (TALK 1–2), two-pore halothane-inhibited K^+ channels (THIK 1–2), two-pore weak inward rectifying K^+ channels (TWIK 1–2), TWIK-related spinal-cord K^+ channel (TRESK), and TWIK-related K^+ channels (TREK 1–2) with TWIK-related arachidonic acid-stimulated K^+ channels (TRAAK).

They control K^+ ions, cell volume, hormonal secretion, and muscular and neuronal excitability. Dysfunction of these channels can lead to pathologies including Birk-Barel syndrome (Barel et al. 2008), migraine (Lafrenière et al. 2010), arterial hypertension (Ma et al. 2013), cancer (Williams, Bateman, et O’Kelly 2013), and cardiac arrhythmia (Friedrich et al. 2014).

1.2 INWARD RECTIFIER K^+ (KIR) CHANNELS: FUNCTION AND RECTIFICATION

Inward rectifier K^+ (Kir) channels were first described in frog skeletal muscle over seven decades ago (in 1949) by B. Katz as having an anomalous rectification (Katz 1949) because their conductance decreased instead of increasing upon cell depolarization. Kir channels are so-called due to their tendency to allow the passage of K^+ ions into the cell than out of the cell. Although outward Kir2.1 currents are much smaller than inward ones, under physiological conditions, the outward currents regulate the excitability and duration of repolarization in excitable cells like neurons and cardiac myocytes. The outward current in K^+ channels sets up the negative electrostatic potential across the membrane, essential for protein orientation within the membrane (Cardozo 2016).

Kir channels are responsible for creating and propagating the action potential in excitable cells, regulating the heartbeat, helping balance the passage of salts and water, and regulating cell volume and muscle contraction. Kir channels regulate K^+ homeostasis by establishing an excitation threshold dependent on membrane voltage

and the regulatory state of the channels (Ruppersberg et Fakler 1996). The overall effect allows Kir channels to generate and control the resting membrane potential achieved when electrochemical equilibrium is reached at -70 mV (M. Zhou et MacKinnon 2004).

The Nernst equation (Equation 1-1) calculates/defines the membrane potential at which any given ion will be at equilibrium based on its valence and concentration gradient across the membrane. Above or below this potential, the ions should flow in a direction that restores the equilibrium.

Equation 1-1

$$E_x = \frac{R \cdot T}{z \cdot F} \ln \left(\frac{X_{out}}{X_{in}} \right) \quad \text{Nernst equation}$$

E_K is the electrical potential of a charged particle (in mV), R is the gas constant $8.314 \text{ J} \cdot \text{K}^{-1} \cdot \text{mol}^{-1}$, T is the temperature in Kelvin, z is the electron valence (1 for K^+), F is the Faraday constant $96,485 \text{ C} \cdot \text{mol}^{-1}$, X_{out}/X_{in} is the ratio of the ion's extracellular concentration over its intracellular concentration in mM. For a K^+ channel at normal physiological conditions, $T = 37^\circ \text{C}$, 310.15 K , with $X_{out} = 4 \text{ mM}$ and $X_{in} = 140 \text{ mM}$ concentrations, the E_K is -95 mV .

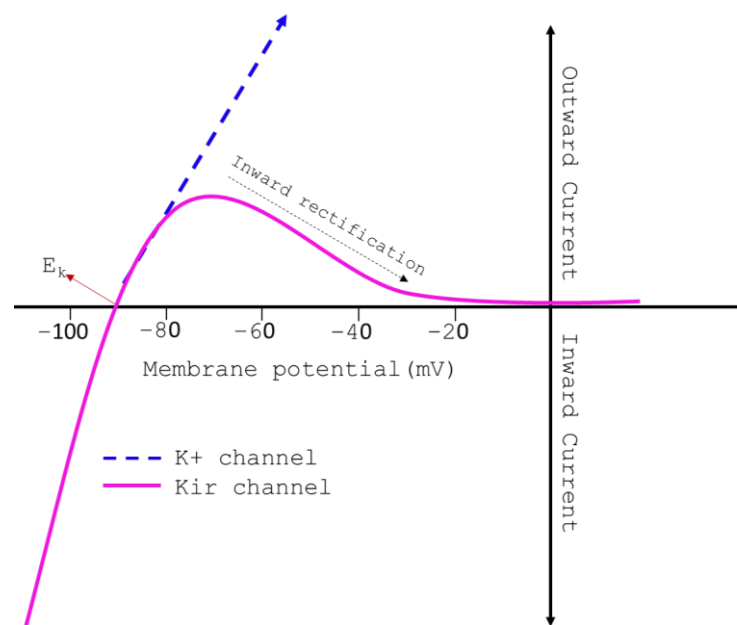


Figure 1-2. Schematic voltage vs. current relationship of Kir channels

At membrane potentials above E_K , a favored outward current is expected. However, in Kir channels, this outward current is attenuated by intracellular molecules that bind to the channel and block the efflux of K^+ ions resulting in an inward rectification. However, the blockade by Mg^{2+} (Matsuda, Saigusa, et Irisawa 1987) and polyamines

(Anatoli N. Lopatin, Makhina, et Nichols 1994; J. Yang, Jan, et Jan 1995a; A N Lopatin, Makhina, et Nichols 1995; Oliver, Baukrowitz, et Fakler 2000), that physically plug the channel, results in a steep voltage-dependent rectification above the resting membrane potential (Baronas et Kurata 2014). At potentials negative to the E_K , these blockers are released into the cell allowing the influx of K^+ ions (A N Lopatin, Makhina, et Nichols 1995). The voltage dependence observed in Kir channels is in response to these interactions as Kir channels lack a voltage-sensing domain and remain constitutively active in the presence of PIP_2 independently of the voltage.

There are sixteen genes encoding Kir channels (KCNJ1–18) that can be classified into seven sub-families (Kir1.x–7.x, Figure 1-3) and four functional groups: classical Kir channels, K^+ transport channels, ATP-sensitive channels (K_{ATP}), and G-protein regulated K^+ channels (GIRK). These channels show different levels of rectification, ranging from weak (Kir1.1 and Kir6.x), intermediate (Kir4.x), to strong (Kir2.x and Kir3.x) (Hibino et al. 2010). Doupnik et al., Bichet et al., and Hibino et al. have published outstanding reviews describing the differences within these subfamilies (Doupnik, Davidson, et Lester 1995; Bichet, Haass, et Jan 2003; Hibino et al. 2010).

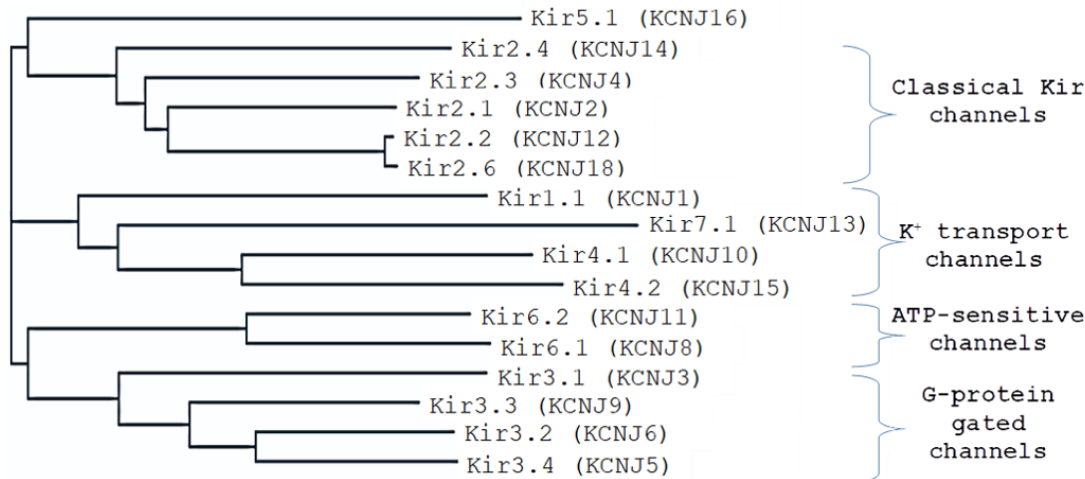


Figure 1-3. Kir channel phylogenetic tree. Sixteen KCNJ genes code for Kir channels and can be divided into four functional groups according to their amino acid sequence.

A sequence alignment of Kir channels (Figure 1-4) revealed highly conserved segments that have been the subject of much research, like the conserved sequence T-I/V-G-Y-G and ligand binding and regulation sites described later in this chapter.

KIRBAC3.1MNVDPFSPHSSDS.....FAQ.....AASPARKPPRGR 29
 KIRBAC1.1 0
 H_KIR7.1MD.....SSNCK.....VIAPLLSQRYR 18
 H_KIR1.1MNASSRNVFDT.....LIRVLTESMFKHLRQVWV.....VTRFFGHSRQRA 40
 H_KIR4.1MTSVAKVYYSQTTQTE.....SRPLMGPRI 28
 H_KIR6.1MLARKSIIPPEEY.....VLARIAAEN.....L.....RKPRIRDRLPKA 34
 H_KIR5.1MSYYGSSYHIINADA.....KYPG.....YPPEHIAEKRRARR 34
 H_KIR2.1MGSVRTNRYSSIVSSEEDGMKLATMAVANGFGNGK.....SKVHTRQQCRS 45
 M_KIR2.1MGSVRTNRYSSIVSSEEDGMKLATMAVANGFGNGK.....SKVHTRQQCRS 45
 C_KIR2.2MTAASRANPYSIVSSEEDGLHLVTMSGANGFGNGK.....VHTRRRCRN 44
 H_KIR2.2MTAGRVNPYSIVSSEEDGLRLTTMPGINGFGNGK.....IHTRRKCRN 43
 M_KIR3.2 MTMAKLTESMTNVLGDSMDQ-DVESPAIHQP.....KLPKQARDDLPRHISRDRTKRKIQ 56
 H_KIR3.1MSALRRKF.....GDDYQVVTSSSGSGLQP.....QGGPQD.....P.....QQQLVPKKKRQ 44
 M_KIR3.1MSALRRKF.....GDDYQVVTSSSGSGLQP.....QGGPQG.....P.....QQQLVPKKKRQ 44



Slide helix

TM1

KIRBAC3.1 RIW--SGTREVIAYGMPA--SVWRDLY-YWALKVSWPVFFASLAALFVNNNTLFFAL--- 80
 KIRBAC1.1MPPMLSGLLARLVKL.....LLGRHGSALHWRAAGAATVL 35
 H_KIR7.1 RMVTKDGHSTLQMDGAQ--RGLAYLRDAWGILMDMRWRWMLLVFSASFVHWLVFAV--LW 75
 H_KIR1.1 RLVSKDGRGRCNIEFGNVEAQSRIFFVDIWTTVL DLKWR YKMTIFITAF LGSWFFFGL--LW 99
 H_KIR4.1 RVLTKDGRSNVRMEHI-ADKRFLYLKDLWTTFIDMQWR YKLLLSATFAGTWFLFGV--VW 86
 H_KIR6.1 RFI AKSGACNLAHKNI R--EQGRFLQDIFTTLV DLKWRHTLVIF TMSFLCSWLLFAI--MW 91
 H_KIR5.1 RLLHKDGCNRYVFKHIF-GEWGSYVVDIFTTLV DLKWRHMFVIFSLSYILSWLIFGS--VF 92
 H_KIR2.1 RFVVKDGHGCVQFINVG-EKGQRYLADIFTTTCVDIRWRWMLVIFCLAFVLSWLF FGC--VF 103
 M_KIR2.1 RFVVKDGHGCVQFINVG-EKGQRYLADIFTTTCVDIRWRWMLVIFCLAFVLSWLF FGC--VF 103
 C_KIR2.2 RFVVKNGQCNI EFANMD-EKSQRYLADMFTTTCVDIRWR YMLLIFSLAF LSWLLFGI--IF 102
 H_KIR2.2 RFVVKNGQCNI EFANMD-DKPQRYIADMFTTTCVDIRWR YMLLIFSLAF LSWLLFGI--IF 101
 M_KIR3.2 RYVRKDGKCNVHGNVR--ETYRYLTDIFTTLV DLKWR FNLLIFVMVYTVTWLFFGM--IW 113
 H_KIR3.1 RFVDKNGRCNVQHGNLG-SETSRYLSDLFTTTLV DLKWRWNLFIFILTYTVAWL FMAS--MW 102
 M_KIR3.1 RFVDKNGRCNVQHGNLG-SETSRYLSDLFTTTLV DLKWRWNLFIFILTYTVAWL FMAS--MW 102

TM1

Pore helix

SF

KIRBAC3.1 ---LYQLGDPIAN-----QSPPGFVGAFFFSVETLA TVGYG DMHPQT VY 122
 KIRBAC1.1 LVI VLLAGSYLAVLA-----ERGAPGAQLITYPRALWWSVETAT TVGYG DLYPVTLLW 87
 H_KIR7.1 YVLAEMNGDLELDH----APPENHTICVKYITSF TAAFSFSL ETQT TIGYG TMFPSGD C 131
 H_KIR1.1 YAVAYIHKDLPEFHP----SANHTPCVENINGLTS AFLFSLETQV TIGYG FRCVTEQ C 153
 H_KIR4.1 YLVAVAHGDLLELDP----PANHTPCVQVQVHTLTG AFLFSLETQV TIGYG FRYISEE C 140
 H_KIR6.1 WLVAFAHGD IYAYMEKSGMEKSGLESTVCVTNVRSTSAFLFSIEVQV TIGYG GRMTEE C 152
 H_KIR5.1 WLIAFHGDL LND-----PDITPCVDNVHSTG AFLFSLETQV TIGYG YRCVTEE C 143
 H_KIR2.1 WLIAL LHGDL DASK-----EGKACVSEVNSFTA AFLFSIETQT TIGYG FRCVTDE C 154
 M_KIR2.1 WLIAL LHGDL DTSK-----VSKACVSEVNSFTA AFLFSIETQT TIGYG FRCVTDE C 154
 C_KIR2.2 WVIAVAHGDLEPAEG-----R-GRTPCVMQVHGFMA AFLFSIETQT TIGYG LRCVTEE C 155
 H_KIR2.2 WLIAL LHGDL ENPGG-----DDTFKPCV LQVNGFVA AFLFSIETQT TIGYG FRCVTEE C 155
 M_KIR3.2 WLIA YIRGDM DHI ED-----PSWTPCVTNLNGFVSA AFLFSIETET TIGYG YRVITDK C 166
 H_KIR3.1 WVIA YTRGDL NKAHV-----GNYTPCVANVYNFPS AFLFFIETEA TIGYG YRYITDK C 155
 M_KIR3.1 WVIA YTRGDL NKAHV-----GNYTPCVANVYNFPS AFLFFIETEA TIGYG YRYITDK C 155

TM2

D/N

beta B1

beta B2

KIRBAC3.1 AHA IATLEIFV---GMS---GIALSTGLV FARFAR PRA--KIMFARHAI V----- 164
 KIRBAC1.1 GRLVAVVVVMVAGITSFGLVTAALATW FVGRE---QERRGHFVRHS EKAAEEAYTRTTR 142
 H_KIR7.1 PSAIALLAIQM---LLGLM---LEAFITGAFVAKIARPKNRAF SIFRDTAVV----- 178
 H_KIR1.1 ATAIFLLIFQS---ILGVI---INSFMCGAILAKISRPKKRAKTITFSKNAVI----- 200
 H_KIR4.1 PLAIVLLIAQL---VLT TI---LEIFITGTFLAKIARPKKRAETIRFSQHAVI----- 187
 H_KIR6.1 PLAITVLILQN---IVGLI---INAVMLGCIFMKTQA AHRR AETLIFSRHAVI----- 199
 H_KIR5.1 SVAVLMVLIQS---ILSCI---INTFII GAALAKMATA RKRAQTIRFSYFALI----- 190
 H_KIR2.1 PIAVFMVVFQS---IVGCI---IDAFIIGAVMAKMAKPKKRN ETLVFSHNAVI----- 201
 M_KIR2.1 PIAVFMVVFQS---IVGCI---IDAFIIGAVMAKMAKPKKRN ETLVFSHNAVI----- 201
 C_KIR2.2 PVAVFMVVAQS---IVGCI---IDSFMI GAIMAKMARPKKRAQTLLFSHNAVV----- 202
 H_KIR2.2 PIAVFMVVFQS---IVGCI---DSFMI GAIMAKMARPKKRAQTLLFSHNAVV----- 202
 M_KIR3.2 PEGIILLLIQS---VLGSI---VNAFMVGCDFVKISQPKKRAETLVFS THAVI----- 213
 H_KIR3.1 PEGIILFLFQS---ILGSI---VDAFLIGCMF IKMSQPKKRAETLMFSEHAVI----- 202
 M_KIR3.1 PEGIILFLFQS---ILGSI---VDAFLIGCMF IKMSQPKKRAETLMFSEHAVI----- 202

beta B2

beta C

beta D

beta E

KIRBAC3.1 --RPFNGRMTLMVRAANA RQNVIAEARAKMRLMRREHSS EGYSLMKI H-----DLKLV RN 217
 KIRBAC1.1 ALHERDGLRLERML--DDNRR----- 160
 H_KIR7.1 --AHMDGRKPLIFQVANTRPSPLTSVRVSAVLYQEREN-----GKLYQTSVDFHLDG ISSD 232
 H_KIR1.1 --SKRGGKLC L LIRVANLRK SLLIGSHIYGKLLKTTVTPEGETIILDQIN--INFVVDAGN 257
 H_KIR4.1 --ASHNGKPC L M IRVANLRK SLLIGCQVTGKLLQTHQTKEGENIRLNQVN--VTFQVDTAS 244
 H_KIR6.1 --AVRNGKLC L MFRVGD L R KSMIISASVRIQVVKTTTPEGEVVP I HQLD--IPVDNPIES 256
 H_KIR5.1 --GMRDGLKCLMWRVIGDFRPNHVV EGTVRAQLLRYTEDSEGRMTMAF-K-----DLKLVN 242
 H_KIR2.1 --AMRDGKLC L MWRVGNLRK SHLVEAHVRAQLLKSRTITSEGEYIPLDQID--INVGFDSGI 258
 M_KIR2.1 --AMRDGKLC L MWRVGNLRK SHLVEAHVRAQLLKSRTITSEGEYIPLDQID--INVGFDSGI 258
 C_KIR2.2 --ALRDGKLC L MWRVGNLRK SHIVEAHVRAQLIKPRVITEEGEYIPLDQID--IDVGFDKGL 259
 H_KIR2.2 --AMRDGKLC L MWRVGNLRK SHIVEAHVRAQLIKPRITEEGEYIPLDQID--IDVGFDKGL 259
 M_KIR3.2 --SMRDGKLC L MFRVGD L R N SHIV EASIRAKLIKSKQTS EGEFIPLNQSD--INVGYTGD 270
 H_KIR3.1 --SMRDGKLC L MFRVGNLRN SHMVS AQIRCKL LKSRQTP EGEFLPLDQLE--LDVGFSTGA 259
 M_KIR3.1 --SMRDGKLC L MFRVGNLRN SHMVS AQIRCKL LKSRQTP EGEFLPLDQLE--LDVGFSTGA 259

	KcsA	KirBac3.1	KirBac1.1	h_Kir7.1	h_Kir1.1	h_Kir4.1	h_Kir6.1	h_Kir5.1	h_Kir2.1	m_Kir2.1	c_Kir2.2	h_Kir2.2	m_Kir3.2	h_Kir3.1	m_Kir3.1
KcsA	100.00%	17.56%	16.15%	14.19%	10.81%	18.92%	14.86%	19.18%	22.60%	21.23%	20.27%	19.59%	17.57%	18.92%	18.92%
KirBac3.1	17.56%	100.00%	39.52%	23.34%	25.26%	25.34%	25.51%	22.34%	24.48%	24.48%	25.09%	25.09%	25.51%	24.66%	24.66%
KirBac1.1	16.15%	39.52%	100.00%	26.14%	24.31%	25.16%	22.73%	20.91%	22.80%	22.80%	24.55%	24.85%	22.29%	24.54%	24.54%
h_Kir7.1	14.19%	23.34%	26.14%	100.00%	35.21%	39.77%	28.90%	29.59%	34.76%	34.94%	33.52%	32.58%	30.11%	30.40%	30.40%
h_Kir1.1	10.81%	25.26%	24.31%	35.21%	100.00%	47.41%	39.19%	36.16%	41.99%	41.62%	42.67%	42.63%	40.85%	41.02%	41.02%
h_Kir4.1	18.92%	25.34%	25.16%	39.77%	47.41%	100.00%	38.14%	34.84%	37.77%	37.94%	39.08%	39.30%	36.16%	37.85%	38.12%
h_Kir6.1	14.86%	25.51%	22.73%	28.90%	39.19%	38.14%	100.00%	36.84%	43.97%	43.61%	43.50%	42.75%	43.29%	41.73%	42.24%
h_Kir5.1	19.18%	22.34%	20.91%	29.59%	36.16%	34.84%	36.84%	100.00%	44.84%	44.72%	42.39%	42.71%	36.25%	36.20%	35.70%
h_Kir2.1	22.60%	24.48%	22.80%	34.76%	41.99%	37.77%	43.97%	44.84%	100.00%	98.59%	70.82%	71.50%	45.68%	46.32%	46.57%
m_Kir2.1	21.23%	24.48%	22.80%	34.94%	41.62%	37.94%	43.61%	44.72%	98.59%	100.00%	70.42%	71.56%	45.68%	46.32%	46.57%
c_Kir2.2	20.27%	25.09%	24.55%	33.52%	42.67%	39.08%	43.50%	42.39%	70.82%	70.42%	100.00%	86.45%	44.61%	43.58%	43.83%
h_Kir2.2	19.59%	25.09%	24.85%	32.58%	42.63%	39.30%	42.75%	42.71%	71.50%	71.56%	86.45%	100.00%	46.06%	44.53%	44.77%
m_Kir3.2	17.57%	25.51%	22.29%	30.11%	40.85%	36.16%	43.29%	36.25%	45.68%	45.68%	44.61%	46.06%	100.00%	54.50%	54.26%
h_Kir3.1	18.92%	24.66%	24.54%	30.40%	41.02%	37.85%	41.73%	36.20%	46.32%	46.32%	43.58%	44.53%	54.50%	100.00%	99.00%
m_Kir3.1	18.92%	24.66%	24.54%	30.40%	41.02%	38.12%	42.24%	35.70%	46.57%	46.57%	43.83%	44.77%	54.26%	99.00%	100.00%

Figure 1-5. The amino acid sequence percent identity between various KirBac, human, mouse, chicken Kir channels, and KcsA.

1.3 KIR CHANNELS' STATE-OF-THE-ART: STRUCTURAL FEATURES, SELECTIVITY, GATING, AND REGULATION

All K^+ channels contain a pore-forming region through which K^+ ions are conducted across the membrane. This pore is lined with polar sidechains that shield the K^+ ion from the otherwise hydrophobic environment. Four pore-forming loops (P-loop) with their respective K^+ -selective filters (SF) make up this pore, with each subunit containing one. Therefore, most K^+ are active as tetramers of the same (homomer) or similar (heteromer) subunits (J. Yang, Jan, et Jan 1995b), except for K_2P channel subunits, which contain two of each and are functional as dimers.

Despite their structure, function, and mechanism diversity, Kir channels have the most primitive structure of all potassium channels. Each subunit shares the same basic topology: a large cytoplasmic domain hosting the C- and N- termini, a slide helix, and two TM domains (TM1-TM2) separated by an extracellular turret, pore helix, and P-loop containing SF (Doupnik, Davidson, et Lester 1995; Minor et al. 1999; Bichet, Haass, et Jan 2003; Hibino et al. 2010). Figure 1-4 shows the h_Kir2.1 solved by C.A.H. Fernandes, D. Zuniga et al. during this Ph.D. (2021) with structural features annotated to use as a reference.

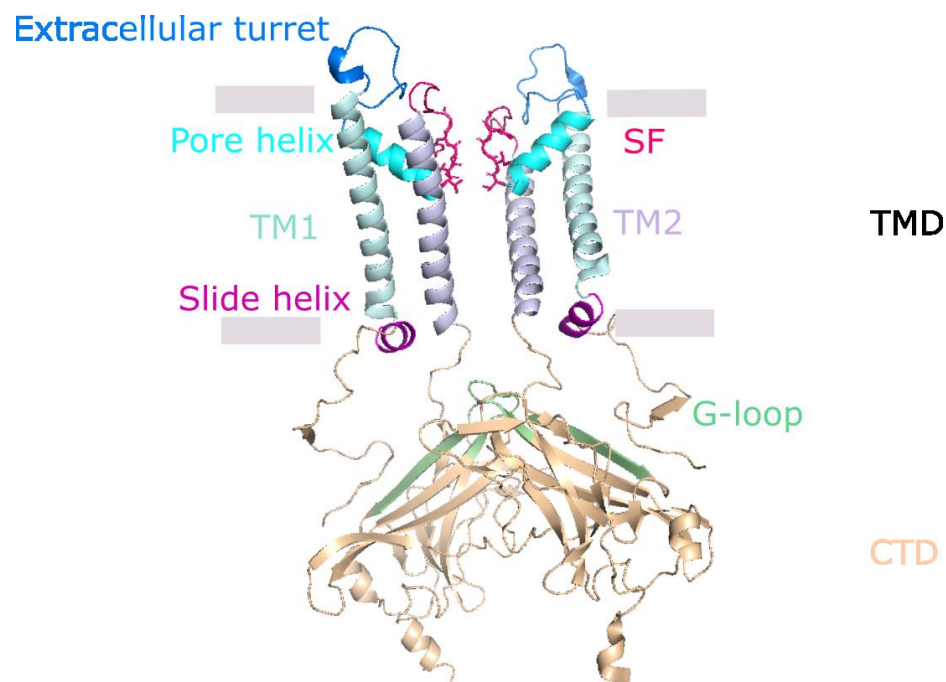


Figure 1-6. Structure of h_Kir2.1 (PDB 7ZDZ) with structural features annotated (result from Chapter 4).

Nowadays, when we hear Kir channel, we have a reasonable idea of what a eukaryotic channel looks like, thanks to incredible work done in the past two decades. It all started with a bacterial K_v channel, KcsA.

When D. Doyle et al. in the R. Mackinnon lab revealed the crystal structure of the KcsA channel from *Streptomyces lividans* in 1998 (Doyle et al. 1998), it provided the first look into the structural features of a K^+ channel. It proposed an explanation for the selectivity and conductivity paradox observed in K^+ channels (discussed in section 1.3.1 below). The KcsA structure showcased a tetrameric assembly of this 2-TM channel with four-fold symmetry. The SF is housed at the center of the pore-shaped domain, forming an inverted teepee where each subunit has the TM1 helix facing the membrane (outer helix) and the TM2 helix facing the central pore (inner helix). The

TM2 were tilted at 25° to the membrane, interacting with other TM2 by subunit-subunit interactions and only with the TM1 of the same subunit.

Noteworthy yeast genetic screens by D. Minor Jr. et al. correctly identified differences in the arrangement of an open Kir(2.1) and KcsA TM helices before any Kir structure was published (Minor et al. 1999). Functional Kir2.1 channels with randomized libraries were used to rescue the growth of a K⁺-transport deficient yeast strain. The amino acid mutation patterns allowing rescue were plotted. A TM architecture was proposed where each TM2 interacts with the TM1 of the same subunit and the adjacent subunit.

Since then, several high-resolution structures of prokaryotic (KirBac) and eukaryotic Kir channels have been solved using primarily X-ray crystallography and, more recently, cryo-electron microscopy: mouse Kir3.1, KirBac1.1, mouse Kir2.1 CTD, chicken Kir2.2 (\pm PIP₂), KirBac3.1, mouse Kir3.2 (\pm PIP₂), and now human Kir2.1.

PDB ID	Protein	Gene	Res (Å)	Method	Sequence Identity	Structure Coverage	Year
1N9P	Kir3.1	mouse	1.8	Xray D	55.38%	41%	2002
1P7B	KirBac1.1	bacteria	3.65	Xray D	26.50%	77%	2003
1U4F	Kir2.1	mouse	2.42	Xray D	98.36%	63%	2005
1U4E	Kir3.1	mouse	2.09	Xray D	55.38%	42%	2005
3JYC	Kir2.2	chicken	3.11	Xray D	70.90%	74%	2009
2WLK	KirBac3.1	bacteria	2.8	Xray D	27.21%	97%	2010
2XKY	Kir2.1	mouse	17.2	neg stain	98.36%	72%	2011
3SPI	Kir2.2	chicken	3.003	Xray D	70.90%	74%	2011
3SYQ	Kir3.2	mouse	3.44	Xray D	55.59%	71%	2011
3ZRS	KirBac3.1	bacteria	3.05	Xray D	27.21%	93%	2012
4LP8	KirBac3.1	bacteria	2.46	Xray D	27.21%	94%	2013
5KUM	Kir2.2	chicken	2.8	Xray D	70.90%	76%	2016
6XIS	Kir3.2	mouse	3.9	Cryo-EM	55.59%	79%	2020
6XIT	Kir3.2	mouse	3.3	Cryo-EM	55.59%	79%	2020
6XEU	Kir3.2	mouse	3.2	Cryo-EM	55.59%	79%	2021

Figure 1-7. Summary of some Kir and KirBac channel structures. The sequence identity refers to the UniProt sequence compared to human Kir2.1. The structure coverage denotes the percentage of amino acid sequence included in the protein construct.

A chimeric construction made of the structure of the CTD of mouse Kir3.1, also known as GIRK1 (PDB: 1N9P), merged to the TMD domain of MthK, a K_{Ca} channel isolated from *Methanothermobacter thermoautotrophicus*, first hinted at the basis of the inward rectification structurally (Motohiko Nishida et MacKinnon 2002). It showed that the cytoplasmic region formed a β -sheet-rich protein with an α helix protruding that aligned

as a tetramer to form a tube-like passage 7–15 Å wide that extended the pore to 50 Å. Hydrophobic and acidic residues lined the cytoplasmic pore. This favorable environment for polyamines could very well thus host the blocker binding sites.

When A. Kuo et al. and D. Doyle solved the structure of the first bacterial Kir channel, KirBac1.1, from *Burkholderia pseudomallei* in 2003, they confirmed a different arrangement between KirBac1.1 and KcsA in the closed state (Kuo et al. 2003). The structure identified two TM helices with an arrangement closer to Minor et al.'s prediction than to the KcsA structure. It portrayed structural features including the extracellular turret, inverted teepee gate, flexible linkers between the CTD and TMD, a large CTD consisting mainly of β sheets, and an additional helix running perpendicular to the membrane with a potentially critical role for the gating: the slide helix. They proposed that the pore extended from the extracellular turret to the cytoplasm, spanning 88 Å.

Two more mouse CTD domains of Kir channels were solved by Pegan et al. (2005), m_Kir2.1 (1U4F) and m_Kir3.1 (1U4E). Comparison of the two allowed them to identify a flexible loop that held the cytoplasmic pore like a girdle, forming the narrowest point in the CTD; they referred to this section as the G loop. Mutations in the G loop resulted in disruptions in gating and inward rectification (Pegan et al. 2005). Several structural studies suggest that it may undergo relevant conformational changes for channel gating (Pegan et al. 2005; M. Nishida et al. 2007; Whorton et MacKinnon 2011; 2013). However, the G-loop gate's integration into channel gating and its impact on the gating kinetics of Kir channels are still unknown.

In 2009, the first eukaryotic (chicken) structure of a Kir channel containing the TMD was solved by Tao et al. by X-ray diffraction to 3.11 Å, without the flexible N- and C-terminal segments (Tao et al. 2009). The structure revealed the typical features expected, including the SF, G loop, and the water cavity, but also the TMD-CTD linker tethering the CTD to the TMD. It showed significant differences with other K⁺ channels, like four polar residues (D173, from each chain) projecting toward the ion pathway in the pore's central cavity in the strong rectifiers. Additionally, residues I177 and M181 on the inner helices (TM2) form two hydrophobic seals that block the pore leading to the cytoplasm beneath the central cavity. As a result, Kir2.2 is physically closed. These large hydrophobic residues acting as two constriction points are conserved in eukaryotic Kir channels (sequence alignment). However, they are replaced by small and occasionally polar amino acids in KcsA and KirBac channels. This structure

provided valuable structural insight into channel conductivity and the voltage-dependent block by polyamines and Mg^{2+} .

Next, with the improvements in data correction, Clarke et al. reinterrogated available raw data on several atomic structures of KirBac1.1 and KirBac3.1, re-solved the structures, and compared them with five new experimental KirBac3.1 structures. Comparison of all the structures ranging from conductive and blocked states allowed them to observe that a rotation and reorientation of the CTD was coupled to a regulation in conductivity (Clarke et al. 2010). However, in all these KirBac channel structures, the bundle-crossing gate is closed, providing poor information about the structural changes that must occur during the gating. Later Bavro et al. and Zubcevic et al. solved KirBac3.1 structures of the engineered mutation S129R that trapped the channel in a stable conformation with the helix bundle crossing open (Bavro et al. 2012; Zubcevic et al. 2014). This made it possible to propose a ‘twist-to-open’ mechanistic model of channel gating for KirBac channels in which “a network of intra- and intersubunit interactions involving the TM2, C-linker, slide helix, G loop, and CD loop link rotational twist of the cytoplasmic domain to the opening of the bundle-crossing gate”(Bavro et al. 2012). C. Venien-Bryan, my Ph.D. director, was involved in this work and we have continued exploring the implication of this mutant S129R to explore the gating behavior of constitutively open channels (Chapter 6).

Since then, more c_Kir2.2 structures have been solved by X-ray diffraction with and without PIP_2 (PDB: 5KUK, 5KUM, 6M84, 6M85, 6M86). The c_Kir2.2 atomic structures with PIP_2 allowed identifying the amino acids interacting directly with PIP_2 , therefore identifying the PIP_2 -binding site. Furthermore, two large conformational states were observed, an extended conformation in the apo state and a compressed conformation bound to PIP_2 . This has led to a proposed hypothetical regulation mechanism in which PIP_2 binding induces a conformational change that leads the channel to open (Figure 1-8 and more information in section 1.3.3.1 below).

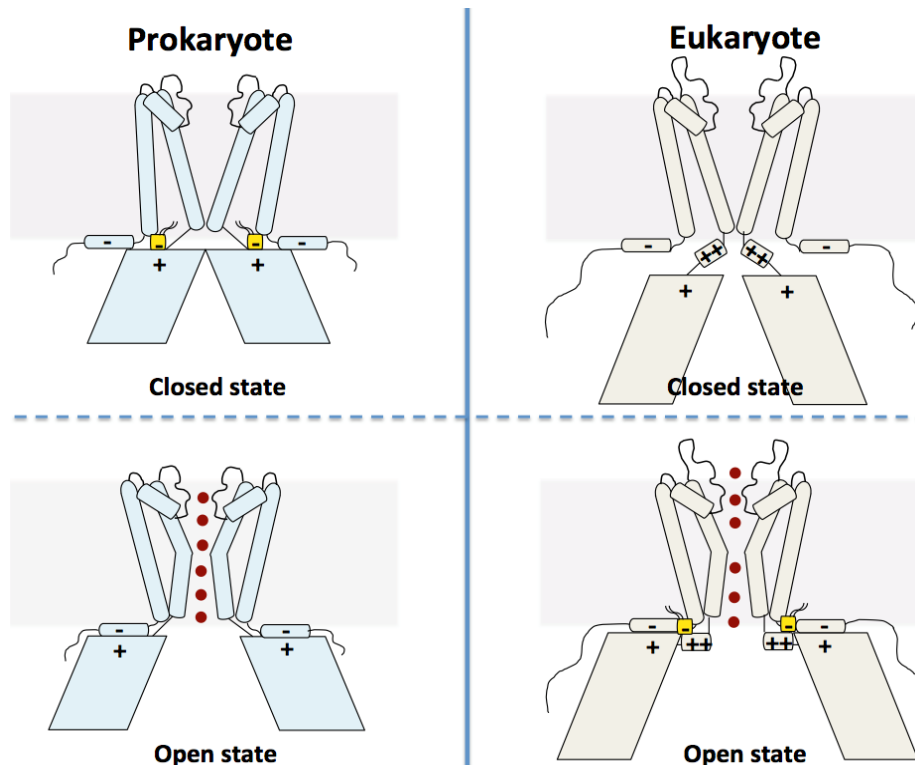


Figure 1-8 Hypothetical PIP₂ activation mechanism in eukaryotic Kir channels and deactivation in KirBac channels.

More recently, structures of m_Kir3.2 and m_Kir3.1/Kir3.4 were solved by cryo-electron microscopy (cryo-EM) (PDB: 6XIS, 6XIT, 6XEU) with and without PIP₂ showed the extended and compressed conformations without and with PIP₂, respectively (Niu et al. 2020). Additionally, they showed increased compression states as the concentration of PIP₂ increased.

1.3.1 K⁺ selectivity and conductivity

In order to fulfill their physiological roles, K⁺ channels must be able to distinguish K⁺ ions from other like-charged ions, like Na⁺ and Li⁺. The high selectivity is made possible by the narrowest point of the K⁺ channel pore domain, the selectivity filter (SF), which contains the consensus amino acid sequence T-I/V-G-Y-G (Heginbotham, Abramson, et MacKinnon 1992; Heginbotham et al. 1994; Doyle et al. 1998; Bichet, Haass, et Jan 2003). The carbonyl oxygen atoms in T-I/V-G-Y-G form four K⁺ binding sites numbered 1–4 (S1–S4) starting from the extracellular domain. Each site contains four carbonyl oxygen atoms from the main chain, and S4 contains four additional hydroxyl oxygen atoms from threonine's (T) side chain.

K^+ ions are surrounded by water molecules (hydrated K^+) inside and outside the cell. The SF is too narrow to allow hydrated K^+ to pass, so K^+ ions are dehydrated before entering and rehydrated upon exiting the SF (Y. Zhou et al. 2001). The backbone oxygen atoms bind K^+ ions (2.66 Å diameter) and perfectly replace (and mimic) the water oxygen atoms with minimal energy expense. In contrast, Na^+ ions (and Li^+ ions) cannot follow the same process: the diameter of Na^+ ions (1.9 Å) is too small to bind to the SF's oxygen atoms and be thoroughly dehydrated (Doyle et al. 1998). Therefore, the permeation of the channel would be energetically unfavorable.

Mutations in this consensus sequence often make the channel less K^+ selective and allow the occasional Na^+ or Li^+ ion. Examples include $K_{Ca2.x}$ channels and the K_{2P} channel TWIK1 (Ma et al. 2011). These natural mutations may enable these channels to regulate their selectivity in the absence of K^+ or under low K^+ conditions. However, this remains the exception rather than the rule. N. D'Avanzo et al. showed that the consensus motif alone is insufficient to confer K^+ selectivity to nonselective channels like HCN4 (D'Avanzo, Pekhletski, et Backx 2009, 4); other amino acids in the region must play an important role.

K^+ channels ensure the passage of K^+ ions with high selectivity ($> 10^4$ times more selective for K^+ than Na^+ ions) (Doyle et al. 1998) while conducting efficiently at near diffusion rates (up to 10^8 ions per channel per second) (Sansom et al. 2002). These two seemingly paradoxical properties of K^+ channels are essential. In order to ensure that the selectivity does not come at the cost of conductivity rates (in either direction), the binding cannot be too strong to achieve this balance (Kuang, Purhonen, et Hebert 2015).

The SF backbone can theoretically accommodate four K^+ ions (Figure 1-6). However, studies by Zhou and Mackinnon propose that only two K^+ ions are present simultaneously in the pore, occupying either sites S1 and S3 (1,3-configuration) or S2 and S4 (2,4-configuration) and alternating with two water molecules (Morais-Cabral, Zhou, et MacKinnon 2001; Y. Zhou et al. 2001; Y. Zhou et MacKinnon 2003; M. Zhou et MacKinnon 2004). The repulsion of two close K^+ ions favors conductivity, forming a queue inside the SF and pushing one K^+ ion out as another enters.

The high-resolution structures of KcsA in high K^+ and low K^+ concentrations, 200 mM and 3 mM, respectively, showed the effect of K^+ presence on the structure of the SF (Y. Zhou et al. 2001). The SF in KirBac1.1 only showed three K^+ -binding sites in the closed state. The authors also proposed that the three ions were an average of two K^+

occupying S1 and S3 and one occupying S2, where S2 had a lower temperature factor than S1 and S3 and was key in triggering the SF into a conductive state and keeping it from collapsing when occupied (Kuo et al. 2003).

These studies proposed that the SF *requires* two K^+ ions to be conductive. The entry of the second K^+ ion induces the SF to change from a non-conductive to a conductive state. This conformational change reduces, in turn, the binding strength between the K^+ ion and the SF, showing that the high selectivity and high conductivity are, in fact, complementary (Morais-Cabral, Zhou, et MacKinnon 2001; Y. Zhou et al. 2001; Y. Zhou et MacKinnon 2003; M. Zhou et MacKinnon 2004). On the contrary, in binding Na^+ ions, the SF may be deformed or stabilized in a non-conductive state, further emphasizing the need for K^+ selectivity.

Extensive studies on the structure and electrophysiology of prokaryotic (KcsA, KirBac1.1, KirBac3.1) and eukaryotic (Kir2.1, Kir2.2) K^+ channels have elucidated the K^+ conductivity pathway. They (Doyle et al. 1998; Kuo et al. 2003; M. Zhou et MacKinnon 2004) propose that as K^+ ions move along the pore to exit the channel from the intracellular side (helical bundle), they are stabilized by a water-filled cavity, move in a single line along the short (12 Å) and narrow SF, and exit one by one through the extracellular entryway. K^+ ions enter the channel following the opposite pathway.

1.3.2 Blockade by endogenous polyamines and Mg^{2+}

In the absence of polyamines and Mg^{2+} ions, Kir channels are constitutively active, showing an increased conductance with increasing concentrations of K^+ ions, except for Kir7.1 (A.N. Lopatin et Nichols 1996). Polyamines are present in the cells at concentrations below the millimolar range. Their slow blocking and unblocking of the Kir channel are believed to cause the putative activation gating behavior. The “deactivation” on depolarization would correspond to polyamines producing a time-dependent decrease in outward current. When a cell is hyperpolarized, the inward Kir current first increases time-independently due to fast Mg^{2+} unblocking and then increases time-dependently by slow polyamine unblocking (Anatoli N. Lopatin, Makhina, et Nichols 1994; A N Lopatin, Makhina, et Nichols 1995; Yamashita et al. 1996; Hibino et al. 2010).

D172 in Kir2.1 in the TM2 helix has been suggested to be a crucial factor in determining inward rectification for different Kir channels (Anatoli N. Lopatin, Makhina, et Nichols 1994; Lu et MacKinnon 1994; Stanfield et al. 1994; Hibino et al. 2010). In Kir1.1 and

Kir6.2, weak rectifiers, the corresponding positions are uncharged, N171 and N160, respectively. Replacing Asn with Asp (N171D or N160D) increased the affinity for Mg^{2+} and resulted in strong rectification (Lu et MacKinnon 1994; Shyng et al. 2000). The position is known as the “D/N site” (Figure 1-4). Nevertheless, this site alone cannot explain differences in the degree of rectification. Mutagenesis studies revealed that Kir channel subunits could have multiple Mg^{2+} and polyamine interacting residues lining the cytoplasmic pore, notably E224 and E299, responsible for polyamine and Mg^{2+} sensitivity (Hibino et al. 2010). Mutations in these residues led to ion permeation changes but not in gating.

A di-aspartate cluster (D255 and D259) was discovered to be involved in rectification (Pegan et al. 2005). Both residues faced the cytoplasmic pore in the Kir2.1 and Kir3.1 CTD crystal structures. It is unclear why both the TMD and CTD contain residues that bind Mg^{2+} and polyamines. It has been suggested that the TMD may act as a plugging site for polyamines. In contrast, the CTD region may act as an intermediary binding site to raise the local concentration of polyamines near the TMD plugging site (Kubo et Murata 2001; Hibino et al. 2010). An electrophysiological study of the concentration-response of Mg^{2+} and spermine on Kir2.1 outward current showed a competition between the two molecules. The competition may be critical to the importance of Kir2.1 outward currents.

1.3.3 Regulation of Kir Channels and gating

Several factors have been shown to affect how Kir channels operate. The gating mechanism is regulated by modulators such as lipids (e.g., PIP_2 , cholesterol, LC-CoA), G protein, protein kinases, nucleotides (ATP), and ions (H^+ , Na^+) (Doupnik, Davidson, et Lester 1995; Hibino et al. 2010). For instance, an acidic pH inhibits the activity of the Kir1.1, Kir2.3, and Kir4.1 channels. For their part, Kir3.2 and Kir3.4 exhibit a dependence on the intracellular Na^+ ion concentration (Ho et Murrell-Lagnado 1999), with a high concentration favoring the channel’s activity. Kir6.2 is regulated by the sulfonylurea receptor (SUR), which activates the channel in the presence of ADP. When intracellular ATP levels are high, ATP binds directly to the Kir6.x cytoplasmic domain and inhibits them (Gribble 1997). Kir2.1 channels have been shown to interact with the PDZ domain via the C-terminus recognition site S-x-I (Fomina et al. 2011), and Kir4.1 currents increased in the presence of PSD95 (Horio et al. 1997). Kir channels also interact with LC-CoA, long-chain fatty acid esters of coenzyme A, which activate

KATP channels but inhibit Kir1.1, Kir2.1, Kir3.4, and Kir7.1 (Rapedius et al. 2005). Phosphorylation can enhance the channel activity, as was shown for Kir6.1 (Quinn, Giblin, et Tinker 2004; Shi et al. 2007). Cholesterol can directly inhibit Kir2.1 channels (D’Avanzo et al. 2011). Finally, the endogenous microRNA, miR1, has been found to directly modulate Kir2.1 in cardiomyocytes through a noncanonical, rapid biophysical mechanism (D. Yang et al. 2021).

1.3.3.1 Kir channel regulation by PIP₂

One of the regulators having a substantial effect on the gating phenomenon is PIP₂. This negatively charged lipid agonist, anchored in the membrane, stimulates the activity of the channels. Since it is widely acknowledged that all Kir channels are only active when connected to PIP₂, their activity is closely correlated with the intricate cellular metabolism of PIPs (Hilgemann, Feng, et Nasuhoglu 2001; Baukrowitz et Fakler 2000). The observation that Kir channel mutations that impair PIP₂ interactions with Kir1.1 and Kir2.1 can result in disease states like Bartter’s syndrome and Andersen’s syndrome, respectively, highlights the physiological importance of this phosphoinositide regulation (Lopes et al. 2002). It is thought that many of the regulatory signals mentioned in the previous paragraph that modulate channel activity do so by altering the channel’s affinity for PIP₂ (Xie et al. 2007; 2008).

In fact, despite PIP₂’s low abundance in the lipid membranes, about 1%, it is intricately implicated in regulating many physiological processes like ion channel activation, exocytosis, enzyme activation, cytoskeletal attachment, and production of second messengers when hydrolyzed (McLaughlin et Murray 2005). Three reviews have described PIP’s organization in the membrane (McLaughlin et Murray 2005), its role as an agonist (Hansen 2015), and the regulation of Kir channels (Fürst, Mondou, et D’Avanzo 2014). Briefly, PIP₂ is thought to bind Kir channels with high affinity, reversibly, dose-dependently, and with high specificity. PIP₂ is dynamically controlled, which means that a signaling cascade can rapidly modify its local concentration, causing the channels to open or close.

Kir2.1 channels are almost exclusively activated by PI(4,5)P₂, referred simply as PIP₂ throughout this text, and inhibited by its isomer, PI(3,4)P₂ (Rapedius et al. 2005; Fürst, D’Avanzo et al. 2013). On the other hand, some Kir channels (e.g., Kir6.2) are less stringent in their specificity for PIP activation and can be equally activated by PIP₂, PI(3,4)P₂, and PIP₃. Mutagenesis experiments combined with electrophysiology

and structural analysis of the PIP₂-bound Kir structures have elucidated a list of various positively charged residues potentially implicated in channel sensitivity to PI(4,5)P₂ activation in Kir2.1 (H53, R67, R82, K182, K185, K187, K188, R189, R218, K219, K228, and R312)(Bichet, Haass, et Jan 2003; D'Avanzo et al. 2013; Fürst, Mondou, et D'Avanzo 2014). Residues K185, R189, R218, and K219 were essential for ligand interaction, whereas H53, R67, R82, K182, K187, K188, K228, and R312, respectively, did not affect PIP₂-binding when mutated to Q (D'Avanzo et al. 2013). The apparent differences in PIP₂ interaction with Kir2.1 and Kir2.2 emphasize the need to solve Kir2.1 structure in the apo state as well as bound to different PIPs.

1.4 DYSFUNCTIONS IN THE HUMAN KIR2.1 CHANNEL LEAD TO ANDERSEN'S SYNDROME

Mutations in the Kir2.1 channel often lead to Andersen syndrome (AS). AS, also called Andersen-Tawil syndrome, is a rare autosomal disorder characterized by cardiac arrhythmias, muscle weakness (periodic paralysis), and multiple developmental abnormalities (dysmorphism). Over 38 loss-of-function mutations in KCNJ2 have been discovered to cause AS in humans (Tristani-Firouzi et Etheridge 2010; Fukumura et al. 2019). These mutations are found in the CTD N-terminal: C54F/Y, R67W/Q, R68Y, D71V/N, T74A, T75R/A/M, D78Y; on the outer helix: R82W/Q, in the extracellular domain: V123G, C154F; on the pore helix and its loops: S136F, G144S/A/D, G146D; and in the CTD at the level of the C-terminal: P186L, R189I, T192A, G215D, N216H, L217P, R218W/Q, V227F, V296F, G300V/D, V302M, E303K, T305A/P, T309I, and R312C/H. Three regions where amino acid deletions occur cause the syndrome: in the outer helix: residues 95 to 98, in the inner helix: residues 163 and 164, and in the CTD: residues 314 and 315. Other mutations have been identified to cause other pathologies such as type 3 short QT syndrome by the D172N mutation on the internal helix or the V93I mutation in the external helix, which leads to atrial fibrillation.

Despite the many mutations that have been discovered and the extensive work done with Kir2.1 channels, without the structure of the human Kir2.1 channel, the exact location of these mutations and their local environments and interactions cannot be pinpointed. Combined with the rarity of this disease, there is difficulty in developing medication. Therefore, to date, the treatment for AS patients is rather empirical. The astounding lack of standard procedure for AS patients is demonstrated by the

significant variation in medication prescribed and the low efficacy of the various drugs prescribed, notably beta-blockers but even Flecainide (Gamper et Wang 2021).

1.5 THESIS PROJECT OBJECTIVES

Given the paramount importance of Kir2.1 channels in human physiology and their implications for genetic disorders, we embarked on this thesis project to acquire insights into the structure-function relation of this channel. The emphasis of this thesis was thus to understand the impact of two clinically-relevant AS-causing mutations on the structure and function of Kir2.1 and provide a structural base for the potential development of pharmaceutical correctors later.

Despite having a 70.80% identity with Kir2.1 (Figure 1-5), there are no mutations in Kir2.2 that have been linked to AS. Therefore, the mechanisms at work must be distinct, and the amino acid sequence differences and potential structural differences may explain variations in channel regulation.

In order to gain insight into the mechanisms involved in channel gating and how PIP₂ induces or stabilizes the compressed state, there is a critical need for human Kir2.1 structures in different closed, intermediate, and open states, which can be incredibly difficult to obtain. Therefore we combined biochemical, biophysical, structural, functional, and *in silico* studies to overcome this barrier.

This ambitious project was divided into four objectives:

- 1) Establishing a robust protocol to obtain pure and homogenous human Kir2.1 recombinantly expressed in *Pichia pastoris* yeast;
- 2) The biophysical and biochemical characterization of human Kir2.1 and two naturally-occurring mutations responsible for AS: R312H and C154Y (Sacconi et al. 2009), described and studied in the next chapter. Both R312 and C154 are absolutely conserved in eukaryotic Kir channels (Figure 1-4, boxed in red);
- 3) To characterize the interaction between the Kir2.1 channel (WT and mutants) and the lipid PIP₂; and
- 4) To determine the structure of human Kir2.1 at high resolution using cryo-EM.

In our search to understand the gating mechanisms of Kir channels, I participated in the investigation of two KirBac3.1 mutations, W46R and S129R, as a collaborator, in order to evaluate the functional implications of a conserved residue in the TMD and

to explore the gating behavior of constitutively open channels. A dedicated chapter will address our findings.

1.6 BIBLIOGRAPHY

- Abbott, Geoffrey W, Margaret H Butler, Saïd Bendahhou, Marinos C Dalakas, Louis J Ptacek, et Steve A.N Goldstein. 2001. « MiRP2 Forms Potassium Channels in Skeletal Muscle with Kv3.4 and Is Associated with Periodic Paralysis ». *Cell* 104 (2): 217-31. [https://doi.org/10.1016/S0092-8674\(01\)00207-0](https://doi.org/10.1016/S0092-8674(01)00207-0).
- A-González, Noelia, et Antonio Castrillo. 2011. « Liver X Receptors as Regulators of Macrophage Inflammatory and Metabolic Pathways ». *Biochimica et Biophysica Acta (BBA) - Molecular Basis of Disease* 1812 (8): 982-94. <https://doi.org/10.1016/j.bbadis.2010.12.015>.
- Barel, Ortal, Stavit A. Shalev, Rivka Ofir, Asi Cohen, Joel Zlotogora, Zamir Shorer, Galia Mazor, et al. 2008. « Maternally Inherited Birk Barel Mental Retardation Dysmorphisms Syndrome Caused by a Mutation in the Genomically Imprinted Potassium Channel KCNK9 ». *The American Journal of Human Genetics* 83 (2): 193-99. <https://doi.org/10.1016/j.ajhg.2008.07.010>.
- Baronas, Victoria A., et Harley T. Kurata. 2014. « Inward rectifiers and their regulation by endogenous polyamines ». *Frontiers in Physiology* 5 (août). <https://doi.org/10.3389/fphys.2014.00325>.
- Baukrowitz, Thomas, et Bernd Fakler. 2000. « KATP Channels: Linker between Phospholipid Metabolism and Excitability ». *Biochemical Pharmacology* 60 (6): 735-40. [https://doi.org/10.1016/S0006-2952\(00\)00267-7](https://doi.org/10.1016/S0006-2952(00)00267-7).
- Bavro, Vassiliy N, Rita De Zorzi, Matthias R Schmidt, João R C Muniz, Lejla Zubcevic, Mark S P Sansom, Catherine Vénien-Bryan, et Stephen J Tucker. 2012. « Structure of a KirBac Potassium Channel with an Open Bundle Crossing Indicates a Mechanism of Channel Gating ». *Nature Structural & Molecular Biology* 19 (2): 158-63. <https://doi.org/10.1038/nsmb.2208>.
- Bichet, Delphine, Friederike A. Haass, et Lily Yeh Jan. 2003. « Merging Functional Studies with Structures of Inward-Rectifier K⁺ Channels ». *Nature Reviews Neuroscience* 4 (12): 957-67. <https://doi.org/10.1038/nrn1244>.
- Butler, Alice, Susan Tsunoda, David P. McCobb, Aguan Wei, et Lawrence Salkoff. 1993. « *MSlo*, a Complex Mouse Gene Encoding “Maxi” Calcium-Activated Potassium Channels ». *Science* 261 (5118): 221-24. <https://doi.org/10.1126/science.7687074>.
- Cardozo, David. 2016. « An Intuitive Approach to Understanding the Resting Membrane Potential ». *Advances in Physiology Education* 40 (4): 543-47. <https://doi.org/10.1152/advan.00049.2016>.
- Clarke, Oliver B., Alessandro T. Caputo, Adam P. Hill, Jamie I. Vandenberg, Brian J. Smith, et Jacqueline M. Gulbis. 2010. « Domain Reorientation and Rotation of an Intracellular Assembly Regulate Conduction in Kir Potassium Channels ». *Cell* 141 (6): 1018-29. <https://doi.org/10.1016/j.cell.2010.05.003>.
- D’Avanzo, Nazzareno, Krzysztof Hyrc, Decha Enkvetchakul, Douglas F. Covey, et Colin G. Nichols. 2011. « Enantioselective Protein-Sterol Interactions Mediate Regulation of Both Prokaryotic and Eukaryotic Inward Rectifier K⁺ Channels by Cholesterol ». Édité par Maria A. Deli. *PLoS ONE* 6 (4): e19393. <https://doi.org/10.1371/journal.pone.0019393>.
- D’Avanzo, Nazzareno, Sun-Joo Lee, Wayland W. L. Cheng, et Colin G. Nichols. 2013. « Energetics and Location of Phosphoinositide Binding in Human Kir2.1 Channels ». *The Journal of Biological Chemistry* 288 (23): 16726-37. <https://doi.org/10.1074/jbc.M113.452540>.
- D’Avanzo, Nazzareno, Roman Pekhletski, et Peter H. Backx. 2009. « P-Loop Residues Critical for Selectivity in K⁺ Channels Fail to Confer Selectivity to Rabbit HCN4 Channels ». Édité par Arnold Schwartz. *PLoS ONE* 4 (11): e7712. <https://doi.org/10.1371/journal.pone.0007712>.

- Diness, Jonas Goldin, Ulrik S. Sørensen, Jakob Dahl Nissen, Baha Al-Shahib, Thomas Jespersen, Morten Grunnet, et Rie Schultz Hansen. 2010. « Inhibition of Small-Conductance Ca^{2+} -Activated K^{+} Channels Terminates and Protects Against Atrial Fibrillation ». *Circulation: Arrhythmia and Electrophysiology* 3 (4): 380-90. <https://doi.org/10.1161/CIRCEP.110.957407>.
- Douppnik, Craig A, Norman Davidson, et Henry A Lester. 1995. « The Inward Rectifier Potassium Channel Family ». *Current Opinion in Neurobiology* 5 (3): 268-77. [https://doi.org/10.1016/0959-4388\(95\)80038-7](https://doi.org/10.1016/0959-4388(95)80038-7).
- Doyle, Declan A., João Morais Cabral, Richard A. Pfuetzner, Anling Kuo, Jacqueline M. Gulbis, Steven L. Cohen, Brian T. Chait, et Roderick MacKinnon. 1998. « The Structure of the Potassium Channel: Molecular Basis of K^{+} Conduction and Selectivity ». *Science* 280 (5360): 69-77. <https://doi.org/10.1126/science.280.5360.69>.
- Fomina, Svetlana, Tina D. Howard, Olivia K. Sleator, Marina Golovanova, Liam O’Ryan, Mark L. Leyland, J. Günter Grossmann, Richard F. Collins, et Stephen M. Prince. 2011. « Self-Directed Assembly and Clustering of the Cytoplasmic Domains of Inwardly Rectifying Kir2.1 Potassium Channels on Association with PSD-95 ». *Biochimica et Biophysica Acta (BBA) - Biomembranes* 1808 (10): 2374-89. <https://doi.org/10.1016/j.bbamem.2011.06.021>.
- Friedrich, Corinna, Susanne Rinné, Sven Zumhagen, Aytug K Kiper, Nicole Silbernagel, Michael F Netter, Birgit Stallmeyer, Eric Schulze-Bahr, et Niels Decher. 2014. « Gain-of-function Mutation in TASK -4 Channels and Severe Cardiac Conduction Disorder ». *EMBO Molecular Medicine* 6 (7): 937-51. <https://doi.org/10.15252/emmm.201303783>.
- Fukumura, Shinobu, Kosuke Yamauchi, Akira Kawanabe, Akiyo Yamamoto, Maki Nakaza, Tomoya Kubota, Shinsuke Kato, Ryogen Sasaki, Yasushi Okamura, et Masanori P. Takahashi. 2019. « Functional Analysis of a Double-Point Mutation in the KCNJ2 Gene Identified in a Family with Andersen-Tawil Syndrome ». *Journal of the Neurological Sciences* 407 (décembre): 116521. <https://doi.org/10.1016/j.jns.2019.116521>.
- Fürst, Oliver, Benoit Mondou, et Nazzareno D’Avanzo. 2014. « Phosphoinositide regulation of inward rectifier potassium (Kir) channels ». *Frontiers in Physiology* 4. <https://doi.org/10.3389/fphys.2013.00404>.
- Gamper, Nikita, et KeWei Wang, éd. 2021. *Pharmacology of Potassium Channels*. Vol. 267. Handbook of Experimental Pharmacology. Cham: Springer International Publishing. <https://doi.org/10.1007/978-3-030-84052-5>.
- Gardos, G. 1958. « The Function of Calcium in the Potassium Permeability of Human Erythrocytes ». *Biochimica et Biophysica Acta* 30 (3): 653-54. [https://doi.org/10.1016/0006-3002\(58\)90124-0](https://doi.org/10.1016/0006-3002(58)90124-0).
- Gribble, F. M. 1997. « The essential role of the Walker A motifs of SUR1 in K-ATP channel activation by Mg-ADP and diazoxide ». *The EMBO Journal* 16 (6): 1145-52. <https://doi.org/10.1093/emboj/16.6.1145>.
- Grube, Sabrina, Martin F. Gerchen, Bartosz Adamcio, Luis A. Pardo, Sabine Martin, Dörthe Malzahn, Sergi Papiol, et al. 2011. « A CAG Repeat Polymorphism of *KCNN3* Predicts SK3 Channel Function and Cognitive Performance in Schizophrenia ». *EMBO Molecular Medicine* 3 (6): 309-19. <https://doi.org/10.1002/emmm.201100135>.
- Hansen, Scott B. 2015. « Lipid Agonism: The PIP2 Paradigm of Ligand-Gated Ion Channels ». *Biochimica et Biophysica Acta (BBA) - Molecular and Cell Biology of Lipids* 1851 (5): 620-28. <https://doi.org/10.1016/j.bbalip.2015.01.011>.
- Heginbotham, Lise, Tatiana Abramson, et Roderick MacKinnon. 1992. « A Functional Connection Between the Pores of Distantly Related Ion Channels as Revealed by Mutant K^{+} Channels ». *Science* 258 (5085): 1152-55. <https://doi.org/10.1126/science.1279807>.
- Heginbotham, Lise, Zhe Lu, Tatiana Abramson, et Roderick MacKinnon. 1994. « Mutations in the K^{+} Channel Signature Sequence ». *Biophysical Journal* 66 (4): 1061-67. [https://doi.org/10.1016/S0006-3495\(94\)80887-2](https://doi.org/10.1016/S0006-3495(94)80887-2).

- Hibino, Hiroshi, Atsushi Inanobe, Kazuharu Furutani, Shingo Murakami, Ian Findlay, et Yoshihisa Kurachi. 2010. « Inwardly Rectifying Potassium Channels: Their Structure, Function, and Physiological Roles ». *Physiological Reviews* 90 (1): 291-366. <https://doi.org/10.1152/physrev.00021.2009>.
- Hilgemann, Donald W., Siyi Feng, et Cem Nasuhoglu. 2001. « The Complex and Intriguing Lives of PIP₂ with Ion Channels and Transporters ». *Science's STKE* 2001 (111). <https://doi.org/10.1126/stke.2001.111.re19>.
- Hille, Bertil. 1986. « Ionic Channels: Molecular Pores of Excitable Membranes ». *Harvey Lectures* 82: 47-69.
- Ho, Ivan H.M., et R.D. Murrell-Lagnado. 1999. « Molecular Determinants for Sodium-Dependent Activation of G Protein-Gated K⁺ Channels ». *Journal of Biological Chemistry* 274 (13): 8639-48. <https://doi.org/10.1074/jbc.274.13.8639>.
- Hodgkin, A. L., et A. F. Huxley. 1945. « Resting and Action Potentials in Single Nerve Fibres ». *The Journal of Physiology* 104 (2): 176-95. <https://doi.org/10.1113/jphysiol.1945.sp004114>.
- . 1952. « Movement of Sodium and Potassium Ions During Nervous Activity ». *Cold Spring Harbor Symposia on Quantitative Biology* 17 (0): 43-52. <https://doi.org/10.1101/SQB.1952.017.01.007>.
- Horio, Yoshiyuki, Hiroshi Hibino, Atsushi Inanobe, Mitsuhiko Yamada, Masaru Ishii, Yoshihiko Tada, Eisaku Satoh, Yutaka Hata, Yoshimi Takai, et Yoshihisa Kurachi. 1997. « Clustering and Enhanced Activity of an Inwardly Rectifying Potassium Channel, Kir4.1, by an Anchoring Protein, PSD-95/SAP90 ». *Journal of Biological Chemistry* 272 (20): 12885-88. <https://doi.org/10.1074/jbc.272.20.12885>.
- Ishii, Takahiro M., Christopher Silvia, Birgit Hirschberg, Chris T. Bond, John P. Adelman, et James Maylie. 1997. « A Human Intermediate Conductance Calcium-Activated Potassium Channel ». *Proceedings of the National Academy of Sciences* 94 (21): 11651-56. <https://doi.org/10.1073/pnas.94.21.11651>.
- Katz, Bernhard. 1949. « Les Constantes Electriques De La Membrane Du Muscle ». *Arch Sci Physiol* 3: 285-300.
- Ketchum, Karen A., William J. Joiner, Andrew J. Sellers, Leonard K. Kaczmarek, et Steve A. N. Goldstein. 1995. « A New Family of Outwardly Rectifying Potassium Channel Proteins with Two Pore Domains in Tandem ». *Nature* 376 (6542): 690-95. <https://doi.org/10.1038/376690a0>.
- Köhler, M., B. Hirschberg, C. T. Bond, J. M. Kinzie, N. V. Marrion, J. Maylie, et J. P. Adelman. 1996. « Small-Conductance, Calcium-Activated Potassium Channels from Mammalian Brain ». *Science* 273 (5282): 1709-14. <https://doi.org/10.1126/science.273.5282.1709>.
- Kuang, Qie, Pasi Purhonen, et Hans Hebert. 2015. « Structure of Potassium Channels ». *Cellular and Molecular Life Sciences* 72 (19): 3677-93. <https://doi.org/10.1007/s00018-015-1948-5>.
- Kubo, Yoshihiro, et Yoshimichi Murata. 2001. « Control of Rectification and Permeation by Two Distinct Sites after the Second Transmembrane Region in Kir2.1 K⁺ Channel ». *The Journal of Physiology* 531 (3): 645-60. <https://doi.org/10.1111/j.1469-7793.2001.0645h.x>.
- Kuo, Anling, Jacqueline M. Gulbis, Jennifer F. Antcliff, Tahmina Rahman, Edward D. Lowe, Jochen Zimmer, Jonathan Cuthbertson, Frances M. Ashcroft, Takayuki Ezaki, et Declan A. Doyle. 2003. « Crystal Structure of the Potassium Channel KirBac1.1 in the Closed State ». *Science* 300 (5627): 1922-26. <https://doi.org/10.1126/science.1085028>.
- Lafrenière, Ronald G, M Zameel Cader, Jean-François Poulin, Isabelle Andres-Enguix, Maryse Simoneau, Namrata Gupta, Karine Boisvert, et al. 2010. « A Dominant-Negative Mutation in the TRESK Potassium Channel Is Linked to Familial Migraine with Aura ». *Nature Medicine* 16 (10): 1157-60. <https://doi.org/10.1038/nm.2216>.

- Lopatin, A N, E N Makhina, et C G Nichols. 1995. « The Mechanism of Inward Rectification of Potassium Channels: “Long-Pore Plugging” by Cytoplasmic Polyamines. » *Journal of General Physiology* 106 (5): 923-55. <https://doi.org/10.1085/jgp.106.5.923>.
- Lopatin, A.N., et C.G. Nichols. 1996. « [K⁺] Dependence of Open-Channel Conductance in Cloned Inward Rectifier Potassium Channels (IRK1, Kir2.1) ». *Biophysical Journal* 71 (2): 682-94. [https://doi.org/10.1016/S0006-3495\(96\)79268-8](https://doi.org/10.1016/S0006-3495(96)79268-8).
- Lopatin, Anatoli N., Elena N. Makhina, et Colin G. Nichols. 1994. « Potassium Channel Block by Cytoplasmic Polyamines as the Mechanism of Intrinsic Rectification ». *Nature* 372 (6504): 366-69. <https://doi.org/10.1038/372366a0>.
- Lopes, Coeli M.B., Hailin Zhang, Tibor Rohacs, Taihao Jin, Jian Yang, et Diomedes E. Logothetis. 2002. « Alterations in Conserved Kir Channel-PIP2 Interactions Underlie Channelopathies ». *Neuron* 34 (6): 933-44. [https://doi.org/10.1016/S0896-6273\(02\)00725-0](https://doi.org/10.1016/S0896-6273(02)00725-0).
- Lu, Zhe, et Roderick MacKinnon. 1994. « Electrostatic Tuning of Mg²⁺ Affinity in an Inward-Rectifier K⁺channel ». *Nature* 371 (6494): 243-46. <https://doi.org/10.1038/371243a0>.
- Luckey, Mary. 2008. « Transporters and Channels ». In *Membrane Structural Biology: With Biochemical and Biophysical Foundations*, 241-70. Cambridge: Cambridge University Press. <https://doi.org/10.1017/CBO9780511811098>.
- Ma, Lijiang, Danilo Roman-Campos, Eric D. Austin, Mélanie Eyries, Kevin S. Sampson, Florent Soubrier, Marine Germain, et al. 2013. « A Novel Channelopathy in Pulmonary Arterial Hypertension ». *New England Journal of Medicine* 369 (4): 351-61. <https://doi.org/10.1056/NEJMoa1211097>.
- Matsuda, Hiroko, Akihiro Saigusa, et Hiroshi Irisawa. 1987. « Ohmic Conductance through the Inwardly Rectifying K Channel and Blocking by Internal Mg²⁺ ». *Nature* 325 (6100): 156-59. <https://doi.org/10.1038/325156a0>.
- McLaughlin, Stuart, et Diana Murray. 2005. « Plasma Membrane Phosphoinositide Organization by Protein Electrostatics ». *Nature* 438 (7068): 605-11. <https://doi.org/10.1038/nature04398>.
- Minor, Daniel L, Susan J Masseling, Yuh Nung Jan, et Lily Yeh Jan. 1999. « Transmembrane Structure of an Inwardly Rectifying Potassium Channel ». *Cell* 96 (6): 879-91. [https://doi.org/10.1016/S0092-8674\(00\)80597-8](https://doi.org/10.1016/S0092-8674(00)80597-8).
- Morais-Cabral, João H., Yufeng Zhou, et Roderick MacKinnon. 2001. « Energetic Optimization of Ion Conduction Rate by the K⁺ Selectivity Filter ». *Nature* 414 (6859): 37-42. <https://doi.org/10.1038/35102000>.
- Nishida, M., M. Cadene, BT Chait, et R. Mackinnon. 2007. « Crystals structure of a Kir3.1-prokaryotic Kir channel chimera ». *Embo Journal* 26 (17): 4005-15.
- Nishida, Motohiko, et Roderick MacKinnon. 2002. « Structural Basis of Inward Rectification ». *Cell* 111 (7): 957-65. [https://doi.org/10.1016/S0092-8674\(02\)01227-8](https://doi.org/10.1016/S0092-8674(02)01227-8).
- Niu, Yiming, Xiao Tao, Kouki K Touhara, et Roderick MacKinnon. 2020. « Cryo-EM Analysis of PIP2 Regulation in Mammalian GIRK Channels ». *ELife* 9 (août): e60552. <https://doi.org/10.7554/eLife.60552>.
- Oliver, Dominik, Thomas Baukrowitz, et Bernd Fakler. 2000. « Polyamines as Gating Molecules of Inward-Rectifier K⁺ Channels: Polyamines as Gating Molecules of K_{ir} Channels ». *European Journal of Biochemistry* 267 (19): 5824-29. <https://doi.org/10.1046/j.1432-1327.2000.01669.x>.
- Pegan, S, C Arrabit, W Zhou, W Kwiatkowski, A Collins, PA Slesinger, et S Choe. 2005. « Cytoplasmic domain structures of Kir2.1 and Kir3.1 show sites for modulating gating and rectification ». *Nature neuroscience* 8 (3): 279-87. <https://doi.org/10.1038/nn1411>.
- Pongs, Olaf, et Jürgen R. Schwarz. 2010. « Ancillary Subunits Associated With Voltage-Dependent K⁺ Channels ». *Physiological Reviews* 90 (2): 755-96. <https://doi.org/10.1152/physrev.00020.2009>.

- Potier, Marie, Virginie Joulin, Sébastien Roger, Pierre Besson, Marie-Lise Jourdan, Jean-Yves LeGuennec, Philippe Bognoux, et Christophe Vandier. 2006. « Identification of SK3 Channel as a New Mediator of Breast Cancer Cell Migration ». *Molecular Cancer Therapeutics* 5 (11): 2946-53. <https://doi.org/10.1158/1535-7163.MCT-06-0194>.
- Quinn, Kathryn V., Jonathan P. Giblin, et Andrew Tinker. 2004. « Multisite Phosphorylation Mechanism for Protein Kinase A Activation of the Smooth Muscle ATP-Sensitive K⁺ Channel ». *Circulation Research* 94 (10): 1359-66. <https://doi.org/10.1161/01.RES.0000128513.34817.c4>.
- Rapedius, Markus, Malle Soom, Ekaterina Shumilina, Dirk Schulze, Roland Schönherr, Cornelia Kirsch, Florian Lang, Stephen J. Tucker, et Thomas Baukowitz. 2005. « Long Chain CoA Esters as Competitive Antagonists of Phosphatidylinositol 4,5-Bisphosphate Activation in Kir Channels ». *Journal of Biological Chemistry* 280 (35): 30760-67. <https://doi.org/10.1074/jbc.M503503200>.
- Ruppertsberg, J.P., et B Fakler. 1996. « Complexity of the Regulation of Kir 2.1 K⁺ Channels ». *Neuropharmacology* 35 (7): 887-93. [https://doi.org/10.1016/0028-3908\(96\)00092-5](https://doi.org/10.1016/0028-3908(96)00092-5).
- Sansom, Mark S.P., Indira H. Shrivastava, Joanne N. Bright, John Tate, Charlotte E. Capener, et Philip C. Biggin. 2002. « Potassium Channels: Structures, Models, Simulations ». *Biochimica et Biophysica Acta (BBA) - Biomembranes* 1565 (2): 294-307. [https://doi.org/10.1016/S0005-2736\(02\)00576-X](https://doi.org/10.1016/S0005-2736(02)00576-X).
- Shi, Yun, Zhongying Wu, Ningren Cui, Weiwei Shi, Yang Yang, Xiaoli Zhang, Ashebo Rojas, Binh T. Ha, et Chun Jiang. 2007. « PKA Phosphorylation of SUR2B Subunit Underscores Vascular Kir_{ATP} Channel Activation by Beta-Adrenergic Receptors ». *American Journal of Physiology-Regulatory, Integrative and Comparative Physiology* 293 (3): R1205-14. <https://doi.org/10.1152/ajpregu.00337.2007>.
- Shyng, Show-Ling, Catherine A. Cukras, Jane Harwood, et Colin G. Nichols. 2000. « Structural Determinants of Pip2 Regulation of Inward Rectifier KATP Channels ». *Journal of General Physiology* 116 (5): 599-608. <https://doi.org/10.1085/jgp.116.5.599>.
- Stanfield, P R, N W Davies, P A Shelton, M J Sutcliffe, I A Khan, W J Brammar, et E C Conley. 1994. « A Single Aspartate Residue Is Involved in Both Intrinsic Gating and Blockage by Mg²⁺ of the Inward Rectifier, IRK1. » *The Journal of Physiology* 478 (1): 1-6. <https://doi.org/10.1113/jphysiol.1994.sp020225>.
- Tao, Xiao, Jose L. Avalos, Jiayun Chen, et Roderick MacKinnon. 2009. « Crystal Structure of the Eukaryotic Strong Inward-Rectifier K⁺ Channel Kir2.2 at 3.1 Å Resolution ». *Science* 326 (5960): 1668-74. <https://doi.org/10.1126/science.1180310>.
- Taura, Jaume, Daniel M. Kircher, Isabel Gameiro-Ros, et Paul A. Slesinger. 2021. « Comparison of K⁺ Channel Families ». In *Pharmacology of Potassium Channels*, édité par Nikita Gamper et KeWei Wang, 267:1-49. Handbook of Experimental Pharmacology. Cham: Springer International Publishing. https://doi.org/10.1007/164_2021_460.
- Tristani-Firouzi, Martin, et Susan P. Etheridge. 2010. « Kir 2.1 Channelopathies: The Andersen–Tawil Syndrome ». *Pflügers Archiv - European Journal of Physiology* 460 (2): 289-94. <https://doi.org/10.1007/s00424-010-0820-6>.
- Whorton, M. R., et R. MacKinnon. 2011. « Crystal Structure of the Mammalian GIRK2 K(+) Channel and Gating Regulation by G Proteins, PIP(2), and Sodium ». *Cell* 147 (1): 199-208. <https://doi.org/10.1016/j.cell.2011.07.046>.
- . 2013. « X-ray structure of the mammalian GIRK2-beta gamma G-protein complex ». *Nature* 498 (7453): 190+. <https://doi.org/10.1038/nature12241>.
- Williams, Sarah, Andrew Bateman, et Ita O'Kelly. 2013. « Altered Expression of Two-Pore Domain Potassium (K2P) Channels in Cancer ». Édité par Sven G. Meuth. *PLoS ONE* 8 (10): e74589. <https://doi.org/10.1371/journal.pone.0074589>.

- Xie, Lai-Hua, Scott A. John, Bernard Ribalet, et James N. Weiss. 2007. « Activation of Inwardly Rectifying Potassium (Kir) Channels by Phosphatidylinositol-4,5-Bisphosphate (PIP₂): Interaction with Other Regulatory Ligands ». *Progress in Biophysics and Molecular Biology* 94 (3): 320-35. <https://doi.org/10.1016/j.pbiomolbio.2006.04.001>.
- . 2008. « Phosphatidylinositol-4,5-Bisphosphate (PIP₂) Regulation of Strong Inward Rectifier Kir2.1 Channels: Multilevel Positive Cooperativity: Regulation of Kir2.1 Channel Gating by PIP₂ ». *The Journal of Physiology* 586 (7): 1833-48. <https://doi.org/10.1113/jphysiol.2007.147868>.
- Yamashita, T, Y Horio, M Yamada, N Takahashi, C Kondo, et Y Kurachi. 1996. « Competition between Mg²⁺ and Spermine for a Cloned IRK2 Channel Expressed in a Human Cell Line. » *The Journal of Physiology* 493 (1): 143-56. <https://doi.org/10.1113/jphysiol.1996.sp021370>.
- Yang, Dandan, Xiaoping Wan, Adrienne T. Dennis, Emre Bektik, Zhihua Wang, Mauricio G.S. Costa, Charline Fagnen, et al. 2021. « MicroRNA Biophysically Modulates Cardiac Action Potential by Direct Binding to Ion Channel ». *Circulation* 143 (16): 1597-1613. <https://doi.org/10.1161/CIRCULATIONAHA.120.050098>.
- Yang, Jian, Yuh Nung Jan, et Lily Y Jan. 1995a. « Control of Rectification and Permeation by Residues in Two Distinct Domains in an Inward Rectifier K⁺ Channel ». *Neuron* 14 (5): 1047-54. [https://doi.org/10.1016/0896-6273\(95\)90343-7](https://doi.org/10.1016/0896-6273(95)90343-7).
- Yang, Jian, Yuh Nung Jan, et Lily Yeh Jan. 1995b. « Determination of the Subunit Stoichiometry of an Inwardly Rectifying Potassium Channel ». *Neuron* 15 (6): 1441-47. [https://doi.org/10.1016/0896-6273\(95\)90021-7](https://doi.org/10.1016/0896-6273(95)90021-7).
- Yuan, Peng, Manuel D. Leonetti, Alexander R. Pico, Yichun Hsiung, et Roderick MacKinnon. 2010. « Structure of the Human BK Channel Ca²⁺-Activation Apparatus at 3.0 Å Resolution ». *Science* 329 (5988): 182-86. <https://doi.org/10.1126/science.1190414>.
- Zhou, Ming, et Roderick MacKinnon. 2004. « A Mutant KcsA K⁺ Channel with Altered Conduction Properties and Selectivity Filter Ion Distribution ». *Journal of Molecular Biology* 338 (4): 839-46. <https://doi.org/10.1016/j.jmb.2004.03.020>.
- Zhou, Yufeng, et Roderick MacKinnon. 2003. « The Occupancy of Ions in the K⁺ Selectivity Filter: Charge Balance and Coupling of Ion Binding to a Protein Conformational Change Underlie High Conduction Rates ». *Journal of Molecular Biology* 333 (5): 965-75. <https://doi.org/10.1016/j.jmb.2003.09.022>.
- Zhou, Yufeng, João H. Morais-Cabral, Amelia Kaufman, et Roderick MacKinnon. 2001. « Chemistry of Ion Coordination and Hydration Revealed by a K⁺ Channel–Fab Complex at 2.0 Å Resolution ». *Nature* 414 (6859): 43-48. <https://doi.org/10.1038/35102009>.
- Zubcevic, Lejla, Vassilij N. Bavro, Joao R.C. Muniz, Matthias R. Schmidt, Shizhen Wang, Rita De Zorzi, Catherine Venien-Bryan, Mark S.P. Sansom, Colin G. Nichols, et Stephen J. Tucker. 2014. « Control of KirBac3.1 Potassium Channel Gating at the Interface between Cytoplasmic Domains ». *Journal of Biological Chemistry* 289 (1): 143-51. <https://doi.org/10.1074/jbc.M113.501833>.

2 MATERIALS AND METHODS

This chapter will describe the materials and protocols used. It will also provide a detailed description of the techniques used and their theory, especially for surface plasmon resonance, SEC-MALLS, transmission electron microscopy, and image analysis. The later chapters will include reminders that were deemed necessary. This chapter is divided into seven sections: Expression and purification of Kir2.1, identification of post-translational modifications, biophysical characterization, functional assays, and lipid-protein interaction, reconstitution into model systems, structure determination, and study of the bacterial homolog KirBac3.1.

2.1 EXPRESSION AND PURIFICATION OF HUMAN KIR2.1 CHANNEL IN *PICHTIA PASTORIS*

2.1.1 Production

The human KCNJ2 gene construction was a gift from our collaborator S. Bendahhou (Université Côte d'Azur). It was integrated by collaborators R. Wagner and V. Kugler (IMPreSs facility) into a stable clone of the *Pichia pastoris* strain SMD1163 (*his4*, *pep4*, *prb1*) in the expression vector pPIC9K (Figure 2-1) by electroporation (Hartmann, Kugler, and Wagner 2016). The plasmid has a strong P_{AOX1} promoter inducible by methanol and has a kanamycin resistance gene which confers resistance to the antibiotic Geneticin 418 Sulfate (G418S, Corning). The synthetic gene encodes residues 1 to 427 of human Kir2.1 WT (Uniprot reference P63252) with a PreScission protease cleavage site (LEVLFQGP) followed by a linker of 11 amino acids and a tag composed of 10 His on the C-terminus.

The resulting Kir2.1 monomer has a theoretical molecular weight of 51.6 kDa and a theoretical isoelectric point of 5.89. Two Andersen Syndrome mutants, Kir2.1_R312H and Kir2.1_C154Y, were also produced.

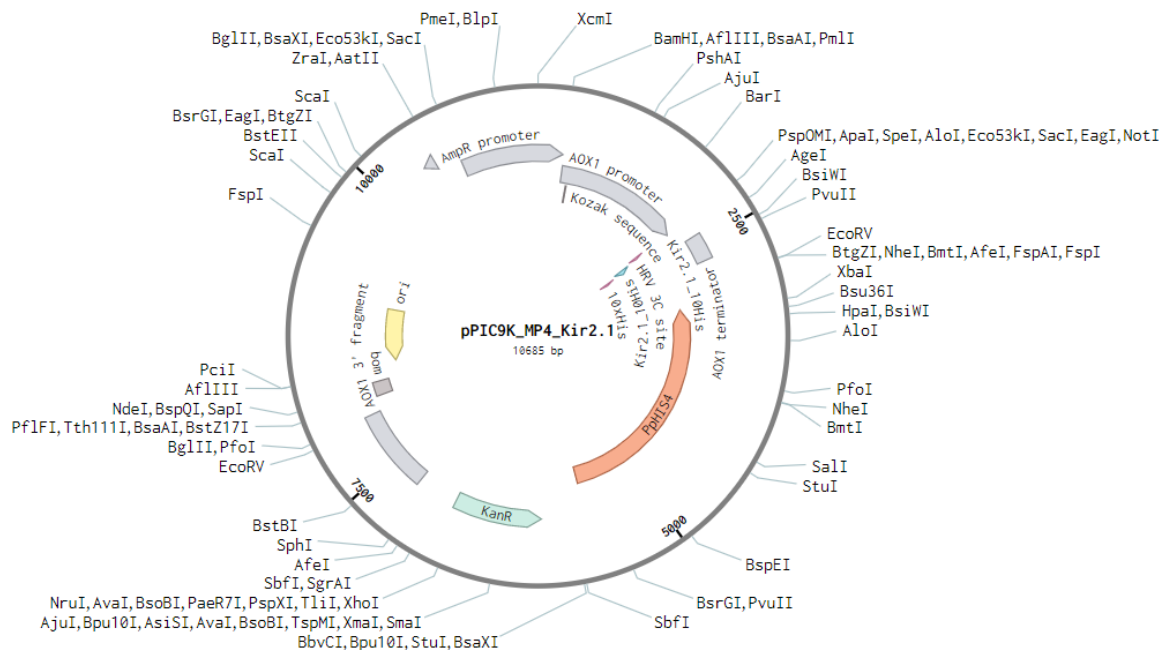


Figure 2-1: pPIC9K expression vector.

The best clones were selected *via* an *in situ* yeastern blot immunoassay. Yeastern blot is a technique where individual yeast colonies can be plotted on a nitrocellulose membrane, directly lysed, and subjected to *in situ* immunodetections (Hartmann, Kugler, and Wagner 2016). The *Pichia pastoris* cells containing the KCNJ2 gene were kept at $-80\text{ }^{\circ}\text{C}$, then spread in a YPGA plate (Table 2-1) at $30\text{ }^{\circ}\text{C}$ for 48 h, and then streaked onto a YPGA plate containing $50\text{ }\mu\text{g}\cdot\text{mL}^{-1}$ G418 Sulfate (Corning) antibiotic. These cells were then used for an overnight 500 mL starter culture in BMGY medium (Table 2-1) with 180–220 rpm agitation using Thompson flasks. The next day, the cells were diluted to an optical density at 600 nm ($\text{OD}_{600\text{nm}}$) of 1 and incubated at $30\text{ }^{\circ}\text{C}$ with 220–250 rpm agitation until the $\text{OD}_{600\text{nm}}$ reached 6–8, as previously described (Hartmann, Kugler, and Wagner 2016). The cells were pelleted via centrifugation at $4,000\cdot\text{g}$ for 10 min at $4\text{ }^{\circ}\text{C}$. Then resuspended into BMMY buffer (Table 2-1) for induction with an initial $\text{OD}_{600\text{nm}}$ of 3–3.5 for 18–24 h at $22\text{ }^{\circ}\text{C}$ with agitation at 220–250 rpm. All these steps, illustrated in Figure 2-2, were done under sterile conditions. The induction was followed by two centrifugations at $4,000\cdot\text{g}$ at $4\text{ }^{\circ}\text{C}$ for 10 min; washing in phosphate buffer saline (PBS, Table 2-1) at pH 7.4 to remove all traces of the BMMY medium. The resulting pellet was frozen at $-80\text{ }^{\circ}\text{C}$.

Table 2-1 Composition of cell culture and induction media

YPGA	%	BMGY pH 6.0	% / M	BMMY pH 6.0	% / M	PBS	%

Yeast extract	1%	Yeast extract	1%	Yeast extract	1%	NaCl	0.8%
Peptone	2%	Peptone	2%	Peptone	2%	KCl	0.02%
Glucose	2%	Glycerol	1%	Methanol	0.5%	Na ₂ HPO ₄	0.14%
Agar	2%	YNB	1.34%	YNB	1.34%	KH ₂ PO ₄	0.02%
		K ₂ HPO ₄	0.013 M	K ₂ HPO ₄	0.013 M		
		KH ₂ PO ₄	0.087 M	KH ₂ PO ₄	0.087 M		

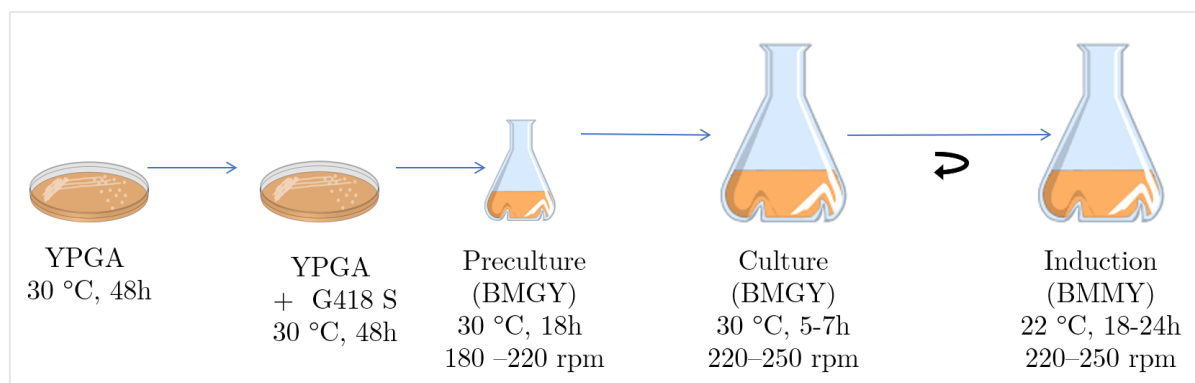


Figure 2-2: Summary of Kir2.1 expression protocol

2.1.2 Cell lysis

2.1.2.1 Enzymatic lysis and Cell Disruptor

The pellet was thawed and suspended in 3 mL of TKE buffer (Table 2-2) per gram of pellet for 0.25 g · mL⁻¹ pellet concentration. Phenylmethylsulfonyl fluoride (PMSF, 1 mM, Merck), a cocktail of protease inhibitors, Benzonase, and 20 U Zymolyase (AMSBio) per g of pellet initially present were added to the pellet. After incubating for 15 min at room temperature (RT) with gentle agitation, the cells were lysed mechanically by 3–6 passes at high pressure (2500–2700 Pa) using a Cell Disruptor (Cell D, Constant systems) at 4 °C.

2.1.2.2 Mechanical lysis by glass beads

Alternatively, the cells were lysed with glass beads (Table 2-3) as described previously (Hartmann, Kugler, and Wagner 2016), with a few modifications. The cell pellet was resuspended in 40 mL of TKGE buffer (Table 2-2), then 1 mM PMSF and glass beads (450–600 μm, Merck) were added, and the cells were lysed mechanically using the FastPrep-24 (MP) at 6.5 m · s⁻¹ for three 40 s cycles.

Table 2-2 Summary of resuspension and solubilization buffers

Name	Composition
TKE buffer	20 mM Tris-HCl pH 7.4, 150 mM KCl, 1 mM EDTA (ethylenediaminetetraacetic acid, Sigma-Aldrich),
TKGE buffer	50 mM Tris-HCl pH 7.4, 500 mM KCl or NaCl, 10% Glycerol, 1 mM EDTA, 1 mM PMSF
TK buffer	20 mM Tris pH 7.4 and 150 mM KCl
TKI buffer	20 mM Tris pH 7.4, 150 mM KCl, and 30 mM Imidazole
Solubilization buffer	TK buffer + 1.5% DDM
TKED	20 mM Tris pH 7.4, 150 mM KCl, 1 mM EDTA, and 0.59 mM DDM
SED buffer	1 M Sorbitol, 25 mM EDTA, 50 mM DTT
CG buffer	20 mM trisodium citrate pH 5.8, 10% glycerol, 1 mM PMSF
Protoplast solubilization buffer	20 mM Tris-HCl pH 7.4, 300 mM KCl, 10% glycerol, 30 mM imidazole, protease inhibitors, 1.5% DDM

Table 2-3 Summary of lysis conditions

Protein Organism	Lysis Method	Equipment	Lysis conditions	Buffer
Kir2.1 <i>Pichia pastoris</i>	Enzymatic	Zymolyase	20 U/g of pellet 15 min at RT	TKE buffer, 1 mM PMSF
	Mechanic	Cell Disruptor	3–6 passes at 2.5 kbar	
		Glass beads	450–600 μm glass beads (Merck) $6.5 \text{ m} \cdot \text{s}^{-1}$, 40 s (x3)	TKGE buffer
MSPs <i>E. coli</i>	Mechanic	Sonicator	Time: 20 min Pulse on: 5 s Pulse off: 15 s Amplitude: 35–40%	20 mM phosphate buffer pH 7.4, 1 mM PMSF, 1% Triton X-100
KirBac3.1 <i>E. coli</i>	Enzymatic	Lysozyme	$500 \mu\text{g} \cdot \text{mL}^{-1}$ 15 min at RT	50 mM Tris-HCl, pH 8, 150 mM KCl, $4 \mu\text{g} \cdot \text{mL}^{-1}$ DNase
	Mechanic	Cell Disruptor	2 passes at 2.0 kbar	

2.1.3 Membrane Preparation

Cell debris was removed by 5 min centrifugation at $4,000 \cdot g$ at $4 \text{ }^\circ\text{C}$. The supernatant was collected, and crude membranes were pelleted at $100,000 \cdot g$ (31,100 rpm, using Beckman rotor JA 30.50) for 30 min.

2.1.4 Quantification of membranes

The MP pellet was resuspended in TKI buffer (20 mM Tris pH 7.4, 150 mM KCl, and 30 mM Imidazole) and quantified by bicinchoninic acid (BCA) assay. The BCA assay is a relative quantification method based on copper reduction (from Cu^{2+} to Cu^+) by the peptide bonds of the proteins present in the solution to be studied under alkaline conditions. Cu^+ ions are chelated by two molecules of BCA, resulting in a purple complex with a maximum absorbance at 562 nm. The protein concentration of the solution was determined by comparing the results with a standard curve with BSA.

2.1.5 Solubilization of membranes

2.1.5.1 *Dodecyl-D-maltoside*

The resuspended membranes were diluted to $2 \text{ mg} \cdot \text{mL}^{-1}$ and solubilized with 1.5% dodecyl-D-maltoside (DDM, Glycon) for 30–45 min at RT with gentle agitation. The sample was centrifugated at $100,000 \cdot \text{g}$ for 30 min at $4 \text{ }^\circ\text{C}$ to clarify solubilized MPs.

2.1.5.2 *FC14*

Alternatively, the resuspended membranes were diluted up to $6 \text{ mg} \cdot \text{mL}^{-1}$ and solubilized with 0.5% Foscholine 14 (FC14, Anatrace) for 30–45 min at RT with gentle agitation. Final centrifugation was performed at $100,000 \cdot \text{g}$ for 30 min at $4 \text{ }^\circ\text{C}$ to clarify solubilized MPs.

2.1.6 Direct extraction by the formation of protoplasts

Alternatively, Kir2.1 WT was extracted in protoplasts and solubilized directly without membrane preparation, following Hartmann's protocol (Hartmann et al. 2017), where the membrane is weakened by osmosis. Briefly, the cell pellet was washed in mQ H_2O , then in SED buffer (Table 2-2), followed by 1 mM Sorbitol wash, with 5 min centrifugation at $5,000 \cdot \text{g}$, $4 \text{ }^\circ\text{C}$ between washes. The pellet was resuspended in CG buffer (Table 2-2), protease inhibitors were added, 20 U Zymolyase per g of pellet, and incubated for 15 min at RT with gentle agitation. The sample was centrifuged for 5 min at $750 \cdot \text{g}$, RT at minimum acceleration and deceleration speeds. The supernatant was discarded carefully, and the protoplast solubilization buffer containing 1.5% DDM (Table 2-2) was added. After 30 min incubation at RT, the suspension was centrifuged for 30 min at $100,000 \cdot \text{g}$ at $4 \text{ }^\circ\text{C}$.

2.1.7 Affinity chromatography

In order to purify the protein of interest, the solubilized protein extract was incubated with Co^{2+} beads (1 mL of TALON resin, ClonTech) overnight at 4 °C and deposited onto a gravity column; the proteins not retained were collected and named Ft (flowthrough). First, two successive washes were carried out with a high salinity buffer (HS) and a low salinity buffer (LS) (Table 2-4). Then, the protein was eluted in elution buffers E1–E4 (Table 2-4) with increasing concentrations of imidazole, which competes with the protein for cobalt chelation. 5 mM 1,4-Dithiothreitol (DTT, Sigma-Aldrich) and 2 mM EDTA were added to the fractions. They were either used immediately or stored overnight at 4 °C.

Table 2-4 Composition of affinity chromatography buffers for Kir2.1

	Tris-HCl pH 7.4 (mM)	KCl (mM)	DDM (mM)	Imidazole (mM)	Volume (CV)
HS	20	500	0.98	30	20
LS	20	150	0.98	30	20
E1	20	150	0.59	90	2
E2	20	150	0.59	150	5
E3	20	150	0.59	350	7
E4	20	150	0.59	500	2

2.1.8 Size exclusion chromatography

The 150-350 mM imidazole fractions containing Kir2.1 were filtered through a 0.22 μm PES membrane and concentrated by centrifugation at 800 $\cdot\text{g}$ in 100 kDa Millipore filter-concentration tubes. Between 200 μL and 400 μL of protein concentrated at 1 $\text{mg}\cdot\text{mL}^{-1}$ were injected into a Superdex 200 Increase 10/300 GL column (Cytiva) previously equilibrated in SEC buffer (20 mM Tris pH 7.4, 150 mM KCl, 1 mM EDTA, and 0.59 mM DDM). The ÄktaPurifier system was used in isocratic mode at a 0.3 $\text{mL}\cdot\text{min}^{-1}$ flow rate and a fraction volume of 0.5 mL.

2.2 IDENTIFICATION OF KIR2.1 FRACTIONS AND POST-TRANSLATIONAL MODIFICATIONS

2.2.1 Identification of Kir2.1 fractions

2.2.1.1 Protein precipitation using TCA

Samples were precipitated by trichloroacetic acid (TCA) before electrophoresis. Pure TCA was added at a 1:10 volume ratio as the fraction to precipitate, mixing well. After 30-min incubation on ice, the samples were centrifuged at $12,000 \cdot g$ for 15 min at RT. The supernatant was carefully discarded. The pellet was resuspended in 5 μL of 4x Laemmli sample buffer (SB, Bio-Rad, Table 2-5), and 5 μL of Tris-HCl pH 8.8 were added to render the pH basic.

2.2.1.2 SDS-PAGE: Sodium dodecyl sulfate-polyacrylamide gel electrophoresis

This technique allows the separation of proteins based on their molecular weight. Following TCA treatment, the samples were mixed with SB containing dithiothreitol (DTT, Euromedex) (Table 2-5) and added to the gels. The gels used were made in the lab using 4% stacking gel and 10% separating gel. The migration occurs at a constant amperage of 20 mA, 180 V between 45 min and 1 h with a Tris-Glycine-SDS buffer (Table 2-5).

2.2.1.3 Native PAGE

Native PAGE gels were made under non-denaturing and non-reducing conditions without TCA precipitation. The samples were mixed with Native-SB (Table 2-5) and loaded onto ready-to-use 4–15% Mini-PROTEAN TGX gels (Bio-Rad). Migration takes place using Tris-Glycine buffer (Table 2-5) at constant amperage, 20 mA, 180 V, in a cold room for up to 4 h. (Wittig, Braun, and Schägger 2006)

2.2.1.4 Gel staining

We reveal with Coomassie blue (G250 Bio-Safe, BioRad) by rinsing the gel after electrophoresis and applying the coomassie solution until the bands turn blue. Then rinse with Milli-Q water. Alternatively, we reveal the gel with silver staining using SilverQuestTM Silver Staining Kit (ThermoFisher Scientific) and following the

manufacturer's instructions. Briefly, the gel was incubated with a fixative reagent (40% ethanol, 10% acetic acid) followed by several washes of 30% ethanol, sensitizing solution, 30% ethanol, and water. The gel was then stained with silver nitrate and developed. What about coomassie blue?

2.2.1.5 Western blot

This technique allows verifying the presence of the protein by immunodetection. We use the antigen-antibody relationship from the histidine tag and the anti-polyhistidine antibody (Abcam). Transfer from the gel to a polyvinylidene fluoride membrane (PVDF, 0.45 μm , Cytiva) takes place for 2 h at a constant voltage, 100 V, in a transfer buffer (Table 2-5). Alternatively, Bio-Rad transblot and reagents were used for a 7-min turbo transfer. The membrane was washed with TBS-T (Table 2-5) and incubated for 1 h in a blocking solution (5% milk) to avoid non-specific interactions; after a quick wash with TBS-T, the membrane was incubated 45 min in a solution of 0.1% (v/v) anti-polyhistidine antibody coupled to alkaline phosphatase. The membrane was then washed with TBS-T for 20 min to remove the excess antibodies. The revelation was carried out by nitro-blue tetrazolium (NBT) and 5-bromo-4-chloro-3'-indolyphosphate (BCIP) (Merck), BCIP being the substrate for the alkaline phosphatase.

Table 2-5 Composition of Electrophoresis and Western blot buffers at working conditions

Name	Composition
4x Laemmli sample buffer (SB)	277.8 mM Tris-HCl pH 6.8, 44.4% glycerol, 4.4% LDS, 0.02% bromophenol blue, 200 mM DTT
Native-SB	40% glycerol, 0.02% bromophenol blue, and 248 mM Tris pH 8.8
Tris-Glycine-SDS running buffer	25 mM Tris pH 8.3, 192 mM glycine, and 0.1% SDS
Tris-Glycine running buffer	25 mM Tris pH 8.3, 192 mM glycine
Transfer Buffer	25 mM Tris pH 8.3, 192 mM glycine, and 0.01% SDS
TBS-T (1X)	20 mM Tris pH 7.4, 150 mM NaCl, 0.05 % Tween 20

2.2.2 Mass Spectrometry and Post-Translational Modifications

Identification of fractions was done by mass spectrometry. Matrix-assisted laser desorption ionization-time of flight (MALDI-TOF) mass spectrometry (MS) was used to determine the protein's molecular weight from the protein's mass to charge (m/z) ratio in linear mode. Then, the sample was desalted and concentrated using Sep-Pak and followed by a digestion step with trypsin gold (Promega). A second MALDI-TOF

test was carried out in tandem (MS/MS), and the peptides obtained were compared with the theoretical sequence.

2.2.2.1 Phosphorylation

Phosphorylation has been investigated by mass spectrometry in solution and in-gel digestion. An enrichment step with titanium oxide (TiO₂) was necessary to determine the phosphorylation sites. Next, an electrospray ionization (ESI) analysis coupled with nanoflow liquid chromatography (nanoLC) with two orbitrap analyzers in tandem was carried out at the IBPS platform (L. Matheron). The analysis from gel digestion was performed at Pasteur Institute (M. Matondo and M. Duchateau).

2.2.2.2 Glycosylation

Kir2.1 was treated with endoglycosidase PNGase F (Sigma-Aldrich) according to the manufacturer's protocol with a few modifications:

For 45 μL of protein solution (up to $5.7 \text{ mg} \cdot \text{mL}^{-1}$) at pH 7.5, 2.5 μL of 2% SDS and 1 M β -ME solution and incubate for 24 h. Add 2.5 μL of 15% (v/v) TRITON X-100 (Anatrace) and 2.0 μL PNGaseF ($2,000 \text{ U} \cdot \text{mL}^{-1}$) to the solution and incubate for 3 h at 37 °C. The reaction was carried out with a positive control (100 kDa contaminant) and a negative control (sample treated with SDS and TRITON but without PNGase F).

Glycosylation was investigated via in-gel digestion of two gel bands using MS/MS on an ESI-Quadrupole-TOF instrument at the I2BC platform (D. Cornu).

2.3 BIOPHYSICAL CHARACTERIZATION OF KIR2.1

2.3.1 Dynamic Light Scattering

2.3.1.1 Introduction

Dynamic light scattering (DLS) is a non-invasive technique that can study the dynamic properties of proteins in solution. By observing the intensity fluctuations caused by particles' random motion as they collide in a fluid (Brownian motion), DLS allows the determination of a particle's size. Because DLS can measure the effects of buffer conditions on the sample, this technique is often used as a buffer optimization step.

The velocity of Brownian motion is defined by the translational diffusion coefficient (D_T), which can then be used in the Stokes-Einstein equation to determine particle size (Stetefeld, McKenna, and Patel 2016):

Equation 2-1

$$R_H = \frac{k_B T}{6\pi\eta D_T}$$

where:

R_H is the hydrodynamic radius, k_B is Boltzmann's constant $1.3806 \cdot 10^{-23} \text{ J} \cdot \text{K}^{-1}$, T is the thermodynamic temperature, η is the medium's viscosity, and D_T is the translational diffusion coefficient.

R_H is the radius of the hypothetical sphere that diffuses at the same velocity as the molecule being measured; it depends on the shape, surface structure, Debye length (κ^{-1}), and ionic strength of the molecule. The Debye length is the distance of a particle's net screening or electrostatic effect in a solution; it is inversely proportional to the ionic strength (Figure 2-3). Samples in a high ionic strength solution show a smaller diameter than samples in a low ionic strength solution (Stetefeld, McKenna, and Patel 2016; Debye and Hückel 1923).

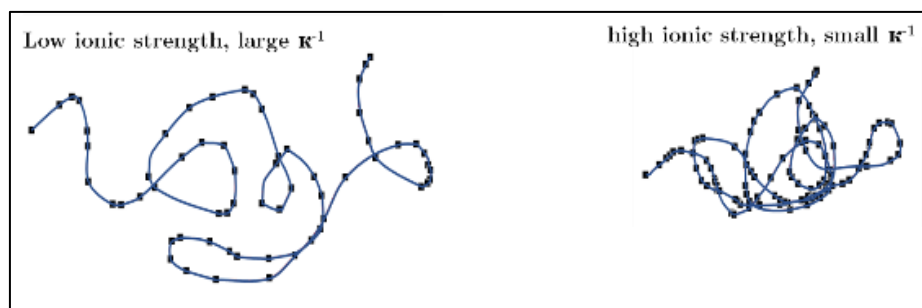


Figure 2-3: Effect of ionic strength on the sample

The DLS detector sees the scattered photons as a function of time; thus, the intensity fluctuates over time. In order to measure these fluctuations, the time scales studied must be rapid: nano- to microseconds. Particles of different sizes fluctuate at different rates. Small particles diffuse rapidly, so the intensity fluctuates quickly over time, whereas large particles diffuse slowly, so there is a slow fluctuation for large particles. The time dependence must be calculated to determine the particle's size.

The time correlation is studied by multiplying the number of photons separated by the delay time. Delay time + fluctuation = loss of correlation. Smaller particles diffuse faster than large particles, so their correlation loss is faster than larger particles. When

comparing the correlation after a short delay, the particles have not diffused much, so the correlation is close to one, and the decay is close to zero. At longer delay times, the correlation decreases, and the decay rate becomes exponential. We get the correlation function if we plot this exponential decay in logarithm.

Equation 2-2

$$G(\tau) = \langle I(t_0) \cdot \frac{I(t_0 + \tau)}{I(t_\infty)^2} \rangle$$

where:

$G(\tau)$ is the time autocorrelation function, I is the scattered intensity, t is the time, and τ is the delay between two points. The brackets $\langle \rangle$ represent averages. The intensity at the initial time (t_0) is multiplied by the intensity at t_0 plus a delay time divided by the intensity at time infinity. In other words, the scattering at t_0 is compared to that at different time intervals, and a correlation is established. Because the diffusion occurs in ns- μ s time scale, t_∞ is just a couple of seconds.

2.3.1.2 *Experimental setup*

A laser shines light onto a cuvette containing the sample to be analyzed. After colliding with molecules, the incident light is scattered at all angles and is collected at a 90° angle by a detector. The resulting scattered (diffracted) photons can either be in a destructive or constructive phase where they cancel each other out or produce a signal (speckle pattern). This signal is analyzed at different time intervals and autocorrelated to extract information about the molecules' dynamics.

2.3.1.3 *Measurements*

DLS was used to investigate the hydrodynamic properties of purified Kir2.1 on a DynaPro instrument (Wyatt Technology Corp., Santa Barbara, CA). The sample temperature was set to 8 °C with TC100-830 Temperature Controlled MicroSampler (Protein Solutions/Wyatt Technology Corp). 20 μ L of Kir2.1 at varying concentrations post-SEC purification were loaded onto a cuvette and placed on the DynaPro. The laser light wavelength was 830 nm, the scattered light was collected at 90° of the incident light, and the correlation time was set to 0.5 ms with an acquisition time of 10 s for a total measurement of up to 1600 s.

2.3.1.4 Data Analysis

Data obtained on DLS were analyzed using Dynamics software versions 6 and 7. First, all data points were plotted as a histogram, and the R_H and the polydispersity percentage (%P, standard deviation) were obtained directly.

2.3.2 SEC-MALLS: a triple detection method to characterize membrane proteins in solution

2.3.2.1 Introduction

The oligomeric state of membrane proteins (MPs) is challenging to study. Due to the detergent micelles associated with MPs, classical methods to estimate the molecular mass of proteins from the hydrodynamic radius, such as SEC, DLS, native gels, and sedimentation velocity measurements, do not work well on MPs. SEC alone, for example, cannot even give a reliable estimate of the MP-detergent hydrodynamic ratio as lipids can also be associated with the complex. Therefore, these methods cannot be used to infer the oligomeric state of MPs. Two methods that can accurately measure the molecular mass of MPs, independently of the amount of detergent bound, are sedimentation equilibrium centrifugation and static light scattering (Slotboom et al. 2008).

Kir2.1 was characterized by size-exclusion chromatography coupled with multiple angle laser light scattering and differential refractive index (SEC-MALLS). This technique determines the mass of the MP-detergent (MPD) complex and MP and D fractions and the homogeneity of the complex without depending on column calibration. Unlike DLS, where the measurements were done in-batch, the SEC column allows the separation of biomolecules by hydrodynamic radius, and each complex can be characterized separately.

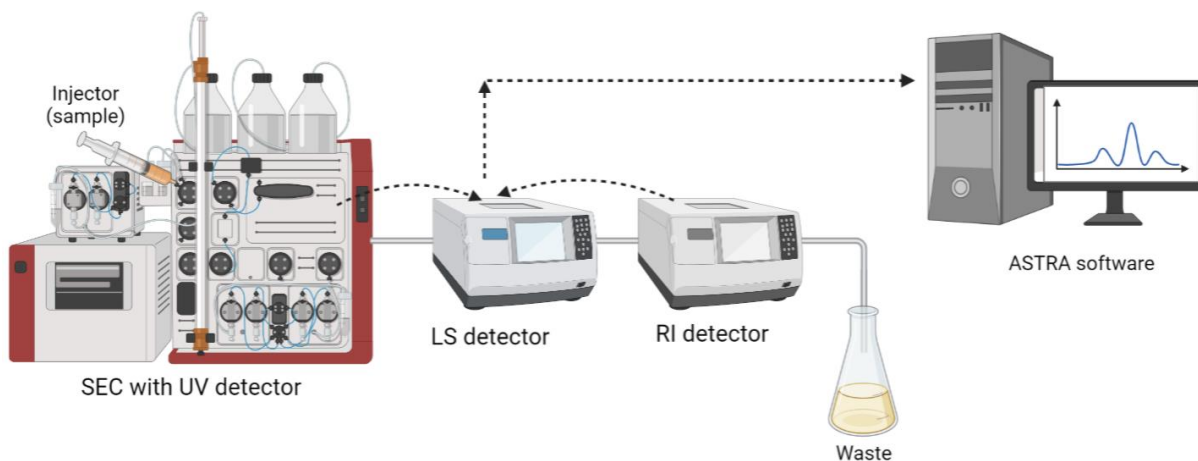


Figure 2-4. SEC-MALLS configuration

The classical Rayleigh relationship describes static light scattering (LS):

Equation 2-3

$$\Delta R_{\theta} = R_{\theta_{sample}} - R_{\theta_{solution}} = K \left(\frac{dn}{dc} \right)^2 M_w c$$

where:

$$\Delta R_{\theta} = \frac{I_{sample} - I_{solvent}}{I_{toluene}} \left(\frac{n_0^2}{n_{toluene}^2} \right) R_{toluene}$$

and

Equation 2-4

$$K = \frac{4\pi^2 n_0^2}{N_A \lambda^4}$$

R_{θ} denotes the Rayleigh ratio, defined as the total intensity of scattered light measured at a scattering angle θ from the scattering point. ΔR_{θ} denotes the excess light scattered by the sample minus that of the solvent normalized by the scattering of a very pure solvent, Toluene. M_w is the weight-averaged molecular mass; K is an optical constant that depends on the RI of the solvent alone (n_0), and the wavelength of the light (λ).

N_A is Avogadro's number.

c is the concentration of the MP (in $\text{mg} \cdot \text{ml}^{-1}$) and is related to the absorbance (UV_{280}) and molar absorptivity (A_{280}) by Beer-Lambert's equation.

Equation 2-5

$$c_{protein} = \frac{\Delta UV_{280}}{A_{280}} \text{ at a 1 cm pathlength;}$$

A_{280} is the molar extinction coefficient expressed in $M^{-1} \cdot cm^{-1}$ and is calculated from the protein's sequence based on the tryptophan (W), tyrosine (Y), and cysteine (C) amino acid composition.

Equation 2-6

$$A_{280} (M^{-1}cm^{-1}) = 5500 \cdot nW + 1490 \cdot nY + 125 \cdot nC$$

Alternatively, $c_{protein}$ can be determined with a refractometer if the dn/dc of the protein is known from literature or has been determined experimentally. The dn/dc is the increment in the specific refractive index; it relates the change in the sample's refractive index (ΔRI , background-corrected signal) to its concentration.

Equation 2-7

$$c_{protein} = \frac{\Delta RI}{\frac{dn}{dc}}$$

Typically, the dn/dc for soluble proteins are well known (around $0.187 \text{ mL} \cdot \text{g}^{-1}$), but it can also be calculated using SEDFIT software from the primary structure. Unlike soluble proteins, MPs are associated with detergents in solution, so we need to account for the mass of the detergent bound per gram of protein (δ). Knowledge of the amount of detergent bound (δ) to the protein can help optimize buffer conditions, as too little detergent can promote aggregation and too much can hinder the stability of the MP (Privé 2007). We thus study the MP-detergent (MPD) complex combining SEC (UV) with LS and RI, which allows us to determine the protein's mass and calculate the amount of detergent bound to it (Gimpl, Klement, and Keller 2016; Slotboom et al. 2008).

Equation 2-8

$$M_{Wcomplex} = (1 + \delta)M_{Wprotein}$$

And thus

Equation 2-9

$$c_{complex} = (1 + \delta)c_{protein}$$

With

Equation 2-10

$$A_{280,complex} = \left(\frac{1}{1+\delta}\right) \cdot A_{280,protein} + \left(\frac{\delta}{1+\delta}\right) \cdot A_{280,detergent}$$

and

Equation 2-11

$$\frac{dn}{dc_{complex}} = \left(\frac{1}{1+\delta}\right) \frac{dn}{dc_{protein}} + \left(\frac{\delta}{1+\delta}\right) \cdot \frac{dn}{dc_{detergent}}$$

Alternatively, dn/dc of the complex can be determined experimentally

Equation 2-12

$$\frac{dn}{dc_{complex}} = \frac{\Delta RI}{\Delta UV_{280}} \left[\left(\frac{1}{1+\delta}\right) \cdot A_{280,protein} + \left(\frac{\delta}{1+\delta}\right) \cdot A_{280,detergent} \right]$$

If the detergent used does not absorb at 280nm, the mass of the protein component within the MPD complex can be easily calculated using the triple detection method:

Equation 2-13

$$M_{Wprotein} = \frac{\Delta LS \cdot \Delta UV_{280}}{K \cdot A_{280,protein} (\Delta RI)^2}$$

Alternatively, the ASTRA software package can calculate the detergent-bound (δ) amount and determine the component masses directly from the refractive index and the UV absorption data using the *Protein Conjugate* procedure if the dn/dc and A_{280} are known for both the protein and detergent.

Equation 2-14

$$\delta = \frac{\left(\frac{\Delta RI \cdot A_{280,protein}}{\Delta UV_{280}}\right) - \left(\frac{dn}{dc}\right)_{protein}}{\left(\frac{dn}{dc}\right)_{detergent} - \left(\frac{\Delta RI \cdot A_{280,detergent}}{\Delta UV_{280}}\right)}$$

Furthermore, solve for the $dn/dc_{complex}$, which is then used to determine the mass of the MPD complex.

Equation 2-15

$$M_{Wcomplex} = \frac{\Delta LS}{K \left(\frac{dn}{dc}\right)_{complex}^2 (1+\delta) \cdot c_{protein}}$$

The software then determines the mass fractions of the protein and detergent.

2.3.2.2 Experimental setup

All buffers were prepared using pure Milli-Q water with a resistivity of 15 M Ω cm using the Elix®, Millipore purification system, filtered through a 0.22 μ m filter, and degassed using Millipore vacuum pumps (Merck). A Superdex 200 Increase 10/300 GL column (S200, Cytiva) was connected to a Shimadzu HPLC in line with a miniDawn™ TREOS

Multi-Angle Laser Light Scattering (MALLS, angles: 43.7°, 90°, and 136.3°) detector (Wyatt Technology) and an Optilab® T-rEX™ refractometer. Data were analyzed by ASTRA software package version 5.3.4.20 (Wyatt Technologies).

Monomeric bovine serum albumin (BSA, Merck, 66.4 kDa, $A_{280}^{0.1\%} = 0.66 \text{ L} \cdot \text{mg}^{-1} \cdot \text{cm}^{-1}$) was used as a standard protein of known molecular mass and oligomeric state for equipment corrections (peak normalization, alignment, and band broadening). The BSA sample was prepared fresh using SEC buffer and centrifuged at $100,000 \cdot \text{g}$ before injection. As previously described (section 2.1.7), histidine-tagged Kir2.1 (WT and R312H) was purified with Co^{2+} resin. The samples concentrated at approximately $0.8 \text{ mg} \cdot \text{mL}^{-1}$ and 20 μL were injected on the S200 column pre-equilibrated overnight with SEC buffer.

The dn/dc and extinction coefficients of Kir2.1 were calculated using the software SEDFIT based on the protein's primary structure (Table 2-6). In contrast, the dn/dc of DDM solubilized in SEC buffer was measured using the Optilab® T-rEX™ refractometer. It was found to be $0.1291 \text{ mL} \cdot \text{g}^{-1}$.

2.3.2.3 System calibration

Equilibration of the system was done overnight with $0.4 \text{ mL} \cdot \text{min}^{-1}$ flow rate using SEC buffer with the RI on purge mode to exchange the reference and measurement chambers. The temperature of the refractometer cell was fixed at 25 °C. The next day, the UV lamp and LS laser were turned on. Once the UV, LS, and RI baselines were stable, the reference RI was noted, the RI purge was switched off, and the RI baseline was set to zero. 20 μL of BSA at $5 \text{ mg} \cdot \text{mL}^{-1}$ were injected. The collection interval was set to 0.125 s.

2.3.2.3.1 Normalization

All detectors were normalized with the 90° LS signal to correct other LS1 and LS3 signals for scattering volume. A corrector coefficient is applied to the photodetectors at different angles relative to LS2 (90°) based on the absolute light intensity calibration performed with a reference (toluene).

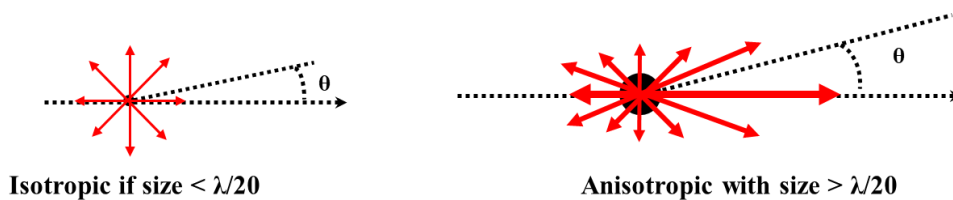


Figure 2-5. Normalization of detectors at different angles is necessary because the light intensity can be anisotropic.

2.3.2.3.2 Inter-detector delay (alignment)

Since the three instruments (UV detector, LS detector, and refractometer) are physically separated and connected by tubing, we needed to calculate the volume between them (Figure 2-4). The instrument-to-instrument volumes were set to zero, and all three BSA curves (UV, LS, RI) were selected and used to calculate the inter-detector delays. This delay was then applied to the subsequent experiments.

2.3.2.3.3 Band broadening

Correcting the enlargement of peaks during elution through the SEC is also necessary. The detector with the widest peak (RI) was chosen as a reference for peak broadening correction. A peak range was selected, covering from mid-height of the RI ascending curve to after all detector signals have returned to the baseline, a fit was performed, and the graph was updated.

2.3.2.3.4 Determining the mass of the Kir2.1-DDM complex

20 μL of Kir2.1 at $0.8 \text{ mg} \cdot \text{mL}^{-1}$ in 0.03% DDM were injected and eluted at $0.4 \text{ mL} \cdot \text{min}^{-1}$ flow rate at RT. The protein mass fraction of Kir2.1 was calculated directly using the *Protein Conjugate* procedure from Astra V software, using the input parameters in Table 2-6.

Table 2-6 ASTRA method settings for Mw measurements

Parameters	BSA	Kir2.1	Kir2.1_R312H
Superdex 200 10/300 Increase			
Flow rate ($\text{mL} \cdot \text{min}^{-1}$)	0.4	0.4	0.4
Solvent			
Refractive Index	1.3308	1.3308	1.3308
Injector			
Injected Volume	0.02	0.02	0.02
Sample			
dn/dc ($\text{mL} \cdot \text{g}^{-1}$)	0.185	0.1929	0.1929

UV ₂₈₀ Extinction coefficient (mL · g ⁻¹ · cm ⁻¹)	0.66 · 10 ³	1.0185 · 10 ³	1.0189 · 10 ³
Detergent (DDM)			
Experimental dn/dc (mL · g ⁻¹)	0.1291	0.1291	0.1291
UV ₂₈₀ Extinction coefficient (mL · g ⁻¹ · cm ⁻¹)	0	0	0
Detergent (PCC-Malt)			
dn/dc (mL · g ⁻¹)	0.1600	0.1600	
UV ₂₈₀ Extinction coefficient (mL · g ⁻¹ · cm ⁻¹)	0	0	
Detergent (FC14)			
dn/dc (mL · g ⁻¹)	0.1188	0.1188	
UV ₂₈₀ Extinction coefficient (mL · g ⁻¹ · cm ⁻¹)	0	0	

2.4 FUNCTIONAL ASSAY AND LIGAND-PROTEIN INTERACTION

2.4.1 Electrophysiology

The function of purified Kir2.1 samples was assessed by black film lipid bilayers using the Orbit mini (Nanion Technologies) by collaborators S. Bendahhou and R. Scala. The Orbit mini is a miniaturized horizontal planar lipid bilayer system with two aqueous chambers divided by a partition containing four 100- μm holes, in which the lipid bilayers are formed by 1,2-diphytanoyl-sn-glycero-3-phosphocholine (DPhPC, capacitance 15–30 pF, $1 \text{ F} = 1 \text{ kg}^{-1} \cdot \text{m}^{-2} \cdot \text{s}^4 \cdot \text{A}^2$). Each hole allows for an independent recording. The aqueous chambers contained the same buffer at different pH (Composition of Buffers used in Electrophysiology). Once the bilayer had formed, 1 μL of detergent-purified Kir2.1 (WT or R312H, in 0.015% DDM) at 90 $\mu\text{g} \cdot \text{mL}^{-1}$ was added to the upper chamber. All currents were sampled in the presence of 1% PIP₂, at -100 mV , for 100 μs , filtered at 1.25 kHz, recorded using Elements Data Reader (Nanion Technologies), and analyzed using Clampfit software (Axon Instrument Inc).

Table 2-7 Composition of Buffers used in Electrophysiology

Location	Buffer Composition
Upper chamber	150 mM KCl, 10 mM MOPS, pH 8
Lower chamber	150 mM KCl, 10 mM MOPS, pH 7.4

2.4.2 Surface Plasmon Resonance (SPR)

2.4.2.1 Introduction

The interaction between Kir2.1 and PIP₂ was characterized by surface plasmon resonance (SPR) biosensors. The SPR is an optical phenomenon based on the oscillations of free electrons on a metal film following excitation. These oscillations, surface plasmon polaritons (SPPs), form an electric field that penetrates the surrounding medium, plasmon wave, and is sensitive to changes in the medium's refractive index (RI). Any change in the medium's RI due to a ligand binding onto the matrix or an analyte onto a ligand will cause changes in the reflection angle of the incident light and shift the SPR angle, the angle at which the intensity of the reflected incident light is reduced.

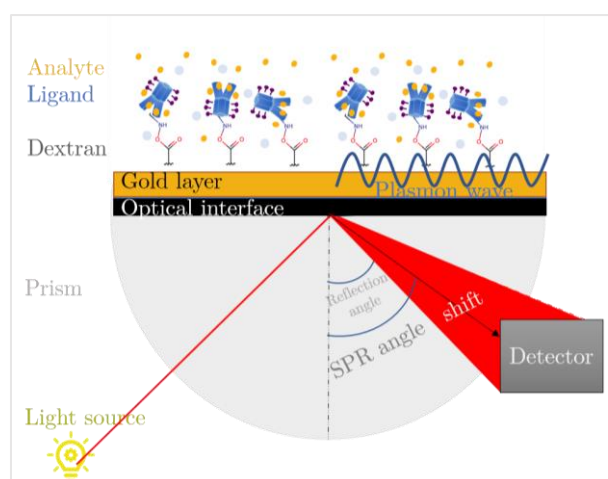


Figure 2-6: SPR phenomenon

The SPR biosensor is a microfluidic system comprised of laser light, an SPR detector, and a fluidic system or *sensor chip* made of glass with a metal film layer, often gold, and multiple flow cells (Figure 2-6). The surface of the sensor chip can be coated with different molecules to interact with various ligands. In SPR, *ligand* refers to the biomolecule that can interact with the sensor chip's matrix by its inherent chemistry or functional groups. The shift in SPR upon binding the analyte to the ligand is recorded in the form of a *sensorgram* using response units (RU) and compared to a reference flow cell.

Protocols vary according to the type of sensor chip and ligand used. However, to characterize the interaction between the ligand and analyte, the sensor chip must be activated and the ligand immobilized. The analyte is then bound to the ligand and allowed to dissociate spontaneously or by adding regeneration buffers. Several analyte

association and dissociation cycles are performed at increasing concentrations to characterize the binding and kinetic parameters.

When regeneration is impossible without compromising the ligand's integrity, single-cycle kinetics (SCK) is used (Karlsson et al. 2006). Five analyte injections at increasing concentrations at a regular interval are titrated onto the ligand following a blank injection. SCK eliminates the need to regenerate between injections by accounting for the changes in analyte concentration over the sensor chip surface over time and adapting the sensor's capacity.

The standard sensor chip, the CM5, has a carboxymethylated dextran matrix covalently bound to the gold film. Amino, carboxyl, thiol, hydroxyl, and aldehyde functional groups on the ligand can be coupled to the CM5 carboxyl groups. Most proteins can be immobilized to the sensor chip using amine coupling, as long as the protein is compatible with acidic pH (Figure 2-7). Alternatively, many sensor chips with different properties are commercially available. NTA sensor chips, for instance, have nitrilotriacetic acid (NTA) attached to the dextran matrix and are used to immobilize proteins with a histidine tag.

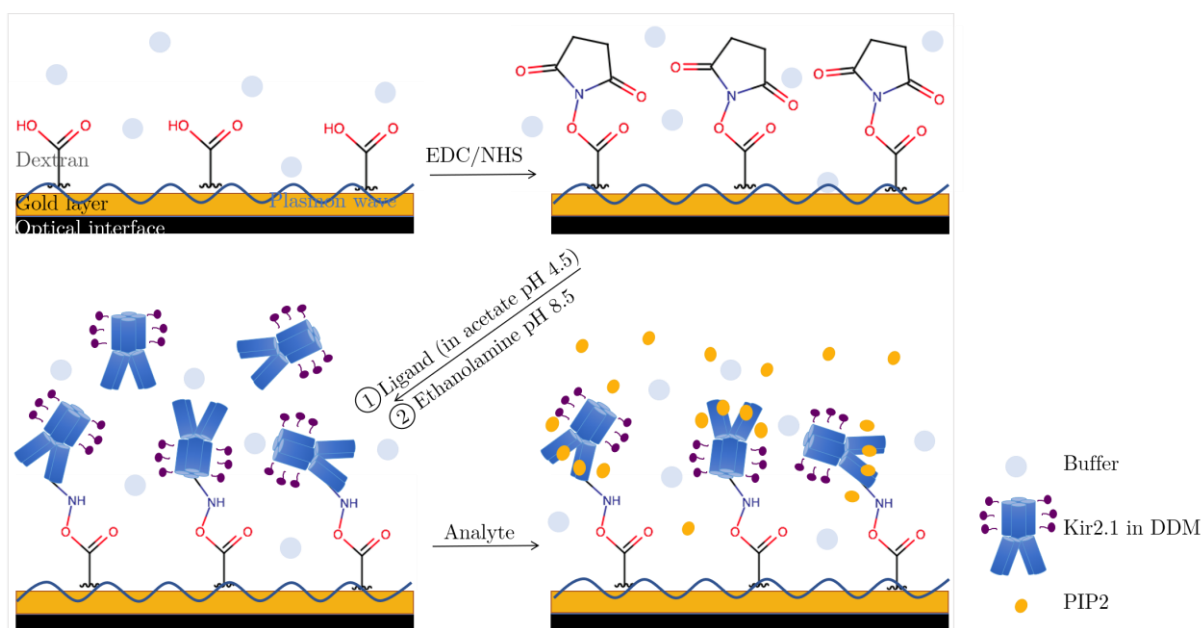


Figure 2-7: Basic SPR protocol. A CM5 sensor chip is activated with EDC/NHS, followed by ligand injection (Kir2.1) in acidic pH and then analyte binding (PIP₂).

2.4.2.2 Experimental setup

Every new sensor chip was inserted into the Biacore™ 3000 (Cytiva) and primed three times with a running buffer using Biacore 3000 Control Software v4.1. A sensorgram

was run on all four flow cells (FCs) to record the baseline resonance units (RU) per channel. Then, a single channel sensorgram was run to activate the chip and immobilize each protein sample one at a time. The binding and kinetics assays were run simultaneously on two or four FCs, including the reference FC. All biosensor experiments were performed either in duplicate or triplicate at 25 °C using the TKED SPR buffer (20 mM Tris-HCl pH 7.5, 150 mM KCl, 0.05 mM EDTA, 0.05% DDM) unless stated otherwise.

2.4.2.1 Activation of sensor chips and protein immobilization

2.4.2.1.1 CM5 sensor chips

The CM5 chip was activated by amine coupling by injecting 0.2 M N-ethyl-N'-(3-dimethylaminopropyl) carbodiimide (EDC) and 0.05 M N-hydroxysuccinimide (NHS) at 10 $\mu\text{L} \cdot \text{min}^{-1}$ for 7 min. Kir2.1 (WT, R312H, and C154Y) was diluted to 25–50 nM using sodium acetate pH 4.0–4.5 (Cytiva) for immobilization. The chip was then saturated with a 10 $\mu\text{L} \cdot \text{min}^{-1}$ flow of 1 M ethanolamine-HCl pH 8.5 (Cytiva) for 7 min.

2.4.2.1.2 NTA sensor chips

The NTA sensor chips (Cytiva) were activated by passing a flow of 0.5 mM NiCl₂ at 10 $\mu\text{L} \cdot \text{min}^{-1}$ for 1 min. His tagged Kir2.1 at 25–50 nM concentration was immobilized with a 5 $\mu\text{L} \cdot \text{min}^{-1}$ flow for 10 min. The RU level was noted as the new baseline for future comparisons.

2.4.2.1.3 L1 sensor chips

A sensor chip containing lipophilic groups (L1, Cytiva) attached to the dextran matrix was first saturated with 200 μM BSA on both FC3 and FC4 channels at a flow rate of 5 $\mu\text{L} \cdot \text{min}^{-1}$ for 5 min using HBS-N commercial buffer (Cytiva). The surface was then cleaned with 40 mM n-octyl- β -D glucopyranoside (OGP) for 30 s at a 30 $\mu\text{L} \cdot \text{min}^{-1}$ flow rate. The lipid PIP₂ was then immobilized at 10 μM concentration for 3 min at a 10 $\mu\text{L} \cdot \text{min}^{-1}$ flow rate. The binding of 50 nM Kir2.1 onto immobilized PIP₂ was then tested at a 5 $\mu\text{L} \cdot \text{min}^{-1}$ flow rate for 5 min using SPR buffer.

2.4.2.2 Control

For the negative control, Kir2.1 WT was immobilized on FC2 and ferritin on FC4 in the same chip to 1358 RU and 1868 RU levels, respectively. 20 μM PIP₂ was injected simultaneously on all channels at 5 $\mu\text{L} \cdot \text{min}^{-1}$ flow.

2.4.2.3 Kinetic assays PIP₂ onto Kir2.1 on CM5 and NTA chips

The binding and kinetic assays were performed using single-cycle kinetics (SCK). PIP₂ was serially diluted in running buffer to working concentrations (0.15 to 80 μM). PIP₂ was injected at increasing concentrations for each cycle with a 5 $\mu\text{L} \cdot \text{min}^{-1}$ flow over the reference and ligand cells. Before the first PIP₂ injection, the running buffer was injected and used as a double reference. Each injection consisted of 300 s contact time with 300 s dissociation time. There was no regeneration step between injections, as these buffers were detrimental to Kir2.1. The data were analyzed using BIAevaluation Software 4.1, and kinetic parameters were determined using General Fit and the titration kinetics 1:1 binding with drift model. The association and dissociation rate constants, k_{on} and k_{off} , respectively, and the dissociation constant (K_{D}), were determined directly from the fitted curves.

2.5 TRANSMISSION ELECTRON MICROSCOPY AND STRUCTURE DETERMINATION

2.5.1 Introduction to electron microscopy

2.5.1.1 Principle and resolution power

The structure of the human Kir2.1 was resolved by transmission electron microscopy (TEM) in cryogenic conditions (cryo-EM). Electron microscopes (EM) are compound microscopes that study nanoscale materials and biomolecules at the atomic level. Where visible-light microscopes (VLM) use photons, EMs use electrons (e^-) that, like photons, have both particle and wave-like properties (De Broglie 1925).

The resolving power of a microscope, or, in other words, its ability to distinguish two points of an object, depends mainly on the wavelength of the source used. The Rayleigh equation can describe the resolution of VLMs:

$$\delta = \frac{0.61\lambda}{\mu \sin \beta} \quad \text{VLM}$$

where:

λ is the wavelength of VL (for green light ~550 nm), μ is the refractive index of radiation, and β is the semi-angle of collection of the magnifying lens. $\mu \sin \beta$ is the numerical aperture and can be roughly approximated to 1. The resolution power of VLMs is about 300 nm, corresponding to the diameter of 1,000 atoms (Williams and Carter 2008). This resolution is insufficient in the structural study of biomolecules.

Electrons can be focused using a lens (Knoll and Ruska, 1932), and TEMs collect e^- that have been transmitted through a specimen. When the electron beam passes through the specimen, one of three scenarios is possible:

- 1) it is unscattered: it goes through the specimen unchanged; it has the same direction and energy.
- 2) it is scattered inelastically: its energy is transferred to the specimen resulting in beam damage and noise.
- 3) it is scattered elastically: its direction is changed, but there is no (detectable) change in wavelength/energy.

The proportion of elastic and inelastic collisions is determined by the energy of the e^- and the nature of the specimen.

Electrons have a tiny wavelength, $\lambda = 0.002$ nm at 300 keV, using de Broglie's equation (De Broglie 1925):

$$\lambda = \frac{1.22}{E^{1/2}}$$

where:

λ is in nm, and E is the electron energy in electron volts (eV).

The resolution (δ) of the electron microscope is thus not limited by the electron λ but rather by the quality of the specimen and the microscope setup. The resolution is also limited by three optical aberrations, such as astigmatism (which should be corrected by the operator), chromatic aberration, and sphericity aberration (Cs), which are characteristics of the microscope. Theoretically, the higher the kV used to accelerate

the e^- in the microscope, the higher its resolving power. For an in-depth explanation of electron microscopy, several texts (P. J. Goodhew and Humphreys 1992; Frank 2006; Williams and Carter 2008; P. Goodhew 2011) and excellent online courses are available (Grant Jensen).

2.5.1.2 Basic anatomy of microscope

Electron microscopes share the same basic anatomy: an electron gun, four EM lens and aperture systems, a vacuum system, a sample chamber, energy filters, and one or more detectors (Figure 2-8). These components are described in section 2.7.1 in the **SUPPLEMENTARY MATERIAL** at the end of this chapter. To reach a high resolution, it is essential to have a coherent electron source (field emission gun, FEG), apertures to screen out inelastic electrons, a high vacuum to avoid collisions, and a camera with a high detection quantum efficiency. The latter's invention, direct electron detection cameras like the Falcon (Thermofisher) and K2-K4 (Gatan), is a major factor in the resolution revolution that cryo-EM has undergone in recent years.

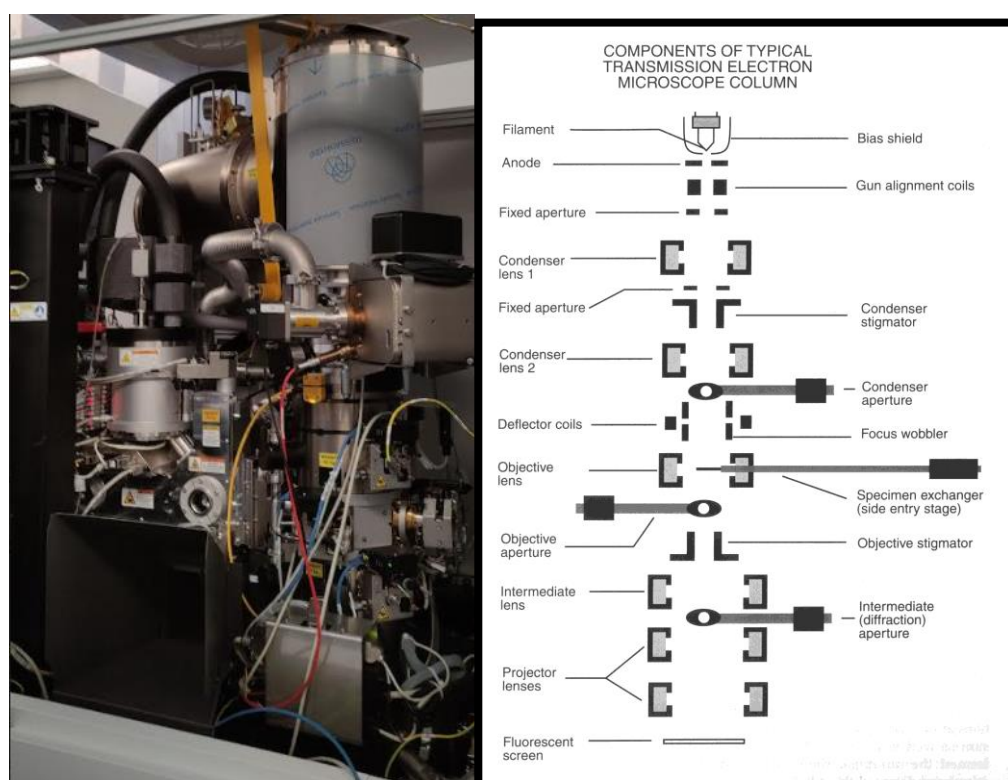


Figure 2-8: Basic anatomy of a transmission electron microscope (from Pasteur Institute).

2.5.1.3 Beam damage, electron dose, and fragmentation

Not all e^- collisions are elastic; some inelastic collisions transfer energy to the sample and produce beam damage and heat. Using EM in cryogenic conditions (cryo-EM), at

high voltage, and with thin samples minimizes heat transfer. However, if the incident beam energy is too great, the chemistry and structure of the sample can be damaged by radiolysis, sputtering, or heating. The electron dose must be adjusted to *low* to reduce beam damage. Since detectors can be quickly saturated even at low doses, the electron dose is fragmented into several frames and later integrated to form an image.

Electron dose can be defined as the e^- charge density ($C \cdot m^{-2}$) bombarding the specimen". The e^- dose can be converted into e^- per unit area using $e^{-1} = 1.6 \cdot 10^{-19} C$ (Williams and Carter 2008).

2.5.2 Image formation and contrast transfer

The image formation on EM depends on the electron beam (source) and its interaction (elastic/inelastic collisions) with the specimen. 3D object information is obtained by analyzing the micrographs as projections at different angle ranges (orientations) and building a 3D model. Various computational corrections are necessary to recover an image with maximum resemblance to the original object.

2.5.2.1 Contrast and the contrast transfer function (CTF)

2.5.2.1.1 Contrast

The relative differences in intensities (contrast) between the object of interest and the background are essential, especially when observing a 2D image representation of a 3D object. Electrons scattered by biological samples (made of C, N, O, H, light chemical elements) do not intrinsically produce sufficient contrast to be observed directly on the microscope. It is often necessary to introduce high-scattering atoms like Au or U to achieve high contrast in the negative staining preparation of the specimen (section 2.5.4 below). In cryogenic conditions, the contrast is increased by a defocus.

There are two kinds of contrast: amplitude contrast and phase contrast.

Amplitude contrast results from scattered e^- stopped by the objective aperture due to differences in the mass or thickness of the objects (Figure 2-9A). Since only a fraction of the scattered e^- is transmitted, it is possible to discriminate between two points on the sample whose diffusing power (i.e., the nature of the constituent atoms, the number of these atoms, and consequently the local thickness) is different. Therefore, the number of e^- collected at a point of the detector $I(x,y)$ differs from that at a neighboring point $I(x + Dx, y + Dy)$.

The scattered e^- that passes through the lens contributes to *phase contrast* (Figure 2-9B). The unscattered and elastically scattered e^- travel different paths. They are out of phase by $\pi/2$ (90°) and can interfere with each other constructively (or destructively), forming Fresnel fringes. This resulting phase contrast can provide high-resolution information about the specimen encountered.

At the focal plane, there is no phase contrast. Data is often collected with a defocus to increase the contrast. Adjusting the height of the sample in the microscope column (ΔZ) enhances differences in amplitude.

However, this increased contrast comes at a cost as the defocusing produces a loss of resolution.

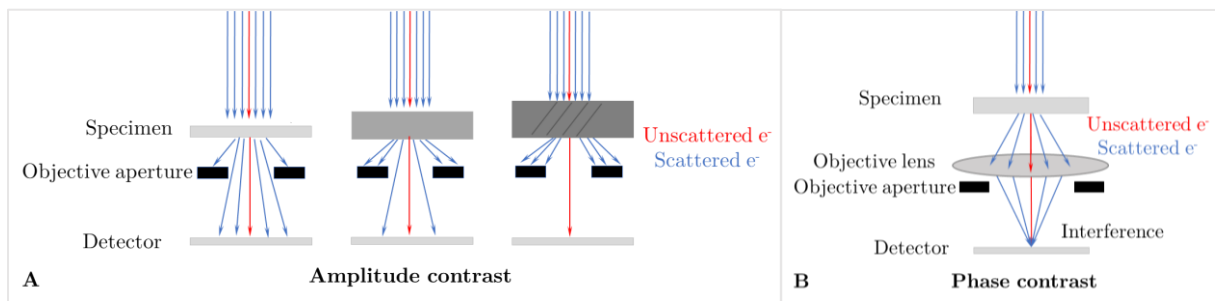


Figure 2-9: Amplitude and phase contrast

2.5.2.1.2 The contrast transfer theory

Finally, the image represents a projection of the object's structure modulated by a term depending on the optical characteristics of the microscope.

The contrast transfer theory (Wade 1992; Zhu et al. 1997; Frank 2006; Spence 2017) describes the relationship between the wave function describing the object (specimen) and the final image. Its function, the contrast transfer function (CTF, Equation 2-18), describes the effects of contrast quality arising from both amplitude W and phase effects $\gamma(k)$ depending on the focus, spherical aberration, and electron beam coherence (Zhu et al. 1997).

Equation 2-18

$$C(k) = 2[\sin \gamma(k) - W \cos \gamma(k)]$$

A simplified version (Frank 2006):

$$H'(k) = \sin \gamma(k) - Q_0 \cos \gamma(k)]$$

where:

Q_0 is a value of amplitude contrast ratio and can be determined manually by recording at a series of defocus and measuring the $H'(k) = 0$ value positions. However, the CTF estimation can be automated from the intensity at each spectral frequency (density power spectrum) and the CTF parameters, which can be estimated using CTFFind programs (Mindell and Grigorieff 2003; Rohou and Grigorieff 2015). The only parameter that the operator can adjust is the stage height of Δz (defocus).

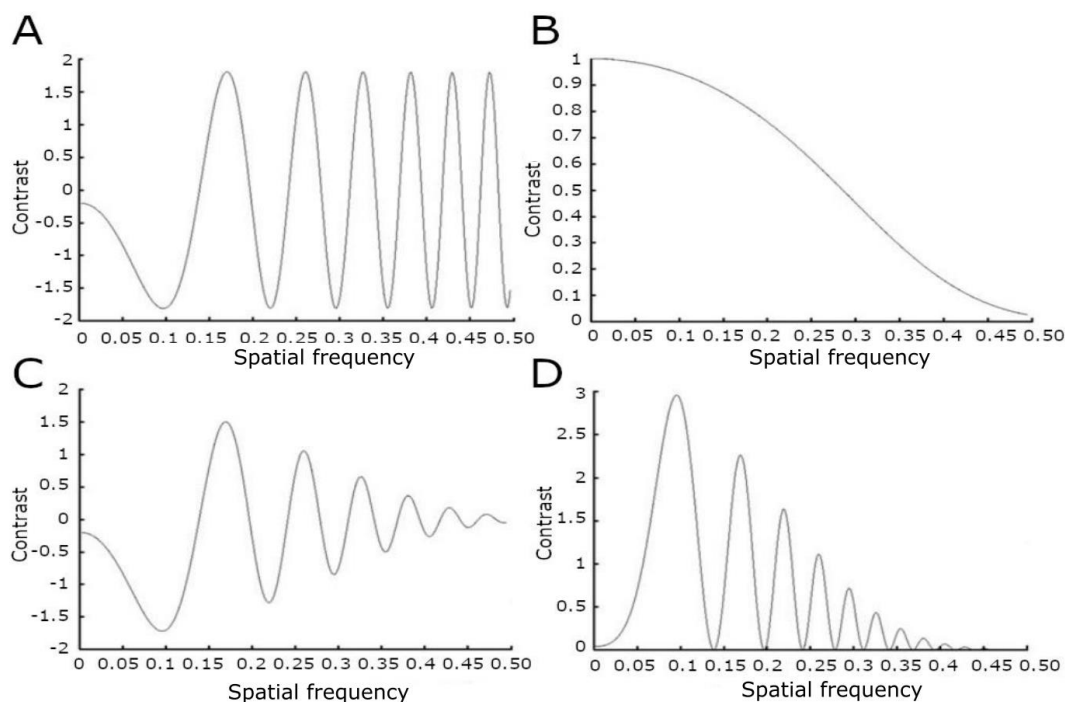


Figure 2-10. CTF and its envelope function are depicted. Unpublished lecture material from N. Boisset. A) CTF representation without the envelope. B) The envelope function is shown. C) Representation of the CTF and envelope function product. D) The product of the CTF and the squared envelope function is shown.

2.5.2.1.3 CTF Correction

The next step is to correct the image's CTF to avoid exaggerated features and distortions in the reconstruction. This correction is necessary because the C_s and applied defocus (among other CTF parameters) degrade the acquired images.

Many automated CTF correction methods are available, including phase flipping and Wiener filtering. *Phase flipping* is the most straightforward CTF correction. It is done by performing the following operation:

Equation 2-19

$$F'(k) = \begin{cases} -F(k) & \text{for } H(k) < 0 \\ F(k) & \text{for } H(k) > 0 \end{cases}$$

This correction results in a modified transform image with the correct phase throughout the resolution domain. However, it does not correct the amplitude attenuation dependent on spatial frequency.

Wiener filtering is a more careful correction and one of the most implemented CTF correction techniques. It amplifies FT components close to zero, correcting the amplitude of the CTF and its phase to a constant value close to 1 while avoiding adding or amplifying background noise. This technique requires at least two defocus series and is improved with more defocus groups. Figure 2-11 shows a typical example using two defocus groups.

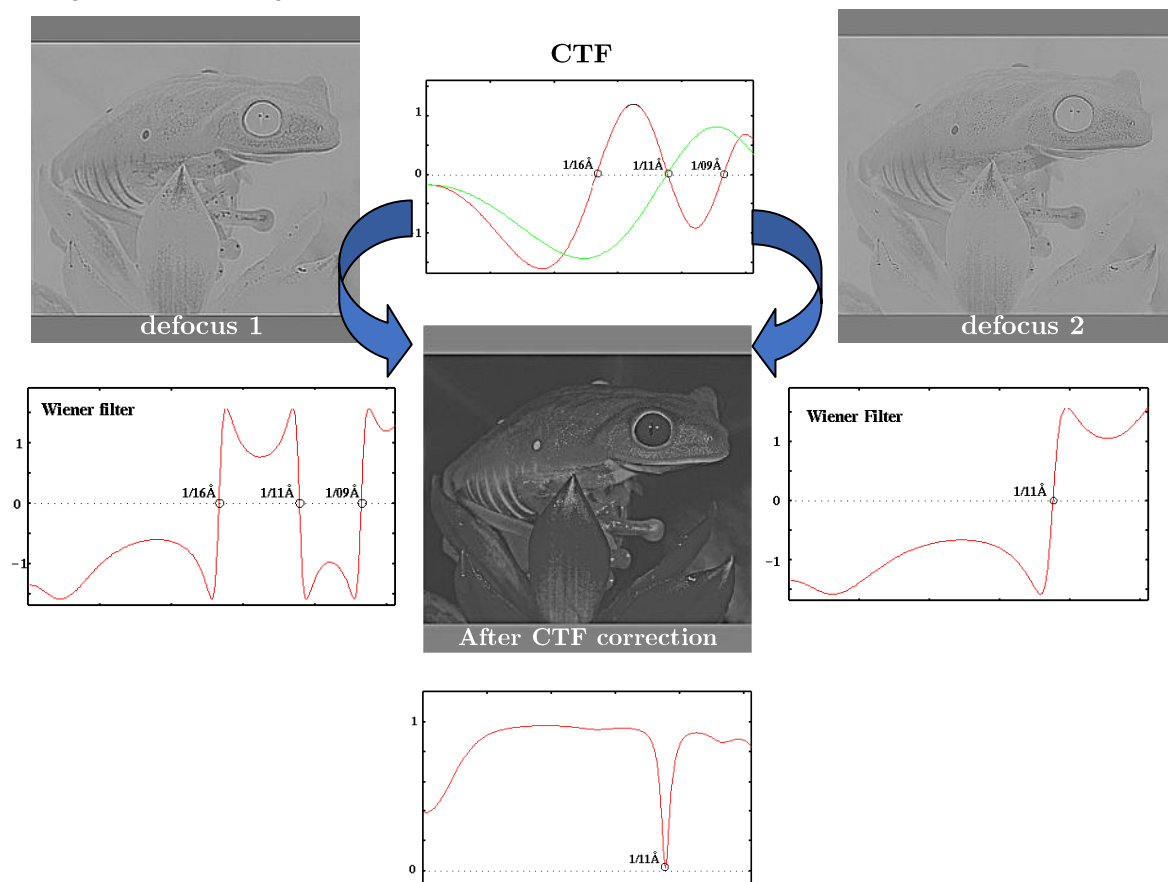


Figure 2-11: Demonstration of Wiener filtering and phase flipping (from N. Boisset, unpublished lecture material)

2.5.3 Single-particle analysis

Many steps are necessary to extract a low-contrast image from noisy data and obtain a high-resolution 3D reconstruction that is true to the original object. After optimizing the sample preparation and data collection method, a critical step is the single particle analysis (SPA). Figure 2-12 depicts a typical flowchart for analyzing noncrystalline cryo-EM samples.

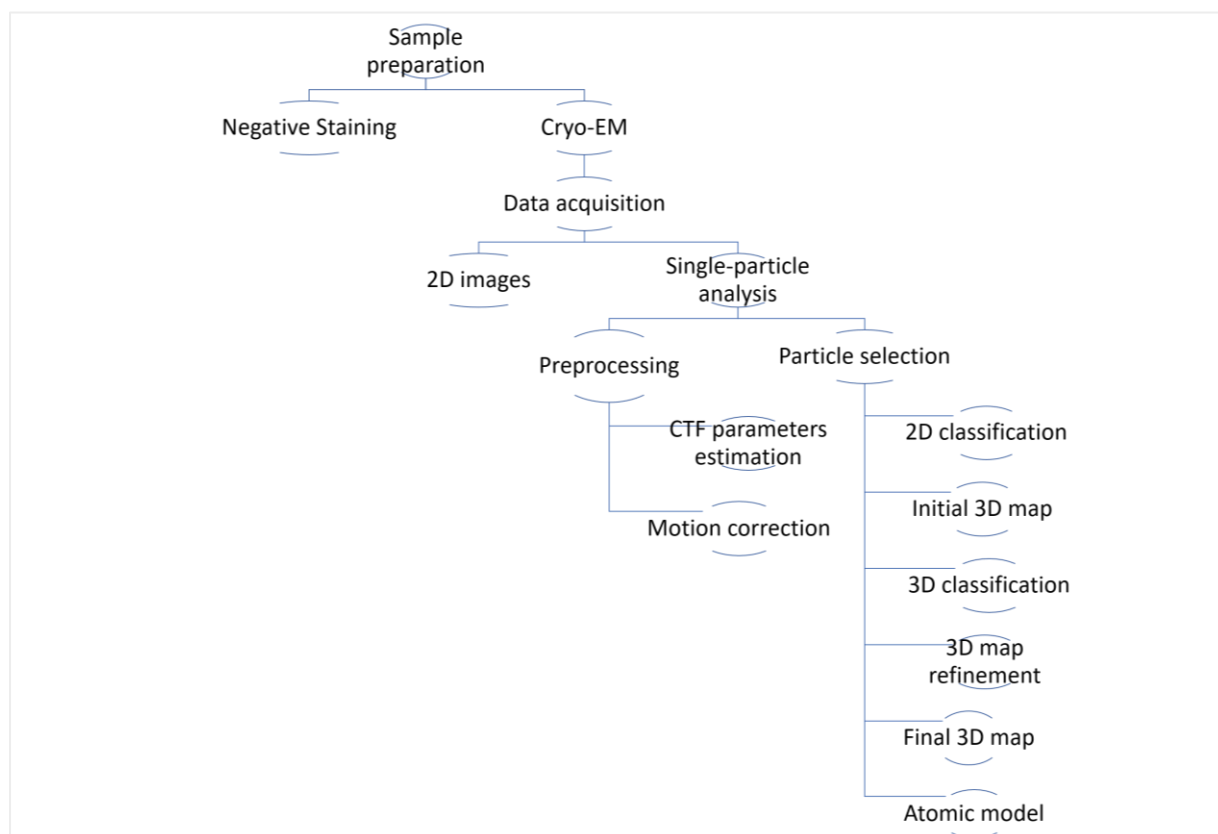


Figure 2-12 Single-particle analysis flowchart

2.5.3.1 Beam-induced motion correction

Sample stage drift degrades the image's resolution. The blurring caused by this beam-induced motion can be mitigated by aligning all the frames in a stack and correcting it using an algorithm (Li et al. 2013) available on software like MotionCor2 (Zheng et al. 2017). The frames are separated into subframes and local areas and aligned to determine the type of motion, which can differ substantially from site to site. The beam-induced motion is significantly higher at the beginning of data acquisition, the first five frames, and markedly diminishes afterward (Li et al. 2013). Therefore, eliminating the first five frames results in considerably lower image motion.

2.5.3.2 Particle picking

The selection of particles can be made manually or automatically from micrographs inspected previously (or not), stacked, and motion-corrected. The quality of the particles selected will heavily influence the final result, so particular attention is required for this step. Softwares are available for picking particles, including crYOLO (Wagner et al. 2019), cryoSPARC, Warp, RELION, EMAN, and Gautomatch (Ludtke, Baldwin, and Chiu 1999), which allow semi-automatic or fully-automatic selections.

2.5.3.3 Particle extraction

The selected particles must now be extracted from the micrograph as individual images or boxes. The box size is chosen so that one particle fits entirely inside without any adjacent particles. The box is typically at least 30% larger than the size of the particle to account for the imprecise location coordinates of the stacked particles (Cheng et al. 2015).

2.5.3.4 Reference-free 2D class averaging

Once the particles have been boxed, they are centered, aligned, and classified by cross-correlation into groups depending on the particle orientation without a reference. Stacking the particles and averaging the image increase the S/N ratio and allows the classification of heterogeneous samples into homogenous subgroups (Figure 2-13). This alignment-classification-alignment process (Frank 2006) is iterated until robust classes are found. The samples can be collapsed into pixel groups or *binned* to accelerate the process. This process is fully unsupervised; the only parameter controlled by the user is the number of output classes. As a general rule, the number of classes is calculated so that at least 200-300 particles will fall into each class (Scheres 2010).

Cross-correlation (CC) assesses the similarities between two functions and where the similarities are found within the test image.

Equation 2-20

$$c = F'[F\{f\} \cdot F\{h\}]$$

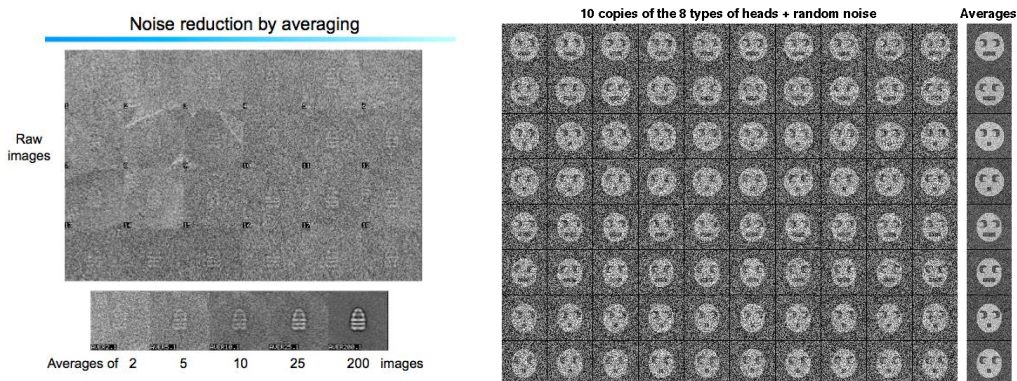


Figure 2-13 Example of noise reduction by averaging and 2D classification (data from N. Boisset)

2.5.3.5 3D initial model

When 2D classes have been selected, they can be used to build an *ab initio* 3D initial model by random conical method or angular reconstitution (Frank 2006) in the absence of suitable structures of similar complexes. Building the 3D model is based on the central section theorem that relates 2D projections of the 3D object to their FT in reciprocal space. Each 2D projection represents a central section of the object and is oriented perpendicular to the direction of the e^- beam (Frank 2006). It is essential to recover the maximum number possible of 2D orientations to create an accurate 3D model.

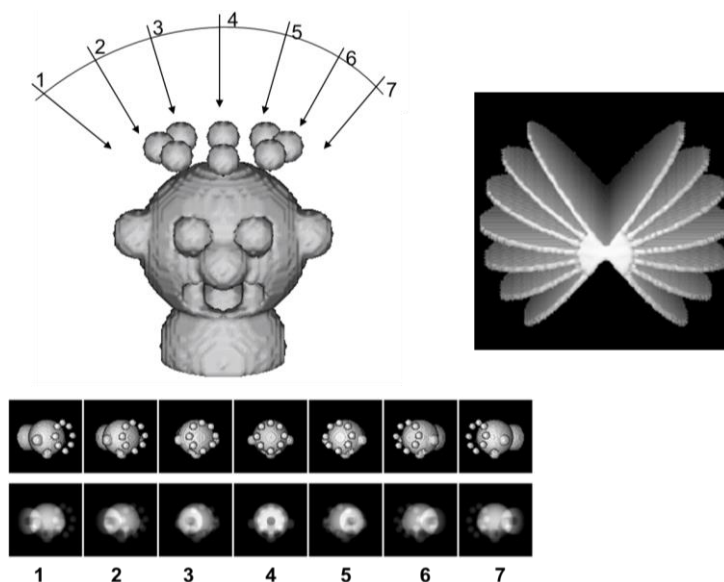


Figure 2-14. Central section theorem. (Data from N. Boisset)

2.5.3.6 3D classification and refinement

The initial 3D model can then be separated into 3D classes and refined using all the data sets and a low-pass filter to remove low-resolution artifacts. A multi-reference

unsupervised refinement method is often used, where the data is separated into different 3D classes that are random variations of one consensus 3D model (Scheres 2010). The number of models to be refined simultaneously, K , depends on the number of structures in the data set. However, since this information is unknown at this step, multiple runs are performed with varying K values until the number of new orientations or classes has stabilized or the log-likelihood increase has leveled off.

2.5.3.1 Bayesian approach

To avoid overfitting noisy data in the 3D reconstruction, RELION uses a Bayesian approach (Scheres 2012a; 2012b) to find a model with the highest probability of being correct. Bayes' law uses the maximum likelihood (ML) of observing the data x with prior information y and assumes that noise is independent and follows a Gaussian distribution.

2.5.3.2 Fourier Shell Correlation

The resolution of the 3D reconstruction can be evaluated using the Fourier shell correlation (FSC). Fourier shell correlation calculates the volume of two independent halved data sets and cross-correlates it with its FT shell (Penczek 2010). Different thresholds have been used, the 0.5 FSC and, more recently, the gold standard, 0.143 FSC, which is more optimistic and is now largely adopted.

2.5.4 Preparation of the specimen using Negative Staining

First introduced by Brenner and Horne in 1959 allows for obtaining images of macromolecules with high contrast. The sample to be observed is applied to a TEM grid coated with carbon and mixed with a high contrasting agent, typically 1–2% uranyl acetate. The excess liquid is removed with paper or “blotted.” The sample is air-dried. As the stain solidifies, it preserves the sample from damage, and the grids can be stored indefinitely if proper care is taken. The stain forms a thin film throughout the grid and penetrates, to some extent, into the crevices, channels, and irregularities in the sample's surface (Frank 2006). Although the stain can introduce slight distortions and artifacts, it allows for obtaining low-medium-resolution structural information about the shape of the molecules observed (up to 20 Å resolution because limited by the size of the grain of the staining). This is a necessary first step to determine if a protein is suitable to be resolved by TEM.

2.5.4.1 Preparation of grids

The purified protein was immediately deposited on a microscopy grid for transmission electron microscopy (TEM) observation. The small copper grids are 3 mm in diameter with a 300–400 mesh (Agar Scientific) and are coated with a thin layer of carbon (either added manually or bought with C film). The grids were made hydrophilic by a 30-s glow discharge at 30 mA. 3 μL of fresh protein at 20–40 $\mu\text{g} \cdot \text{mL}^{-1}$ were placed on the grid and allowed to rest for 30–60 s. Excess fluid was removed (blotting) with Whatman paper (Cytiva). Two sequential drops of 2% uranyl acetate, a heavy metal salt, were used as a contrast agent. The extra fluid was blotted with Whatman paper and allowed to dry before storing it in a grid box at RT.

2.5.4.2 Preparing carbon-coated grids for negative staining

Two carbon rods were sharpened and placed in high-current electrical terminals in a vacuum machine in contact with each other. The carbon was evaporated in the air at 10^{-4} to 10^{-5} mbar and deposited as a thin film on a freshly separated mica sheet (Agar Scientific). The carbon was transferred onto the copper grids by placing the grids on Whatman paper submerged in water in a crystallizing dish, placing the carbon-coated mica sheet at the water surface, carbon side up. The mica sheet sunk to the bottom, and the carbon film floated on the surface. The Whatman paper was lifted with tweezers until the grids encountered the carbon film. The grids were then left to dry.

2.5.4.3 Acquisition and data collection

Micrographs were collected from a Jeol 2100 200 kV electron microscope equipped with a LaB₆ electron gun and Gatan US 1000 (2k x 2k) camera with a high sensitivity model U scintillator. Micrographs were manually recorded at RT using a 30,000-x magnification with varying defocus values.

2.5.4.4 Data procession and image analysis of Kir2.1WT solubilized in FC14 and purified in DDM

Forty-nine micrographs of the best grid (determined by contrast, concentration, particle distribution, and stain quality) were imported to EMAN 2.3 software for particle picking and image analysis with the following parameters: 3.57 Å/pixel (apix), 80% amplitude contrast (AC), particle size 54, and spherical aberration coefficient (CS) 2.0 mm (Table 2-8). Nearly 10,000 particles were picked manually and semi-

automatically using 76 x 76 px box size using the “e2boxer.py” feature of EMAN2 (Tang et al. 2007, 2).

The micrograph’s CTF parameters were estimated using the CTF auto-process function set to mid-resolution. The 2D analysis used reference-free class averaging, 20 classes, and 8 iterations. The initial 2D alignment contained all the particles. The 2D classes were then divided into “good” and “bad,” depending on how clear the image was. The bad particles were removed from consideration for the initial model. The box size was increased to 80 x 80 px using the “e2proc3d.py” script, and an initial 3D model was made with no applied symmetry. This initial model was subsequently refined two times using C4 symmetry.

Table 2-8 Summary of EMAN2 parameters for negative staining

Parameter	Value
Data collection	
Microscope	Jeol 2100
Detector	Gatan US 1000
Voltage (kV)	200
Pixel size (apix)	3.57
Reconstruction	
Micrographs	49
Particles picked	~10,000
Amplitude contrast (%)	80
CS (mm)	2.0
Box size (pix ²)	80 x 80

2.5.5 Cryo-EM

Negative staining is an essential step in visualizing biomolecules at a low resolution. However, there are several limits to this technique. Whereas negative staining observes samples in a dehydrated state with potential minor artifacts caused by the stain’s possibly uneven distribution, cryo-EM allows the observation of fully hydrated macromolecules embedded in vitreous ice and preserved in their true shape (Dubochet et al. 1988; Frank 2006).

In cryo-EM, the sample is applied to the grid, excess liquid is blotted, leaving a thin sample layer, and it is very rapidly plunged into liquid ethane, where a thin layer of vitreous ice will form (Frank 2006). To avoid creating crystalline ice, achieving a very high sample cooling rate is necessary. Crystalline ice is too thick and is therefore opaque

to the electron beam. The grids must always be kept on liquid nitrogen to preserve the sample at $-180\text{ }^{\circ}\text{C}$. The temperature must be kept at $-180\text{ }^{\circ}\text{C}$ to prevent water from transitioning from the vitreous to the crystalline phase because its volume changes, damaging the macromolecule (Dubochet et al. 1988; Frank 2006). The liquid ethane is supercooled by surrounding liquid nitrogen and an atmosphere of gaseous nitrogen to maintain a low temperature and avoid water vapor contamination. The temperature range of ethane in the liquid state is broader than that of liquid nitrogen. The quality of the sample to be studied and the quality of the grid preparation are the limiting factors to obtaining high-resolution images in cryo-EM when using a state-of-the-art microscope and a direct electron detector.

Cryo-EM structure determination can be divided into three critical parts: sample preparation, data collection, and image processing (image analysis).

2.5.5.1 Sample preparation

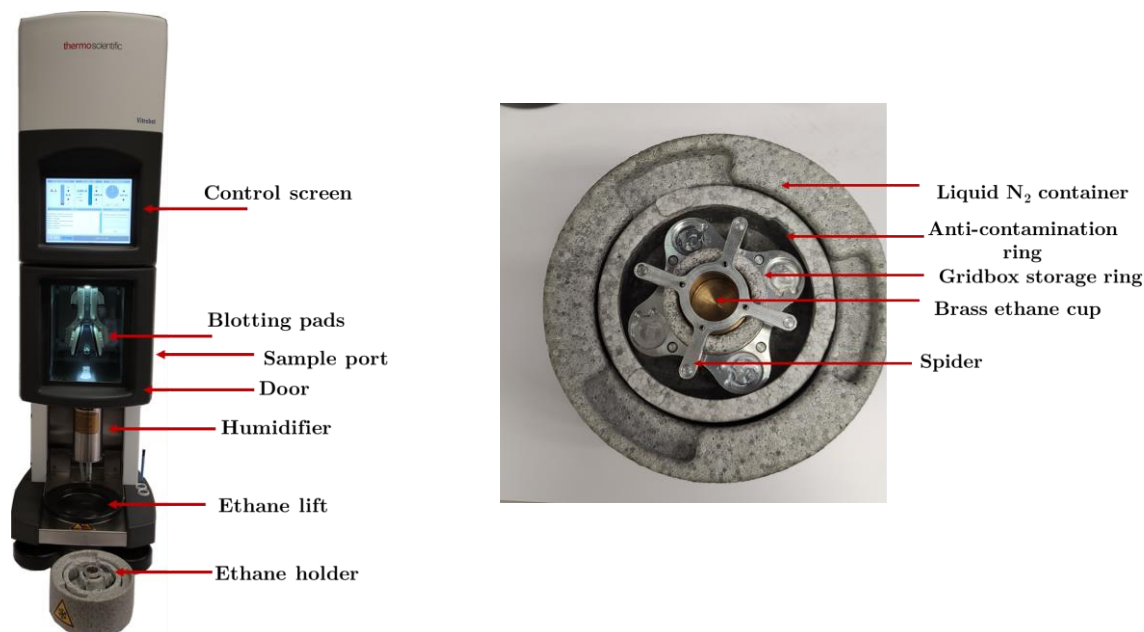


Figure 2-15: Vitrobot Mark IV for the preparation of frozen-hydrated specimens.

In cryo-EM, there is a wide choice of grids for sample preparation. The specimen support can be made of copper, nickel, or gold, with a thin carbon foil, but sometimes gold (UltraUfoil grids) containing circular or square holes. The holes can be small or larger with a regular hole size, spacing, and period (Quantifoil, QF). Sometimes an irregular array is preferred, in which case the Lacey grids can be chosen (Figure 2-16).

For the preparation of h_Kir2.1 in DDM, we chose R1.2_1.3 copper QF grids with 300 mesh. The round foil holes are $1.2\text{ }\mu\text{m}$ in diameter with $1.3\text{ }\mu\text{m}$ spacing. $3\text{ }\mu\text{L}$ of

Kir2.1 at $0.7 \text{ mg} \cdot \text{mL}^{-1}$ in 0.03% DDM were deposited onto the R1.2_1.3 copper QF grids with an additional 2 nm carbon film and previously rendered hydrophilic by 20-25 s glow discharge at 20-25 mA. The grids were blotted for 4 s with zero force at 4 °C and 100% humidity and flash-frozen in liquid ethane using Vitrobot Mark IV (ThermoFisher, Figure 2-15). All grids were stored in liquid nitrogen, clipped, placed on a grid holder (cassette), and docked onto the microscope for automatic loading. Sample freezing conditions were tested on various grids, including Lacey and QF (copper QF with carbon film, gold QF grids, and UltrAuFoil grids) (Figure 2-16). The good preparation of the grids was checked in a Glacios 200 kV electron microscope equipped with Falcon 3 direct electron detectors.

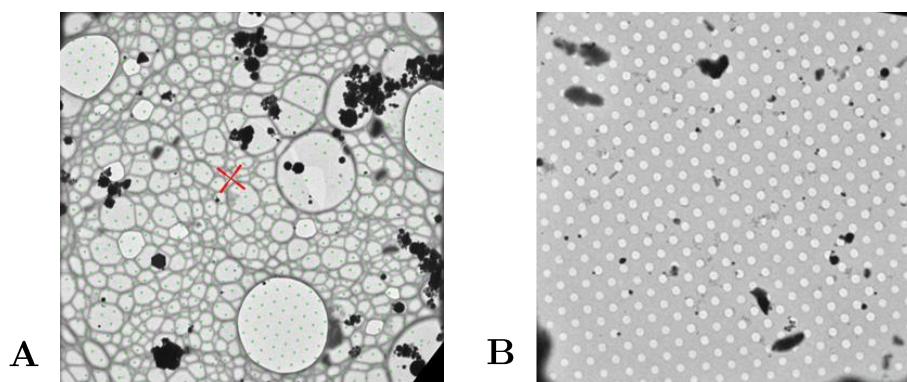


Figure 2-16: Lacey vs. QF grid

2.5.5.2 Data collection of Kir2.1 in DDM

9,895 images were collected at 105,000x magnification on the Krios Titan 300 kV equipped with a Bioquantum energy filter and K3 (Gatan) camera. The automation of the data collection was done with the software EPU. Movies were recorded in electron-counting mode using exposures of 4 s dose-fractionated into 36 frames with a dose rate of $1.7139 \text{ e}^-/\text{\AA}^2$, resulting in a total dose of $61.7 \text{ e}^-/\text{\AA}^2$. A defocus ranging from -1.2 to $-3.0 \text{ }\mu\text{m}$ was used. The pixel size was $0.86 \text{ \AA}/\text{pixel}$.

2.5.5.3 Image analysis and building the 3D atomic structure

The image analysis protocol for h_Kir2.1 is detailed in Chapter 4. Briefly, after manual inspection, the movies were motion-corrected and dose-weighted using MotionCor2 (Zheng et al. 2017), and CTF parameters were estimated using CTFFIND4 (Rohou and Grigorieff 2015). Particles were picked using SHIRE-crYOLO and were submitted to 2D classification using RELION. A 3D initial model was done using a C4 symmetry, and after 3D classification using no imposed symmetry, a map from a 3D class was

obtained. A mask was applied to remove the detergent layer. 3D refinements with decreasing values of initial angular sampling and local search degrees from auto-sampling were done. The cryo-EM map was sharpened using the Auto-sharpen map tool from the PHENIX program and subjected to handedness correction. The docking of the TMD from an *in silico* model and the CTD from a crystal structure from mouse Kir2.1 (PDB 1U4F) and real space refinements were done in PHENIX with a manual refinement in Coot (Emsley and Cowtan 2004).

2.6 EXPRESSION AND PURIFICATION OF BACTERIAL HOMOLOG MUTANTS: KIRBAC3.1 W46R AND S129R

2.6.1 Production

The synthetic KirBac3.1 gene was integrated into the pET-30a (+) (Novagen) plasmid coding for a C-terminal 6x histidine tag and a Kan resistance gene, with an optimized open reading frame (ORF) for expression in *E. coli*. The mutations W46R and S129R were introduced by site-directed mutagenesis. The plasmid was introduced into BL21-Codon Plus (DE3) (Agilent), containing resistance to Chloramphenicol (Cam) antibiotic. The resulting KirBac3.1 monomer has a theoretical molecular weight of 34 kDa. The competent cells were transformed by heat shock following the manufacturer's protocol. The transformed cells were incubated overnight at 37 on LB-agar plates containing Kan and Cam antibiotics.

2.6.2 Culture medium and growth conditions

A 20-mL starter LB culture containing 30 $\mu\text{g} \cdot \text{mL}^{-1}$ Kan and 34 $\mu\text{g} \cdot \text{mL}^{-1}$ Cam was inoculated with a single colony of cells and incubated at 37 °C, 180 rpm overnight. The next day, 1-L LB was inoculated with ~10 mL of the starting culture. The culture was then separated onto two Erlenmeyer flasks and incubated at 37 °C, 180 rpm, until an $\text{OD}_{600\text{nm}}$ between 0.6–0.7 (about 3–4 h) was obtained. 500 μL were aliquoted and labeled pre-induction for SDS PAGE analysis. The culture was placed in the cold room for 1 hr. The cells were induced overnight with 0.4 mM IPTG at 19 °C, 180 rpm. The cells were pelleted at 4,000 $\cdot \text{g}$ for 30 min at 4 °C, the supernatant was discarded, and the pellet was resuspended with cold PBS pH 7.3 and separated onto Falcon tubes. 500 μL were aliquoted and labeled post-induction for SDS PAGE analysis. After the cells were

pelleted at $4,000 \cdot g$ for 30 min at $4 \text{ }^{\circ}\text{C}$, the supernatant was discarded, and the pellets were used immediately or stored at $-80 \text{ }^{\circ}\text{C}$.

2.6.3 Purification of KirBac 3.1 W46R and S129R

The pellet was resuspended in 10 mL of lysis buffer (50 mM Tris-HCl pH 8, 150 mM KCl, $4 \mu\text{g} \cdot \text{mL}^{-1}$ DNase I, $500 \mu\text{g} \cdot \text{mL}^{-1}$ Lysozyme, and EDTA-free protease inhibitor cocktail). The sample was incubated at RT for 15 min and then homogenized by Potter. Two Cell D passes at 2 kbar followed the enzymatic lysis.

The lysate was solubilized directly with 68 mM n-decyl- β -D-maltoside (DM, Anatrace) detergent for 4 h at RT with gentle agitation. The solubilized MPs are clarified by centrifugation at $100,000 \cdot g$ for 30 min at $4 \text{ }^{\circ}\text{C}$. The supernatant is mixed with 1 mL of pre-equilibrated Ni^{2+} resin and 5 mM imidazole and incubated for 1.5 h in the cold room.

The mixture was deposited onto a gravity column; the proteins not retained were collected and labeled Ft. The resin was thoroughly washed with HS and LS buffer containing high concentrations of n-tridecyl- β -D-maltoside (TriDM, Glycon). Then, the protein was eluted with a one-step 400 mM imidazole (Table 2-9). The fractions containing KirBac3.1 were pooled, filtered, and concentrated using a 50 kDa MWCO and loaded onto an S200 column previously equilibrated with 50 mM Tris-HCl pH 8.0, 150 mM KCl and 0.5 mM TriDM. The protein was eluted in isocratic mode at $0.3 \text{ mL} \cdot \text{min}^{-1}$.

Table 2-9 Composition of affinity chromatography buffers for purification of KirBac3.1 mutants

Buffer	Tris-HCl pH 8 (mM)	KCl (mM)	TriDM (mM)	Imidazole (mM)	Volume (CV)
HS	20	500	2	10	10
LS	20	150	2	20	7
E	20	150	0.5	400	2

2.7 SUPPLEMENTARY MATERIAL

2.7.1 Transmission Electron Microscope

2.7.1.1 Electron gun

The Electron gun consists of a tungsten filament held at a very low voltage (-100 to -300 kV) through which a current passes. Electrons are accelerated through a potential drop which gives them kinetic energy. Different filaments exist, including tungsten, lanthanum hexaboride crystals (LaB_6), and field emission guns (FEG). FEG filaments are the preferred choice to achieve high resolution as they produce e^- that have spatial and temporal coherence; that is, they come out from the same position and with the same initial speed.

As e^- escape this filament, they pass through a Wehnelt cylinder, a cup-shaped electrode that focuses them before going through an accelerator stack. The accelerator stack contains discs at sequentially higher voltages through which the electron drops. Once it reaches the lowest plate, grounded at 0V, the electron will have gained 100 kV to 300 kV, depending on the microscope used. This potential energy is transformed into kinetic energy, and the resulting electron will have about 70% of the speed of light.

EM lens and aperture systems

EM lenses consist of wires that focus e^- through an electromagnetic field to a focal point and produce a magnified image of the original object. EMs are compound microscopes comprised of a condenser lens system, an objective lens system, and a projector lens system. Since the dimensions of these lenses are very small, they are not perfectly aligned; therefore, each lens system contains deflectors that correct the path of e^- . Because the lens field must be symmetrical to avoid image distortions and aberrations, stigmators are included in each lens system. Another critical component of an EM lens system is the aperture, which removes e^- scattered too far from the beam path (online lectures by Grant Jensen).

The condenser lenses define how the beam impacts the sample. Depending on the microscope, there can be two or three condenser lenses, designated C1, C2, and C3. They control the beam's intensity, spot size, and convergence angle.

The objective lens focuses the beam that came through the specimen into the back focal plane, forming a first magnified image. The objective lens and aperture determine the quality of the image. Its aperture screens out e^- that have scattered too far.

Objective aberrations (spherical aberrations (C_s), chromatic aberration (C_c), and axial astigmatism) can be present and need to be corrected as they would otherwise limit the resolution of the microscope.

One to several intermediate lenses between the objective and the projector lens add to the image's magnification. Finally, the projector lens directs the image onto the detector (Grant Jensen and (Frank 2006).

2.7.1.2 Detectors

In TEM, images formed can be projected onto a viewing screen or detectors. The image observed on the viewing screen is analog and cannot be manipulated. It can, however, be digitized by a detector. The digital image can then be electronically adjusted to reduce noise or improve contrast and processed mathematically.

Fluorescent screens allow direct viewing of the specimen. They are often made of a metal coated with fluorescent, or rather phosphorescent, a scintillator that converts electron energy into light via cathodoluminescence (CL). The scintillator typically has a long delay, so the screen can continue to emit light long after the electron hits it.

Photographic film is located below the fluorescent screen and records large high-resolution images. Modern microscopes are still equipped with these films as they provide excellent results; however, it is time-consuming as they must be developed and then digitized.

Charge-coupled device (CCD) detectors are photosensitive silicon fiber optics, often coupled to a scintillator, that capture signals from incoming light/electron beams and store them in an array. The array (pixels) signals must be read out or transferred to an output amplifier and integrated to form the digital image (Williams and Carter 2008; Frank 2006).

While CCD cameras allow recording images and spectra, integrating them into a digital image, and storing them in a computer, they are not ideal for achieving high-resolution structures as their detection quantum efficiency (DQE) is not optimal. DQE refers to how the detector degraded the incoming signal into noise.

Equation 2-21

$$DQE = \frac{\left(\frac{S_{out}}{N_{out}}\right)^2}{\left(\frac{S_{in}}{N_{in}}\right)^2}$$

where:

$S_{\text{out}}/N_{\text{out}}$ is the output signal-to-noise ratio (S/N), and $S_{\text{in}}/N_{\text{in}}$ is the input S/N. The ideal detector would have a DQE close to 1.

Direct-electron detectors combine the convenience of CCD cameras with the high DQE provided by the photographic film (McMullan et al. 2009). These detectors have monolithic active pixel sensors (MAPS) that detect individual e^- passing through their semiconductor membrane (Bai, McMullan, and Scheres 2015). These cameras are now widely used to determine high-resolution structures; a few examples include the Falcon (Thermofisher), K2, K3, and K4 (Gatan) cameras.

The default linear detection mode has a linear relationship between the incident electron intensity and the output image signal. However, in this mode, the image can be affected by variabilities in electron energy, which introduce noise. Like K2 and onwards, recent electron detector cameras can avoid this limitation by counting the individual electron events rather than integrating the signal. For the counting mode to be efficient, the camera requires a high frame rate (>400 frames per second) to identify the e^- separately and a long exposure time (Bai, McMullan, and Scheres 2015). Our images were done using the counting mode.

2.7.1.3 Vacuum system, energy filters, and specimen stage

A high vacuum is necessary because the electrons interact highly with materials and would be stopped in a normal atmosphere, and to ensure that only one electron hits the specimen at a given time. Nevertheless, as e^- behave as waves, we still experience constructive and destructive interference and electron diffraction, so filtering e^- of different energies is necessary. The energy filter, located in-column or post-column, separates inelastically scattered e^- from unscattered and elastically scattered e^- (Williams and Carter 2008).

2.8 BIBLIOGRAPHY

- Bai, Xiao-chen, Greg McMullan, and Sjors H.W Scheres. 2015. "How Cryo-EM Is Revolutionizing Structural Biology." *Trends in Biochemical Sciences* 40 (1): 49–57. <https://doi.org/10.1016/j.tibs.2014.10.005>.
- Cheng, Yifan, Nikolaus Grigorieff, Pawel A. Penczek, and Thomas Walz. 2015. "A Primer to Single-Particle Cryo-Electron Microscopy." *Cell* 161 (3): 438–49. <https://doi.org/10.1016/j.cell.2015.03.050>.

- De Broglie, Louis. 1925. “Recherches Sur La Théorie Des Quanta.” *Annales de Physique* 10 (3): 22–128. <https://doi.org/10.1051/anphys/192510030022>.
- Debye, Peter, and Erich Hückel. 1923. “Zur Theorie Der Elektrolyte. I. Gefrierpunktserniedrigung Und Verwandte Erscheinungen.” Translated by Michael J. Braus. *Physikalische Zeitschrift* 24: 185–206.
- Dubochet, Jacques, Marc Adrian, Jiin-Ju Chang, Jean-Claude Homo, Jean Lepault, Alasdair W. McDowall, and Patrick Schultz. 1988. “Cryo-Electron Microscopy of Vitrified Specimens.” *Quarterly Reviews of Biophysics* 21 (2): 129–228. <https://doi.org/10.1017/S0033583500004297>.
- Emsley, Paul, and Kevin Cowtan. 2004. “Coot: Model-Building Tools for Molecular Graphics.” *Acta Crystallographica Section D Biological Crystallography* 60 (12): 2126–32. <https://doi.org/10.1107/S0907444904019158>.
- Frank, Joachim. 2006. *Three-Dimensional Electron Microscopy of Macromolecular Assemblies: Visualization of Biological Molecules in Their Native State*. 2. ed. Oxford: Oxford University Press.
- Gimpl, Katharina, Jessica Klement, and Sandro Keller. 2016. “Characterising Protein/Detergent Complexes by Triple-Detection Size-Exclusion Chromatography.” *Biological Procedures Online* 18 (1): 4. <https://doi.org/10.1186/s12575-015-0031-9>.
- Goodhew, Peter. 2011. “General Introduction to Transmission Electron Microscopy (TEM).” In *Aberration-Corrected Analytical Transmission Electron Microscopy*, edited by Rik Brydson, 1–19. Chichester, UK: John Wiley & Sons, Ltd. <https://doi.org/10.1002/9781119978848.ch1>.
- Goodhew, Peter John, and Frederick John Humphreys. 1992. *Electron Microscopy and Analysis*. 2nd ed., Repr. London: Taylor & Francis.
- Hartmann, Lucie, Valérie Kugler, and Renaud Wagner. 2016. “Expression of Eukaryotic Membrane Proteins in *Pichia Pastoris*.” In *Heterologous Expression of Membrane Proteins*, edited by Isabelle Mus-Veteau, 1432:143–62. Methods in Molecular Biology. New York, NY: Springer New York. https://doi.org/10.1007/978-1-4939-3637-3_10.
- Hartmann, Lucie, Estelle Metzger, Noémie Ottelard, and Renaud Wagner. 2017. “Direct Extraction and Purification of Recombinant Membrane Proteins from *Pichia Pastoris* Protoplasts.” In *Membrane Protein Structure and Function Characterization*, edited by Jean-Jacques Lacapere, 1635:45–56. Methods in Molecular Biology. New York, NY: Springer New York. https://doi.org/10.1007/978-1-4939-7151-0_3.
- Karlsson, Robert, Phinikoula S. Katsamba, Helena Nordin, Ewa Pol, and David G. Myszka. 2006. “Analyzing a Kinetic Titration Series Using Affinity Biosensors.” *Analytical Biochemistry* 349 (1): 136–47. <https://doi.org/10.1016/j.ab.2005.09.034>.
- Li, Xueming, Paul Mooney, Shawn Zheng, Christopher R Booth, Michael B Braunfeld, Sander Gubbens, David A Agard, and Yifan Cheng. 2013. “Electron Counting and Beam-Induced Motion Correction Enable near-Atomic-Resolution Single-Particle Cryo-EM.” *Nature Methods* 10 (6): 584–90. <https://doi.org/10.1038/nmeth.2472>.
- Ludtke, Steven J., Philip R. Baldwin, and Wah Chiu. 1999. “EMAN: Semiautomated Software for High-Resolution Single-Particle Reconstructions.” *Journal of Structural Biology* 128 (1): 82–97. <https://doi.org/10.1006/jsbi.1999.4174>.
- McMullan, G., S. Chen, R. Henderson, and A.R. Faruqi. 2009. “Detective Quantum Efficiency of Electron Area Detectors in Electron Microscopy.” *Ultramicroscopy* 109 (9): 1126–43. <https://doi.org/10.1016/j.ultramic.2009.04.002>.
- Mindell, Joseph A., and Nikolaus Grigorieff. 2003. “Accurate Determination of Local Defocus and Specimen Tilt in Electron Microscopy.” *Journal of Structural Biology* 142 (3): 334–47. [https://doi.org/10.1016/S1047-8477\(03\)00069-8](https://doi.org/10.1016/S1047-8477(03)00069-8).
- Penczek, Pawel A. 2010. “Image Restoration in Cryo-Electron Microscopy.” In *Methods in Enzymology*, 482:35–72. Elsevier. [https://doi.org/10.1016/S0076-6879\(10\)82002-6](https://doi.org/10.1016/S0076-6879(10)82002-6).

- Privé, Gilbert G. 2007. “Detergents for the Stabilization and Crystallization of Membrane Proteins.” *Methods* 41 (4): 388–97. <https://doi.org/10.1016/j.ymeth.2007.01.007>.
- Rohou, Alexis, and Nikolaus Grigorieff. 2015. “CTFFIND4: Fast and Accurate Defocus Estimation from Electron Micrographs.” *Journal of Structural Biology* 192 (2): 216–21. <https://doi.org/10.1016/j.jsb.2015.08.008>.
- Scheres, Sjors H.W. 2010. “Classification of Structural Heterogeneity by Maximum-Likelihood Methods.” In *Methods in Enzymology*, 482:295–320. Elsevier. [https://doi.org/10.1016/S0076-6879\(10\)82012-9](https://doi.org/10.1016/S0076-6879(10)82012-9).
- . 2012a. “A Bayesian View on Cryo-EM Structure Determination.” *Journal of Molecular Biology* 415 (2): 406–18. <https://doi.org/10.1016/j.jmb.2011.11.010>.
- . 2012b. “RELION: Implementation of a Bayesian Approach to Cryo-EM Structure Determination.” *Journal of Structural Biology* 180 (3): 519–30. <https://doi.org/10.1016/j.jsb.2012.09.006>.
- Slotboom, Dirk Jan, Ria H. Duurkens, Kees Olieman, and Guus B. Erkens. 2008. “Static Light Scattering to Characterize Membrane Proteins in Detergent Solution.” *Methods* 46 (2): 73–82. <https://doi.org/10.1016/j.ymeth.2008.06.012>.
- Spence, John C. H. 2017. *High-Resolution Electron Microscopy*. Fourth edition, First published in paperback. Oxford: Oxford University Press.
- Stetefeld, Jörg, Sean A. McKenna, and Trushar R. Patel. 2016. “Dynamic Light Scattering: A Practical Guide and Applications in Biomedical Sciences.” *Biophysical Reviews* 8 (4): 409–27. <https://doi.org/10.1007/s12551-016-0218-6>.
- Tang, Guang, Liwei Peng, Philip R. Baldwin, Deepinder S. Mann, Wen Jiang, Ian Rees, and Steven J. Ludtke. 2007. “EMAN2: An Extensible Image Processing Suite for Electron Microscopy.” *Journal of Structural Biology* 157 (1): 38–46. <https://doi.org/10.1016/j.jsb.2006.05.009>.
- Wade, R.H. 1992. “A Brief Look at Imaging and Contrast Transfer.” *Ultramicroscopy* 46 (1–4): 145–56. [https://doi.org/10.1016/0304-3991\(92\)90011-8](https://doi.org/10.1016/0304-3991(92)90011-8).
- Wagner, Thorsten, Felipe Merino, Markus Stabrin, Toshio Moriya, Claudia Antoni, Amir Apelbaum, Philine Hagel, et al. 2019. “SPHIRE-CrYOLO Is a Fast and Accurate Fully Automated Particle Picker for Cryo-EM.” *Communications Biology* 2 (1): 218. <https://doi.org/10.1038/s42003-019-0437-z>.
- Williams, David Bernard, and C. Barry Carter. 2008. *Transmission Electron Microscopy: A Textbook for Materials Science*. 2nd ed. Cambridge Library Collection. New York: Springer.
- Wittig, Ilka, Hans-Peter Braun, and Hermann Schägger. 2006. “Blue Native PAGE.” *Nature Protocols* 1 (1): 418–28. <https://doi.org/10.1038/nprot.2006.62>.
- Zheng, Shawn Q., Eugene Palovcak, Jean-Paul Armache, Kliment A. Verba, Yifan Cheng, and David A. Agard. 2017. “MotionCor2: Anisotropic Correction of Beam-Induced Motion for Improved Cryo-Electron Microscopy.” *Nature Methods* 14 (4): 331–32. <https://doi.org/10.1038/nmeth.4193>.
- Zhu, Jun, Pawel A. Penczek, Rasmus Schröder, and Joachim Frank. 1997. “Three-Dimensional Reconstruction with Contrast Transfer Function Correction from Energy-Filtered Cryoelectron Micrographs: Procedure and Application to the 70S *Escherichia Coli* Ribosome.” *Journal of Structural Biology* 118 (3): 197–219. <https://doi.org/10.1006/jsbi.1997.3845>.

3 BIOCHEMICAL AND BIOPHYSICAL CHARACTERIZATION OF KIR2.1 AND MUTANTS

3.1 INTRODUCTION

Despite MPs' tremendous significance and the astronomical advances in structural biology (notably cryo-EM), they constitute a minority of resolved structures. There is an inherent difficulty that surrounds the study of MPs (Seddon, Curnow, and Booth 2004): 1) MPs are often expressed in low concentrations in their native cells (bacteriorhodopsin being a notable exception), making recombinant expression (and optimization) necessary, and even in heterologous systems, overexpression of mammalian MPs may prove particularly tricky. 2) MPs are embedded in the cell membranes; extracting them intact, in sufficient quantities, and functionally active is still a challenge. 3) MPs' intrinsic hydrophobicity forces them to aggregate in aqueous solutions, creating the need to mimic the biological membrane to keep them stable in aqueous solutions. 4) Finally, the environment chosen for stabilizing the MP must be compatible with the biophysical and biochemical techniques used to characterize it.

The difficulties in the structural determination of membrane proteins can arise at any step in the workflow from gene to structure, from insufficient protein production to poor solubilization to aggregation and protein instability. This chapter will describe the heterologous expression of human Kir2.1 in *Pichia pastoris* yeast. It will address the production, solubilization, and purification steps necessary to establish a robust protocol for obtaining Kir2.1 for structural studies. Then I will characterize the purified Kir2.1 biophysically and biochemically, as well as two mutants responsible for AS and their effects.

3.1.1 Recombinant expression of membrane proteins

Different expression systems are available to overproduce MPs recombinantly, including bacteria, yeast, insect cells, fruit fly eyes, mammalian cells, and even cell-free systems. Each system has its advantages and inconveniences; for details, please read (Mus-Veteau 2010). The most used system to overexpress prokaryotic MPs is *Escherichia coli* due to its convenience and low price. Although *E. coli* is unsuitable for producing properly-folded eukaryotic MPs, a typical strategy is first to characterize the bacterial homolog and then pursue the eukaryotic MP in a different system. For a human protein, it would be best to produce it in mammalian cells, which will contain a lipid environment closer to the native one; however, the expression levels are low, and the production is costly. Yeast provides an excellent compromise, particularly *Pichia pastoris*, which can be grown to very high densities with a tight regulation

through the AOX1 promoter and can produce properly folded MP with post-translational modifications (Byrne 2015; Hartmann, Kugler, and Wagner 2016).

3.1.2 Detergents

Once the MP is produced, it must be extracted from the host membrane. Many surfactants (surface-active agents) allow the solubilization and purification of MPs, including detergents. Detergents are amphipathic surfactants comprised of a polar head and a hydrophobic tail. Detergents have been indispensable for creating model membranes to isolate MPs and protect them *in vitro*. Unfortunately, there is no universal one-size-fits-all detergent, and finding the optimal conditions is very protein and system-dependent. Many parameters, including the critical micellar concentration (CMC), detergent aggregation number (N_{agg}), length of detergent chain, nature of the MP, the lipid composition of the membrane it is embedded in, and the ionic strength of the aqueous environment, play a non-negligible role in how good one detergent is compared to another. Where one detergent could extract the MP effectively, it may be too harsh to keep it stable. In contrast, a milder detergent could provide adequate stability but low solubilization.

Much literature details detergents and how they interact with lipid membranes; a reader with avid curiosity is invited to check out some excellent reviews (Helenius and Simons 1975; le Maire, Champeil, and Møller 2000; Seddon, Curnow, and Booth 2004; Heerklotz 2008; Linke 2009).

A wide range of detergents exists, with different polar head chemistries including maltosides, amine oxides, glucosides, glucopyranoside, propane sulfonate, and neopentyl glycols. These categories can be grouped into three classes based on their charge: 1) ionic detergents, 2) zwitterionic detergents, and 3) nonionic detergents.

Generally, for membrane proteins, nonionic detergents are preferred. More specifically, maltosides are the detergents most widely used for the solubilization of proteins (Choy et al. 2021; Le Bon et al. 2021).

3.1.2.1 Critical Micellar Concentration

Detergents can be solubilized in aqueous solutions, and their solubility depends on the strength of the polarity of the head and the length of their hydrophobic tail. The solubility is a tug-of-war between entropically unfavorable interactions and favorable

hydrogen bonds formed by the head group and water. The strong interactions between water molecules are primarily responsible for apolar groups' limited solubility in an aqueous solution (Tanford 1973; Helenius and Simons 1975). These water interactions must be broken or deformed when introducing a detergent molecule. As there is little compensatory attraction between water and the hydrocarbon, the water molecules nearest to it are pushed into organized cage-like structures. Furthermore, the internal mobility of hydrocarbon chains, and thus the entropy, is decreased (Aranow 1963; Helenius and Simons 1975).

At low concentrations, the polar interactions gained between the water and the polar head are enough to keep the individual molecules in suspension. At a particular concentration, called the critical micellar concentration (CMC), the negative entropy will drive the hydrophobic tails to be sequestered away from water and organize themselves in somewhat spherical arrangements. In these noncovalent arrangements, called micelles, the polar heads face the water, and the tails are tucked away. The detergent solubility and the number of molecules per micelle (aggregation number) will depend on the length of the tail and the size and extent of the polarity of the headgroup. The individual detergent molecules within the micelle are in thermodynamic equilibrium with detergent monomers in the surrounding medium (Yeagle 2016). Overall, the CMC is an influential parameter when discussing the effectiveness of a detergent.

When considering the solubilization of MP from a biological membrane, one must add detergent in great abundance, considerably above its CMC, to achieve the solubilization of membrane fragments and eventually accommodate for the MP alone (**SUPPLEMENTARY MATERIAL** section 3.6.1.2). Once solubilized in detergent, MPs can be treated like soluble proteins as long as the detergent concentration is kept above the CMC.

3.2 MATERIALS AND METHODS

See Materials and Methods section 2.1 and 2.3 (specifically 2.1.1, 2.1.2, 2.1.3, 2.1.4, 2.1.5, 2.1.7, 2.1.8, 2.3.1, 2.3.2)

3.3 RESULTS

Finding the optimal conditions for obtaining large amounts of high-quality membrane protein for structural studies can be very time-consuming. Each step of the process is

subject to optimization: production, lysis, solubilization, and purification. To facilitate the reading, I have included the optimization steps in the **SUPPLEMENTARY MATERIAL** section at the end of this chapter. Altogether, the results section and the corresponding supplementary material will explore the development of the expression and purification protocol for Kir2.1 and some of the limitations encountered.

3.3.1 Heterologous expression of human Kir2.1 in *Pichia pastoris*

The synthetic KCNJ2 gene encoding the entire h_Kir2.1 sequence (427 amino acids, Uniprot P63252) with a PreScission protease cleavage site followed by 11 linker residues, and a 10 histidine tag, was integrated into *P. pastoris* strain SMD1163 genome through pPIC9K vector containing a strong methanol-inducible P_{AOX1} promoter and Kan resistance gene. The resulting protein has a theoretical Mw of 51.6 kDa as a monomer and 206.4 kDa as a tetramer. The two AS-mutants, R312H and C154Y, were also produced.

Collaborators R. Wagner and V. Kugler screened the clones by yeastern blot and compared expressions by western blot (Figure 3-23). The clone showcasing the highest expression levels were selected for Kir2.1 and mutants C154Y and R312H (Figure 3-1).

The production protocol in *P. pastoris* followed previously established protocol (Hartmann, Kugler, and Wagner 2016) with minor variations. The pH (Figure 3-22, top), agitation speed (Figure 3-22, bottom), culture growth times, induction starting concentrations (Figure 3-23), and incubation times were varied to ensure optimal conditions to produce Kir2.1. The initial Erlenmeyer culture flasks were traded for Ultra High Yield Thompson flasks with a paper filter top, allowing better aeration. This change increased cell culture growth by three and the cell yield by 1.34 after induction (from 14.3 ± 0.8 g to 19.2 ± 0.5 g pellet per L induced).

The optimized production protocol included an overnight starter culture in BMGY pH 6.0 without antibiotics. A 5-7 h culture step with an initial concentration of $3.5 \cdot 10^7$ cells \cdot mL⁻¹, followed by 18-24 h induction in BMMY (0.5% methanol) at RT with $1.2 \cdot 10^8$ cells \cdot mL⁻¹, with 220-250 rpm agitation (details in Materials and Methods section 2.1.1).

Once the culture and induction conditions were established, they were used to produce the mutant counterparts, R312H and C154Y. The stable clones expressing Kir2.1 were selected by yeastern blot and western blot. Kir2.1_R312H had the same expression

levels as Kir2.1 (not shown), whereas Kir2.1_C154Y yield was reduced in half (Figure 3-1 bottom right panel). No significant differences in culture growth were observed (Figure 3-1 top right panel).

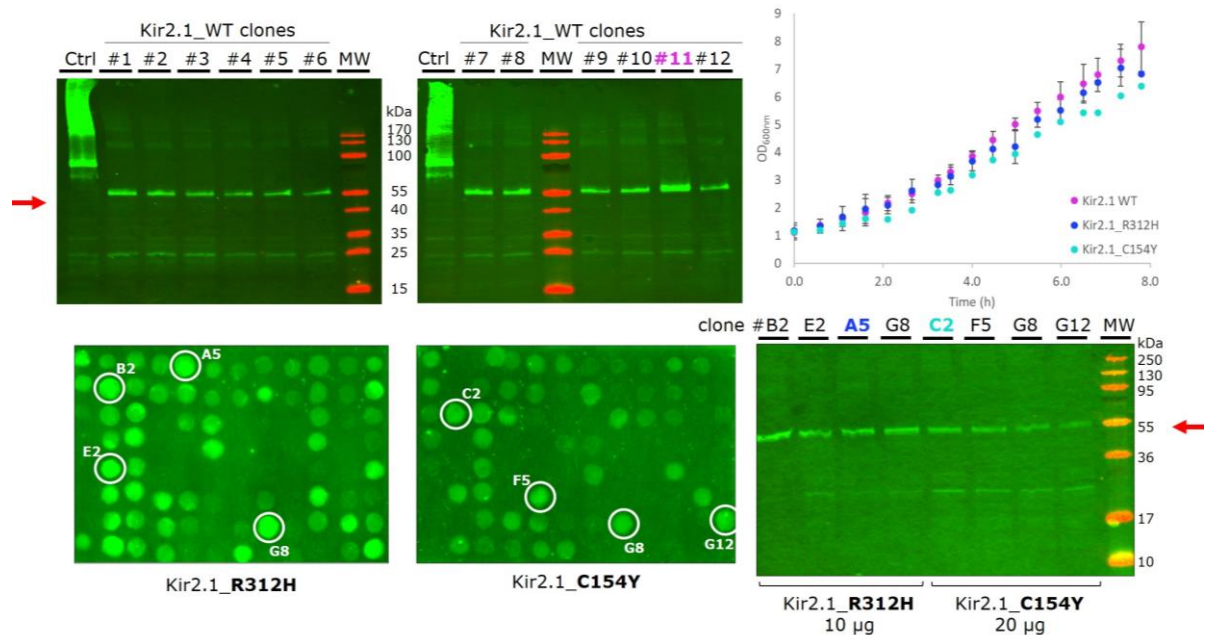


Figure 3-1. Cell growth and expression of Kir2.1 and mutants in *P.pastoris*. Top panel: western blot of Kir2.1_WT expressing clones and comparison of cell growth of best-expressing clone for Kir2.1, R312H and C154Y mutants, respectively, at 30 °C. Bottom panel: yeastern blot selection of Kir2.1_R312H (left) and Kir2.1_C154Y (center) expressing clones and western blot comparing protein expression (right).

After obtaining Kir2.1 in *P. pastoris* cells, the next step is to lyse the cells and extract Kir2.1 from the cell membranes.

3.3.2 Extracting human Kir2.1 from *Pichia pastoris* cell membranes

3.3.2.1 Cell lysis

Extracting Kir2.1 from *Pichia pastoris* proved particularly difficult. *P. pastoris* cells contain a thick cell wall consisting of an outer layer containing mannoproteins and an inner layer containing β -1,6-glycan, β -1,3-glycan, and chitin (Cabib and Arroyo 2013). Enzymatic lysis with Zymolyase was followed by mechanical lysis using pressure (Cell Disruptor) or milling with glass beads. The lysis with glass beads provided better results and was used when possible. For more details, please refer to **SUPPLEMENTARY MATERIAL** section 3.6.3 *Optimizing cellular lysis* at the end of this chapter.

3.3.2.2 Finding the suitable membrane solubilization parameters

Initially, fifteen detergents were screened to determine the best choice (Table 3-1). The yeast cells were lysed (with Cell D), and the MPs were pelleted. The MP pellet was resuspended thoroughly and diluted to $5 \text{ mg} \cdot \text{mL}^{-1}$. The detergent was added in significant excess ($\sim 100 \cdot \text{CMC}$) except for the detergents with CMC higher than 0.2% or lower than 0.001% (Table 3-1). The sample was incubated for 45 min at RT under gentle rotation and centrifuged at $100,000 \cdot \text{g}$ for 30 min at $4 \text{ }^\circ\text{C}$. The cell pellet containing the insoluble MPs fraction was weighed after detergent treatment to test the solubilization efficiency of these detergents. A large pellet indicated that the detergent did not dissolve well; conversely, a small pellet indicated a detergent that solubilized well.

Table 3-1 Detergent assay

#	Head group/ nature	Detergent	CMC (mM, %)	Conc (mM, %)	Unsol. pellet
1	Phosphocholine (Lipid-like surfactant)	FC14 n-Tetradecylphospho- choline	0.12 mM (0.0046%)	18 mM, 0.7% (150 · CMC)	16 mg
2	Maltoside (Nonionic)	Cymal-6 6-Cyclohexylhexyl- β -D- maltoside	0.56 mM (0.028%)	55.2 mM, 2.8% (98.6 · CMC)	26 mg
3	Dimethylamine- oxide (Zwitterionic)	LDAO n-Dodecyl-N-N- Dimethylamine N-Oxide	H ₂ O:1–2 mM (0.023%) 0.1 M NaCl: 0.14 mM	145.4 mM, 2.2% (97 · CMC)	30 mg
4	Maltoside (Nonionic)	DDM/TriDM		4.5 mg TriDM & 6 mg DDM	35 mg
5	Propane sulfonate (Zwitterionic)	CHAPS 3-[(3-cholamidopropyl)- dimethylammonio]-1- propane sulfonate	8 mM (0.49%)	86.5 mM, 5.3% (10.8 · CMC)	36 mg
6	Glucoside (Nonionic)	OG n-octyl- β -D glucoside	H ₂ O:18–20 mM (0.53%) 0.1 M NaCl: 23.4 mM	265.3 mM, 7.4% (14 · CMC)	36 mg
7	Maltoside (Nonionic)	DDM n-Dodecyl- β -D-maltoside	H ₂ O: 0.17 mM (0.0087%) (0.2M NaCl) ~ 0.12 mM (0.0061%)	19.5 mM, 1.0% (114.9 · CMC)	36 mg
8	Neopentyl Glycol (Nonionic)	LMNG Lauryl Maltose Neopentyl Glycol	0.01mM (0.001%)	9 mM, 0.9% (900 · CMC)	36 mg
9	Maltoside (Nonionic)	DM n-Decyl- β -D-maltoside	1.8 mM (0.087%)	165.5 mM, 8% (92 · CMC)	37 mg
10	Maltoside (Nonionic)	HexaDM	0.0006 mM (0.00003%)	3.8 mM, 0.19% (6333 · CMC)	44 mg

11	Glucoside (Nonionic)	NG Nonyl- glucoside	H ₂ O: 6.5 mM (0.20%) 0.15 M NaCl: 6 mM	412.8 mM, 12.7% (63.5 · CMC)	46 mg
12	(Nonionic)	TRITON X-100 α -[4-(1,1,3,3-Tetramethyl butyl)-phenyl]- ω -hydroxy- poly(oxy-1,2-ethanediyl)	H ₂ O: 0.010 - 0.016% (1-4)(w/v) 16 mg · mL ⁻¹	1.6% (100 · CMC)	46 mg
13	Maltoside (Nonionic)	TriDM n-Tridecyl- β -D-maltoside	H ₂ O: 0.033 mM (0.0017%) 0.15 M NaCl: 0.024 mM (0.0013%)	5.8 mM, 0.3% (176 · CMC)	50 mg
14	Maltoside (Nonionic)	TetraDM n-Tetradecyl- β -D- maltoside	0.01 mM (0.00054%)	6.5 mM, 0.4% (648 · CMC)	51 mg
15	(Zwitterionic)	FOS-MEA 12 Dodecylphospho-N- Methylethanolamine	0.43 mM (0.014%)	34.7 mM, 1.1% (80.7 · CMC)	52 mg
16	Phosphocholine (Lipid-like surfactant)	FC16 n-Hexadecylphospho- choline	0.013 mM (0.00053%)	3.9 mM, 0.2% (302 · CMC)	57 mg

Table 3-1 and Figure 3-2 present the detergents ranked in descending order of solubilization efficacy in the conditions tested. FC14 resulted in the best solubilization (Figure 3-2), followed by Cymal-6, LDAO, and DDM-TriDM mixture. Although CHAPS, OG, DDM, and LMNG gave equally-weighted pellets, CHAPS and OG solubilized better as they were only at 10 · CMC, whereas DDM was at 117 · CMC and LMNG at 900 · CMC (Table 3-1).

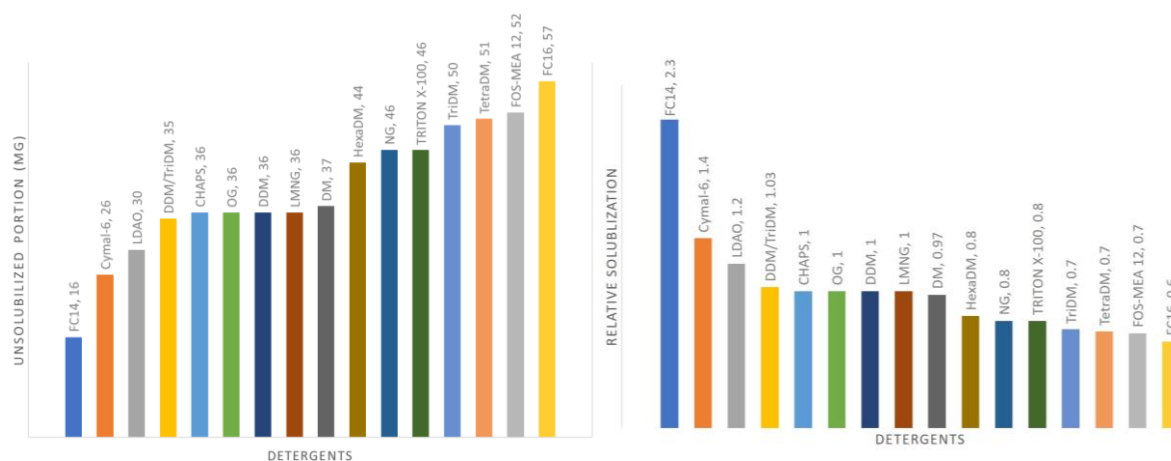


Figure 3-2. Detergent screen for optimal solubilization of human Kir2.1 expressed in *Pichia pastoris*. The detergent was added to a 5.12 mg · mL⁻¹ resuspended membrane pellet at concentrations indicated in Table 3-1. On the left, the chart shows the mass of the insoluble pellet after treatment with detergent. On the right, the chart indicates the relative solubilization normalized by setting the DDM solubilization to equal 1.

Aside from solubilization efficiency, I was also looking for detergents compatible with biochemical assays, used commonly for structure determination, not too expensive, and

did not denature Kir2.1. Among the 15 detergents screened for solubilization, I chose to go further with four: FC14, which provided the best solubilization, and DDM, LMNG, and DM, three nonionic detergents with low CMC.

To describe these four detergents:

FC14 is a lipid-like surfactant. It efficiently solubilizes MPs from the membrane. However, some literature points to denaturing and destabilizing properties, especially α -helical proteins (Chipot et al. 2018). It has previously been used to purify Kir2.1 (D'Avanzo et al. 2010) and for structural determination using NMR (Choy et al. 2021).

DDM is a mild nonionic detergent in the maltoside category. It is compatible with biochemical column purification steps, cryo-electron microscopy, crystallization, mass spectrometry, SPR, and reconstitution in membranes for functional studies. It has widely been used for the structure determination of membrane proteins and is generally a safe starting point (Choy et al. 2021).

DM is similar to DDM but has a shorter tail (10 instead of 12 carbons) and a higher CMC (10x).

LMNG is a mild nonionic detergent with a very low CMC. It has been increasingly used for ion channels and GPCRs, particularly as an exchange after solubilization. (Choy et al. 2021; Le Bon et al. 2021).

I then performed a second detergent screen using these four detergents. The lysis was done using glass beads instead of Cell D. The membrane pellet was resuspended thoroughly, diluted to $1.7 \text{ mg} \cdot \text{mL}^{-1}$, and treated with 1% detergent. The results were observed using a western blot (Figure 3-3). These results were coherent with those obtained by weighing the pellets (Table 3-1, Figure 3-2). FC14 solubilized exceptionally well; only a faint band was discernible in the pellet. DDM (with and without cholesteryl hemisuccinate lipid, CHS) solubilized better than LMNG and DM. Only FC14 and DDM were considered for future experiments as they provided the best solubilizations.

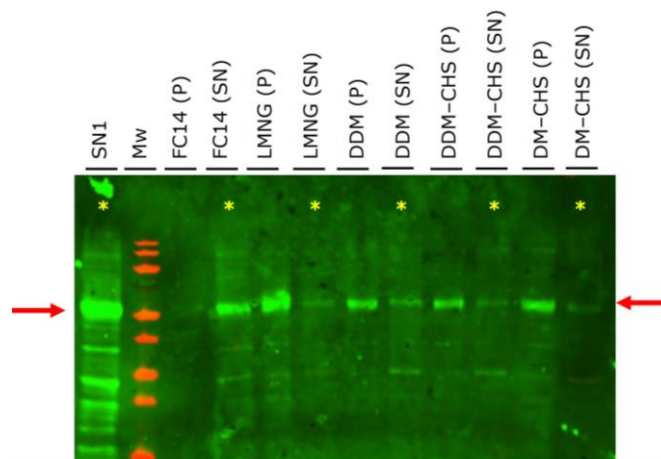


Figure 3-3. Western blot of Kir2.1 solubilization test using different detergents with or without added lipids. SN1 indicates the lysed fraction post-glass-beads treatment. (P) designates the unsolubilized MP pellet and (SN) the supernatant containing the solubilized MPs. The bands at 50 kDa, highlighted by red arrows, indicate the presence of the Kir2.1-His tag.

The best solubilization conditions for FC14 were $6 \text{ mg} \cdot \text{mL}^{-1}$ Kir2.1 with 0.5% FC14, and the best results in DDM were obtained after incubation of $2 \text{ mg} \cdot \text{mL}^{-1}$ Kir2.1 with 1.5% DDM for 30–60 minutes at RT.

3.3.3 Two-step purification, identification of Kir2.1, and analysis of post-translational modifications by mass spectrometry

After extraction from the membranes, Kir2.1 followed a classic 2-step purification where an affinity chromatography was followed by size exclusion chromatography (SEC). Taking advantage of the histidine tag, a cobalt resin was used to separate Kir2.1 from contaminants, and then Kir2.1 was eluted in steps of 90 mM, 150 mM, 350 mM, and 500 mM imidazole.

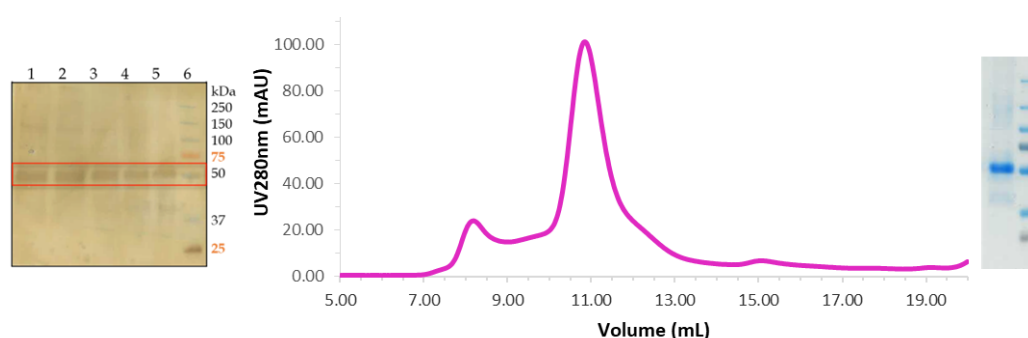


Figure 3-4. two-step purification of Kir2.1. Left; SDS PAGE of affinity chromatography elution fractions at 350 mM imidazole (1-6) revealed by silver nitrate. The Kir2.1 monomer (51.6 kDa) is visible at the 50 kDa band. Center: SEC elution profile of Kir2.1. Right: SDS PAGE of Kir2.1 after SEC purification (center of the peak).

The SDS PAGE gels of the affinity chromatography fractions revealed two prominent bands, one at 50 kDa, compatible with a Kir2.1 monomer, and another at 100 kDa.

For some productions, we observed a double band at 50 kDa, which raised the question of post-translational modifications (PTMs). PTMs are numerous in eukaryotic proteins, all the more so for membrane proteins. The hypothesis of phosphorylation and glycosylation, in particular, was thus advanced since phosphorylation is involved in biological regulation and the response to intracellular stimuli. Both are involved in cell addressing.

Mass spectrometry (MS) experiments at Pasteur Institute done by in-gel digestion of the 50 kDa and 100 kDa bands after affinity chromatography allowed us to confirm the identity of Kir2.1 in the 50 kDa band (53.3% sequence coverage identified). They characterized the band present at 100 kDa to be primarily an uncharacterized transmembrane protein native to *P. pastoris* (C4R5N2_KOMPG) and some Kir2.1 dimer. One phosphorylated residue (S-14) was confirmed (without TiO₂ enrichment, which has a high affinity for phosphopeptides).

MS experiments at the IBPS platform from the SEC fractions used for cryo-EM were confirmed to be Kir2.1 (45% sequence coverage identified), including the beginning, middle, and end. Kir2.1 was not truncated in any way. Three phosphorylation sites (S-13, S-14, and T-353, Figure 3-5) were determined with probability scores greater than 97%.

```

MGSVRTNRYSIVSSEEDGMKLATMAVANGFGNGKSKVHTRQQCRSRFVKDGHCNVQFINVGEKQRYLAD
IFTTCVDIRWRWMLVIFCLAFVLSWLFFGCVFWLIALLLHGDLDASKEGKACVSEVNSFTAAFLFSIETQTT
IGYGFRCVTDECPIAVFMVVFQSIVGCIIDAFIIGAVMAKMAKPKKRNETLVFSHNAVIAMRDGKLCLMWR
VGNLRKSHLVEAHVRAQLLKSRITSEGEYIPLDQIDINVGFDSGIDRIFLVSPITIVHEIDEDSPLYDLSK
QDIDNADFEIVVILEGMVEATAMTTQCRSSYLANEILWGHRYEPVLFEEKHYYKVDSRFHKTYEVPNTPL
CSARDLAEKKYILSNANSFCYENEVALTSKEEDDSENGVPESTSTDTPPDIDLHNQASVPLEPRLRRESE
ILEVLFQGPTSLERAPGGGSHHHHHHHHHHH

```

Figure 3-5. Kir2.1 sequence with segments identified by mass spectrometry. In red are the peptide segments identified by in-gel digestion, and underlined are the peptide segments identified in solution. In bold, the phosphorylation sites found with one phosphorylation site in blue were identified in both runs, even without TiO₂ enrichment.

The contaminant at 100 kDa was reduced/eliminated by adding a 90 mM imidazole step in the affinity chromatography. The presence of a faint band at 100 kDa is expected as it contains the Kir2.1 dimer.

Although a unique N-glycosylation site was predicted for Kir2.1 (N-192) using NetNGlyc 1.0 with a 0.6998 probability score, treatment with PNGase F enzyme did not elucidate glycosylation in Kir2.1. Both 50 kDa bands were sent to MS, at the I2BC platform, which identified Kir2.1 in both bands, but no glycol groups were identified. We concluded that Kir2.1 was not glycosylated in this expression system.

3.3.4 Evaluating the hydrodynamic radius of Kir2.1

3.3.4.1 Determination of Stokes radius from Size-exclusion chromatography and column calibration with standard proteins

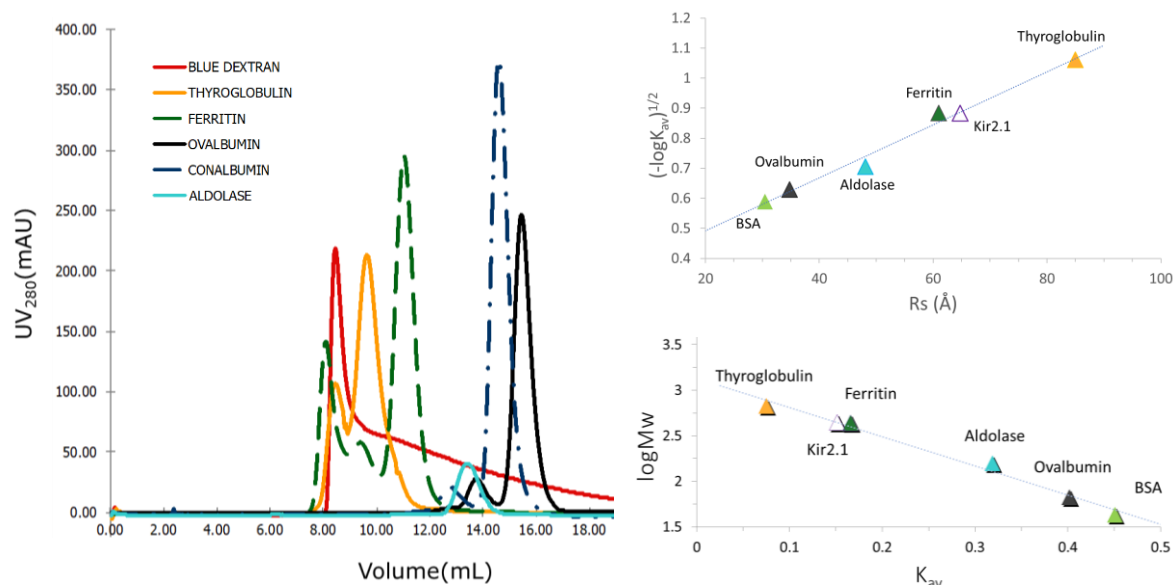


Figure 3-6. Determination of Kir2.1 Stokes radius based on SEC elution profile. The partition coefficient (K_{av}) of the standard proteins and Kir2.1 (0.1) were determined experimentally using the elution volumes from Superdex 200 10/300 GL and Superdex 200 10/300 Increase columns.

Kir2.1-DDM complex elutes at a similar volume as Ferritin, with an apparent Mw of 421.4 ± 19.8 kDa. The hydrodynamic radius (R_s) of the Kir2.1-DDM complex was calculated to be 64.7 ± 1.3 Å (6.5 nm, $n=9$) by relating the partition coefficient (K_{av}) of standard proteins against their known Stokes radius (Figure 3-6). The partition coefficient is the fraction of the column volume available to the sample (Equation 3-1).

Equation 3-1

$$K_{av} = \frac{V_e - V_0}{V_t - V_0}$$

V_e is the elution volume, V_t is the total volume, and V_0 is the void column volume (Laurent and Killander 1964).

While the R_s obtained through this method, 64.7 ± 1.3 Å, does not indicate the protein's actual hydrodynamic radius, it can provide valuable information on the elution of the protein-detergent-lipid complex. It can be handy when comparing the elution profiles in different detergents. This R_s is coherent with the previously described radius of Kir2.1, 62.3 Å (D'Avanzo et al. 2010). This slight discrepancy (within 1–3 Å) can be explained by any of the following differences in the two Kir2.1 proteins: they

were expressed in different systems (*P. pastoris* vs. *S. cerevisiae*), from different constructs (His-tag vs. flag-tag), and purified with different detergents (DDM vs. FC14) that can leave or remove different amounts of lipids surrounding Kir2.1.

3.3.4.2 Dynamic Light Scattering – a method to check the quality of membrane protein

Similar to the calibration of the SEC column, dynamic light scattering (DLS) provided the Kir2.1-DDM complex Stokes radius, as this in-batch analysis cannot separate the complex into its components. Its ability to evaluate the overall complex in different buffers in a short time and gauge the quality of the sample made DLS a convenient, complementary technique. During this thesis, I used DLS as quality control to assess the polydispersity and aggregation of the sample (in conjunction with negative staining analysis) before proceeding to cryo-EM imaging.

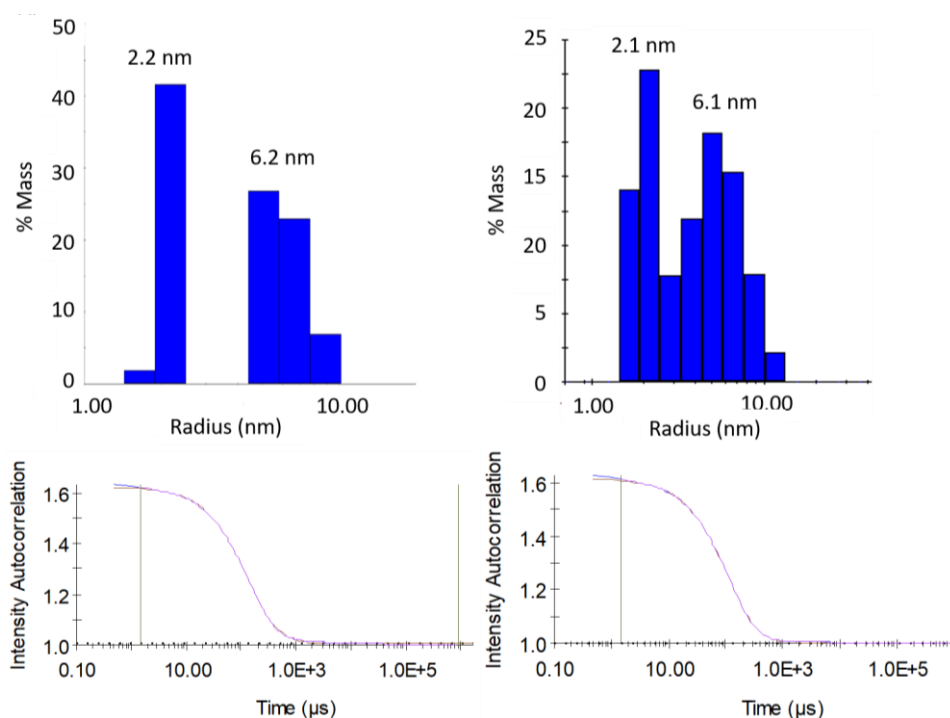


Figure 3-7. DLS measurements showing R_s values for Kir2.1 complex and DDM micelles. Two replicates are shown, the first peak at 2 nm radius is the diffusion of the free detergent micelles in the solution and the second one is consistent with Kir2.1-DDM. The autocorrelation functions for the samples are shown at the bottom.

The autocorrelation curves of Kir2.1 showed an expected exponential decay as the delay time increased (Equation 2-2) and the curves were fitted using Dynamics V7 to determine the parameters, including R_s . DLS provided an R_s of $60.8 \pm 8.5 \text{ \AA}$ ($n=6$) for Kir2.1 with a weighted average polydispersity (%Pd) of $27.5\% \pm 9.8\%$. The %Pd gives an indication of the heterogeneity in the sample; typically, a sample with $<20\%$

polydispersity is a monodisperse sample. DLS provided an average R_s value of Kir2.1 consistent with that obtained through SEC calibration.

3.3.5 SEC-MALLS – a triple detection method to characterize membrane proteins in solution

3.3.5.1 Analysis of Kir2.1 in DDM

Two SEC columns were used for the following experiments, the Superdex 200 10/300 GL (S200) and the Superdex 200 10/300 GL Increase (S200 Increase). These two columns have equal separation properties; the latter is the newer version able to withstand higher pressure. Although the elution profiles for both columns are similar, there is approximately a 2 mL shift in elution volumes, which does not affect the results but needs to be considered when comparing the profiles.

3.3.5.2 Kir2.1 in 0.018% DDM

Kir2.1 eluted as one main peak at 11 mL using the S200 column (Figure 3-8, A) in 20 mM Tris-HCl, pH 8, 200 mM KCl, 1 mM EDTA, 0.018% DDM buffer (0.018%-DDM). This peak showed UV absorbance and was visible in the LS and Δ RI spectra. All three signals aligned well at the center of the peak (data not shown).

Kir2.1 was homogeneous only at the center of the peak between 11.3 mL and 11.6 mL (Figure 3-8, B). The Kir2.1-DDM complex displayed a molar mass of 254 ± 20 kDa, with Kir2.1 having a 215.2 ± 17.4 kDa molar mass and the DDM component a 38.7 ± 20.8 kDa mass. Therefore, this elution volume corresponded to a Kir2.1 tetramer, as the monomer is 51.6 kDa. This peak will from now on be referred to as the tetramer peak. From 10.9 mL to 11.2 mL, the beginning of the peak showed some polydispersity with a mixture of larger Kir2.1 molecules.

A prominent LS peak was visible at 9 mL with little UV contribution and no RI signal (Figure 3-8, A). It points to substantial objects that diffuse prominently (in LS) with absorbance at 280 nm but are few in quantity, as observed by the UV and Δ RI profiles. This peak will henceforth be labeled as aggregates.

A third peak was observed at 15.6 mL in the LS and Δ RI spectra, consistent with DDM micelles in control injection (Figure 3-8, C). This peak will be referred to as the detergent peak. Figure 3-8, D shows that the DDM peak is homogeneous throughout.

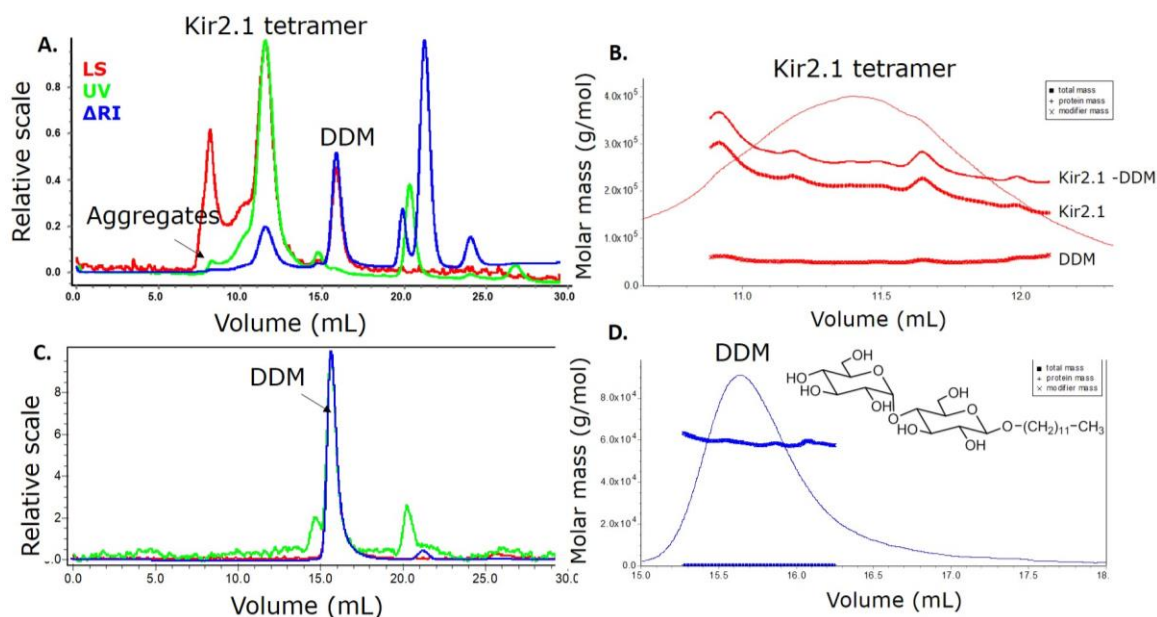


Figure 3-8. A) Kir2.1 SEC-MALLS elution profile in 20 mM Tris-HCl, pH 8, 200 mM KCl, 1 mM EDTA, 0.018% DDM (0.018% DDM SEC buffer) using Superdex 200 column (S200). LS, UV, and Δ RI spectra are shown in red, green, and blue, respectively. B) Molar mass vs. volume distribution of the Kir2.1 and DDM complex. The total molar mass, Kir2.1 molar mass, and DDM molar mass are shown. C.) 5% DDM profile in S200 column equilibrated with 0.018% DDM SEC buffer. DDM elutes at ~15.6 mL (in S200) with no UV contribution. D) Molar mass distribution vs. volume of DDM, DDM elutes as a monodisperse entity; its structure is represented for reference.

Although the Kir2.1 tetramer was homogeneous at the center of the peak (Figure 3-8), the beginning and end were polydisperse. The size of the micelles around Kir2.1 was 38.7 ± 20.8 kDa. The detergent peak had a micelle size of 57.3 ± 13.7 kDa was on average significantly smaller than the 72 kDa (Table 3-2) previously reported (Strop and Brunger 2005). The calculated N_{agg} of DDM within the Kir2.1-DDM complex is 75 ± 40 and the N_{agg} for the free DDM micelles in solution is 111.

3.3.5.3 Optimization of SEC-MALLS

The S200 and S200 Increase columns allowed analysis of Kir2.1 and mutant Kir2.1_R312H. These same S200 columns were used for Kir2.1 purification for all structural and functional assays. A few other columns were tested, including Agilent Bio SEC-3 and Phenomenex Biozen SEC-2, when optimizing the SEC-MALLS protocol. However, these did not produce exploitable results as the protein interacted with the matrix. No exploitable signal was observed even at the highest concentrations tested.

The Kir2.1 samples were first analyzed following isolation of the presumed tetramer portion post-SEC purification, concentrated ~100 times with a 100 kDa cutoff filter,

and reinjected into S200 for SEC-MALLS analysis. The additional concentration step resulted in aggregation, or the UV signal was insufficient to extract from the background. The best results were obtained when the protein was injected into SEC-MALLS right after affinity chromatography. The flow rate was reduced from $0.4 \text{ mL} \cdot \text{min}^{-1}$ to $0.3 \text{ mL} \cdot \text{min}^{-1}$ and the columns were systematically washed with NaOH to remove background noise coming from the column. These conditions were used in SEC-MALLS data presented hereafter.

3.3.5.4 *Kir2.1 in 0.03% DDM*

After optimization, the SEC buffer was adjusted to 20 mM Tris-HCl, pH 7.4, 150 mM KCl, 1 mM EDTA, and 0.03% DDM. The Kir2.1 profile (Figure 3-9, A) using the S200 Increase showed the tetramer peak shifted to 9.5 mL. Zoom on this peak showed that all signals aligned perfectly at the center (Figure 3-9, B), allowing the ASTRA software to determine the molar mass. The conjugate protein mass distribution showed Kir2.1 was extremely homogenous (Figure 3-9, C) throughout the peak in these buffer conditions. This peak was consistent with a tetrameric assembly of Kir2.1. The Kir2.1-DDM complex was determined to have a molar mass of $304.9 \pm 0.9 \text{ kDa}$, Kir2.1 being $203.9 \pm 0.6 \text{ kDa}$ surrounded by $100.1 \pm 0.9 \text{ kDa}$ of DDM, with a corresponding N_{agg} of 194 ± 2 . This free micelle mass, $76.4 \pm 1.7 \text{ kDa}$, seemed more congruent with published micelle sizes, 72 kDa (Table 3-2)(Strop and Brunger 2005), than at 0.018% DDM, $57.3 \pm 13.74 \text{ kDa}$ (Table 3-2). The control injection (Figure 18) showed that the peak at 14.1 mL corresponded to DDM micelles with a N_{agg} of 148.

The profile at 0.03% DDM ($4.5 \cdot \text{CMC}$) was more homogeneous than that at 0.018% DDM ($2.7 \cdot \text{CMC}$), possibly the concentration of DDM was simply not high enough. The average molar mass of the free DDM micelles in 0.018% seemed too low compared to the values found in the literature. Increasing the concentration of detergent in the solution, increased the number of molecules coupled with Kir2.1 by at least the same factor. In 0.018% DDM, 75 ± 40 DDM molecules aggregate per Kir2.1 tetramer, whereas in 0.03% there are 194 molecules per Kir2.1 tetramer. The mass-to-mass ratio of accessible TMD of Kir2.1 to DDM is 1:3.75 in 0.03% DDM.

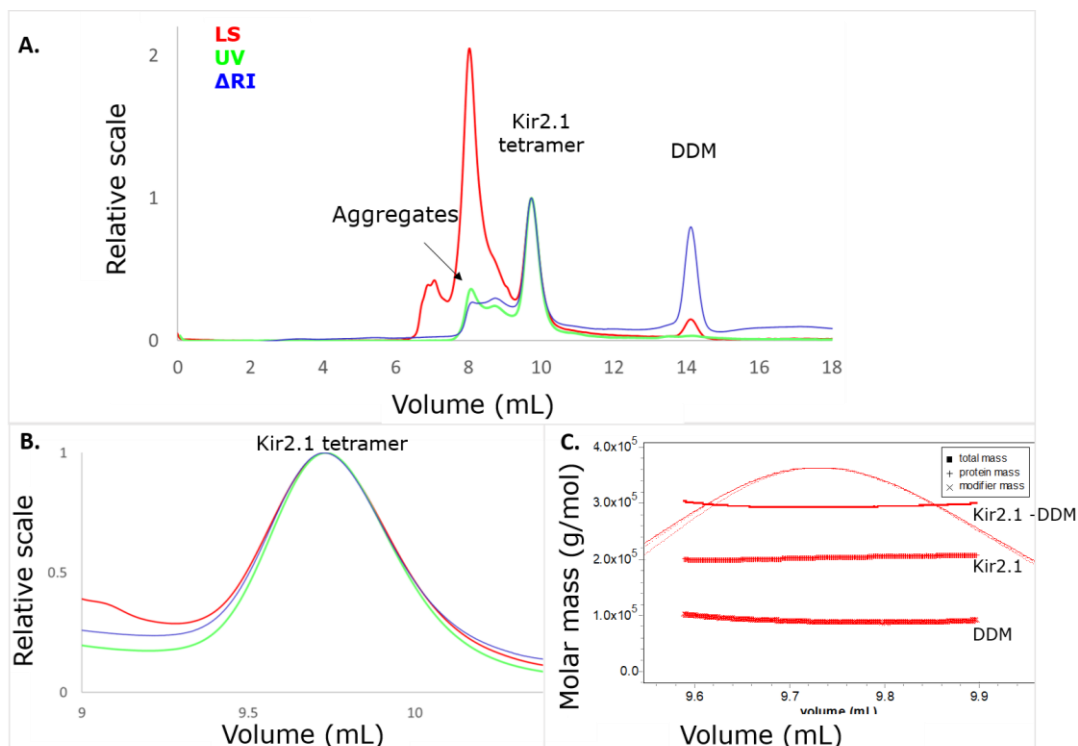


Figure 3-9. A) SEC-MALLS profile of Kir2.1 in 20 mM Tris-HCl pH 7.4, 150 mM KCl, 1 mM EDTA, 0.03% DDM. LS, UV, and Δ RI are shown in red, green, and blue, respectively. B) Zoom on Kir2.1 tetramer peak at 9.5 mL showing perfect signal alignment at the center of the peak. C) Conjugate protein molar mass distribution vs. volume of Kir2.1 and DDM complex. The total molar mass, Kir2.1 molar mass, and DDM molar mass are shown.

3.3.6 Analysis of Kir2.1 solubilized in FC14

3.3.6.1 Biochemical analysis of Kir2.1 solubilized in FC14 and purified in DDM

FC14 provided excellent solubilization yields (Figure 3-2 and Figure 3-3). Previous work demonstrated that functional Kir2.1 could be isolated from *S. cerevisiae* cells using 1% FC14 (D'Avanzo et al. 2010). For our construction, I observed that solubilizing and purifying Kir2.1 exclusively in FC14 resulted in 55% of Kir2.1 being purified as tetramers with an R_s of 59.4 Å (Figure 3-10, yellow) and 43% eluting as monomers (R_s : 31.3 Å). The stability of the Kir2.1 tetramer in FC14 and being able to fully reconstitute Kir2.1 in other models to assess its interaction with ligands, among other reasons, were concerns to our team. For this, I attempted detergent exchanges.

I recovered the tetrameric peak by exchanging FC14 with DDM in the affinity chromatography step (Kir2.1-FC14-DDM, Figure 3-10, purple). However, the sample produced some aggregates when concentrated by a factor of ~ 25 (Figure 3-10, red).

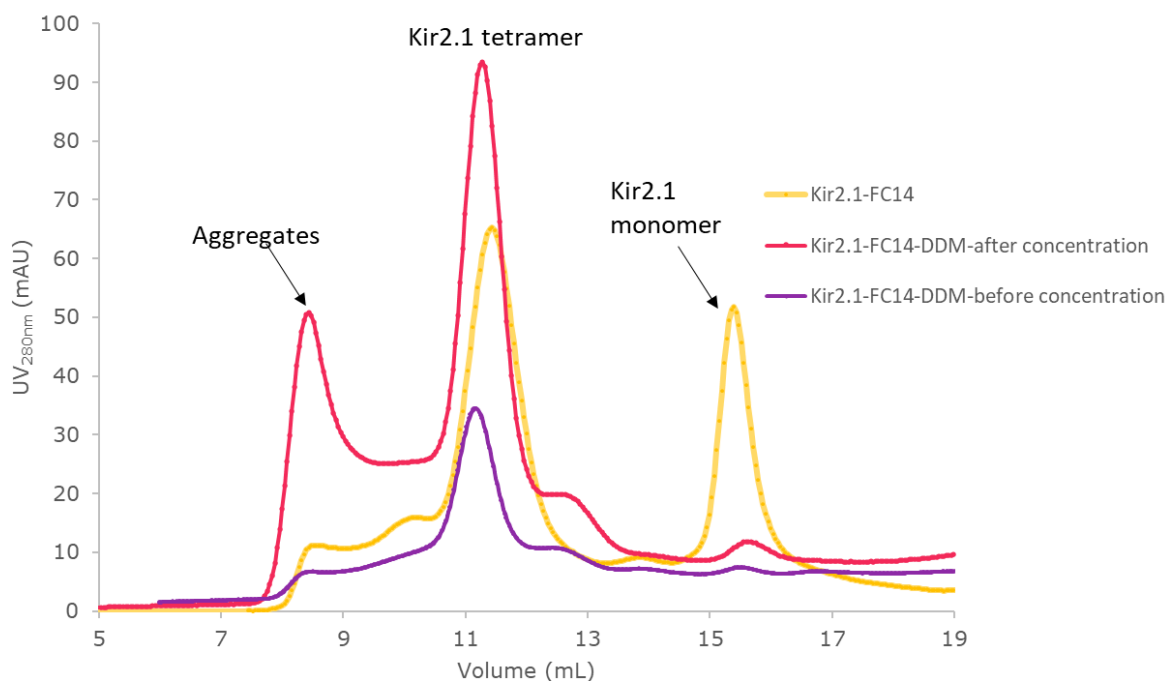


Figure 3-10. SEC profile of Kir2.1 extracted in 0.5% FC14. Kir2.1 purified in 0.03% FC14 (shown in yellow) elutes mainly as a tetramer at 11.55 mL (R_s : 59.4 Å) with a prominent peak at 15.43 mL (R_s : 31.3 Å) corresponding to the monomer. The purification in 0.03% DDM (shown in purple) resulted in one tetramer peak. This sample tended to aggregate when concentrating by a factor of 25 (red).

The following section will investigate Kir2.1 extracted in 0.5% FC14 and purified in either 0.03% DDM or 0.03% PCC-Malt.

3.3.6.2 Biophysical analysis of Kir2.1 WT solubilized in FC14 and purified in DDM

An extraction with FC14 was tested, followed by an exchange to DDM detergent at the affinity chromatography step (Kir2.1 FC14-DDM). 20-30 CV of buffer containing DDM at 0.05% was added to the Kir2.1 immobilized in a Co^{2+} resin, followed by the usual elution steps and SEC. This amount was enough to stabilize Kir2.1 and recover the tetrameric peak but insufficient to exchange FC14 fully, as SEC-MALLS analysis will soon show.

The SEC-MALLS profile of Kir2.1 FC14-DDM (Figure 3-11) was similar to Kir2.1 WT in DDM (Figure 3-9): the tetrameric peak eluted at the expected volume (9.5 mL). However, we observed a few notable differences i) although all three signals were visible, they could not align. Consequently, the ASTRA method could not determine the protein molar mass. ii) A dip in the LS and RI baselines was observed at 15 mL (Figure 3-11, A). iii) Throughout the peak, the sample was not homogeneous (Figure 3-11, B). iv)

the detergent molar mass appeared negative, resulting in a predicted molar mass of the complex lower than the protein.

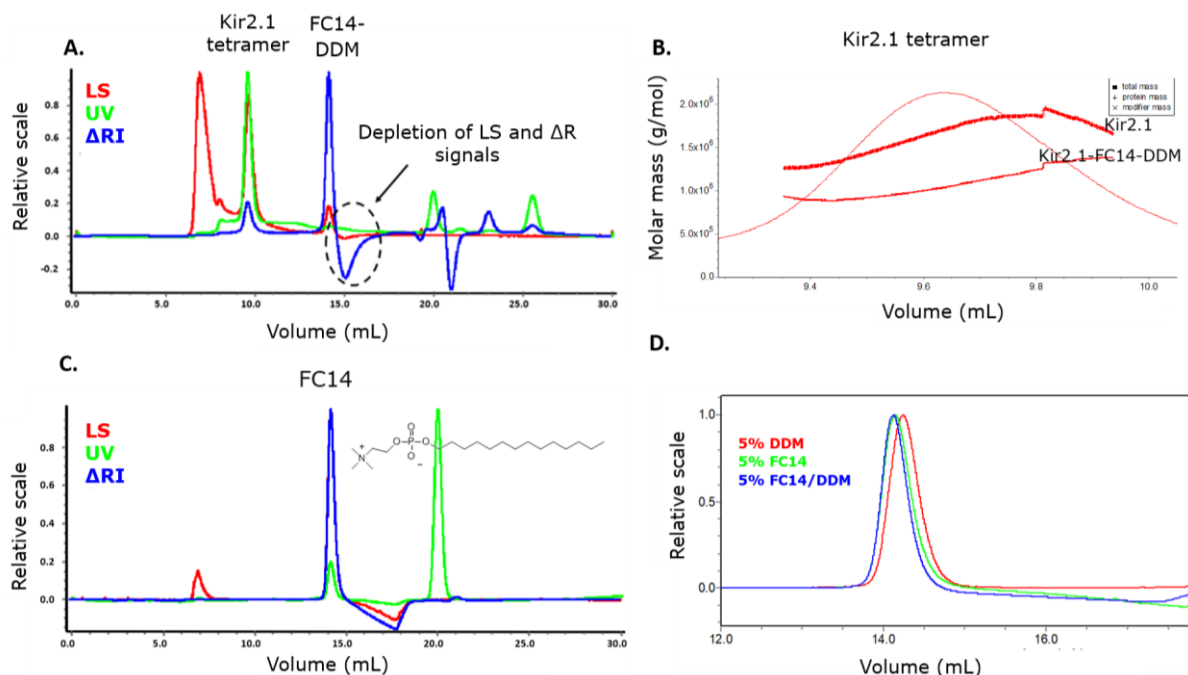


Figure 3-11. SEC-MALLS profile of Kir2.1-WT FC14-DDM in 0.03% DDM SEC buffer. The LS, UV, and Δ RI spectra are shown in red, green, and blue, respectively. B) Molar mass distribution vs. volume of Kir2.1-WT FC14-DDM. The Kir2.1-detergent complex total molar mass and Kir2.1 molar mass are shown with varying mass values. C) 5% FC14 profile in the same buffer. FC14 eluted at 14.1 mL. A dip in the LS and RI baselines is observed. D) Superposition of the Δ RI spectra components of 5% DDM (red), 5% FC14 (green), and 5% FC14-DDM mix (blue).

FC14 eluted at 14.1 mL with equal LS and Δ RI peak contribution and little UV. The dip in the LS and Δ RI baselines was also observed in the two controls where 5% FC14 (Figure 3-11, C) and 5% FC14-DDM were injected, and the superposition of FC14, DDM, and FC14-DDM (Figure 3-11, D) revealed a shift to the left in all detergent injections containing FC14. The detergent peak obtained in the sample (Figure 3-11, A) is similar to that of the FC14-DDM mixture, confirming an incomplete exchange of FC14. Nonetheless, the depletion of DDM from the baselines implies that FC14 and DDM are miscible; therefore, a complete exchange could be possible under different exchange conditions. The DDM concentrations should be significantly increased to displace FC14, which has a very low CMC.

3.3.6.3 Biophysical analysis of Kir2.1 WT solubilized in FC14 and purified in PCC-Malt

I momentarily explored 4-trans-(4-trans-Propylcyclohexyl)-cyclohexyl α -maltoside (PCC-Malt) during the purification steps (after solubilization with 0.5% FC14). PCC-Malt is a new detergent that has a maltoside head like DDM. It has been increasingly used recently and has been shown to increase membrane protein stability (Wagner, Smits, and Schmitt 2019). The exchange was performed using the same conditions as FC14-DDM (in parallel).

The Kir2.1 WT solubilized in FC14 and purified in PCC-Malt detergent (Kir2.1 FC14-PCC-Malt) was also investigated by SEC-MALLS. The Kir2.1 FC14-PCC-Malt tetramer peak eluted at the expected volume (9.5 mL, Figure 3-12, A). Still, similarly to the Kir2.1 FC14-DDM profile, the three signals did not align, and the sample was not homogeneous as there was variation in molar mass distribution (Figure 3-12, B). Interestingly, the detergent component was not homogeneous throughout the peak either; its molar mass varied significantly. This is indicative of a detergent mixture. The dip at 15 mL was also present; however, it was less pronounced than FC14-DDM (Figure 3-11). Superposition of 5% FC14 and 5% FC14-PCC-Malt (Figure 3-12, D) revealed similar profiles, characterized by a shift to the left compared to 5% PCC-Malt and depletion of the LS and RI signals. The FC14-PCC-Malt profile was identical to FC14; however, the dip was considerably less in the protein profile (Figure 3-12, A).

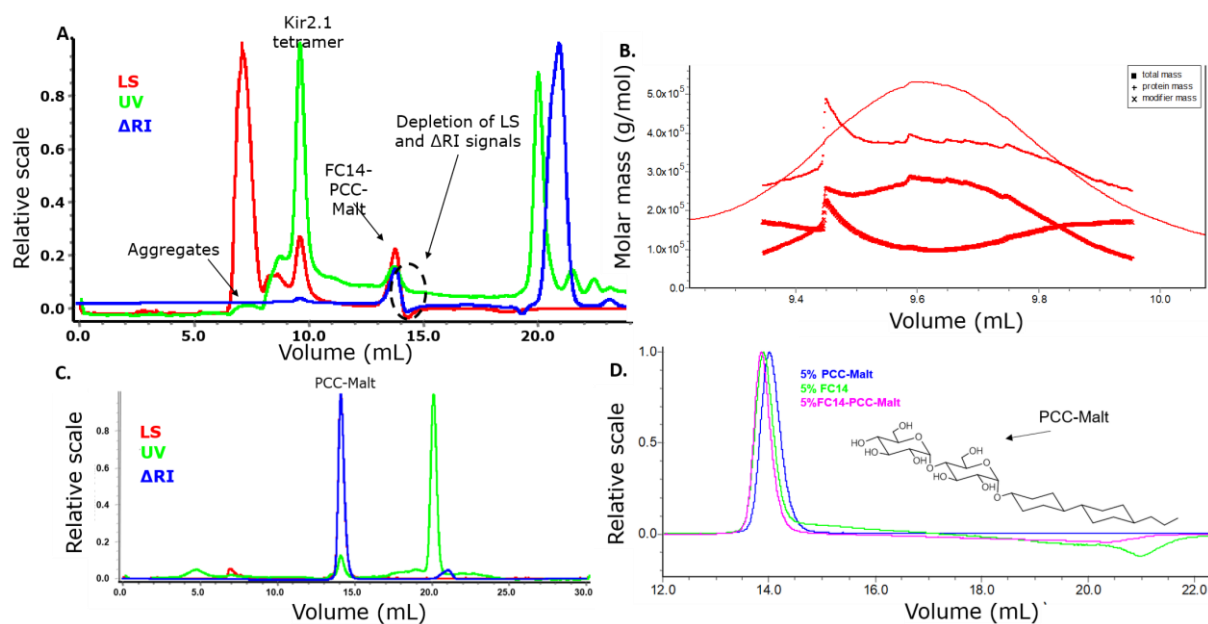


Figure 3-12. A) SEC-MALLS profile of FC14-PCC-Malt Kir2.1 in 0.03% PCC-Malt SEC buffer. The LS, UV, and Δ RI spectra are shown in red, green, and blue, respectively. B) Molar mass distribution vs. volume of FC14- PCC-Malt Kir2.1-WT. The Kir2.1-detergent complex total molar mass, Kir2.1 molar mass, and detergent mass are shown with varying mass values. C) 5% PCC-Malt profile. D) Superposition of the Δ RI spectra components of 5% PCC-Malt (blue), 5% FC14 (green), and 5% FC14-PCC-Malt mix (pink) in S200 Increase column equilibrated with 0.03% PCC-Malt SEC buffer.

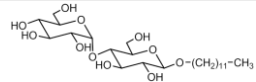
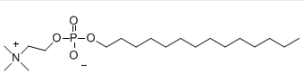
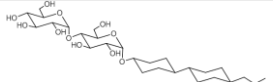
3.3.6.4 Note on SEC-MALLS and incomplete detergent exchange

Neither Kir2.1-FC14-DDM nor Kir2.1-FC14-PCC-Malt profile could align correctly. Indeed, the analysis quantifies the amount of detergent around the MP TMD via the refractive increment index (dn/dc), among other parameters. Generally, the exchange of detergents can be tricky because not all exchange methods are equivalent in exchange efficiency. In addition, not all pairs of detergents have the same ability to be exchanged. If there remains a mixed belt of detergent (FC14-DDM, FC14-PCC-Malt) around the protein or mostly FC14, the results are difficult to interpret using SEC-MALLS. Therefore, the analysis will be inaccurate if the detergent belt comprises several detergents with a different refractive increment index.

This incomplete exchange may not pose any issues for techniques that do not rely on quantifying complex components. A mixture of detergents may even improve membrane protein extraction or purification. Here the mixture resulted in a sample that was no longer destabilized into monomers.

Table 3-2 Summary of detergents parameters

Parameters	DDM	FC14	PCC-Malt
Type	Nonionic	Lipid-like surfactant	Nonionic

Molecular formula	C ₂₄ H ₄₆ O ₁₁	C ₁₉ H ₄₂ NO ₄ P	C ₂₇ H ₄₇ O ₁₁
Formula weight	510.63	379.5	547.67
CMC: (H ₂ O)	0.17 mM (0.0087%)	~ 0.12 mM (0.0046%)	0.036 mM (0.0002%)
Aggregation Number: (H ₂ O)	~ 78–149 (Vanaken et al. 1986)	~ 108 Ryan et al 2013)	164 (Barret et al. 2013)
dn/dc (mL · g ⁻¹) (H ₂ O)	0.1291	0.1416	0.1600
Micelle Size:	72 kDa (Strop and Brunger 2005)	47 kDa	60–90 kDa
A280 nm:	< 0.04	< 0.08	
			

3.3.6.5 Structural analysis of Kir2.1 WT solubilized in FC14 and purified in DDM

Kir2.1 FC14-DDM was further analyzed by TEM in negative staining (see Materials and Methods 2.5.4). Approximately 10,000 particles were picked manually and semi-automatically and were extracted using EMAN2 from 49 micrographs. Figure 3-13 shows a micrograph with a few particles picked. Negative-stained particles appeared white on a gray background.

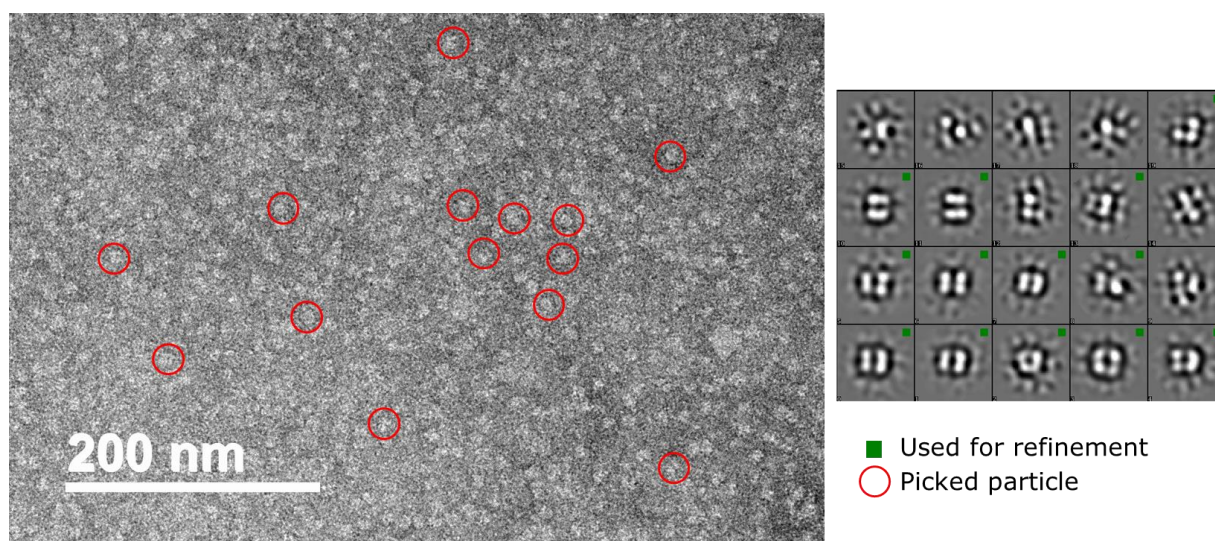


Figure 3-13. Micrograph of Kir2.1 FC14-DDM and 2D classification. Left) Example of picking. Right) 2D classes. The particles in the 2D classes shown in yellow circles were selected for the initial model. Refinements were done using those shown in green squares.

These particles were sorted into twenty 2D classes. These 2D classes hinted at a tetrameric assembly of Kir2.1 as four sections could be distinguished in most. All the particles were used for the initial 3D model with C1 symmetry and an initial model

with C4 symmetry. Both models contained four clear sections. The C4 model displayed the channel pore going through the channel longitudinally.

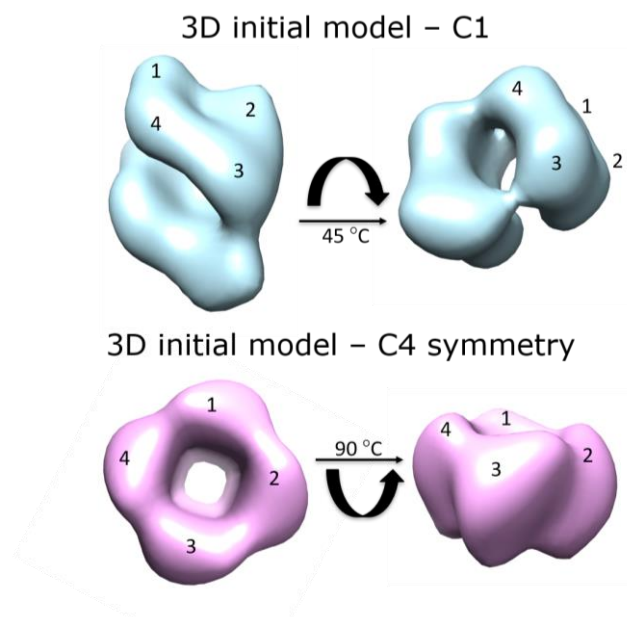


Figure 3-14. 3D initial models of Kir2.1-FC14-DDM in negative staining. The top panel (blue) shows the initial model with no imposed symmetry (C1); four sections are visible. The bottom panel (pink) shows the initial model with a C4 symmetry applied.

The C4 initial model (Figure 3-14) was refined twice using C4 symmetry using 3244 particles from thirteen classes (Figure 3-13). The final map was obtained at 18.4 Å resolution (Figure 3-15).

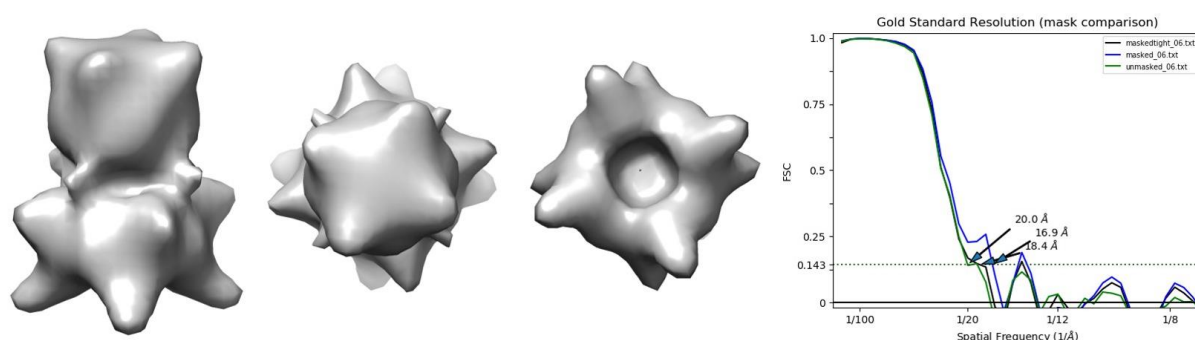


Figure 3-15. 3D map from Kir2.1 FC14-DDM obtained by negative staining at 18.4 Å resolution using EMAN2. The side, top, and bottom views and the gold standard resolution graph are shown.

This low-resolution 3D reconstruction showed that Kir2.1 was amenable for single-particle analysis (SPA) and confirmed that it was possible to retrieve a tetramer despite solubilizing Kir2.1 in FC14. However, FC14 dissociated some of the tetramers into monomers and these monomers are not easily seen on the EM image because they are too small.

Ultimately, the solubilization and purification in DDM provided remarkable homogeneity, despite not solubilizing everything. Due to the presence of monomer using FC14 and the excellent results obtained with DDM, I chose quality over quantity and decided to focus on DDM.

3.3.7 Analysis of Kir2.1 mutants: R312H and C154Y

The expression and purification protocol established for Kir2.1 was used to characterize the mutants. The Kir2.1_R312H and Kir2.1_C154Y mutants have loss-of-function mutations responsible for AS in humans. Both mutations were first identified in 2009 (Sacconi et al. 2009). R312 is located in the cytoplasmic region in the PIP₂ putative binding site. In contrast, C154 is in the extracellular loop connecting the selectivity filter and the internal helix. These two different profiles have the same effect, a defective channel that does not conduct K⁺ current across the membrane.

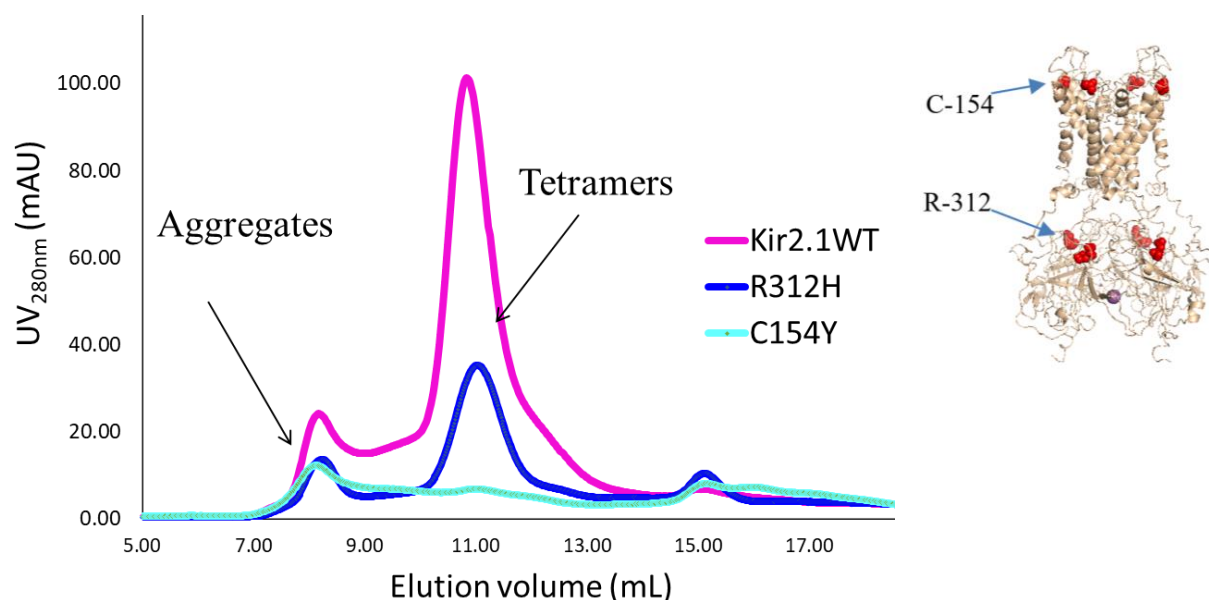


Figure 3-16. Comparison of SEC purification of Kir2.1 WT and R312H and C154Y mutants.

3.3.7.1 Analysis of Kir2.1_R312H

The next chapter will thoroughly discuss the role of residue R312 and the effect of the R312H mutation on the function of the h_Kir2.1 channel. This section will briefly explore the biochemical and biophysical characteristics of the Kir2.1_R312H mutant expressed in *P. pastoris* yeast.

Kir2.1_R312H mutant was produced and purified following the same protocol as Kir2.1_WT. The culture growth and induction were similar to the WT, and no

significant spectral or molecular weight differences were observed (Figure 3-16, Figure 3-17 A-C).

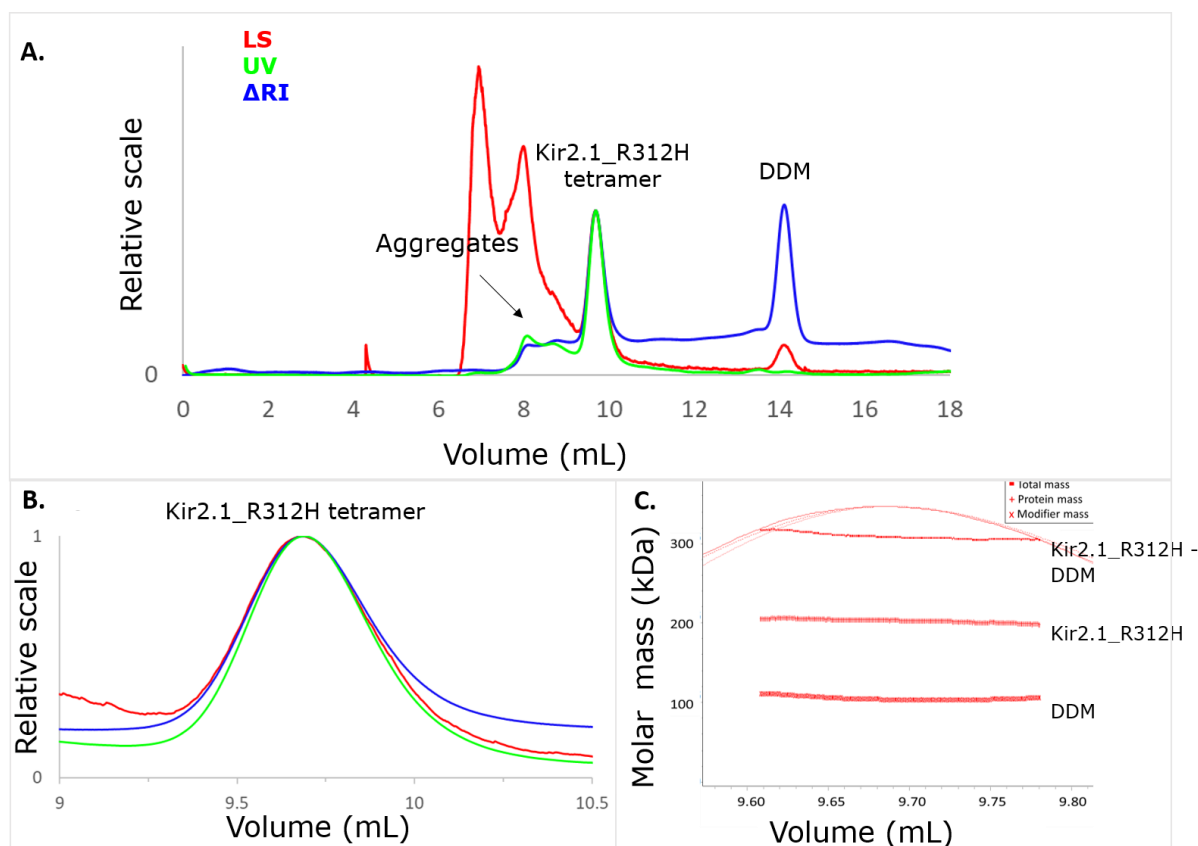


Figure 3-17. SEC-MALLS profile of Kir2.1_R312H in 20 mM Tris-HCl pH 7.4, 150 mM KCl, 1 mM EDTA, 0.03% DDM. The LS, UV, and Δ RI spectra are shown in red, green, and blue, respectively. B: Zoom on Kir2.1_R312H tetramer peak at 9.5 mL. The LS, UV, and Δ RI (shown in red, green, and blue, respectively) align perfectly at the center of the peak. C: Molar mass distribution vs. volume of Kir2.1_R312H and DDM complex.

The Kir2.1_R312H-DDM complex was very homogenous throughout the peak and had a molar mass of 307.1 ± 4.4 kDa consisting of tetrameric Kir2.1_R312H with 206.8 ± 3.2 kDa molar mass and 100.3 ± 4.9 kDa DDM (Figure 3-17, C). The N_{agg} of DDM in the Kir2.1_R312H-DDM complex was 194 ± 9 , similar to the N_{agg} in the Kir2.1_WT-DDM complex, 194 ± 2 .

In conclusion, Kir2.1_R312H formed a homogeneous tetramer, like the WT counterpart (Figure 3-17, C). Therefore, the mutation did not significantly disrupt its structure or affect its ability to form a tetramer. These findings further support our conclusion that the mutation does not have a significant effect on the protein's structure but is a functional effect.

3.3.7.2 Analysis of Kir2.1_C154Y mutant

Residue C154 is conserved in all eukaryotic Kir members. Two mutations at this site are responsible for AS in patients, C154F (Bendahhou et al. 2005) and C154Y (Sacconi et al. 2009). Mutations at this site, C154, to even alanine or serine, abolished current in *Xenopus laevis* oocytes (Cho et al. 2000). Cho et al. recorded whole-cell and single-channel currents of oocytes that expressed tetrameric constructs of Kir2.1 with one or two C154Y mutant subunits. They found that one mutant subunit was enough to abolish channel function in the tetramer (Cho et al. 2000). Similarly, Bendahhou et al. attested to this dominant-negative effect in HEK293 cells (Bendahhou et al. 2005).

Cho et al. reported that mutating any C in Kir2.1 except for C154 and C122 resulted in currents recorded (although diminished). However, mutating C122 or C154 completely abolished the signal, suggesting an intramolecular disulfide bond between the two residues. The structure of the chicken Kir2.2 homolog revealed a disulfide bond between C155 and C123 (Tao et al. 2009), Kir2.2 equivalent to C154 and C122 in Kir2.1.

In this thesis, all the production, extraction, and purification steps followed the same protocol established for Kir2.1 WT. Although the Kir2.1_C154Y mutation did not affect the growth of *P. pastoris* cells (Figure 3-16), and the cell pellets obtained were of comparable masses, C154Y had lower expression levels than R312H and WT (less than 50%, Figure 3-1 right panel). The chromatography profile of Kir2.1_C154Y revealed a single discernable peak at the volume corresponding to aggregates Figure 3-16, right panel, cyan). A small portion eluted at the tetramer peak. Attempts to increase the concentration only increased the percentage of aggregates (Figure 3-18).

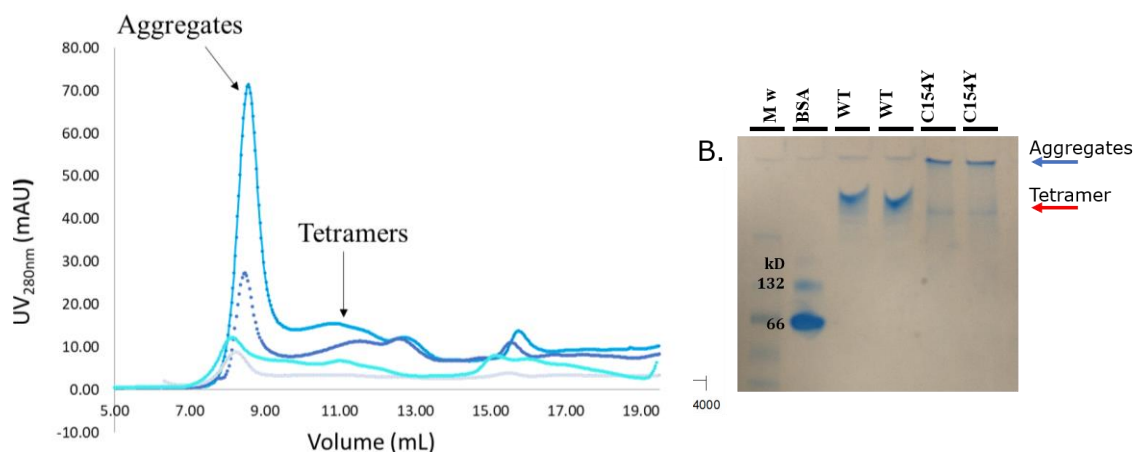


Figure 3-18 C154Y elution profiles and Native PAGE B) Native PAGE comparing Kir2.1 WT and C154Y. Kir2.1 WT migrates as one entity, well above BSA. C154Y shows a band at the same level and a more prominent one at the well level.

Nevertheless, the minuscule tetrameric fraction was used to conduct a few experiments. A native PAGE (Figure 3-18, B) revealed that the tetramer fraction was polydisperse and consisted primarily of aggregates and a faint amount of molecules that migrated at the same level as the WT tetramer. C154Y tends to aggregate and the tetramers formed are probably not correctly folded (Figure 3-18, A-B).

SPR analysis of the interaction between Kir2.1_C154Y tetramer fraction with PIP₂ revealed that PIP₂ was able to bind to C154Y with no significant differences in kinetic parameters between C154Y ($K_D = 6.98 \pm 2.25 \mu\text{M}$) and the WT ($K_D = 3.2 \pm 0.8 \mu\text{M}$), suggesting that a properly-folded tetramer with an intra-disulfide bond is not a prerequisite for PIP₂-binding.

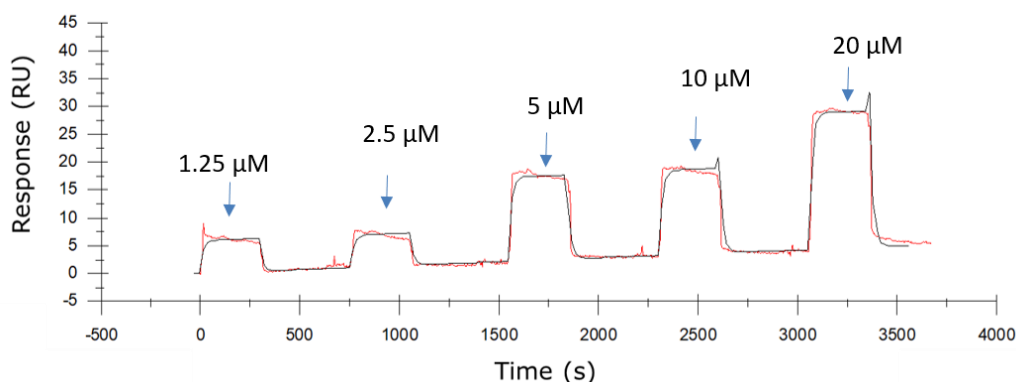


Figure 3-19. SPR sensorgram of Kir2.1_C154Y (5844 RU level) immobilized onto a CM5 chip. Five sequential injections of PIP₂ are shown, at 1.25–20 μM , at 25 $\mu\text{L} \cdot 5 \text{ mL}^{-1}$. In color, experimental data; in black, the fitted curve. The SCK assay was carried out in duplicate; only one replica is shown. The sensorgram is expressed in response units (RU) relative to the time in s.

channel misfolding may explain the low expression levels observed due to poor trafficking or protein degradation.

3.4 DISCUSSION

The protein solubilization was more efficient using FC14 than DDM. However, FC14 dissociated some of the tetramers into monomers when used during the purification as well as solubilization. This dissociation was corrected when FC14 was exchanged into DDM during the purification steps.

Inability to fully exchange FC14 in current conditions. The dip in the LS and RI signals indicated that the exchange was incomplete. Using thin-layer chromatography to monitor the detergent exchange could help determine the proper conditions for exchanging FC14 completely if needed. The concentration of DDM used was not enough, the concentration of DDM in the wash buffer should be increased as well as the number of CVs.

The aggregation effect of C154Y observed *in vitro* most likely results from misfolding. With the mutation and dissociation of the disulfide bond, C122 is now available to form disulfide bonds with other cysteines. Indeed, residue C149 in the selectivity filter loop could replace C154 if the protein undergoes rearrangement.

Another hypothesis would be that the improper folding and instability would result in a protein that is more easily degraded or not addressed correctly to the membrane. Ideally, it would be interesting to test in a KCNJ2-deprived system if Kir2.1_C154Y is addressed to the membrane. Given the importance of this channel in action potential and development, this may not be feasible. Therefore, constructing a crosslinked tetrameric Kir2.1_C154Y mutant with a GFP tag would elucidate the effect of C154-C122 disruption on proper trafficking. It would be interesting to know if this protein is addressed to the membrane without WT Kir2.1.

3.5 BIBLIOGRAPHY

- Aranow, R. H. 1963. "PERIODIC BEHAVIOR IN CHARGED MEMBRANES AND ITS PHYSICAL AND BIOLOGICAL IMPLICATIONS." *Proceedings of the National Academy of Sciences* 50 (6): 1066–70. <https://doi.org/10.1073/pnas.50.6.1066>.
- Barret, Laurie-Anne, Cherone Barrot-Ivolot, Simon Raynal, Colette Jungas, Ange Polidori, and Françoise Bonneté. 2013. "Influence of Hydrophobic Micelle Structure on Crystallization of the Photosynthetic RC-LH1-PufX Complex from *Rhodobacter Blasticus*." *The Journal of Physical Chemistry B* 117 (29): 8770–81. <https://doi.org/10.1021/jp403483q>.
- Bendahhou, Saïd, Emmanuel Fournier, Damien Sternberg, Guillaume Bassez, Alain Furby, Carole Sereni, Matthew R. Donaldson, Marie-Madeleine Larroque, Bertrand Fontaine, and Jacques Barhanin. 2005. "In Vivo and in Vitro Functional Characterization of Andersen's Syndrome Mutations: Andersen's Syndrome in Vivo and in Vitro." *The Journal of Physiology* 565 (3): 731–41. <https://doi.org/10.1113/jphysiol.2004.081620>.
- Byrne, Bernadette. 2015. "Pichia Pastoris as an Expression Host for Membrane Protein Structural Biology." *Current Opinion in Structural Biology* 32 (June): 9–17. <https://doi.org/10.1016/j.sbi.2015.01.005>.
- Cabib, Enrico, and Javier Arroyo. 2013. "How Carbohydrates Sculpt Cells: Chemical Control of Morphogenesis in the Yeast Cell Wall." *Nature Reviews Microbiology* 11 (9): 648–55. <https://doi.org/10.1038/nrmicro3090>.
- Chipot, Christophe, François Dehez, Jason R. Schnell, Nicole Zitzmann, Eva Pebay-Peyroula, Laurent J. Catoire, Bruno Miroux, et al. 2018. "Perturbations of Native Membrane Protein Structure in Alkyl Phosphocholine Detergents: A Critical Assessment of NMR and Biophysical Studies." *Chemical Reviews* 118 (7): 3559–3607. <https://doi.org/10.1021/acs.chemrev.7b00570>.
- Cho, Hee Cheol, Robert G. Tsushima, The-Tin T. Nguyen, H. Robert Guy, and Peter H. Backx. 2000. "Two Critical Cysteine Residues Implicated in Disulfide Bond Formation and Proper Folding of Kir2.1." *Biochemistry* 39 (16): 4649–57. <https://doi.org/10.1021/bi992469g>.
- Choy, Brendon C., Rosemary J. Cater, Filippo Mancina, and Edward E. Pryor. 2021. "A 10-Year Meta-Analysis of Membrane Protein Structural Biology: Detergents, Membrane Mimetics, and Structure Determination Techniques." *Biochimica et Biophysica Acta (BBA) - Biomembranes* 1863 (3): 183533. <https://doi.org/10.1016/j.bbamem.2020.183533>.
- D'Avanzo, Nazzareno, Wayland W.L. Cheng, Xiaobing Xia, Liang Dong, Pavel Savitsky, Colin G. Nichols, and Declan A. Doyle. 2010. "Expression and Purification of Recombinant Human Inward Rectifier K⁺ (KCNJ) Channels in *Saccharomyces Cerevisiae*." *Protein Expression and Purification* 71 (1): 115–21. <https://doi.org/10.1016/j.pep.2010.01.010>.
- Hartmann, Lucie, Valérie Kugler, and Renaud Wagner. 2016. "Expression of Eukaryotic Membrane Proteins in *Pichia Pastoris*." In *Heterologous Expression of Membrane Proteins*, edited by Isabelle Mus-Veteau, 1432:143–62. *Methods in Molecular Biology*. New York, NY: Springer New York. https://doi.org/10.1007/978-1-4939-3637-3_10.
- Hartmann, Lucie, Estelle Metzger, Noémie Ottelard, and Renaud Wagner. 2017. "Direct Extraction and Purification of Recombinant Membrane Proteins from *Pichia Pastoris* Protoplasts." In *Membrane Protein Structure and Function Characterization*, edited by Jean-Jacques Lacapere, 1635:45–56. *Methods in Molecular Biology*. New York, NY: Springer New York. https://doi.org/10.1007/978-1-4939-7151-0_3.
- Heerklotz, Heiko. 2008. "Interactions of Surfactants with Lipid Membranes." *Quarterly Reviews of Biophysics* 41 (3–4): 205–64. <https://doi.org/10.1017/S0033583508004721>.

- Helenius, Ari, and Kai Simons. 1975. "Solubilization of Membranes by Detergents." *Biochimica et Biophysica Acta (BBA) - Reviews on Biomembranes* 415 (1): 29–79. [https://doi.org/10.1016/0304-4157\(75\)90016-7](https://doi.org/10.1016/0304-4157(75)90016-7).
- Laurent, Torvard C., and Johan Killander. 1964. "A Theory of Gel Filtration and Its Experimental Verification." *Journal of Chromatography A* 14 (January): 317–30. [https://doi.org/10.1016/S0021-9673\(00\)86637-6](https://doi.org/10.1016/S0021-9673(00)86637-6).
- Le Bon, Christel, Baptiste Michon, Jean-Luc Popot, and Manuela Zoonens. 2021. "Amphipathic Environments for Determining the Structure of Membrane Proteins by Single-Particle Electron Cryo-Microscopy." *Quarterly Reviews of Biophysics* 54: e6. <https://doi.org/10.1017/S0033583521000044>.
- Linke, Dirk. 2009. "Chapter 34 Detergents." In *Methods in Enzymology*, 463:603–17. Elsevier. [https://doi.org/10.1016/S0076-6879\(09\)63034-2](https://doi.org/10.1016/S0076-6879(09)63034-2).
- Maire, Marc le, Philippe Champeil, and Jesper V Møller. 2000. "Interaction of Membrane Proteins and Lipids with Solubilizing Detergents." *Biochimica et Biophysica Acta (BBA) - Biomembranes* 1508 (1–2): 86–111. [https://doi.org/10.1016/S0304-4157\(00\)00010-1](https://doi.org/10.1016/S0304-4157(00)00010-1).
- Mus-Veteau, Isabelle. 2010. "Heterologous Expression of Membrane Proteins for Structural Analysis." In *Heterologous Expression of Membrane Proteins*, edited by Isabelle Mus-Veteau, 601:1–16. Methods in Molecular Biology. Totowa, NJ: Humana Press. https://doi.org/10.1007/978-1-60761-344-2_1.
- Sacconi, S., D. Simkin, N. Arrighi, F. Chapon, M. M. Larroque, S. Vicart, D. Sternberg, et al. 2009. "Mechanisms Underlying Andersen's Syndrome Pathology in Skeletal Muscle Are Revealed in Human Myotubes." *American Journal of Physiology-Cell Physiology* 297 (4): C876–85. <https://doi.org/10.1152/ajpcell.00519.2008>.
- Seddon, Annela M., Paul Curnow, and Paula J. Booth. 2004. "Membrane Proteins, Lipids and Detergents: Not Just a Soap Opera." *Biochimica et Biophysica Acta (BBA) - Biomembranes* 1666 (1–2): 105–17. <https://doi.org/10.1016/j.bbamem.2004.04.011>.
- Strop, Pavel, and Axel T. Brunger. 2005. "Refractive Index-Based Determination of Detergent Concentration and Its Application to the Study of Membrane Proteins." *Protein Science* 14 (8): 2207–11. <https://doi.org/10.1110/ps.051543805>.
- Tanford, Charles. 1973. *The Hydrophobic Effect: Formation of Micelles and Biological Membranes*. New York: Wiley.
- Tao, Xiao, Jose L. Avalos, Jiayun Chen, and Roderick MacKinnon. 2009. "Crystal Structure of the Eukaryotic Strong Inward-Rectifier K⁺ Channel Kir2.2 at 3.1 Å Resolution." *Science* 326 (5960): 1668–74. <https://doi.org/10.1126/science.1180310>.
- Vanaken, T., S. Foxall-Vanaken, S. Castleman, and S. Ferguson-Miller. 1986. "[3] Alkyl Glycoside Detergents: Synthesis and Applications to the Study of Membrane Proteins." In *Methods in Enzymology*, 125:27–35. Elsevier. [https://doi.org/10.1016/S0076-6879\(86\)25005-3](https://doi.org/10.1016/S0076-6879(86)25005-3).
- Wagner, Manuel, Sander H. J. Smits, and Lutz Schmitt. 2019. "In Vitro NTPase Activity of Highly Purified Pdr5, a Major Yeast ABC Multidrug Transporter." *Scientific Reports* 9 (1): 7761. <https://doi.org/10.1038/s41598-019-44327-8>.
- Yeagle, Philip L. 2016. "Detergents." In *The Membranes of Cells*, 73–84. Elsevier. <https://doi.org/10.1016/B978-0-12-800047-2.00004-8>.

3.6 SUPPLEMENTARY MATERIAL

3.6.1 Solubilization of membrane proteins

3.6.1.1 Types of detergents

1. *Ionic detergents* contain a net charge. They are highly effective at solubilizing MPs but tend to denature them. Ex: SDS is a well-known ionic detergent commonly used to denature proteins for electrophoresis.
2. *Zwitterionic detergents* have both positive and negative charged groups but no overall charge. They can be effective but are less harsh than ionic detergents. Ex: CHAPS
3. *Nonionic detergents* have no charge. They are generally milder than ionic or zwitterionic detergents though they can be deactivating depending on chain length. Ex: Maltosides (DM, DDM), TRITON-100X

3.6.1.2 Stages of solubilization

In their renowned review, Helenius and Simons proposed a three-stage model of solubilization of lipid bilayers which can be extended to understand the detergent-membrane interaction (Helenius and Simons 1975). As the concentration of detergent introduced to a suspension of pure phospholipid liposomes increases, they propose the following sequence of events:

- I) In the *detergent binding* stage, the micelles break down and partition into the membrane changing its physical properties.
- II) In the *lamellar-micellar phase transition* stage, the membrane becomes saturated with detergent, and mixed lipid-micelles form, eventually leading to a complete phase transition into micelles.
- III) The *size decrease of mixed-micelles* stage: as additional detergent molecules are added, the ratio of detergent/phospholipid increases in the mixed micelles, and their size decreases.

This outstanding description is still used nearly universally in membrane solubilization (Seddon, Curnow, and Booth 2004; Heerklotz 2008) and has been demonstrated by many methods, including turbidimetry, fluorescence energy transfer, and electron microscopy. Please see (Seddon, Curnow, and Booth 2004) and the references cited for more details.

3.6.2 Cell culture optimization

Three different pHs were tested to establish the best cell growth conditions: pH 5.5, 6.0, and 6.5. The highest growth was observed at pH 6.0 (Figure 3-22). Since this agreed with Hartmann et al., pH 6.0 was established for all future cultures and inductions. The culture incubation time was tested at 18–24 h and 5–7 h with comparable results after induction. Therefore, the shorter incubation time was chosen to gain time. Antibiotics were tested throughout the production versus exclusively in the initial stages. The cells grew faster without antibiotics, and no contamination was observed when including them during the initial selection of agar plates up to the starter culture. Contamination was closely monitored by inspection using an optical microscope, which shows clearly each *P. pastoris* cell (represented by white dots in Figure 3-21)

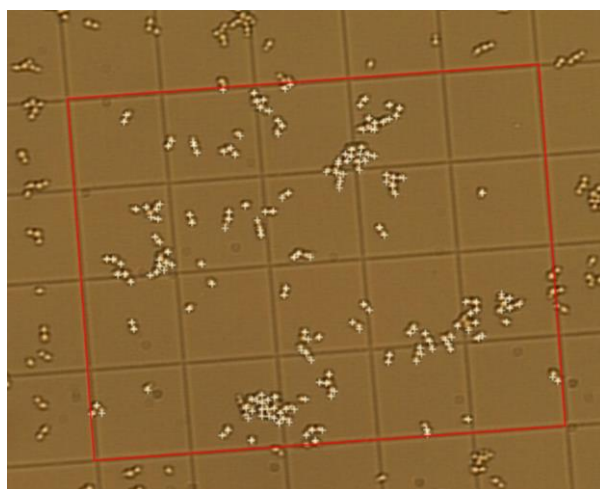


Figure 3-21. *Pichia pastoris* cell culture at 0.5 OD_{600nm} in a Malassez chamber for counting cells. Each round white object is a live *Pichia pastoris* cell. 188 cells have been selected inside the large rectangle shown in red. The rectangle has an area of 0.05 mm² and 0.2 mm depth, accommodating 0.01 μL volume.

Cell cultures were incubated in parallel at comparable starting OD_{600nm} ~1 with identical parameters except for pH. This 1 OD_{600nm} was equivalent to $3.5 \pm 0.3 \cdot 10^7$ cells · mL⁻¹ in the log phase using a Malassez cell (Figure 3-21). Different agitation speeds and induction times were explored. Higher agitation speeds (>220 rpm) improved growth, as expected.

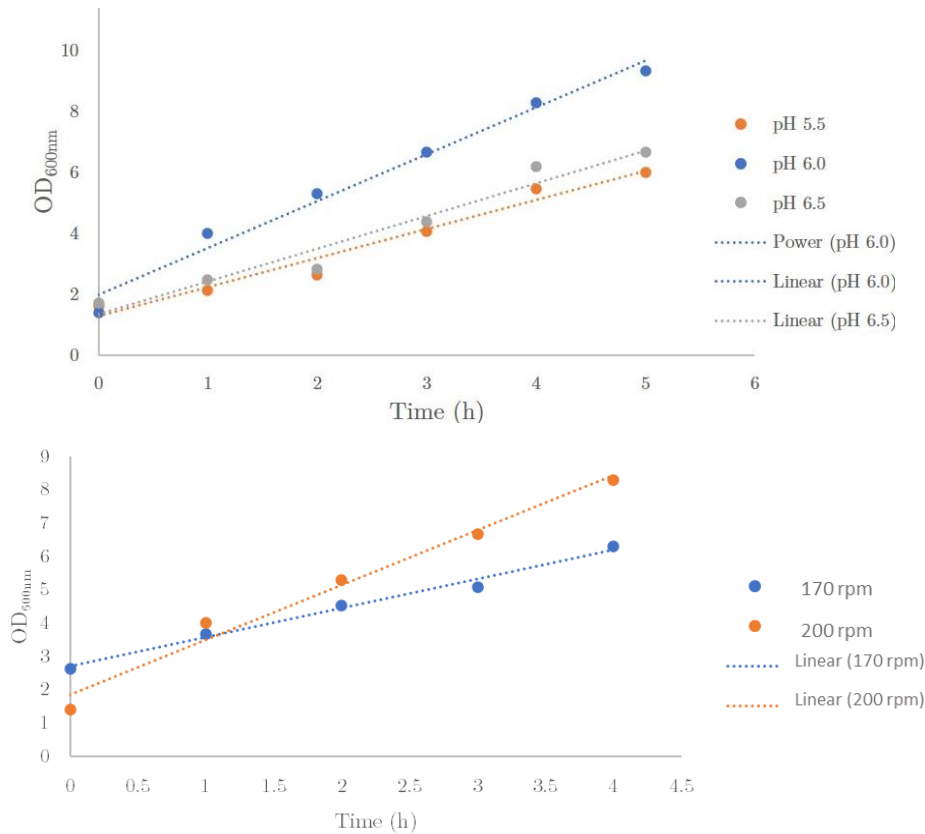


Figure 3-22. Effect of pH and agitation speed on the growth of *Pichia pastoris* culture. Top panel: Cell cultures were incubated at comparable starting OD_{600nm} ~1 in parallel with identical parameters except for pH. The curves at pH 5.5 (orange), 6.0 (blue), and 6.5 (gray) are shown with a linear trendline traced in a dotted line. The bottom panel shows culture growth at 170 rpm (blue) and 200 rpm (orange) agitation.

The starting OD₆₀₀ for expression was also explored, varying up to 10 (

Figure 3-23). At these high cell concentrations, the protein was not recovered, it was all degraded. The best results were obtained with a starting OD₆₀₀ of 3–3.5 corresponding to $1-1.2 \cdot 10^8$ cells · mL⁻¹.

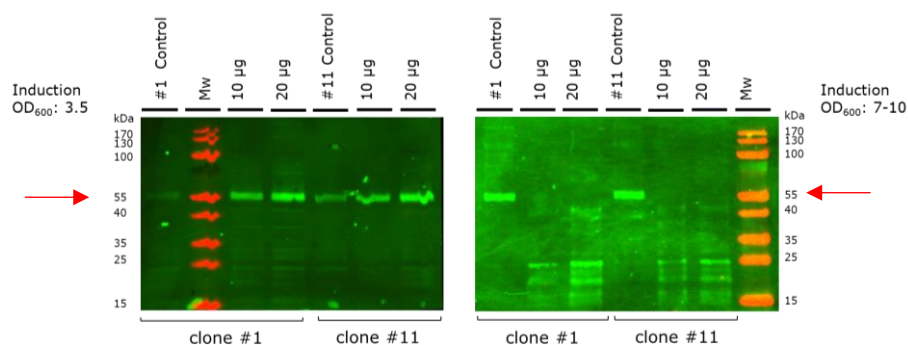


Figure 3-23. Western blot of clones expressing Kir2.1_WT. The top shows a screening of the twelve transformed clones. The bottom panel shows the expression of clones #1 and #11, induced at starting OD₆₀₀ of 3.5 (left) and at 7 (right).

Induction times in *Pichia pastoris* have been reported to vary between 16 h and 60 h. I was looking for short induction times that provided high-quality protein in sufficient amounts. I observed no significant differences (~3% cell growth) in protein production between 18 and 24 h induction times.

3.6.3 Optimizing cellular lysis

3.6.3.1 Enzymatic lysis

Enzymatic lysis with Zymolyase (AMSBio), a solution of enzymes that digest the yeast cell walls, preceded the mechanical lysis. Initially, it was tested at 20 U per g of pellet and was incubated for 1 h at 4 °C. The first test increased the incubation temperature from 4 °C to RT while reducing the time from 1 h to 15 min. Although no significant improvement was noted, this change did not have any adverse effects, such as proteolysis of our protein Kir2.1; therefore, it was chosen for future lysis.

3.6.3.2 Mechanical lysis of *Pichia pastoris* with the Cell Disruptor

Six passes through the Cell Disruptor (Cell D, Constant Systems) at 2.7 kbar initially followed these conditions of enzymatic lysis. The lysis efficiency was tested at 2.4 kbar, 2.5 kbar, and 2.7 kbar (maximum pressure). The cell pellets were resuspended to 0.25 g · mL⁻¹ concentration in buffer, and the system was cooled to 4–7 °C. The lysates were observed by optical microscopy and further purified to assess the effect of the lysis (if any) on the solubilization of Kir2.1.

The microscopy results showed that Cell D effectively lysed *P. pastoris* cells at the lowest pressure tested (2.4 kbar) after one pass (Figure 3-25 A-D). More live cells were present at 2.4 kbar than at 2.5 and 2.7 kbar. Surprisingly, there was no significant increase in the number of cells lysed from the first pass to the second or even the sixth (Figure 3-25, A0-AIV).

Despite the efficient cell lysis observed on the microscope (Figure 3-25 A-D), after separation by centrifugation, a significant amount of protein was found in the pellet containing the cell debris and unlysed cells (P1) during the western blot (WB) analysis (50%, Figure 3-25 E). P1 and SN1 lysis fractions at 2.4 and 2.5 kbar showed comparable results, while 2.7 kbar showed little protein in the lysed fraction (SN1). All three lysis pellets (P1) were resuspended, pooled, and lysed at 2.5 kbar. 36 mg of membrane

proteins were recovered by adding this centrifugation, resuspension, and lysis cycle (referred to as ‘mixed pellet’).

Next, the MPs contained in SN1 were pelleted at $100,000 \cdot g$, resuspended in TK buffer, diluted to $2 \text{ mg} \cdot \text{mL}^{-1}$, and solubilized with 1.5% DDM. The solubilization of Kir2.1 was poor in all three lysis conditions, 2.4, 2.5, and 2.7 kbar (Figure 3-25 F), although the test was performed at optimized solubilization conditions (section 3.3.2.2 above).

3.6.3.1 DDM CMC in buffer conditions

I wished to determine the lowest concentration of detergent that we could use in the cryo-EM grids to keep the protein stable. For this, we corroborated the CMC of DDM in our buffer in conjunction with Jean-Jacques Lacapère at the LBM. The CMC of DDM was experimentally determined by fluorescence using anilino-naphthalene sulfonic acid (ANS) as a probe (Anatrace) on a MOS-200/M spectrometer (BioLogic) set to 400 nm excitation and 490 nm emission. 4 μL increments of DDM at 17 mM ($100 \cdot$ expected CMC) were titrated onto our buffer solution containing ANS until obtaining at least five recordings above the expected CMC. The CMC is defined by the breakpoint in fluorescence and is determined by plotting the change in fluorescence against the concentration of DDM. We found the CMC to be: 0.17 mM (0.0087%) in H_2O , 0.14 mM (0.0072%) in 0.2 M NaCl buffer, and 0.13 mM (0.0067%) in 0.2 M KCl buffer, which consistent (slightly higher) with the 0.12 mM (0.0061%) value provided by Anatrace. This simple experiment provides a fast way to verify the CMC of a nonionic detergent in a specific buffer. It can be handy when working with detergents that have only been characterized in water or not at all.

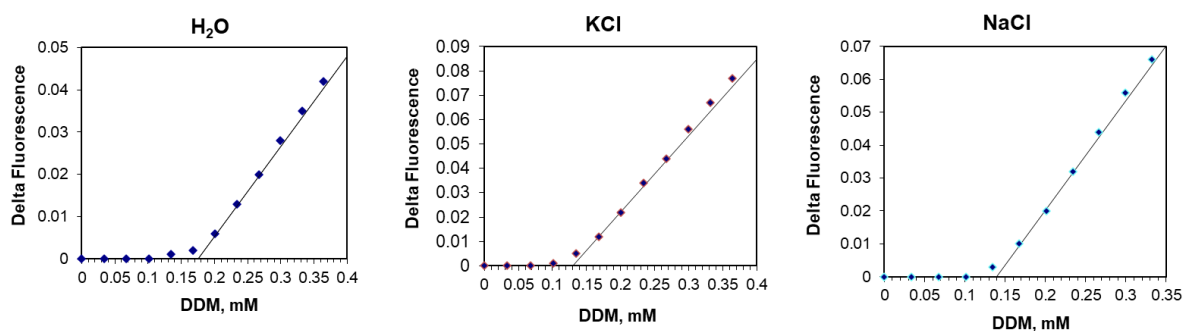


Figure 3-24. Determination of the DDM’s critical micellar concentration using fluorescence spectroscopy. A plot of change in fluorescence against the concentration of DDM in water (left, blue), 0.2 M KCl buffer (center, red), and 0.2 M NaCl (right, cyan). The breakpoint in fluorescence defines the CMC.

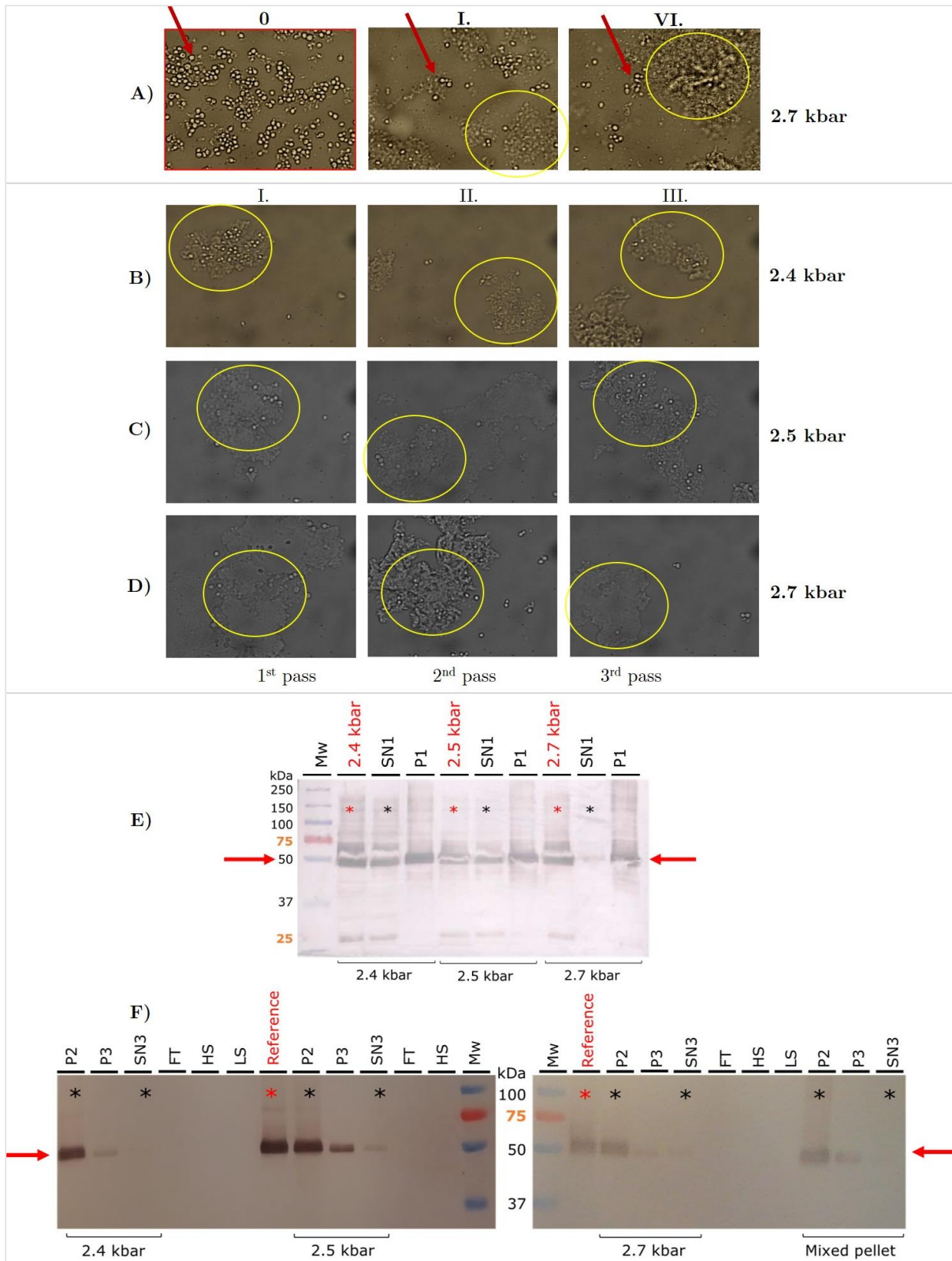


Figure 3-25. Lysis tests of *P. pastoris* using 2.4, 2.5, and 2.5 kbar pressure. In the top panel (A), 0 denotes the *P.pastoris* cells before lysis. I. and VI. show the cells after one and six passes through Cell D at 2.7 kbar, respectively. The red arrows point to whole cells in the first row, and the yellow circles showcase ruptured cells. The middle panel (B-D) corresponds to lysis tests performed at 2.4, 2.5, and 2.7 kbar, respectively, after one (I.), two (II.), and three (III.) passes. The bottom panel presents a western blot with the lysis fractions (E) containing the lysed supernatant (SN1) and the cell debris and the unlysed cell fraction (P1). Row F shows the pellets containing the MPs (P2) and P3 and SN3 denote

the fractions post solubilization with 1.5% DDM indicating the insoluble and solubilized fractions, respectively. Black stars indicate where most of the protein was expected, while red stars show the reference samples. The red arrows indicate the height where the Kir2.1 monomer is expected (50 kDa).

Solubilization was attempted at six different detergent-to-MP ratios (Figure 3-26), but all yielded poorly.

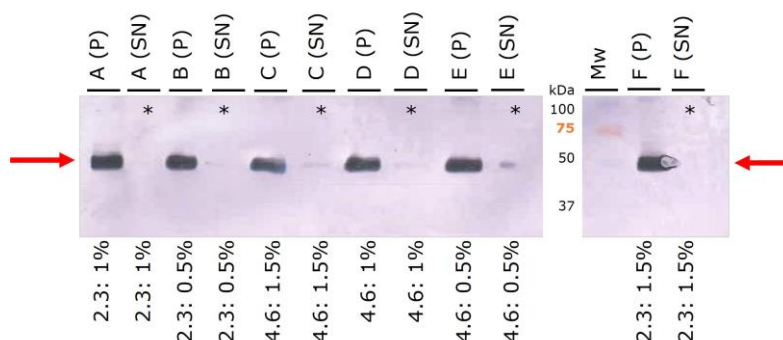


Figure 3-26. Western blot of Kir2.1 solubilization test using different membrane proteins (MP) to DDM detergent concentration ratios following poor lysis. Fractions P (pellet) and SN (supernatant) designate unsolubilized and solubilized fractions, respectively. A: $2.3 \text{ mg} \cdot \text{mL}^{-1}$ MP: 1% DDM. B: $2.3 \text{ mg} \cdot \text{mL}^{-1}$ MP: 0.5% DDM, C: $4.6 \text{ mg} \cdot \text{mL}^{-1}$ MP: 1.5% DDM, D: $4.6 \text{ mg} \cdot \text{mL}^{-1}$ MP: 1% DDM, E: $4.6 \text{ mg} \cdot \text{mL}^{-1}$ MP: 0.5% DDM, F: $2.3 \text{ mg} \cdot \text{mL}^{-1}$ MP: 1.5% DDM. The stars denote the lanes where a Kir2.1 band was expected.

A qualitative test was then performed to compare the effect of additional passes through the Cell D versus removing the lysed fraction and resuspending the unlysed pellet.

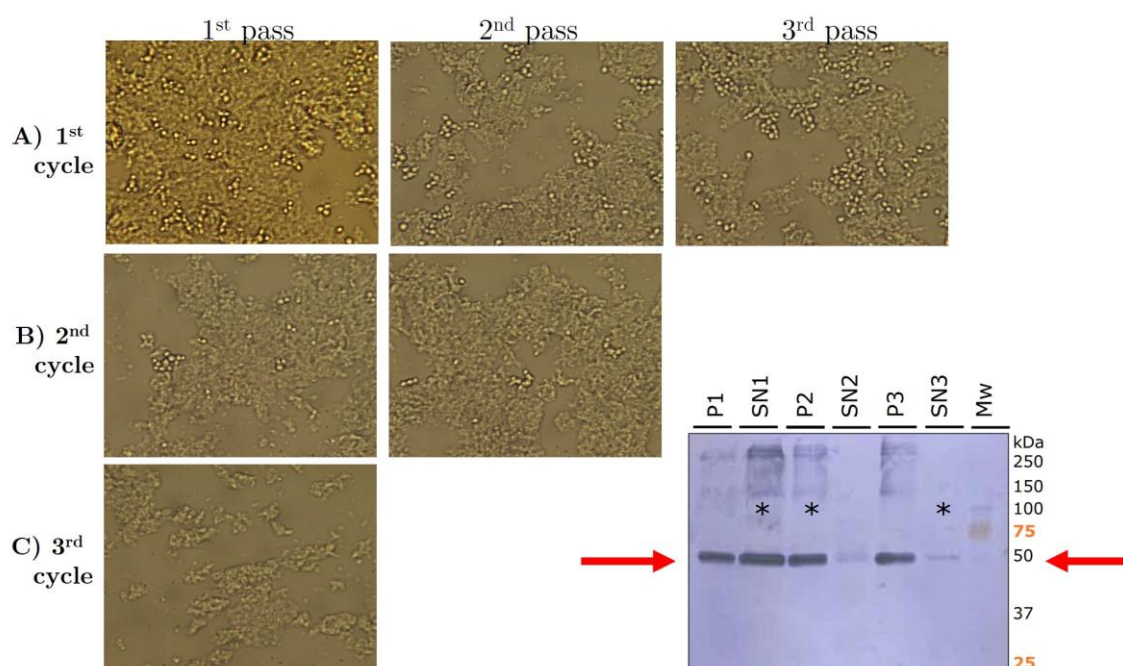


Figure 3-27. Optical microscopy and western blot analysis of lysis at 2.7 kbar. A-C show the effect of lysis. Horizontally (from 1 to 3) is the effect of adding additional passes through Cell D. Moving vertically

(from A to C) is the effect of centrifuging and resuspending before passing through Cell D. The western blot shows the pellet and supernatant after three-cycle lysis at 2.7 kbar without zymolyase (P1/SN1), membrane protein pelleting (P2/SN2), and solubilization fractions (P3/SN3). Stars indicate where Kir2.1 is expected. Red arrows show the expected molecular weight of the monomer (~50 kDa).

These microscopy results (Figure 3-27) confirmed that one pass was enough to lyse most *P. pastoris* cells and showed that the percentage of cells lysed could only be improved through centrifugation-resuspension-lysis cycles. However, increasing the number of passes could have an effect on the size of the membrane fractions recovered. There was a ~20% increase in lysis efficiency at the end of the third cycle. However, WB (Figure 3-27) showed roughly 40% of Kir2.1 remaining in the fraction containing cell debris and possibly large membrane segments (P1). Additionally, this increase in lysis did not increase the solubilization efficiency. Indeed, more protein was extracted as more cells were lysed, but the solubilization remained poor; most Kir2.1 remained unsolubilized (P3). Finally, this may indicate that a combination of several passes (≥ 6) and cycles are required to maximize the amount of protein extracted by this method.

Several obstacles were encountered when using the Cell D. Much foam was created for each cycle. Volume was lost as some exited through the entrance and bypassed the jet, requiring an additional buffer to push out the remaining volume. Many runs stopped before completion, and there was an altogether steady decline in performance (prior to maintenance). Altogether, the lysis was improved by increasing the Zymolyase concentration to 30 U per g of pellet, increasing the number of passes, and adding three centrifugation-resuspension-lysis cycles to separate the lysed cells from the unlysed cells. Nevertheless, the technical difficulties and the tedious, time-consuming protocol pushed me to try different lysis methods.

3.6.3.2 *Direct extraction by the formation of protoplasts*

A strategy to bypass the mechanical lysis altogether was developed. Direct extraction from protoplasts was performed, following the protocol described by Hartmann et al. (Hartmann et al. 2017) and AMSBio. Protoplast refers to an entire cell without its cell wall. The protocol for protoplast formation consisted of washes and buffers (Materials and Methods section 2.1.6, and Table 2-2) that induced an osmotic shock that weakened the cell wall. The cell wall was then lysed by Zymolyase treatment at pH 5.8, inducing protoplast formation. The membrane protein could then be directly solubilized from these protoplasts.

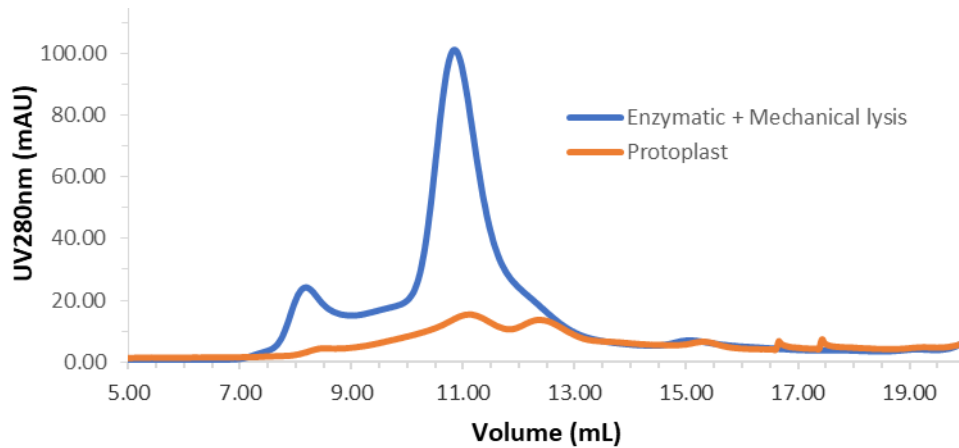


Figure 3-28. Comparison of SEC elution profiles after mechanical lysis vs. direct extraction. The SEC profile of Kir2.1 lysed enzymatically and mechanically is shown in blue (10 g pellet). The direct extraction from protoplast is shown in orange (20 g pellet).

This technique resulted in a yield reduction that varied from a factor of 2 to 8.5. Figure 3-28 illustrates two cell pellets from the same culture, one treated with mechanical lysis (blue, 10 g) and the other by protoplast extraction (orange, 19 g). The protoplast method yielded 8.5 times less protein.

Extraction through protoplast alone was not adequate. Therefore, I also explored protoplast treatment combined with mechanical lysis. This combination resulted in excellent lysis; however, roughly 40% of Kir2.1 wound up in the soluble fraction (SN2) when combined with three cycles of Cell D. The remainder was poorly solubilized (Figure 3-29).

Here we see that the extraction of MPs relies on efficient cell lysis. If not enough cell wall is removed, the detergent cannot adequately penetrate the plasma membrane to solubilize enough protein (Figure 3-30). On the other hand, the plasma membrane can be disrupted if the lysis conditions are too harsh (Figure 3-29, III).

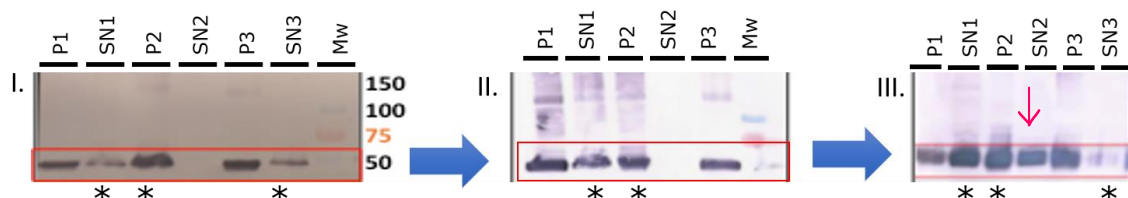


Figure 3-29. Comparison of lysis in Kir2.1. P1 (pellet) and SN1 (supernatant) I.) 20 U Zymolyase per gram of cell pellet, 6 passes on Cell D. II.) 30 U Zymolyase/g + 6 x Cell D. III.) Protoplast formation (30 U Zymolyase + an osmotic shock)+ 3 cycles Cell D. The red arrow shows Kir2.1 in the soluble fraction (SN2). The stars denote the fraction where most Kir2.1 is expected.

Combining protoplast formation and one Cell D pass at 2.5 kbar provided better results (Figure 3-30); only a small amount of Kir2.1 was found in the soluble fraction, and

solubilization was better than either protoplast treatment or Cell D alone (Figure 3-30); roughly 40% solubilization. These results emphasize the need for adequate lysis conditions to solubilize Kir2.1 efficiently.

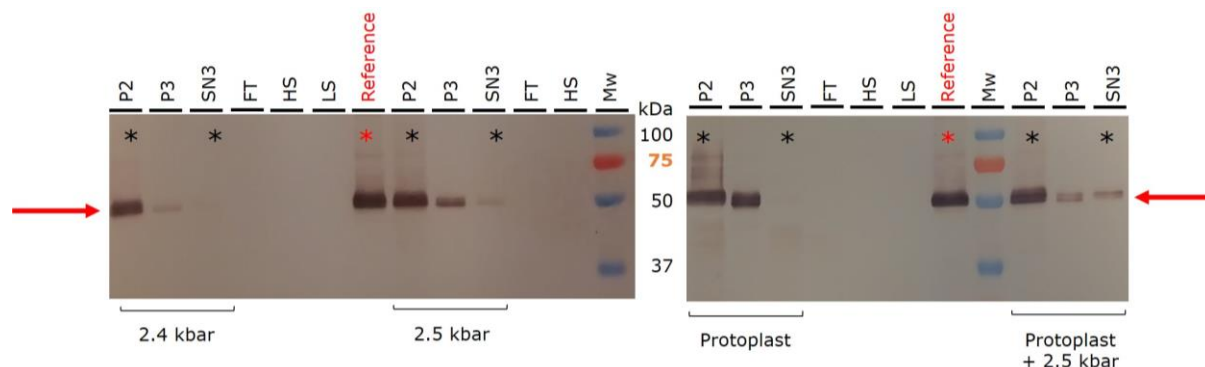


Figure 3-30 Western blots of solubilization of Kir2.1 after lysis with Cell D, protoplasts, and protoplast plus Cell D. On the left, Figure 3-25 F for comparison. On the right, WB shows the pellet (P3) and supernatant (SN3) fractions post-solubilization with 1.5% DDM. The black stars indicate where most protein is expected, and the red stars indicate the reference sample used as a control.

After purification, I compared the SEC profiles, but no significant differences were observed. After all these experiments, we decided that protoplast treatment was not ideal for our system, and it was better to pursue mechanical lysis.

3.6.3.3 Lysis of *Pichia pastoris* with the glass beads

Toward the end of my thesis, I had the opportunity to test another mechanical method, glass beads using the FastPrep24™ 5G homogenizer (MP Biomedicals) for reproducibility (Materials and Methods section 2.1.2.2 and Table 2-3) (Hartmann, Kugler, and Wagner 2016). Although there was no improvement in the number of cells lysed (Figure 3-31) compared to Cell D (Figure 3-27), the solubilization step was significantly more efficient (Figure 3-31) post glass bead lysis than the Cell D. Perhaps due to a difference in the size of the membrane fractions formed.

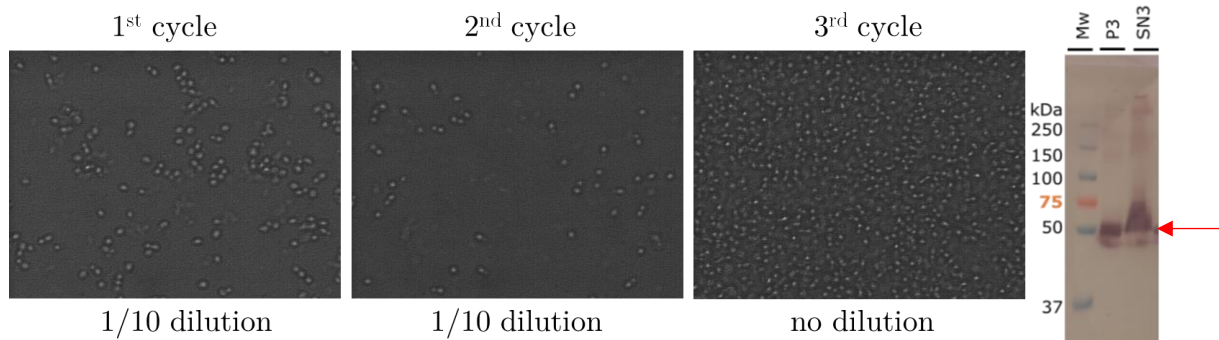


Figure 3-31. Lysis of *P. pastoris* cells using glass beads and WB analysis of Kir2.1 solubilization. WB shows more protein in the solubilized fraction (SN3, 60%) than in the pellet (P3, 40%).

The overall performance of this method was much better than with Cell D; we now routinely use the glass beads.

3.6.4 Conclusion

The solubilization of Kir2.1 from *P. pastoris* membranes was better after lysis using the glass beads instead of the Cell D, perhaps due to a difference in the size of the membrane fractions formed. A combination of good lysis with glass beads and solubilization buffer conditions seems a prerequisite.

The direct extraction from protoplast was not successful. Perhaps the poor results are due to an inefficient protoplast formation. If there is insufficient lysis, the detergent cannot penetrate the membranes to extract the protein.

Perspective: survey protoplast efficiency OD800. The efficiency and time required for protoplast formation can be determined by plotting OD800 of the treated yeast cells vs. time. To calculate efficiency, divide the OD800 at each time point by the starting OD800, then multiply by 100.

4 CRYO-EM STRUCTURE OF THE HUMAN KIR2.1 CHANNEL

4.1 INTRODUCTION TO CHAPTER

With the protocol established in the previous chapter, we obtained pure and homogenous tetrameric protein that could be used for subsequent studies. This chapter focuses on determining the structure of h_Kir2.1 by cryo-EM, and the interaction of Kir2.1 WT and R312H mutant with PIP₂, fulfilling my thesis' third and fourth objectives. The structure of h_Kir2.1 was solved with a global resolution of 4.3 Å with local resolutions at 3.7 Å. The structural features, notably the G loop, are explored and compared to available structures. Even when comparing to the c_Kir2.2 homolog that shares 70% identity, we find significant discrepancies with potential implications in the functional differences observed between the two.

To consolidate our findings and explore the conformational states available to Kir2.1 in the apo state, we used *in silico* studies. With molecular dynamics (MD) simulations and normal mode (NM) analysis were able to recover, in the apo state, the large conformational movements seen with other Kir structures bound to PIP₂. These conformational changes observed through *in silico* studies were subsequently validated by the cryo-EM 3D classification maps.

These structural studies were combined with functional and binding assays to evaluate the effect of the R312H mutation on the structure and function h_Kir2.1. For this, the interaction with the essential modulator PIP₂ was characterized by surface plasmon resonance and compared to that of the R312H mutant.

Cryo-electron microscopy unveils unique structural features of the human Kir2.1 channel

Carlos A. H. Fernandes^{1†}, Dania Zuniga^{1†}, Charline Fagnen^{1‡}, Valérie Kugler², Rosa Scala³, Gérard Péhau-Arnaudet⁴, Renaud Wagner², David Perahia⁵, Saïd Bendahhou³, and Catherine Vénien-Bryan^{1*}

¹ Sorbonne Université, UMR 7590, CNRS, Muséum National d'Histoire Naturelle, IRD, Institut de Minéralogie, Physique des Matériaux et de Cosmochimie, IMPMC, 75005 Paris, France.

² IMPReSs Facility, Biotechnology and Cell Signaling UMR 7242, CNRS-University of Strasbourg, Illkirch, Cedex, France.

³ CNRS UMR7370, LP2M, Labex ICST, Université Côte d'Azur, Faculté de Médecine, Nice, France.

⁴ Ultrastructural BioImaging core facility/UMR 3528, Institut Pasteur, 75724 Paris Cedex 15, France.

⁵ Laboratoire de Biologie et Pharmacologie Appliquée, Ecole Normale Supérieure Paris-Saclay, 4 Ave. des Sciences, 91190 Gif-sur-Yvette, France.

†These authors contributed equally to this work

‡ present address: University of Leeds

* catherine.venien-bryan@sorbonne-universite.fr

This is the author's version of the work. It is posted here by permission of the AAAS for personal use, not for redistribution. The definitive version was published in Science Advances on Vol 8, Issue 38 (23 Sep 2022), doi: 10.1126/sciadv.abq8489.

Keywords: Cryo-EM structure, Kir2.1, PIP₂, gating, normal modes, molecular dynamics, K⁺ channels

4.2 ABSTRACT

We present the first structure of the human Kir2.1 channel containing both transmembrane (TMD) and cytoplasmic (CTD) domains. Kir2.1 channels are strongly inward rectifying K⁺ channels that play a key role in maintaining resting membrane potential. Their gating is modulated by phosphatidylinositol-4,5-bisphosphate (PIP₂). Genetically-inherited defects in Kir2.1 channels are responsible for several rare human diseases, including Andersen's syndrome. The structural analysis (cryo-EM), surface plasmon resonance, and electrophysiological experiments revealed a well-connected network of interactions between the PIP₂-binding site and the G-loop through residues R312 and H221. Additionally, molecular dynamics simulations and normal mode analysis showed the intrinsic tendency of the CTD to tether to the TMD and a movement of the secondary anionic binding site to the membrane even without PIP₂. Our results revealed structural features unique to human Kir2.1 and provided insights into the connection between G-loop and gating and the pathological mechanisms associated with this channel.

Teaser

First human Kir2.1 structure reveals the G-loop connection with gating for the loss of function in Andersen's syndrome mutant

4.3 INTRODUCTION

Inward-rectifier potassium (Kir) channels are a group of integral membrane proteins that selectively control the permeation of K^+ ions across cell membranes. They are particular in that the channels conduct K^+ ions easier in the inward direction (into the cell) than in the outward direction (out of the cell). The small outward K^+ current through Kir channels controls the resting membrane potential and membrane excitability, regulates cardiac and neuronal electrical activities, couples insulin secretion to blood glucose levels, and maintains electrolyte balance (1).

All Kir channels are tetramers of identical or related subunits and share characteristic structural features. They possess a canonical pore-forming transmembrane domain (TMD) made of two transmembrane helices (M1 and M2) separated by a K^+ ion selectivity filter and a large cytoplasmic domain (CTD) containing both amino (N-) and carboxy (C-) termini. The CTD extends the ion conduction pathway and provides docking sites for regulatory ions, proteins, and ligands (2). The inward-rectification mechanism results from a block on the cytoplasmic side of the channels by endogenous polyamines and Mg^{2+} that plug the channel pore at depolarized potentials, resulting in decreased outward currents. The blockers are then removed from the pore when the K^+ ions flow into the cell at hyperpolarized potentials. This voltage-dependent block results in efficient conduction of current only in the inward direction (3–5). In addition to being inwardly rectifying, Kir channels respond to a variety of intracellular messengers that directly control the channel gating, including phosphoinositides (PIPs), G proteins (Kir3 channels), ATP (Kir6 channels), and changes in pH (Kir1 channels) (1). The Kir family is encoded by 16 genes (*KCNJ1-18*), and classified into seven sub-families (Kir1–7).

To fulfill crucial biological roles, the gating of all eukaryotic Kir channels is directly controlled by regulatory lipid ligands such as PIPs. Different Kir isoforms display distinct specificities for the activating PIPs (2). Kir2.1 channels are selectively activated by the signaling lipid phosphatidylinositol-4,5-bisphosphate (PIP_2), while some members (such as Kir3.1/3.4) are less stringent in their PIP sensitivity, and all PIPs indiscriminately activate others such as Kir6.2. PIP_2 binds to a “primary site” (6, 7), and its sensitivity is enhanced by the binding of a bulk of anionic lipids (positive allosteric regulators) to a “secondary site” (8, 9). On the other hand, the bacterial KirBac channels are inhibited by PIPs (6, 10).

Kir2.1 is the protein product of the *KCNJ2* gene, which has been shown to play a critical role in excitable cells and developmental processes (11). Kir2.1 is expressed at high levels in the heart, skeletal muscle, and neural tissue. The extent of rectification varies among the different subfamilies, ranging from weak (Kir1) to strong (Kir2). Several crystallographic structures of Kir channels with Mg^{2+} have been published. One study has reported the crystallographic structure of KirBac3.1 channel with an electron density attributed to spermine. Yet, KirBac3.1 is missing numerous critical spermine-interacting residues (12). The molecular blocking mechanisms of polyamines and Mg^{2+} are still under scrutiny. *KCNJ2* mutations are associated with four disorders, namely Andersen's syndrome (AS), atrial fibrillation (AF), short QT syndrome (SQT), and catecholaminergic polymorphic ventricular tachycardia (CPTV) (11, 13–15). While AF- and SQT-associated mutations lead to a gain of channel function, those associated with AS and CPTV are all loss of function mutations. AS is a rare and complex

disorder showing variability in patient diagnosis. The most common phenotypes are periodic paralysis, cardiac arrhythmias, and distinctive physical features with development anomalies (16).

It has been proposed that the G-loop is involved in channel modulation by PIP₂ and other ligands (17, 18). The G-loop is a conserved motif extending from G300 to Y315, composed predominantly of residues with short hydrophobic side chains that may constrict the pore diameter in some states of the channel (19). Even though the role of the G-loop is yet to be fully understood, several structural studies raise the possibility that this motif undergoes relevant conformational changes for channel gating (17–20). However, it is not known how the G-loop gate integrates into channel gating and how it affects the gating kinetics of Kir channels.

In order to shed light on the structural mechanism of the human Kir channels and the associated rearrangements underlying PIP₂, Mg²⁺, and polyamines-dependent gating, detailed structural information is crucial. Here we used cryo-electron microscopy (cryo-EM) combined with image analysis to elucidate for the first time the structure of a human Kir channel, Kir2.1, at atomic resolution in the closed state. Our findings reveal unique structural features of the human Kir2.1 channel, among other eukaryotic Kir channels. Furthermore, computational investigations (normal mode analysis and molecular dynamics simulation) reveal crucial conformational movements, including compaction of the structure and opening movements at the interface between the TMD and CTD, which could facilitate the binding of PIP₂. In addition, we provide biophysical and functional data on the Kir2.1 channel (WT and the mutant R312H, a mutant responsible for AS disease (21)), and we propose a putative activation mechanism involving the transmission of the signal to the G-loop upon PIP₂ binding.

4.4 RESULTS

4.4.1 Protein expression and purification of human Kir2.1 WT and R312H.

Until recently, the effect of residue R312 on the binding of PIP₂ to Kir2.1 was still controversial. The R312Q mutation has been suggested to weaken the interaction of Kir2.1 with PIP₂ (22). However, more recent biochemical binding assays have indicated that this mutation does not significantly affect the PIP₂ binding (23). To clarify this point, we investigated the affinity of PIP₂ to the WT channel and R312H mutant (naturally occurring AS-causing mutation) and the impact of this mutant on the Kir2.1 function. The human Kir2.1 wild-type (WT) channel and its R312H mutant counterpart were recombinantly-produced in and purified from the yeast *Pichia pastoris*. The size exclusion chromatography (SEC) elution profile of the Kir2.1 WT (Fig. S1) shows a prominent elution peak at 11.80 mL, corresponding to its tetrameric quaternary structure. SDS-PAGE and Western blot analyses reveal the monomeric form of Kir2.1 at its expected size (~50 kDa, Fig. S1). Similar results were obtained with the Kir2.1 R312H mutant (data not shown).

4.4.2 Overall cryo-EM structure of the human Kir2.1 channel

The structure of the human Kir2.1 channel was resolved by single-particle cryo-EM analysis (Fig. S2, Fig. 1A) to an average resolution of 4.3 Å (Fig. S3) for the whole protein. The local resolution map shows that some regions, especially in CTD, can reach 3.7 Å resolution, mainly: the G-loop region, the PIP₂ binding site, residue R312, and its vicinity (Fig. S3B). The final

structural model contains all typical structural features of Kir channels (Fig. 1 A-B). In the TMD, the outer (M1) and inner (M2) transmembrane helices are observed, in addition to two short helical elements (the slide and the pore helices) and the selectivity filter which contains the K⁺ channel signature sequence (T-X-G-Y/F-G). The CTD is rich in β -strands and encompasses the G-loop in the apex of the cytoplasmic pore. This is the first time that the entire human Kir2.1 channel has been resolved at high resolution; it is also the first cryo-EM structure of a Kir2 channel. This Kir2.1 structure covers an external flexible N-terminal loop (region 41–54) that interacts with CTD and PIP₂, which has only been continuously modeled in Kir2.2 PIP₂-bound crystal structures (3SPI, 3SPG, and 5KUM) (7, 24). This segment has been shown to be important in the gating process (25).

The resolved Kir2.1 structure exhibits ion-conduction pore constrictions along the helix bundle crossing region (HBC) and the G-loop (see following sections). It is 121 Å long and 78 Å wide (Fig. 1). This extended conformation is also observed in the apo-Kir2.2 crystal structure (3JYC) (26) and the apo-Kir3.2 cryo-EM structure (6XIS) (27), both of which are in a closed state. Thus, these data suggest that the human Kir2.1 structure was obtained in the non-conductive closed state. A single disulfide bridge between C122 and C154 residues of the same chain is observed in the outermost region of the TMD, close to the extracellular loops (Fig. 1C). Finally, it was possible to accurately map the location of most of the AS-causing mutations in the Kir2.1 structure (Fig. S4). Moreover, we studied in detail the impact of one of them, R312H, located outside the PIP₂-binding site, on the structure and function of the human Kir2.1 channel (see following sections). The accession code for these structures are PDB 7ZDZ and EMD 14678.

4.4.3 Ions' location in the pore channel

No density consistent with K⁺ ions or any other ions were observed in the selectivity filter. The cryo-EM structure of apo-Kir3.2 (6XIS) is another structure reported with no K⁺ ions inside the selectivity filter, despite its slightly larger pore diameter than Kir2.1 (see next section). Nevertheless, the presence of three K⁺ ions is observed when the same channel is in complex with PIP₂ (cryo-EM PIP₂-Kir3.2 structure, 6XIT) (27). In most crystallographic structures, four K⁺ ions are present at the selectivity filter; this includes the crystal structures of apo-Kir2.2, PIP₂-Kir2.2 (3JYC and 3SPI, respectively), apo-Kir3.2, PIP₂-Kir3.2 (3SYO and 3SYA, respectively), and KirBac3.1 (i.e., 3ZRS) (7, 17, 26, 28). Note that for crystallization assays and cryo-EM sample preparation, the concentration of KCl in the medium is approximately the same (150–200 mM).

Three ions (two Sr²⁺ and one K⁺, Fig. 2 in blue and green, respectively) are present in the pore below the selectivity filter. The two circular densities, located just below the selectivity filter and slightly below the G-loop, were attributed to Sr²⁺ ions. These cryo-EM densities show a high magnitude (still persistent at 13 σ and 15 σ map threshold respectively) and exhibit higher cross-correlation values (cc = 0.82 and 0.76, respectively) when modeled as Sr²⁺ ions, compared to when modeled as Mg²⁺ (0.51 and 0.57) or K⁺ ions (0.41 and 0.49). The divalent cation Sr²⁺ mimics Mg²⁺, a biologically important metal ion blocker of eukaryotic Kir channels (29). The first Sr²⁺ ion is located below the selectivity filter at equidistance from the O δ 2 of the D172 side chains (~7 Å) and the O γ 1 of the T142 side chains (~6–7 Å), the innermost residue of the selectivity filter. The second Sr²⁺ ion is located below the G-loop at ~8–11 Å from O ϵ 1/O ϵ 2 of the E299 side chains and ~9–10 Å from O ϵ 1/O ϵ 2 of the E224 side chains. It is, interestingly, closer (~6 Å) to the carbonyl backbone of the A306 in the G-loop region. Sr²⁺ ions at similar positions have also been found in the crystal structure of chicken Kir2.2 (26), where crystals were grown in the presence of 10 mM Sr²⁺. However, no Sr²⁺ was added in the sample

preparation for cryo-EM analysis, but there are traces of Sr^{2+} ions in the yeast medium.

A third circular cryo-EM density with a persistent magnitude up to a 6σ map threshold is observed in the outermost region of the CTD. This density was interpreted as a K^+ ion (cc=0.84). This K^+ ion is dehydrated and directly coordinated to two D255 residues from opposite chains with typical K-O distances of 2.8 Å (Fig. 2). This confirms that the long pore extends quite far from the cytoplasm (20). A K^+ ion in a similar position has been found in the crystal structure of the CTD domain of mouse Kir2.1 R218Q/T309K (2GIX) (30). However, in this structure (2GIX), the K^+ ion is hydrated and interacts with the four D255 residues through eight water molecules.

4.4.4 Four constriction points (gates) in the Kir2.1 channel

The analysis of the radius between the van der Waals surfaces of the central ion conduction pore using the HOLE software (31) shows four constriction points located at the selectivity filter and residues I176, M180, and A306 (Fig. 3, A and B). The selectivity filter has a very tight structure (pore radius less than 0.2 Å). Two of the other narrow points, I176 and M180, are located in the TMD immediately below the Sr^{2+} ion present in this region. These constriction points have a minimum pore radius of 0.77 Å (I176) and 1.05 Å (M180) and close the pore leading to the CTD. Similarly, in the apo-Kir2.2 crystal structure (3JYC) (26), I177, equivalent to I176 in Kir2.1, is also described as a constriction point with a similar pore radius (Fig. 3C). M180 is equivalent to residue Y132 of KirBac3.1 located at the helix bundle crossing, a well-described constriction point in the bacterial channel (12, 32). The fourth constriction point is located at A306 at the apex of the G-loop at the pore entrance into the CTD; this feature has also been observed in the mouse CTD Kir2.1 crystal structure (1U4F) (20). This constriction point is unique to Kir2.1 and is not present in Kir2.2 (3JYC) and Kir3.2 (3SYO) structures (Fig. 3C).

4.4.5 Structural comparison between Kir2.1 and Kir2.2 structures

The superposition of $\text{C}\alpha$ atoms of TMD and extracellular region (a.a 72–182) of the four chains of human Kir2.1 channel cryo-EM structure resulted in a root mean square deviation (RMSD) of 1.0–1.4 Å (Table S1A). The region that presents the most significant deviation is the extracellular region (a.a 112–121), including the C-terminal end of the M1 helix and the extracellular loops, indicating high conformational flexibility (Fig. S5A). Moreover, $\text{C}\alpha$ superposition between the four chains of Kir2.1 structure and the crystal structures of Kir2.2 in the absence and presence of PIP_2 (3SPI and 3JYC, respectively) resulted in an RMSD of 4.6–5.0 Å (Table S1A). These high RMSD values are mainly due to deviations observed in extracellular and selectivity filter regions (a.a 141–147) (Fig. S5B). This $\text{C}\alpha$ superposition reveals that the selectivity filter in human Kir2.1 is closer to the center of the pore channel compared with the Kir2.2 structures (Fig. S5B), resulting in a narrower pore (as shown in the previous section). The superposition of $\text{C}\alpha$ TMD and the extracellular region between the Kir2.2 crystal structures reveals lower RMSD values than the comparison between the Kir2.1 chains (0.8 Å and 1.0–1.4 Å, respectively, Table S1A). This is due mainly to a smaller deviation in the extracellular region (Fig. S5A-B), suggesting this region of Kir2.1 channels can present higher conformational flexibility than the same region in Kir2.2.

Superposition between $\text{C}\alpha$ atoms of CTD (a.a 192–364) from the four chains of human Kir2.1 channel cryo-EM structure resulted in RMSD values of 0.9–1.6 Å (Table S1B). When compared with the crystal structure of mouse Kir2.1 CTD (1U4F), $\text{C}\alpha$ CTD superposition resulted in

RMSD values of 1.3–1.9 Å (Table S1B). In both superpositions, the CTD regions that present the greatest deviation are two flexible loops exposed to the solvent (a.a 281–291 and a.a 330–340) and the C-terminal end (a.a 357–364). The G-loop presented low C α RMSD values in both comparisons (0.4–0.7 Å between the four human Kir2.1 chains (Table S1C) and 0.5–0.7 Å between human and mouse CTD) (Table S1C). These data indicate that the G-loop displays a stable backbone conformation in the Kir2.1 CTD structures, although previously described as intrinsically flexible (20).

4.4.6 PIP₂ binding interaction with Kir2.1 WT and mutant R312H

The association and dissociation rate constants, k_{on} and k_{off} , respectively, and the dissociation constant (K_D) of the Kir2.1 WT and R312H mutant were determined directly from surface plasmon resonance (SPR) experiments and the fitted curves using CM5 sensor chips. Kir2.1 WT was immobilized at 3,900–6,500 RU (response units) levels on CM5 sensor chips. Sequential injections of PIP₂ ranged from 0.15 to 20 μ M (Fig. 4A). The K_D , derived from k_{off}/k_{on} , was determined to be $3.2 \pm 0.7 \cdot 10^{-6}$ M. The average k_{on} and k_{off} are $1.8 \pm 1.1 \cdot 10^3$ Ms⁻¹ and $5.2 \pm 3.5 \cdot 10^{-3}$ s⁻¹, respectively. Kir2.1 R312H was immobilized to 4,000–4,130 RU level on CM5 sensor chips. Sequential injections of PIP₂ ranged from 0.15 to 20 μ M. The derived K_D , was determined to be $3.7 \pm 1.2 \cdot 10^{-5}$ M with an average k_{on} of $4.5 \pm 2.3 \cdot 10^2$ Ms⁻¹ and k_{off} of $1.4 \pm 4.5 \cdot 10^{-2}$ s⁻¹ (Fig. 4B). R312H showed a ten-fold difference in affinity compared to WT. However, both have affinities in the micromolar range, which corresponds to generally low binding affinity. This indicates that the R312H mutation slightly modifies the K_D but does not impede the binding.

4.4.7 Functional studies on Kir2.1 WT and mutant R312H

The purified proteins (Kir2.1 WT and R312H) were investigated in reconstituted planar lipid bilayers. The electrophysiological recordings of Kir2.1 WT and R312H mutant in the absence of PIP₂ showed no channel activity (data not shown). However, recordings in the presence of 1% PIP₂ at –100 mV revealed an open probability (P_o) of 70% for the WT form (Fig. 4C) and less than 1% for the Kir2.1 R312H mutant (Fig. 4D). These activities were all silenced by applying 100 μ M BaCl₂ to the upper chamber.

4.4.8 Interaction network between R312, H221, and E303 residues

In the human Kir2.1 channel structure, residue R312 is involved in an inter-subunit interaction network with residues H221 and E303 of the clockwise-adjacent chain (top view from the extracellular side) (Fig. 5 and Fig. S6). Except for chain C, the oxygen atoms of the R312 side chain can establish inter-subunit contacts at distances of 3–3.4 Å with the oxygen atoms of the H221 imidazole ring of the adjacent chain, although both are positively charged. Indeed, computational approaches have demonstrated that arginine can form strong like-charged contact pairs with histidine, which are not weakened by the unfavorable electrostatic interaction between the side chains (33). Moreover, except for chain B, R312 can establish inter-subunit salt bridges (3.4–3.7 Å) with E303 of the adjacent chain, a residue present in the G-loop. E303 can also establish intra-subunit salt bridges (3.4 Å) with H221 near residues K219 and R218. These two critical residues have been previously reported to control the binding of PIP₂ to the Kir2.1 channel, with the mutation R218Q abolishing such a binding (23, 34). Fig. S7 highlights the cryo-EM density map quality for H221, E303, and R312 in the four Kir2.1 chains, with a

local resolution of 3.7 Å (Fig. S3).

The R312H mutation was modeled in the human Kir2.1 channel to understand its implication in the interaction network described above. Arginine was changed to histidine using Chimera software, followed by local energy minimization. The analysis of the interaction network distances showed that the nitrogen atoms of the H312 imidazole ring were further away from the nitrogen atoms of the H221 imidazole ring of the adjacent chain than the distances observed in the WT structure (Fig. 5 and Fig. S6). Furthermore, all salt bridges involving E303 are lost because the distances between Oε2 of E303 and nitrogen atoms from H312 and H221 increased to 4.9–9.0 Å. These data suggest that R312 helps coordinate the position of H221 and E303 side chains to maintain the salt bridges established by E303 with the two other residues. The mutation R312H abolishes this particular network of interactions.

4.4.9 Investigation of global motions of the Kir2.1 channel by normal mode analysis

The first Kir2.2 channel crystal structures revealed significant structural differences between the apo and PIP₂-bound structures. In the apo-Kir2.2 crystal structure, the protein is observed in an extended conformation, and the linker between CTD and TMD is disordered in the outer region (a.a 57-70). On the other hand, in the PIP₂-bound structures, this linker adopts a helical conformation, and the CTD approaches the membrane's inner surface, translating toward the TMD by 6 Å (7, 26). Similar results about PIP₂-induced channel compaction were observed in Kir3.2 cryo-EM structures (27). Furthermore, this compact structure has also been associated with a gating conformational change (35). However, it is uncertain that PIP₂ binding could be responsible for the movement of CTD toward TMD since the crystal structures of Kir2.2 (5KUM) and Kir3.2 (3SYO and 3SYP) have been obtained in the compact form without PIP₂ (17). This suggests that large conformational movements are involved in the gating of this channel. These large-scale conformational movements generally take place on nanoseconds to microseconds time scale, often not reached in classical molecular dynamics simulations. Low-frequency normal mode (NM) analysis is a relevant tool to overcome this limitation and characterize these conformational movements and has been successfully used to describe structural aspects of several proteins (36, 37). NM analysis was performed to assess whether the lowest frequency modes would describe the channel's compaction/extension movement in the absence of PIP₂. We calculated the first five lowest frequency modes as they are sufficient to get the overall collective motions (38).

The longitudinal length of Kir2.1 (Fig. S8 left panel) was evaluated by the Cα-Cα distance between the most distal points of the structure: residues K117 (in the extracellular loop) and E363 (lowest part of the C-terminal region). Tethering of the CTD to the TMD was assessed by the Cα-Cα distance between D78, located in the slide helix at the interface between the membrane and the CTD, and K219, located in the CTD; the latter has been identified as a PIP₂ binding controller, being close to H221 (2). In the extended structure of the Kir2.1 channel obtained here, the protein is seen to be 121 Å long and has a D78/K219 Cα-Cα distance of ~15 Å (Fig. S8 left panel). After the initial energy minimization necessary for the all-atom NM calculation (constituting the reference structure), a slight decrease in the protein's longitudinal length and a slightly closer distance between the CTD and TMD were observed (Fig. S8 middle panel). To better analyze the motions corresponding to the five lowest frequency modes, ±3.0 Å structural displacements were achieved along each of them. Then, the absolute value of the longitudinal length difference between the two extremes of the displaced structures along each of the mode vectors and the CTD-TMD tethering length were calculated.

Mode 5 was the only NM for which the C α K117/E363 and D78/K219 distances varied cooperatively by at least 6 Å between the displaced structures at +3 Å and -3 Å (Fig. S8 right panel). A displacement of -3 Å along the mode 5 from the energy-minimized reference structure leads to a compaction of the entire protein down to 113 Å and a reduction of C α -C α D78/K219 down to 9.7 Å (Fig. 6). On the other hand, the reverse +3 Å displacement leads to an extension up to 121 Å and to an increase of the C α -C α D78/K219 distance up to 15.8 Å, which are values close to those observed in the cryo-EM structure (Fig. 6A). These data show that NM 5 was able to recover and describe the extension/compression conformational motion of the Kir2.1 channel even without PIP₂ (Fig. 6A; Video S1).

Modes 1 and 2 describe a swing motion that results in a lateral opening of the area located at the interface between CTD and TMD in adjacent chains (Figs. 7 and S9, Videos S2 and S3). Mode 1 describes a swing motion between chains B and C in this interface area and chains A and D (Figs. 7A and S9A, Video S2). The extent of this motion was evaluated by the C α -C α distance between R82 and K219 from adjacent chains (R82(B)/K219(C) and R82(D)/K219(A)) (Fig. S9A). A displacement of +3 Å along the mode 1 from the reference structure leads to an increase of C α R82(B)/K219(C) distance of 5.1 Å, and the reverse -3 Å displacement leads to a 1.8 Å increase of C α R82(D)/K219(A) distance (Fig. S9A). K187 is a residue that interacts directly with a PIP₂ phosphate group (7) and is located in the central region of the inner loop between TMD and CTD. We observed a significant increase in the solvent-accessible surface area (SASA) of the residue K187 from chains B and D by 10.0 Å² and 20.0 Å², respectively, after applying ± 3 Å displacements along the NM 1 (Fig. S9A). Mode 2 describes the same swing motion as mode 1, but between chains A and B and chains C and D (Figs. 7B and S9B, Video S3). Likewise, the C α R82/K219 distances increase in the ± 3 Å displaced structures along the NM 2 (by 2.1 Å and 5.8 Å for R82(A)/K219(B) and R82(C)/K219(D) distances, respectively) as well as the SASA of the K187 residues (by 13.7 Å² and 15.3 Å² for K187(A) and K187(C), respectively) (Fig. S9B and Video S3). In conclusion, modes 1 and 2 may describe an inherent movement of opening the PIP₂ binding site in the four possible PIP₂ binding sites available in the Kir2.1 structure. The residues involved in putative PIP₂ binding for Kir2.x (R80, W81, R82, K182, K185, K187, K188, R189, R218, and K219) (2) are shown in Videos S2 and S3.

Finally, the motions referring to modes 3 and 4 can be seen in Videos S4 and S5; we do not address them in detail.

To identify in our cryo-EM data sets the different conformational states described by NM analysis, we followed the protocol described by Scheres et al. (39). The compression/extension conformations, were observed when the particles from class 3 of the second 3D classification round (blue box, Fig. S2) were submitted to 3D classification using local angular searches (Fig. S10). This 3D classification provided two classes (classes 2 and 6; Fig. S10), which after 3D refinement, resulted in maps with size-length of 120 Å and 113 Å (Fig. S10), values similar to those observed along the ± 3.0 Å structural displacements in NM5 (Fig. 6). Concerning the lateral opening at the interface between CTD and TMD similar to that described by modes 1 and 2, we noticed that class 3 from the first round of 3D classification presented already this feature (red box, Figure S2). This was confirmed when we submitted the particles of this class to a 3D classification using local angular searches. In all classes resulting from this 3D classification, it was possible to observe the lateral opening of the structure (Figure S11). This interesting conformation can lead to increased accessibility of the PIP₂-binding site, as described by the NM1 and NM2 (Fig.7).

4.4.10 Investigation by MD simulations of local motions of residues K64 and R67

Residues K64 and K219 have been identified as constituting a secondary binding site, directly interacting with non-specific anionic phospholipids (PL⁻). These positive allosteric regulators increase the PIP₂ sensitivity by 10–100 fold (8, 9, 24). We studied the local motion of K64 (at the N-terminal end of the slide helix) by carrying out molecular dynamics (MD) simulations on the cryo-EM structure of Kir2.1 (extended conformation) embedded in a POPC lipid bilayer for 200 ns in triplicate. Snapshots of the K64 position during MD simulations show that this residue can approach the membrane significantly in most of the chains and replicas. Moreover, for three of the chains, we observed that K64 can enter the membrane (Figs. 8 and S12, Video S6). These data support the previously proposed movement of K64 tethering to the membrane (9, 24), which would be required for the PL⁻ binding to this secondary binding site. In addition, the dynamics of R67 (in the vicinity of K64 and closer to the membrane) were also examined. Snapshots of the R67 position along the MD simulations show that this residue can penetrate the membrane for most of the chains and therefore gets significantly closer to the membrane than K64 residue (Figs. 8 and S12, Video S5). The analysis of the distances between the K64 and R67 residues to the phosphate groups of the inner membrane shows that these residues move toward the membrane (Figs. 8 and S12). Furthermore, this analysis also shows that K64 and R67 have similar trajectory profiles and may have inherent coupled local motions. Finally, the C α RMSD and C α root mean square fluctuations (RMSF) from the MD simulations are shown in Fig. S13. All three replicas exhibited C α RMSD variation of less than 0.5 Å in the last 50 ns of the MD simulations (Fig. S13A). C α RMSF analysis shows that extracellular loops have the highest RMSF values in all four chains of the human Kir2.1 structure (Fig. S13B), indicating a high level of backbone flexibility. On the other hand, G-loop exhibits low C α RMSF values, indicating a low level of backbone flexibility in this region.

4.5 DISCUSSION

4.5.1 Conducting ions and blocking ions compete for sites in the pore

Strong rectification of Kir2.1 has been attributed to two principal electronegative regions: D172 in the M2 helix (40) and E224/E299 below the G-loop (41). The arrangement of residues is essential for blockade because they create negatively charged rings in the channel pore, which is crucial for the blocking and rectification of Kir2.1 channels (4). Mutations of these residues decreased the affinity for blockers such as Mg²⁺ and polyamines and reduced the intensity of inward rectification (1, 42). Our data support these findings, as one of the Sr²⁺ blocking ions is located in the TMD, below the selectivity filter near D172, and in the cytoplasmic domain near E224 and E299 just below the G-loop (Fig. 2). Each site contains several negatively charged carboxyl groups that create a strong electric field that easily accommodates multivalent cations. Sr²⁺ ions are used in electrophysiological experiments to promote the blockade of Kir2.1 channels (43). The Sr²⁺ blocker just below the selectivity filter is stabilized not only with the negatively charged ring made of D172 but also with T142 (conserved in all Kir members) located at the same distance as D172 (~6–7 Å), which could help stabilize Sr²⁺ (Fig. 2). However, this site is too wide (diameter of ~14 Å) to ensure the direct coordination of a dehydrated ion in the center. The Sr²⁺ ions at the center of the site should most likely interact

with D172 and T142 through bridging water molecules. The second Sr^{2+} , just below the G-loop, is stabilized by the negatively charged residues E224 and E299. In addition, the backbone carbonyl group of A306 is closer to the Sr^{2+} than the other negatively charged groups (Fig. 2). Interestingly, A306 is conserved only in the Kir2 subfamily (the strongest rectifiers) and KirBac (1.1 and 3.1). But, again, the pore diameter is too large (diameter of ~ 13 Å) to allow direct coordination; presumably, bridging with water molecules seems important. The presence of blocking ions could influence the conformation of the pore and, in particular, the radial size of the selectivity filter, which is very narrow (less than 0.5 Å in diameter, Fig. 3) and cannot accommodate a K^+ ion whose diameter is 2.67 Å when dehydrated (44).

Another di-aspartate cluster (D255/D259) has been described as important in determining the extent of inward rectification of the Kir2.1 channel (20). Multivalent blocking ions can occupy this site. For instance, the chicken Kir2.2 channel structure shows an Sr^{2+} ion in this position (D256) when the crystals were grown in the presence of Sr^{2+} (26). In our case, we identified one K^+ ion at this position, which suggests that conducting and blocking ions may compete for the same sites in the pore. The high concentration of KCl present in the buffer for cryo-EM analysis (150 mM) probably favors the occupation of this site.

4.5.2 Inherent local and large-amplitude motions of the human Kir2.1 channel structure may describe the mechanism of CTD tethering to TMD

It has been suggested that the PIP_2 binding displaces the CTD by approximately 6 Å in Kir2 and Kir3 channels: the CTD becomes tethered to the TMD, resulting in a compacted shape of the channel (from 120 to 114 Å longitudinally) (7, 27) (3SPI and 6XIT). However, some apo-Kir2.2 and apo-Kir3.2 crystal structures exhibited a compact conformation even in the absence of PIP_2 (17, 24) (3SYO and 5KUM). The 5th lowest frequency NM describes the extension/compression conformational motion of the human Kir2.1 channel (Fig. 6 and Video S1) and shows that the Kir2.1 longitudinal length can vary from 121 Å (extended form) to 113 Å (compact form) as the CTD moves closer to the TMD in the compact form of the channel (Fig. 6 and Video S1). These conformation states were also found on cryo-EM experimental data (Fig. S10). These findings demonstrate that extension/compression movement is a natural large-amplitude motion of the Kir2.1 channel and that its compact form can be achieved even in the absence of PIP_2 . In addition, the PIP_2 binding sites can be more accessible due to a swinging movement that results in a lateral opening at the interface between CTD and TMD described in modes 1 and 2 (Figs. 7 and S9 Videos S2 and S3). Interestingly, protein conformations presenting this lateral opening with various amplitudes were identified in our cryo-EM study (Fig. S11).

Using MD simulations, we then investigated the motions of residue K64, which is part of the secondary binding site (9, 24). We recovered its tethering motion to the membrane and demonstrated that R67, in a coupled local movement with K64, can penetrate the membrane (Figs. 8 and S12, Video S5). Note that the conformation of Kir2.1 remained in its extended form along the MD simulations. The movement of K219, also considered part of the secondary binding site (9) and pointed out to be PIP_2 -binding controller (2), toward the membrane is noticed during normal mode analysis (large movements, Fig. 6 and Video S1), but not in MD simulations.

Altogether, our observations support the intrinsic Kir2.1 compaction and an inherent opening

of the PIP₂ binding site in the absence of PIP₂. The former large conformational movement could possibly be initiated by the local movements of K64 and R67 residues into the membrane. Therefore, PIP₂ binding would not induce the compact conformation but would instead stabilize the compressed state.

4.5.3 Central role of the G-loop in the gating and mechanism for releasing the constriction point

Previous studies have supported a functional role of the G-loop region. For instance, endogenous miRNAs could physically bind to Kir2.1 at the G-loop, modulating cardiac electrophysiology (45). In addition, two residues in the G-loop, E303 (20) and C311 (46), are important for channel conductance and gating.

The crystal structure of the CTD domain of mouse Kir2.1 R218Q/T309K (2GIX) (30) indicated a possible role of two salt bridges, E303/R312 and R218/T309, for G-loop gating. MD simulations from Li et al. suggest that G-loop gating may be regulated by three pairs of weak electrostatic interactions (E303-H221, H221-R189, and E303-R312)(47).

Previous studies by Pegan *et al.* describe the G-loop as an intrinsically flexible region (20). Our structural comparison of the human and mouse Kir2.1 shows that the G-loop backbone exhibits a similar conformation in both structures. In addition, MD simulations indicate that the G-loop adopts a rigid structure in the closed conformation without PIP₂ (one of the lowest RMSF values, Fig. S13). Both mouse and human Kir2.1 structures exhibit a constriction point in the G-loop at residue A306. Although we showed that the G-loop is rigid in the absence of PIP₂, it must undergo a conformational change in order to release the constriction point and gate.

Here, we demonstrated by SPR experiments on Kir2.1 WT and its R312H mutation counterpart that residue R312 does not significantly alter the affinity of human Kir2.1 for PIP₂. Nonetheless, electrophysiological recordings clearly showed that the Kir2.1 R312H mutant channels could not open despite binding PIP₂. These data indicated that binding of PIP₂ to Kir2.1 alone is insufficient to induce channel opening, emphasizing the requirement for structural signal transmission of PIP₂-binding at gating.

Structural analysis of R312 in the human Kir2.1 cryo-EM structure shows that this residue is involved in a strong network of inter-subunit interactions (salt bridges and like-charged contact pairs) with residues H221 and E303 (on G-loop, close to the A306 constriction point), both on the adjacent chain. Our studies highlight the relevance of the structural integrity of E303-mediated salt bridges with R312 and H221 for proper G-loop gating. These findings support the previous work of S. Pegan *et al.* (27) and of J. Li *et al.* (45) with significant differences: i) where Li *et al.* found weak interactions (E303-H221 and E303-R312) on the Kir2.1 modeled structure, we found strong interactions. In addition, they observed the weak interaction H221-R189, which we have not identified because both side chains are far away in our cryo-EM structure (separation distance > 10 Å). ii) the R218/T309 salt bridge described in Pegan *et al.*'s work is not seen in our structure; because the distance between the two side chains in the human Kir2.1 channel cryo-EM structure is too large to allow any interaction (> 12 Å).

In conclusion, our human Kir2.1 channel cryo-EM structure describes a well-connected interaction network between the PIP₂-binding site residues, R218 and K219, and the G-loop region (E303) via residues R312 and H221. Our data suggest that the conformational changes

required for the G-loop opening are most likely controlled by PIP₂-binding. The replacement of R312 with histidine leads to a complete loss of the interaction network described above. Therefore, the interaction network integrity between subunits seems necessary for the proper allosteric transmission of the signal between R312 and the G-loop of the adjacent subunit upon PIP₂ binding, which possibly allows the release of the constriction point on the G-loop. We can then hypothesize a PIP₂-dependent G-loop gating mechanism that consists of the following: PIP₂ binding triggers local conformational changes in the position of the side and main chains of R218 and K219, which, due to the structural proximity, lead to significant changes in the position of H221, displacing it laterally toward the intracellular medium. This movement would, in turn, cause E303 and R312 of the adjacent chain to move in the same direction, causing the G-loop to open. This, of course, needs to be confirmed by detailed experiments. Finally, the results regarding R312H mutation indicate a direct involvement of an AS-causing mutation in the G-loop gating of the Kir2.1 channels.

4.6 MATERIALS AND METHODS

4.6.1 Protein expression

Protein expression was handled according to Hartmann et al. (48). Briefly, the synthetic KCNJ2 genes encoding residues 1 to 427 (the whole sequence Uniprot reference P63252) of human Kir2.1 WT and R312H mutant were cloned in a pPIC9K vector upstream of a sequence coding for a PreScission protease cleavage site (LEVLFQGP) followed by a linker of 11 amino acids and a 10His tag. The plasmids were introduced in *Pichia pastoris* strain SMD1163 (*his4*, *pep4*, *prb1*), and the resulting colonies were further analyzed *via* an *in situ* Yeastern blot immunoassay in order to identify the best expressing clones. For protein production, a freshly streaked colony was grown overnight in BMGY (1% (w/v) yeast extract, 2% (w/v) peptone, 1.34% (w/v) yeast nitrogen base without amino acids, 1% (w/v) glycerol, and 0.1 M phosphate buffer at pH 6.0) at 30 °C with shaking at 250 rpm until an OD₆₀₀ of 3–5. Expression of the recombinant Kir2.1 was induced with methanol by transferring yeast cells in a BMMY medium (1% (w/v) yeast extract, 2% (w/v) peptone, 1.34% (w/v) yeast nitrogen base without amino acids, 0.5% (v/v) methanol, and 0.1 M phosphate buffer at pH 6.0) and incubating them for about 20 h at 22 °C. Cells were harvested by centrifugation, washed in PBS buffer (pH 7.4), and stored at –80 °C until use.

4.6.2 Protein purification

To purify, the Kir2.1 WT and Kir2.1 R312H cells were resuspended in buffer A (50 mM Tris-HCl pH 7.4, 200 mM KCl, 1 mM EDTA, 1 mM PMSF) and protease inhibitor cocktail tablets (Roche and Merck). Cells were first incubated with 20U Zymolase 20T (Amsbio) per gram of pellet for 15 min at room temperature, then ruptured using a Constant System Cell Disruptor or, better, a FastPrep 24 (MP Biomedicals). Cell debris was removed by a 5 min centrifugation at 4,000×g, 4 °C. The supernatant was collected and centrifuged for 30 min at 100,000×g, 4 °C to collect crude membranes. The pellet was subsequently resuspended in buffer B (50 mM Tris-HCl pH 7.4 and 150 mM KCl), and the membrane proteins were solubilized by addition of 29.3 mM DDM (1.5% n-Dodecyl-D-maltoside, Glycon) for 30 min at room temperature with stirring, and then centrifuged for 30 min at 100,000×g at 4 °C. Supernatant was added to pre-equilibrated (50 mM Tris-HCl pH 7.4, 150 mM KCl, 30 mM imidazole, 0.03% DDM) 1 mL cobalt affinity resin (TALON, Clontech) at 4 °C incubated for 45 min. The protein was eluted

with an increasing concentration of imidazole. After the addition of 5 mM DTT, the eluted protein was concentrated on 100 kDa cutoff Vivaspin concentrator, filtered through 0.22 μM pore size PES membrane, and injected on a superdex-200 size exclusion chromatography column Increase 10/300 GL (Cytiva) pre-equilibrated with buffer C (20 mM Tris-HCl pH 7.4, 150 mM KCl, 0.03%/0.59 mM DDM, 1 mM EDTA) using the Äkta Purifier system (Cytiva). Fractions corresponding to the tetramer were pooled, added 2 mM DTT, and concentrated to reach about 0.7–1 mg/ml concentration

4.6.3 Surface plasmon resonance (SPR)

The interaction between Kir2.1 and the lipid PIP₂ was characterized by SPR on a Biacore™ 3000 instrument (Cytiva) controlled by Biacore 3000 Control Software v4.1. All biosensor experiments were performed in triplicate at 25 °C using the running buffer (20 mM Tris-HCl pH 7.5, 150 mM KCl, 0.05 mM EDTA, 0.05% DDM). In all experiments, a flow cell was left blank to be used as a reference for the sensorgrams. Kir2.1 (WT/R312H) was immobilized onto a carboxymethylated dextran (CM5) sensor chip. The activation of CM5 chips and immobilization of the protein steps were done using standard Biacore procedures (Flow: 10 $\mu\text{L}/\text{min}$, Contact time: 7 min, Protein concentration: 25–50 nM). Briefly, the CM5 chip was activated by amine coupling by injecting 0.2 M N-ethyl-N'-(3-dimethylaminopropyl) carbodiimide (EDC) and 0.05 M N-hydroxysuccinimide (NHS). For immobilization, the protein was diluted to 25–50 nM using sodium acetate pH 4.0–4.5, and saturation was achieved with 1 M ethanolamine HCl pH 8.5 (Cytiva).

The binding and kinetic assays were performed using single-cycle kinetics (SCK). PIP₂ was serially diluted in running buffer to working concentrations (0.15 to 20 μM). For each cycle, PIP₂ was injected at increasing concentration with a 5 $\mu\text{L}/\text{min}$ flow over both the reference cell and the ligand cell. Before the first PIP₂ injection, a running buffer was injected and used as a double reference. Each injection consisted of 300 s contact time with 300 s dissociation time. No regeneration step was done between injections, as these buffers were detrimental to Kir2.1. The data were analyzed using BIA evaluation Software 4.1, and kinetic parameters were determined using General Fit and the titration kinetics 1:1 binding with drift model. The association and dissociation rate constants, k_{on} and k_{off} , respectively, and the dissociation constant (K_{D}), were determined directly from the fitted curves.

4.6.4 Functional reconstitution of Kir2.1 WT and R312H mutant in lipid bilayer

Kir2.1 (WT and R312H) protein purified in DDM detergent (0.03%) was added to the upper chamber (150 μL) to a preformed bilayer. The Orbit mini apparatus was used (Nanion, Germany, horizontal planar lipid bilayer system), with two chambers separated by a partition with a 100 μm hole where the lipid bilayer is formed by 1,2-diphytanoyl-sn-glycero-3-phosphocholine (DPhPC, 10–30 pF). The upper and lower chambers contained 150 mM KCl, 10 mM MOPS, pH 7.4. Currents were recorded using Elements Data Reader (Nanion, Germany) and analyzed using Clampfit (Molecular Devices, CA, USA) software, sampled at 100 μs , and filtered at 1.25 kHz. The recording was performed at 24 °C using a Nanion temperature control unit.

4.6.5 Sample preparation and cryo-EM data collection

Negatively-stained electron microscopy showed good homogeneity and optimal distribution of a K⁺ channel molecule. After optimizing the cryo grid preparations, quantifoil (1.2/1.3) Cu 300 mesh grids with a thin carbon layer were glow discharged for 25 s prior to sample freezing. 3 μ L of Kir2.1 at 0.6 mg/ml concentration were placed on the grid, blotted for 3.0 s, and flash-frozen in liquid ethane using a Vitrobot Mark III (ThermoFisher) operated at 4 °C and 100% humidity. The EM data collection statistics are available in Table S2. A total of 9,895 micrographs were collected on a Titan Krios G3 microscope operated at 300 kV equipped with a K3 direct electron detectors and a bioquantum/K3 energy filter (Gatan Inc.). The automation of the data collection was done with the software EPU. Movies were recorded in electron-counting mode using exposures of 4 s dose-fractionated into 36 frames with a dose rate of 1.7139 electrons/ \AA^2 , resulting in a total dose of 61.7 electrons/ \AA^2 . A defocus range of -1.2 to -2.8 μ m was used. The pixel size was 0.86 \AA /pixel.

4.6.6 Cryo-EM data processing

After a visual inspection to remove poor quality micrographs (containing ice contamination, thick ice, low contrast, abnormal background), a total of 7,188 micrographs were selected for further cryo-EM data processing. The movies were motion-corrected and dose-weighted using MotionCor2 (49), and contrast function parameters (CTF) were estimated using CTFFIND4 (50). A total of 1,031,472 particles were automated picked using SPHIRE-crYOLO (51) and a trained network of about 2,000 particles. The image processing was then performed using RELION (52, 53). The extracted particles were binned 4 times and subject to one round of 2D classification. A total of 837,808 particles were extracted (no binned) from 45 2D-class averages and subjected to 3D Initial Model ab-initio construction using C4 symmetry. Then, the obtained 3D initial model was submitted to three rounds of 3D classification, the first two using C1 symmetry and the last one using C4 symmetry. The best class from the last round of 3D classification contained 63,584 particles. After the creation of mask to masking out the detergent layer, the map resulted from this class was refined using 3D Auto-Refine using C4 symmetry with decreasing values of initial angular sampling and local searches from auto-sampling, being the final map obtained using 1.8 and 0.5 degrees, respectively. The resolution of the final map is 4.3 \AA (gold-standard FSC= 0.143). This final map was subjected to handedness correction and B-factor map sharpening using the Auto-sharpen tool available in the PHENIX software suite (54). Fig. S2 shows the complete cryo-EM processing workflow. Cryo-EM data collection information is summarized in Table S2.

4.6.7 Model building and refinement

An initial *in silico* homology model of human Kir2.1 was generated using I-TASSER (55) and the crystal structure of the chicken Kir2.2 channel (3JYC) (26) as a template. For building and refinement of the atomic model, the TMD (55–184 region) of this *in silico* model was placed into the final sharpened cryo-EM map using the Dock in Map tool available in PHENIX (54). For the CTD (188–367 region), the crystal structure of the CTD from mouse Kir2.1 channel (1U4F) (20) was placed into the final cryo-EM map using the same approach. Once the models were placed in the cryo-EM density map, the loops that connect the two domains (185–187 region) and an N-terminal loop (41–54 region) absent in the *in silico* model were manually built using Coot (56). Visual inspection of the cryo-EM density map revealed that it was also possible to manually build a fraction of the N-terminal region that reaches the CTD (41–54 region).

After these manual builds, several iterative cycles of refinement using the `phenix.real_space_refine` in PHENIX with secondary structure restraints and manual adjustments in Coot provided the final cryo-EM model for the human Kir2.1 channel. Refinement statistics are summarized in Table S2. All figures were generated using Chimera, ChimeraX, PyMOL, and VMD software.

4.6.8 R312H mutation modeling

The R312H mutation was modeled on the human Kir2.1 channel cryo-EM structure by replacing the arginine residue with the most likely rotamer of histidine in the Chimera software. Next, local energy minimization was performed using Chimera (around 6.5 Å of the modeled histidine, keeping other protein atoms fixed) using 1,000 steepest descent steps (0.02 Å step size), 20 conjugate gradient steps (0.02 Å step size), and the AMBER ff14SB force field. After energy minimization, no clashes and bad contacts were observed between the modeled histidine and its vicinity.

4.6.9 Normal mode analysis

The first five internal lowest frequency modes of the entire Kir2.1 channel structure were obtained by carrying out all-atom NM calculations using a physical force field. The protein was first energy minimized in vacuum to a low energy gradient of 10^{-6} kcal \times mol \times Å⁻¹ by applying 10,000 conjugate gradient (CONJ) steps, followed by 100,000 adopted basis Newton-Raphson (ABNR) steps by using the CHARMM36m force field (57). Electrostatic interactions were calculated with a distance-dependent dielectric constant. The NMs were calculated using the DIMB diagonalization method (58) in CHARMM under the same force field parameters as those described previously for initial energy minimization.

Two outer structures were generated for each mode, one corresponding to a structural displacement of 3.0 Å RMSD along the mode with respect to the minimum energy structure and the other in the inverse direction with the same RMSD value. These outer structures were, in turn, energy minimized by applying an umbrella potential to maintain their positions along the modes. CHARMM's VMOD module was applied to generate these structures. In addition, intermediate structures between -3.0 Å and 3.0 Å RMSD were also generated by steps of 0.1 Å to make the video animations for each mode. The first six NMs were not taken into account as they are rigid-body overall modes (three rotations and three translations). Thus, the five NMs described here refer to modes 7–11, but they were renumbered from 1 to 5.

4.6.10 Molecular dynamics (MD) simulations

The structure of the human Kir2.1 channel was subjected to MD simulations using NAMD software (59) under the CHARMM36m force field. All preparation steps were performed using CHARMM-GUI server (60). The Kir2.1 channel was embedded in a lipid bilayer containing 176 POPC molecules, with a size of 80 Å in the x and y directions. The complete system has box dimensions of 106.8 \times 106.8 \times 165.1 Å and contains 44,276 molecules of water and 246 neutralizing ions. The KCl concentration was 0.15 M. The system was heated and equilibrated in the standard equilibration protocol suggested by CHARMM-GUI developers, gradually decreasing protein and membrane atomic positional restraints during a duration of 2 ns. Finally, the production run was performed without any positional restraints for 200 ns in triplicate. The

distances between the K64 and R67 residues to the plane of the phosphate groups from the inner membrane were calculated, with the inner membrane centered at $Z=0$.

Accession numbers: PDB 7ZDZ and EMD 14678

4.7 REFERENCES

1. H. Hibino, A. Inanobe, K. Furutani, S. Murakami, I. Findlay, Y. Kurachi, Inwardly Rectifying Potassium Channels: Their Structure, Function, and Physiological Roles. *Physiol. Rev.* **90**, 291–366 (2010).
2. O. Fürst, B. Mondou, N. D'Avanzo, Phosphoinositide regulation of inward rectifier potassium (Kir) channels. *Front. Physiol.* **4**, 404 (2014).
3. C. Nichols, A. Lopatin, Inward rectifier potassium channels. *Annu. Rev. Physiol.* **59**, 171–191 (1997).
4. V. A. Baronas, H. T. Kurata, Inward rectifiers and their regulation by endogenous polyamines. *Front. Physiol.* **5**, 325 (2014).
5. Z. Lu, Mechanism of rectification in inward-rectifier K^+ channels. *Annu. Rev. Physiol.* **66**, 103–129 (2004).
6. N. D'Avanzo, W. W. L. Cheng, D. A. Doyle, C. G. Nichols, Direct and Specific Activation of Human Inward Rectifier K^+ Channels by Membrane Phosphatidylinositol 4,5-Bisphosphate. *J. Biol. Chem.* **285**, 37129–37132 (2010).
7. S. B. Hansen, X. Tao, R. MacKinnon, Structural basis of PIP2 activation of the classical inward rectifier K^+ channel Kir2.2. *Nature.* **477**, 495–U152 (2011).
8. W. W. L. Cheng, N. D'Avanzo, D. A. Doyle, C. G. Nichols, Dual-mode phospholipid regulation of human inward rectifying potassium channels. *Biophys. J.* **100**, 620–628 (2011).
9. S.-J. Lee, S. Wang, W. Borschel, S. Heyman, J. Gyore, C. G. Nichols, Secondary anionic phospholipid binding site and gating mechanism in Kir2.1 inward rectifier channels. *Nat. Commun.* **4**, 2786 (2013).
10. T. Rohacs, C. M. B. Lopes, T. H. Jin, P. P. Ramdya, Z. Molnar, D. E. Logothetis, Specificity of activation by phosphoinositides determines lipid regulation of Kir channels. *Proc. Natl. Acad. Sci. U. S. A.* **100**, 745–750 (2003).
11. N. M. Plaster, R. Tawil, M. Tristani-Firouzi, S. Canun, S. Bendahhou, A. Tsunoda, M. R. Donaldson, S. T. Iannaccone, E. Brunt, R. Barohn, J. Clark, F. Deymeer, A. L. George Jr., F. A. Fish, A. Hahn, A. Nitu, C. Ozdemir, P. Serdaroglu, S. H. Subramony, G. Wolfe, Y. H. Fu, L. J. Ptacek, Mutations in Kir2.1 cause the developmental and episodic electrical phenotypes of Andersen's syndrome. *Cell.* **105**, 511–9 (2001).
12. O. B. Clarke, A. Caputo, A. P. Hills, J. I. Vandenberg, B. J. Smith, J. M. Gulbis, Domain reorientation and rotation of an intracellular assembly regulate conduction in Kir Potassium Channels. *Cell.* **141**, 1018–1029 (2010).
13. M. Xia, Q. F. Jin, S. Bendahhou, Y. S. He, M. M. Larroque, Y. P. Chen, Q. S. Zhou, Y. Q. Yang, Y. Liu, B. Liu, Q. Zhu, Y. T. Zhou, J. Lin, B. Liang, L. Li, X. J. Dong, Z. W. Pan, R. G. Wang, H. Y. Wan, W. Q. Qiu, W. Y. Xu, P. Eurlings, J. Barhanin, Y. H. Chen, A Kir2.1 gain-of-function mutation underlies familial atrial fibrillation. *Biochem. Biophys. Res. Commun.* **332**, 1012–1019 (2005).
14. S. G. Priori, S. V. Pandit, I. Rivolta, O. Berenfeld, E. Ronchetti, A. Dhamoon, C. Napolitano, J. Anumonwo, M. R. di Barletta, S. Gudapakkam, G. Bosi, M. S. Badiale, J. Jalife, A novel form of short QT syndrome (SQT3) is caused by a mutation in the KCNJ2 gene. *Circ. Res.* **96**, 800–807 (2005).
15. D. J. Tester, P. Arya, M. Will, C. M. Haglund, A. L. Farley, J. C. Makielski, M. J. Ackerman, Genotypic heterogeneity and phenotypic mimicry among unrelated patients referred for catecholaminergic polymorphic ventricular tachycardia genetic testing. *Heart Rhythm.* **3**, 800–805 (2006).
16. E. D. Andersen, P. A. Krasilnikoff, H. Overvad, Intermittent muscular weakness, extrasystoles, and multiple developmental anomalies. A new syndrome? *Acta Paediatr Scand.* **60**, 559–64 (1971).
17. M. R. Whorton, R. MacKinnon, Crystal Structure of the Mammalian GIRK2 $K(+)$ Channel and Gating Regulation by G Proteins, PIP(2), and Sodium. *Cell.* **147**, 199–208 (2011).
18. M. R. Whorton, R. MacKinnon, X-ray structure of the mammalian GIRK2-beta gamma G-protein complex. *Nature.* **498**, 190–+ (2013).
19. M. Nishida, M. Cadene, B. Chait, R. Mackinnon, Crystals structure of a Kir3.1-prokaryotic Kir channel chimera. *Embo J.* **26**, 4005–4015 (2007).
20. S. Pegan, C. Arrabit, W. Zhou, W. Kwiatkowski, A. Collins, P. Slesinger, S. Choe, Cytoplasmic domain structures of Kir2.1 and Kir3.1 show sites for modulating gating and rectification. *Nat. Neurosci.* **8**, 279–287 (2005).

21. S. Sacconi, D. Simkin, N. Arrighi, F. Chapon, M. M. Larroque, S. Vicart, D. Sternberg, B. Fontaine, J. Barhanin, C. Desnuelle, S. Bendahhou, Mechanisms underlying Andersen's syndrome pathology in skeletal muscle are revealed in human myotubes. *Am. J. Physiol. Cell Physiol.* **297**, C876-85 (2009).
22. C. M. B. Lopes, H. Zhang, T. Rohacs, T. Jin, J. Yang, D. E. Logothetis, Alterations in conserved Kir channel-PIP2 interactions underlie channelopathies. *Neuron*. **34**, 933-944 (2002).
23. N. D'Avanzo, S.-J. Lee, W. W. L. Cheng, C. G. Nichols, Energetics and location of phosphoinositide binding in human Kir2.1 channels. *J. Biol. Chem.* **288**, 16726-16737 (2013).
24. S.-J. Lee, F. Ren, E.-M. Zangerl-Plessl, S. Heyman, A. Stary-Weinzinger, P. Yuan, C. G. Nichols, Structural basis of control of inward rectifier Kir2 channel gating by bulk anionic phospholipids. *J. Gen. Physiol.* **148**, 227-237 (2016).
25. H.-L. An, S.-Q. Lü, J.-W. Li, X.-Y. Meng, Y. Zhan, M. Cui, M. Long, H.-L. Zhang, D. E. Logothetis, The cytosolic GH loop regulates the phosphatidylinositol 4,5-bisphosphate-induced gating kinetics of Kir2 channels. *J. Biol. Chem.* **287**, 42278-42287 (2012).
26. X. Tao, J. L. Avalos, J. Y. Chen, R. MacKinnon, Crystal Structure of the Eukaryotic Strong Inward-Rectifier K⁺ Channel Kir2.2 at 3.1 angstrom Resolution. *Science*. **326**, 1668-1674 (2009).
27. Y. Niu, X. Tao, K. K. Touhara, R. MacKinnon, Cryo-EM analysis of PIP2 regulation in mammalian GIRK channels. *eLife*. **9**, e60552 (2020).
28. V. N. Bavro, R. De Zorzi, M. R. Schmidt, J. R. C. Muniz, L. Zubcevic, M. S. P. Sansom, C. Vénien-Bryan, S. J. Tucker, Structure of a KirBac potassium channel with an open bundle crossing indicates a mechanism of channel gating. *Nat. Struct. Mol. Biol.* **19**, 158-163 (2012).
29. H. Matsuda, A. Saigusa, H. Irisawa, Ohmic Conductance through the Inwardly Rectifying K-Channel and Blocking by Internal Mg-2+. *Nature*. **325**, 156-159 (1987).
30. S. Pegan, C. Arrabit, P. A. Slesinger, S. Choe, Andersen's syndrome mutation effects on the structure and assembly of the cytoplasmic domains of Kir2.1. *Biochemistry*. **45**, 8599-8606 (2006).
31. O. S. Smart, J. G. Neduvellil, X. Wang, B. A. Wallace, M. S. P. Sansom, HOLE: A program for the analysis of the pore dimensions of ion channel structural models. *J. Mol. Graph. Model.* **14**, 354- (1996).
32. C. Fagnen, L. Bannwarth, I. Oubella, E. Forest, R. De Zorzi, A. de Araujo, Y. Mhoumadi, S. Bendahhou, D. Perahia, C. Vénien-Bryan, New Structural insights into Kir channel gating from molecular simulations, HDX-MS and functional studies. *Sci. Rep.* **10**, 8392 (2020).
33. J. Heyda, P. E. Mason, P. Jungwirth, Attractive interactions between side chains of histidine-histidine and histidine-arginine-based cationic dipeptides in water. *J. Phys. Chem. B.* **114**, 8744-8749 (2010).
34. O. Fuerst, C. G. Nichols, G. Lamoureux, N. D'Avanzo, Identification of a Cholesterol-Binding Pocket in Inward Rectifier K⁺ (Kir) Channels. *Biophys. J.* **107**, 2786-2796 (2014).
35. E.-M. Zangerl-Plessl, S.-J. Lee, G. Maksaev, H. Bernsteiner, F. Ren, P. Yuan, A. Stary-Weinzinger, C. G. Nichols, Atomistic basis of opening and conduction in mammalian inward rectifier potassium (Kir2.2) channels. *J. Gen. Physiol.* **152** (2020), doi:10.1085/jgp.201912422.
36. L. Mouawad, D. Perahia, Motions in hemoglobin studied by normal mode analysis and energy minimization: Evidence for the existence of tertiary T-like, quaternary R-like intermediate structures. *J. Mol. Biol.* **258**, 393-410 (1996).
37. I. Bahar, T. R. Lezon, L.-W. Yang, E. Eyal, Global dynamics of proteins: bridging between structure and function. *Annu. Rev. Biophys.* **39**, 23-42 (2010).
38. B. T. Kaynak, J. M. Krieger, B. Dudas, Z. L. Dahmani, M. G. S. Costa, E. Balog, A. L. Scott, P. Doruker, D. Perahia, I. Bahar, Sampling of Protein Conformational Space Using Hybrid Simulations: A Critical Assessment of Recent Methods. *Front. Mol. Biosci.* **9**, 832847 (2022).
39. S. H. W. Scheres, Processing of Structurally Heterogeneous Cryo-EM Data in RELION. *Methods Enzymol.* **579**, 125-157 (2016).
40. Z. Lu, R. MacKinnon, Electrostatic tuning of Mg²⁺ affinity in an inward-rectifier K⁺ channel. *Nature*. **371**, 243-246 (1994).
41. Y. Kubo, Y. Murata, Control of rectification and permeation by two distinct sites after the second transmembrane region in Kir2.1 K⁺ channel. *J. Physiol.* **531**, 645-660 (2001).
42. Y. Fujiwara, Y. Kubo, Functional roles of charged amino acid residues on the wall of the cytoplasmic pore of Kir2.1. *J. Gen. Physiol.* **127**, 401-419 (2006).
43. N. Uchimura, E. Cherubini, R. North, Inward Rectification in rat nucleus accumbens neurons. *J. Neurophysiol.* **62**, 1280-1286 (1989).
44. H. Moldenhauer, I. Díaz-Franulic, F. González-Nilo, D. Naranjo, Effective pore size and radius of capture for K(+) ions in K-channels. *Sci. Rep.* **6**, 19893 (2016).
45. D. Yang, X. Wan, A. T. Dennis, E. Bektik, Z. Wang, M. G. Costa, C. Fagnen, C. Venien-Bryan, X. Xu, T. J. Hund, P. J. Mohler, K. R. Laurita, I. Deschenes, J.-D. Fu, MicroRNA Biophysically Modulates Cardiac Physiology via Directly Binding to Ion Channel. *CIRCULATION*. **142** (2020).

46. L. Garneau, H. Klein, L. Parent, R. Sauvé, Contribution of cytosolic cysteine residues to the gating properties of the Kir2.1 inward rectifier. *Biophys. J.* **84**, 3717–3729 (2003).
47. J. Li, S. Xiao, X. Xie, H. Zhou, C. Pang, S. Li, H. Zhang, D. E. Logothetis, Y. Zhan, H. An, Three pairs of weak interactions precisely regulate the G-loop gate of Kir2.1 channel. *Proteins.* **84**, 1929–1937 (2016).
48. L. Hartmann, V. Kugler, R. Wagner, in *Heterologous Expression of Membrane Proteins: Methods and Protocols, 2nd Edition*, I. MusVeteau, Ed. (Humana Press Inc, Totowa, 2016; <https://www.webofscience.com/wos/woscc/summary/d2fa6128-1783-46fe-bf75-ff2c82819c51-2dfd5b3c/relevance/1>), vol. 1432, pp. 143–162.
49. S. Q. Zheng, E. Palovcak, J.-P. Armache, K. A. Verba, Y. Cheng, D. A. Agard, MotionCor2: anisotropic correction of beam-induced motion for improved cryo-electron microscopy. *Nat. Methods.* **14**, 331–332 (2017).
50. A. Rohou, N. Grigorieff, CTFFIND4: Fast and accurate defocus estimation from electron micrographs. *J. Struct. Biol.* **192**, 216–221 (2015).
51. T. Wagner, F. Merino, M. Stabrin, T. Moriya, C. Antoni, A. Apelbaum, P. Hagel, O. Sitsel, T. Raisch, D. Prumbaum, D. Quentin, D. Roderer, S. Tacke, B. Siebolds, E. Schubert, T. R. Shaikh, P. Lill, C. Gatsogiannis, S. Raunser, SPHIRE-crYOLO is a fast and accurate fully automated particle picker for cryo-EM. *Commun. Biol.* **2**, 218 (2019).
52. S. H. W. Scheres, RELION: implementation of a Bayesian approach to cryo-EM structure determination. *J. Struct. Biol.* **180**, 519–530 (2012).
53. J. Zivanov, T. Nakane, B. O. Forsberg, D. Kimanius, W. J. Hagen, E. Lindahl, S. H. Scheres, New tools for automated high-resolution cryo-EM structure determination in RELION-3. *eLife.* **7**, e42166 (2018).
54. D. Lieschner, P. V. Afonine, M. L. Baker, G. Bunkoczi, V. B. Chen, T. I. Croll, B. Hintze, L.-W. Hung, S. Jain, A. J. McCoy, N. W. Moriarty, R. D. Oeffner, B. K. Poon, M. G. Prisant, R. J. Read, J. S. Richardson, D. C. Richardson, M. D. Sammito, O. V. Sobolev, D. H. Stockwell, T. C. Terwilliger, A. G. Urzhumtsev, L. L. Videau, C. J. Williams, P. D. Adams, Macromolecular structure determination using X-rays, neutrons and electrons: recent developments in Phenix. *Acta Crystallogr. Sect. -Struct. Biol.* **75**, 861–877 (2019).
55. J. Yang, R. Yan, A. Roy, D. Xu, J. Poisson, Y. Zhang, The I-TASSER Suite: protein structure and function prediction. *Nat. Methods.* **12**, 7–8 (2015).
56. P. Emsley, B. Lohkamp, W. G. Scott, K. Cowtan, Features and development of Coot. *Acta Crystallogr. Sect. -Biol. Crystallogr.* **66**, 486–501 (2010).
57. J. Huang, A. D. MacKerell Jr., CHARMM36 all-atom additive protein force field: Validation based on comparison to NMR data. *J. Comput. Chem.* **34**, 2135–2145 (2013).
58. D. Perahia, L. Mouawad, Computation of low-frequency normal modes in macromolecules: improvements to the method of diagonalization in a mixed basis and application to hemoglobin. *Comput. Chem.* **19**, 241–246 (1995).
59. J. Phillips, R. Braun, W. Wang, J. Gumbart, E. Tajkhorshid, E. Villa, C. Chipot, R. Skeel, L. Kale, K. Schulten, Scalable molecular dynamics with NAMD. *J. Comput. Chem.* **26**, 1781–1802 (2005).
60. S. Jo, T. Kim, V. G. Iyer, W. Im, Software news and updates - CHARNIM-GUI: A web-based graphical user interface for CHARMM. *J. Comput. Chem.* **29**, 1859–1865 (2008).

Acknowledgments

We thank Dr J-M Guigner for initial EM images, Dr MGS Costa for discussions and Dr M Dezi for preliminary work (IMPMC). Instruct-ERIC facility at IGBMC Strasbourg, France and Dr B Klaholz; Nanoimaging core facility (C2RT) at Institut Pasteur and the help of J-M Winter, and Dr M Vos. Core-facility molecular interactions (IBPS) at Sorbonne University and T. Bouceba.

Funding: AFM-Téléthon #23207 for SB and CVB, AFM-Téléthon #23210 for CAHF, Ecole Doctorale ED515 Sorbonne Université for DZ and CF, EQUIPEX CACSICE ANR-11-EQPX-0008 (CVB and Dr M. Nilges). The project received funding from the European Union’s Horizon Europe Research and Innovation Program under agreement N° 101026386.

Author contributions:

Conceptualization CVB, SB, DP

Project coordination: CVB

Protein expression and purification: DZ, RW, VK, CVB

Surface plasmon resonance: DZ

Cryo-EM sample preparation and data collection: DZ, GPA, CVB

Cryo-EM image analysis and structure determination: CAHF, CF, CVB

Computational investigations: CAHF, DP

Electrophysiology: RS, SB

Writing—original draft: CAHF, DZ, CVB,

Writing—review & editing: CAHF, DZ, CF, RW, DP, SB, CVB

Funding acquisition: CVB, SB, CAHF

Data and materials availability:

All data needed to evaluate the conclusions in the paper are present in the paper and the Supplementary Materials. Cryo-EM density maps and coordinates of human Kir2.1 cryo-EM structure have been deposited in the EMDB with ID code EMD-14678 and RCSB PDB with ID code 7ZDZ.

Competing interests

The authors declare that no competing interest exists.

Supplementary materials include Figs. S1 to S13, Tables S1 to S2, and Videos S1 to S6

4.8 FIGURES

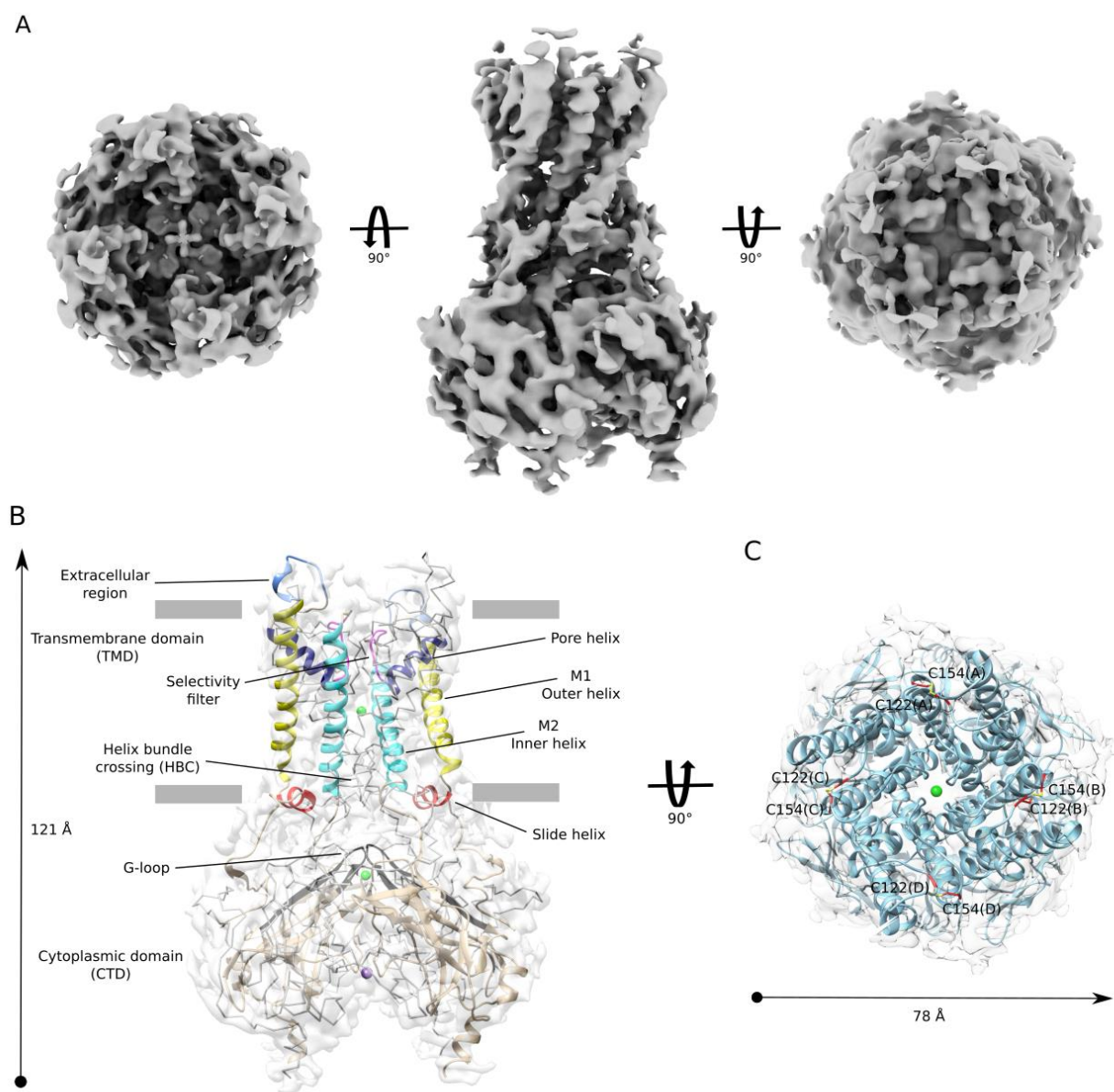


Fig. 1 Cryo-EM map and atomic structure of the human Kir2.1 channel. (A) Sharpened cryo-EM map of human Kir2.1 obtained at 4.3 Å resolution (bottom, side, and top views). (B) Side view of human Kir2.1 atomic structure fitted in the cryo-EM map (white surface). The chains A and C are in cartoon and highlight the typical structural features of Kir channels: Outer helix (M1, yellow), inner helix (M2, cyan), pore helix (dark blue), slide helix (red), selectivity filter (magenta), extracellular region (light blue), G-loop (black) and helix bundle crossing (HBC) region. The Sr^{2+} (green) and K^{+} (purple) ions inside the pore channel are represented as spheres. Chains B and D are in gray ribbons for clarity. Gray horizontal bars indicate the plasma membrane. The TMD and CTD are indicated. (C) Top view of the human Kir2.1 atomic structure fitted in the cryo-EM map. The four chains (A, B, C, and D) are in a blue cartoon. The cysteine residues (C122 and C154) involved in the intra-subunit disulfide bridge are highlighted as red sticks. Protein dimensions are shown.

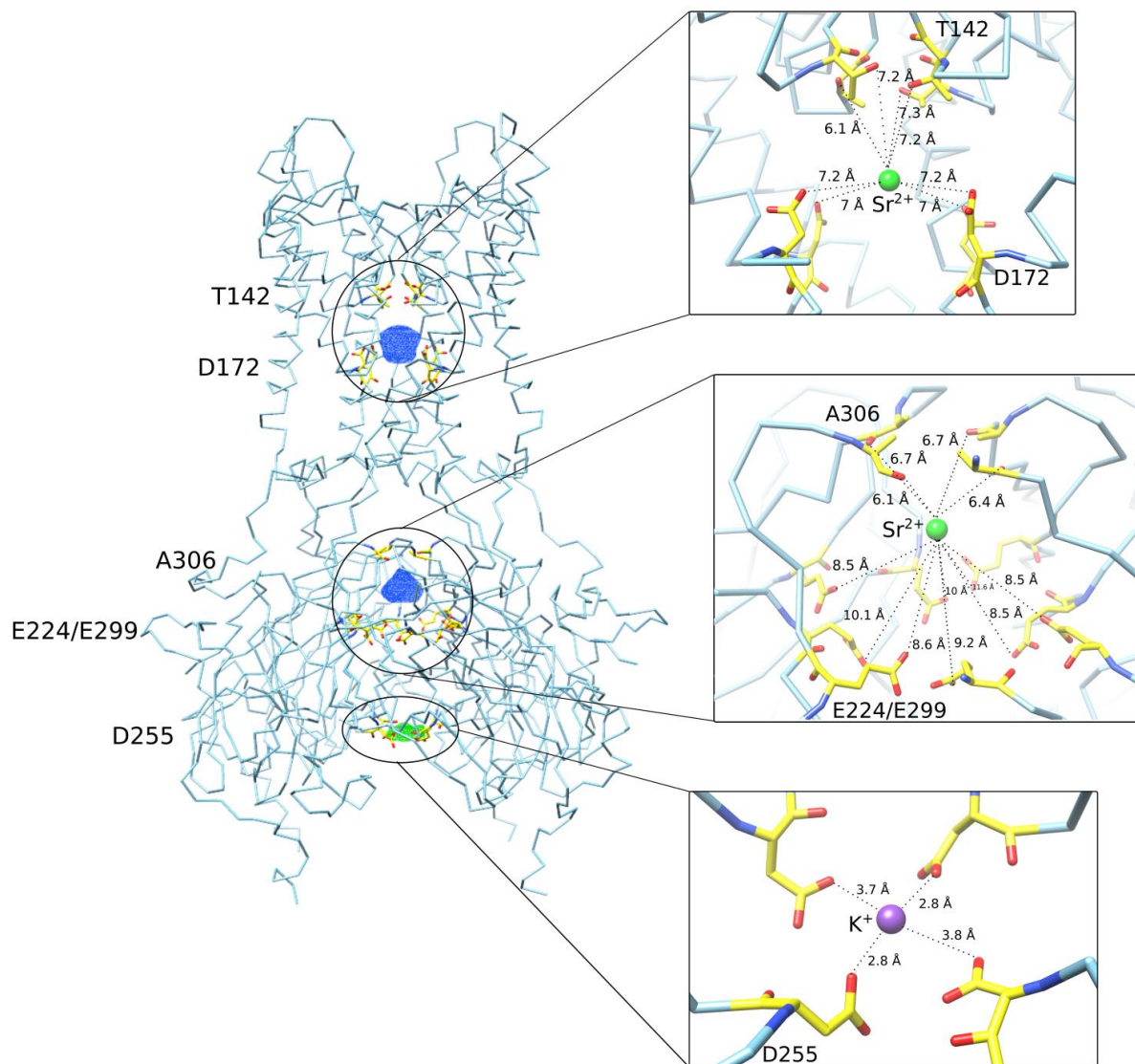


Fig. 2 Ions' location along the pore in the human Kir2.1 channel cryo-EM structure. Cryo-EM densities modeled as Sr²⁺ (blue mesh at 5 σ) and K⁺ (green mesh at 2.5 σ) ions inside the pore of human Kir2.1 cryo-EM atomic structure (blue ribbon). Insets: detailed views of the regions where the ions are located. The distances between these ions and the negatively charged atoms of the closest residues (yellow sticks) inside the pore channel are indicated.

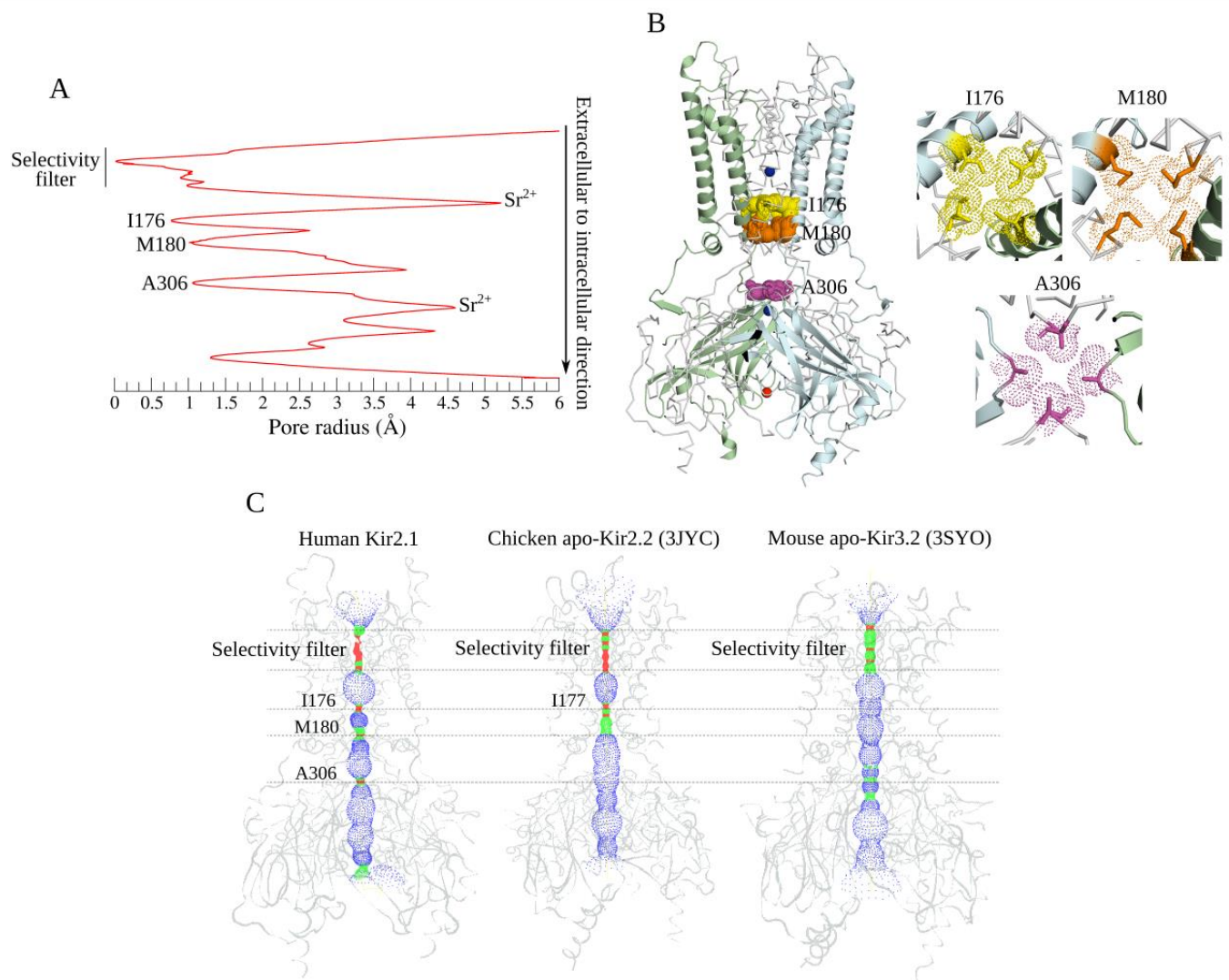


Fig. 3 Pore radius analysis of human Kir2.1 channel structure and constriction points. (A) Plot of the pore radius between van der Waals surfaces. The constriction points (selectivity filter, I176, M180, and A306) and the position of the two Sr^{2+} ions are highlighted. (B) Three constriction points below the selectivity filter: I176 (yellow sphere), M180 (orange sphere), and A306 (purple sphere). Chains A and C are in light blue and green cartoons, respectively. Chains B and D are in gray ribbons for clarity. Sr^{2+} (blue) and K^+ (red) ions are represented as spheres. The insets show the zoom of the three constriction points, where the spheres represent the van der Waals surfaces. (C) Comparative analysis of pore radius (stippled surface) between van der Waals surfaces among human Kir2.1, chicken Kir2.2, and mouse Kir3.2 channel structures (light gray ribbons). Along the central ion conduction, red: insufficient space for a water molecule, green: one or two water molecules could fit, and blue: many water molecules could fit. Constriction points were considered where the red volume was visualized. Horizontal dashes were placed to compare the constriction points in human Kir2.1, apo-Kir2.2, and apo-Kir3.2 pore channels. Molecular graphics images were prepared with VMD. Pore radius was analyzed using the HOLE software.

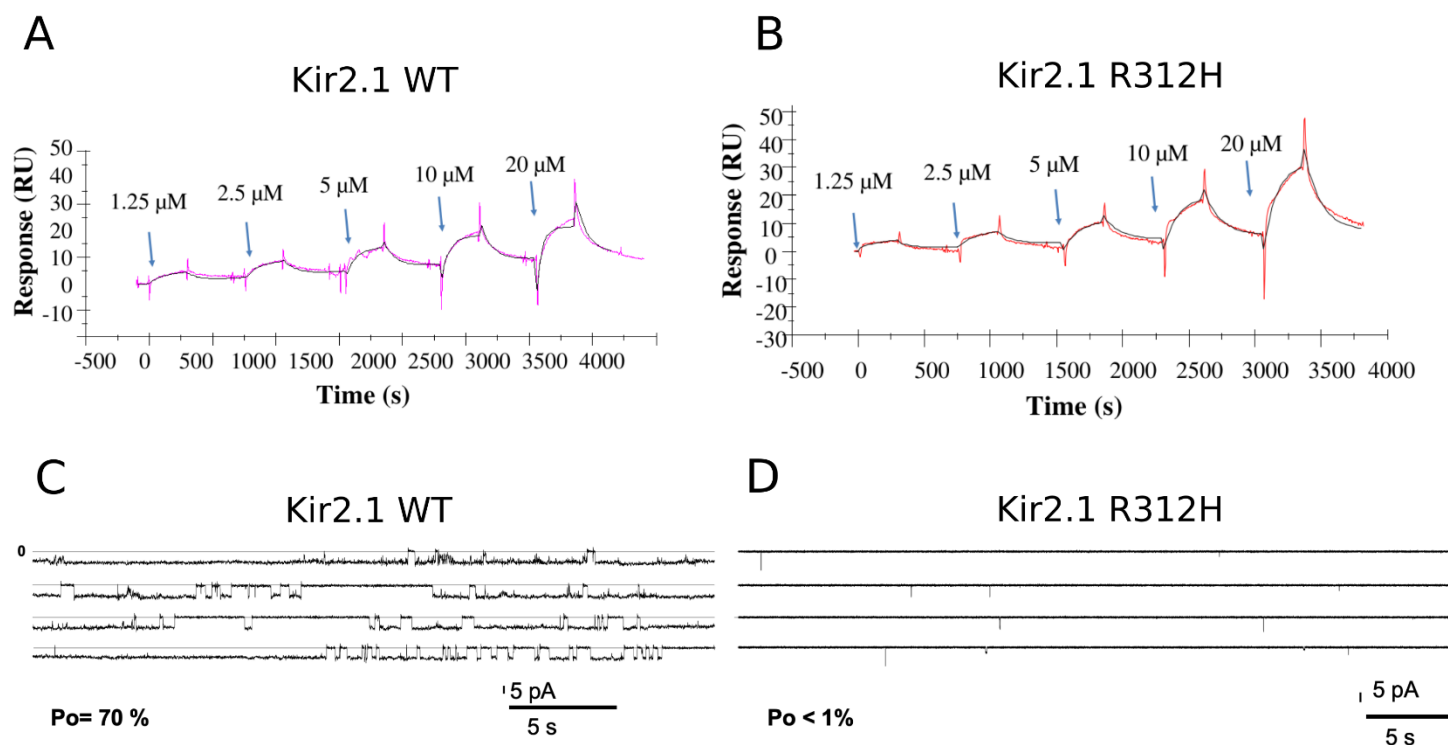


Fig. 4 Biophysical and functional assays on Kir2.1 WT and R312H mutant. (A-B) Comparative binding kinetics of PIP₂ on Kir2.1 WT (A) and R312H mutant (B) immobilized on a CM5 chip. Five sequential injections of PIP₂ are shown, 1.25–20 μ M, at 25 μ L/5min. In color, experimental data; in black, fitted curve. The single-cycle kinetics assays were carried out in triplicate; only one replica is shown. The SPR response is expressed in response units (RU) relative to the time in seconds. (C-D) Electrophysiological recordings of Kir2.1 WT (C) and R312H (D) reconstituted in lipid bilayers in the presence of 1% PIP₂ at -100 mV. Kir2.1 WT shows an open probability (Po) of 70%, and Kir2.1 R312H has a Po of less than 1%.

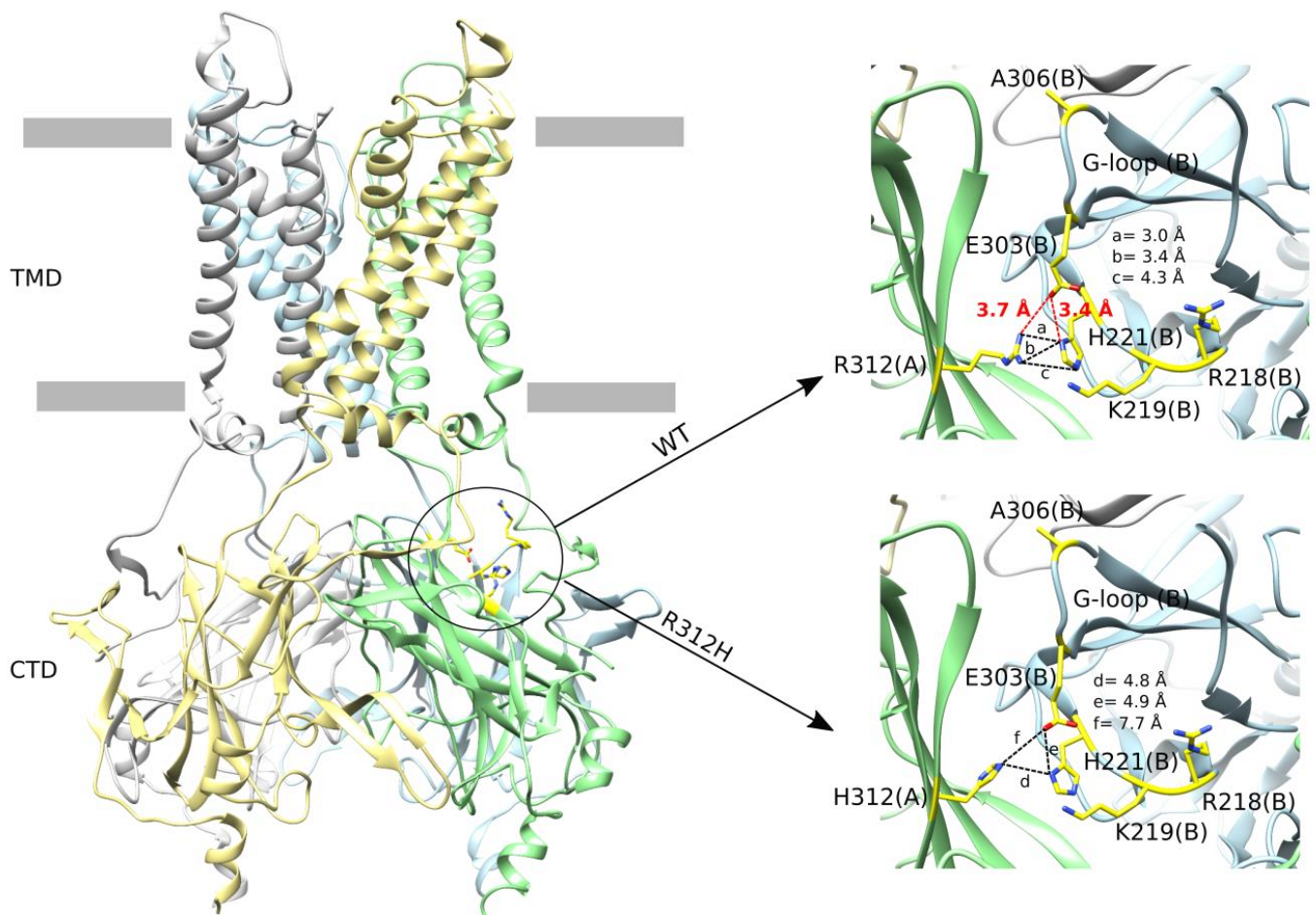


Fig. 5 Interaction network between R312, H221, and E303 residues in the human Kir2.1 channel cryo-EM structure. Cartoon representation of the human Kir2.1 channel cryo-EM structure highlighting (inside the circle) the location of the R312 residue. The insets show the intersubunit interaction network of R312 in the WT (top) and that of H312 in the R312H mutant (bottom) between chains A and B. The chains A, B, C, and D are shown in green, blue, gray, and yellow, respectively. Residues R218, K219, H221, E303, and A306 are represented as yellow sticks. The chains are indicated in parenthesis. Salt bridge distances are highlighted in red dashes and the other distances in black dashes.

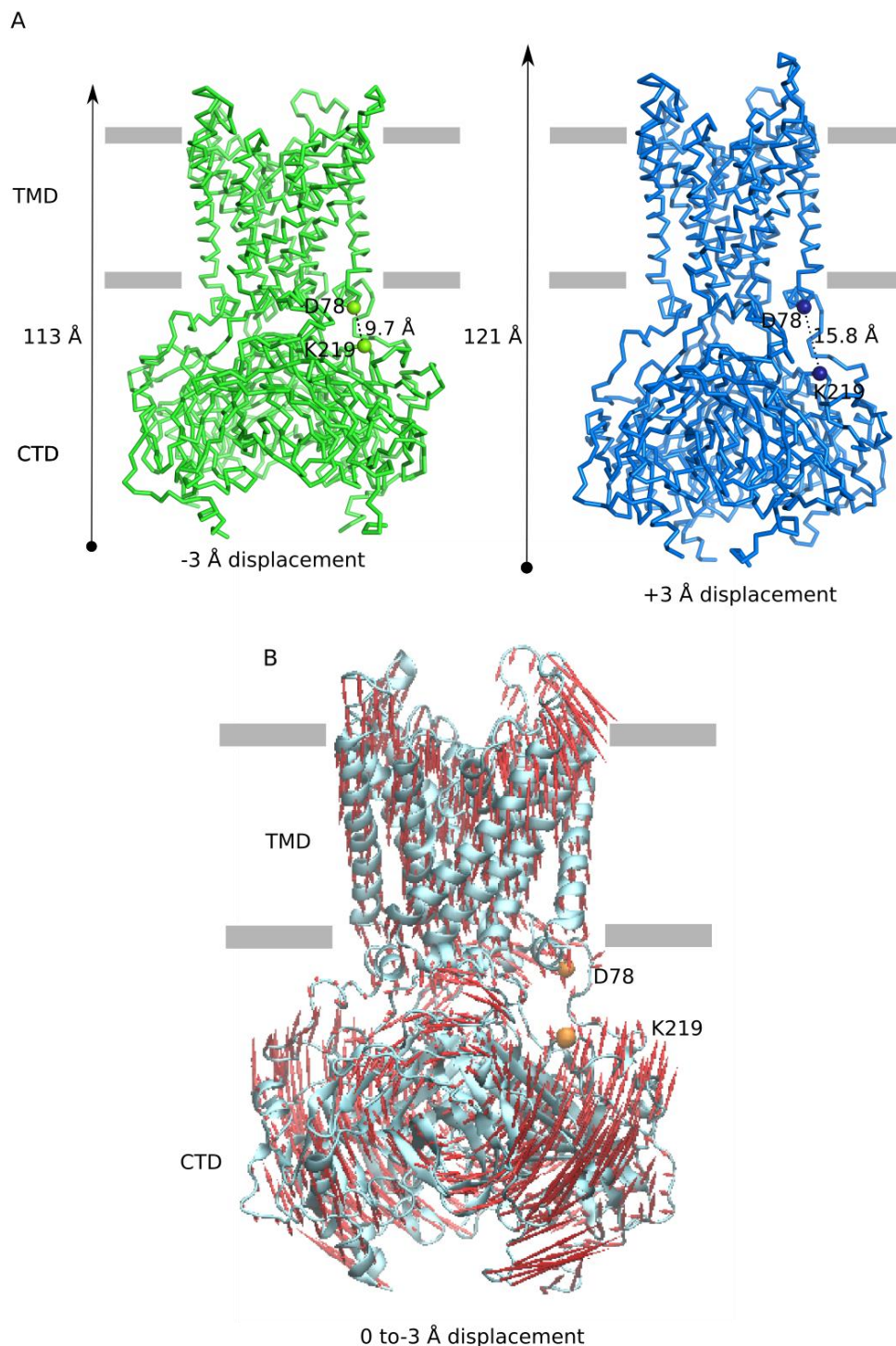


Fig. 6 Description of extension/compression conformational movement of the human Kir2.1 channel using normal mode analysis. (A) Ribbon representation of the human Kir2.1 cryo-EM structure after displacement of -3 \AA (green; compacted structure) and $+3 \text{ \AA}$ (blue; expanded structure) along mode 5. The longitudinal length and the $C\alpha$ - $C\alpha$ distance between residues D78 and K219 (represented by spheres) are indicated in \AA . (B) Description of the compression movement on the cartoon representation of the human Kir2.1 structure (cyan). Red arrows show $C\alpha$ displacement from the reference structure toward the -3 \AA compacted structure along the mode 5. Orange spheres represent D78 and K219. Gray horizontal bars indicate plasma membrane boundaries.

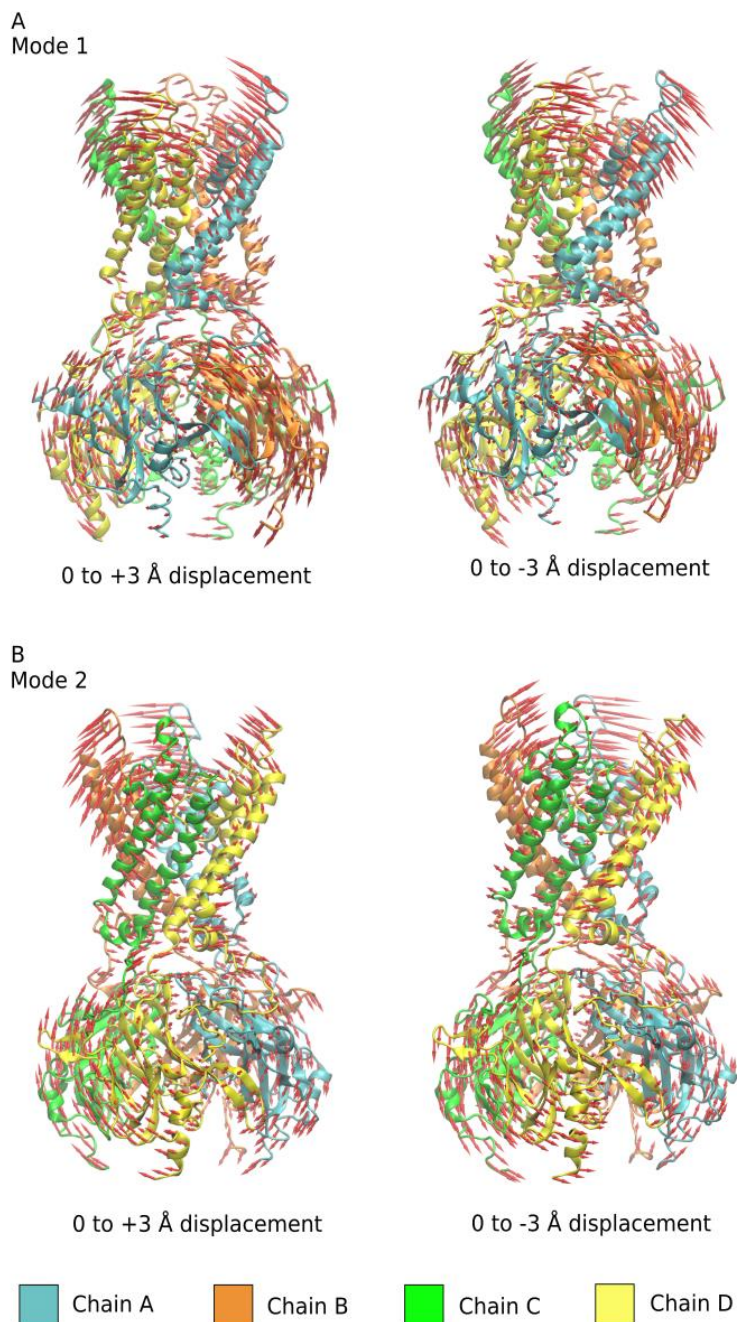


Fig. 7 Description of the opening of the PIP₂ binding site of the human Kir2.1 channel using normal mode analysis. (A-B) Description of the conformational movement on the cartoon representation of the human Kir2.1 structure. Chains A, B, C, and D in cyan, orange, green and yellow, respectively. Red arrows show C α displacement from the reference structure toward the displacement of +3 Å and -3 Å along the modes 1 (A) and 2 (B).

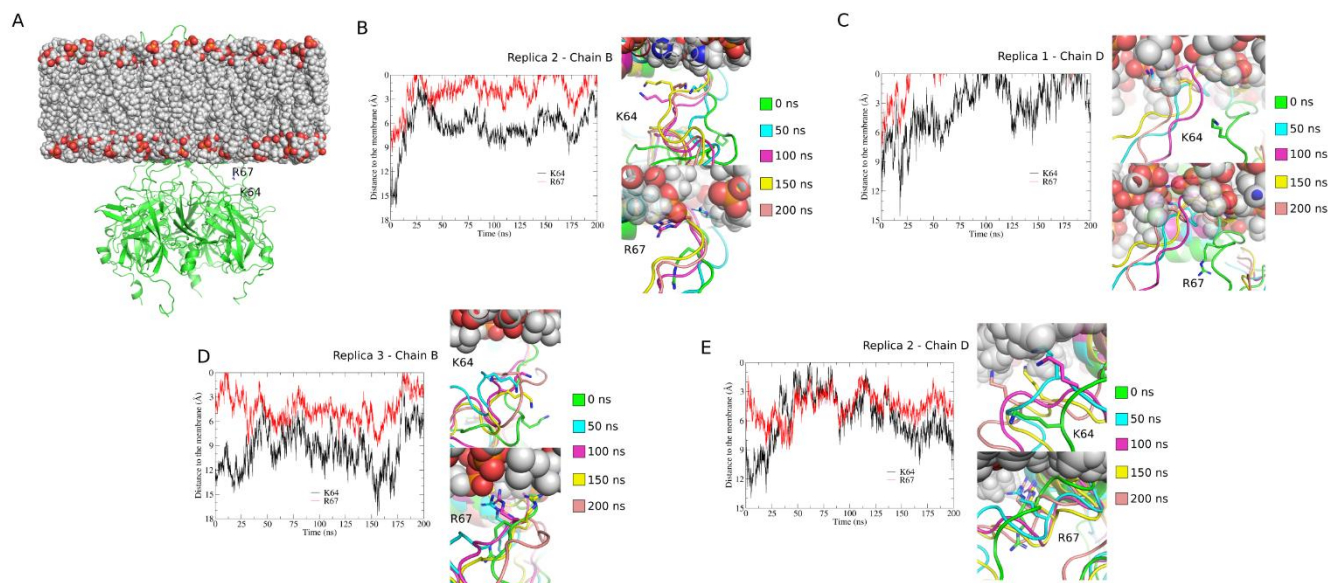


Fig. 8 Tethering of K64 and R67 to the membrane displayed in molecular dynamics simulations. (A) Human Kir2.1 cryo-EM structure and membrane (POPC bilayer) system used in MD simulations. The Kir2.1 channel structure is represented in a green cartoon, and the residues K64 and R67 of chain B are highlighted. (B-E) show the trajectories analysis of the K64 and R67 residues along the 200 ns of MD simulations in some representative chains of the three replicates. In each of these panels, snapshots along MD simulations are shown: 0 ns (green), 50 ns (cyan), 100 ns (magenta), 150 ns (yellow), and 200 ns (salmon). K64 and R67 residues are highlighted in sticks. (B-E) show the distances between the K64 and R67 residues to the plane of the phosphate groups from the inner membrane. To calculate these distances, the inner membrane was centered at $Z=0$. The 0 value represents the membrane level. (B) Chain B, replica 2. (C) Chain D, replica 1. (D) Chain B, replica 3. (E) Chain D, replica 2.

4.9 SUPPLEMENTARY MATERIALS

This PDF file includes:

Figs. S1 to S13

Tables S1 to S2

Videos S1 to S6

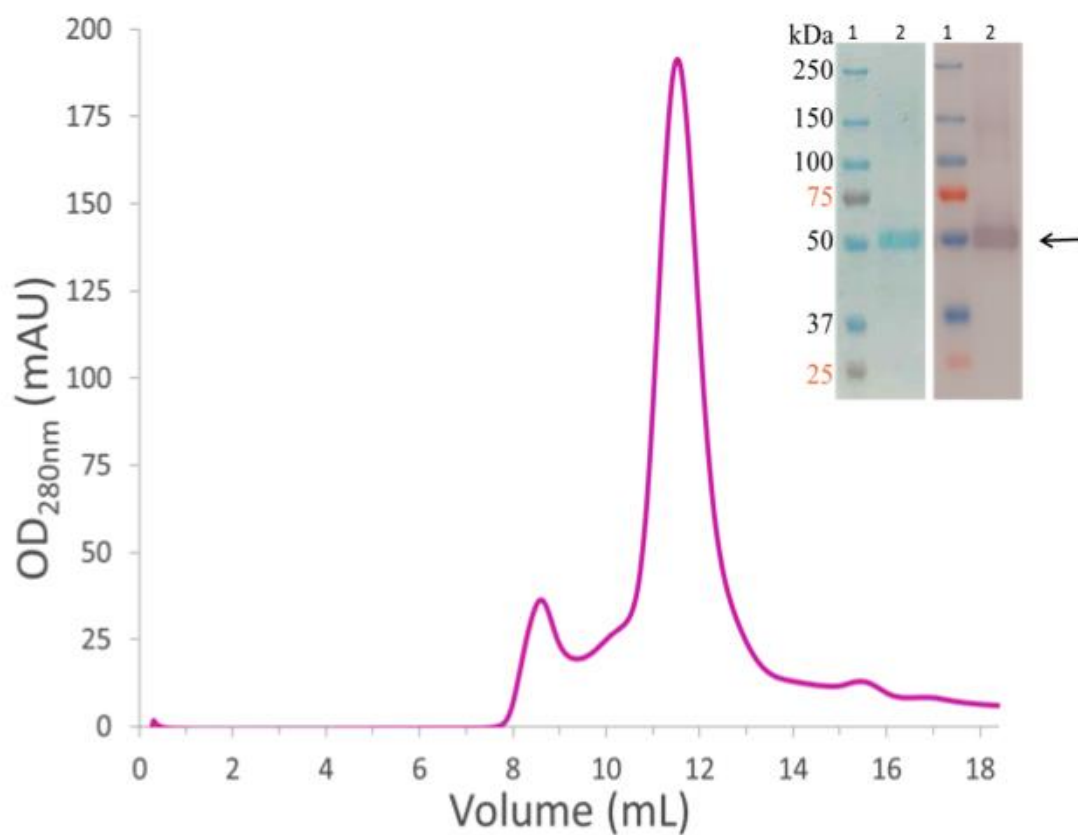


Fig. S1.

Sample preparation. Gel-filtration profile of human Kir2.1 obtained on a Superdex 200 10/300 column with absorbance measured at 280 nm at 0.3 mL/min in 0.5 mL fractions. Analysis of SDS-PAGE (insert left) and Western Blot detection using anti-His antibodies (insert right) show one band at 50 kDa, corresponding to Kir2.1 monomer. The sample has been identified by LC-MS/MS.

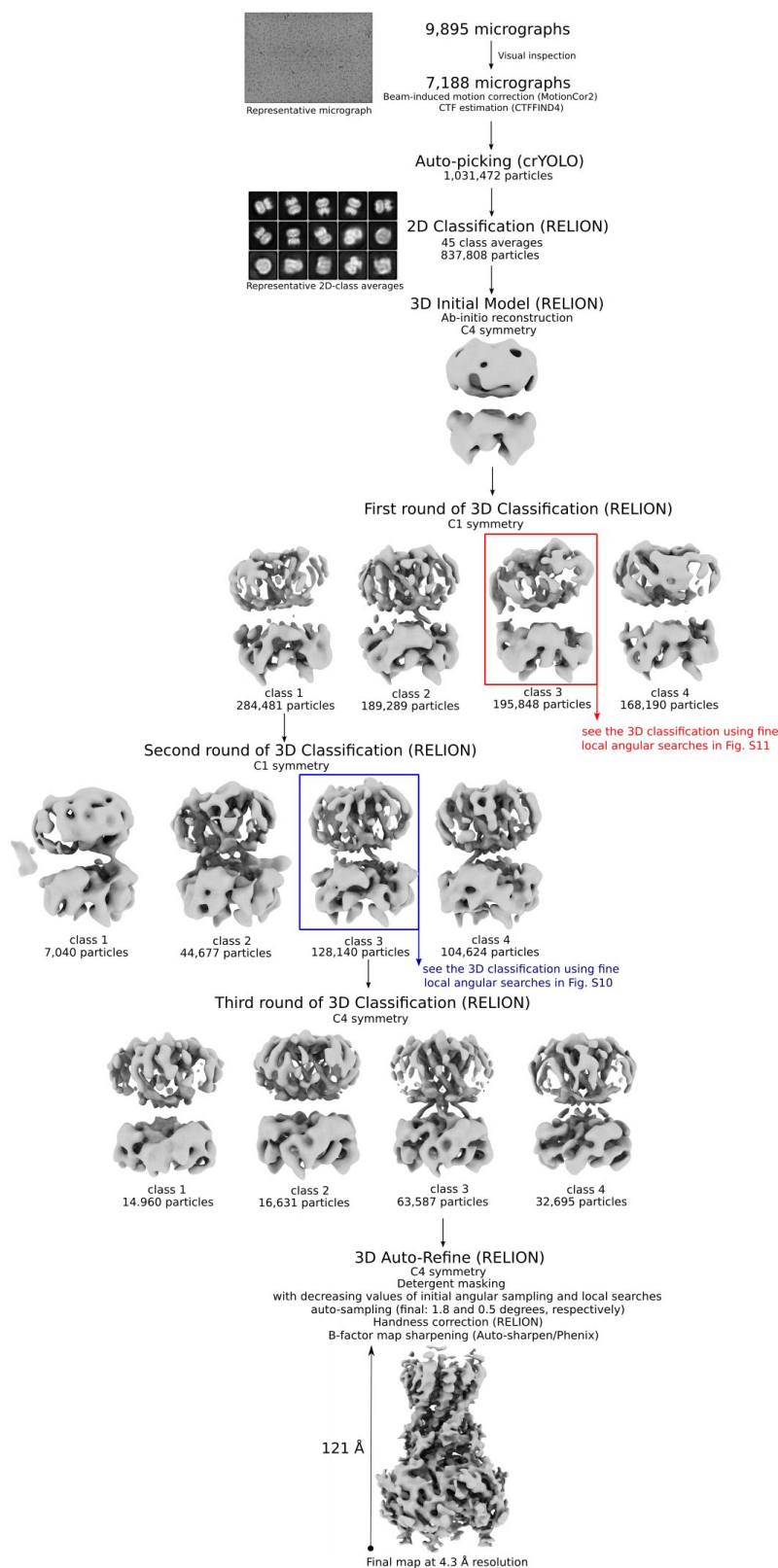


Fig. S2. Data processing workflow for the single-particle cryo-EM analysis of the human Kir2.1 channel. All steps to obtain the final cryo-EM map of the human Kir2.1 channel at 4.3 Å resolution are shown, including the number of particles presented in all steps, the maps from all classes obtained in the three rounds of 3D classification and the symmetry applied. Red and blue squares indicate the classes whose particles were subjected to a round of 3D

classification using fine angular searches to assess the structural heterogeneity of the particles (see Figs. S9 and S11). The insets show a representative micrograph obtained at Titan Krios G3 microscope operated at 300 kV equipped with a K3 direct electron detectors and a bioquantum/K3 energy filter and representative 2D-class averages of the particles showing the most frequent views.

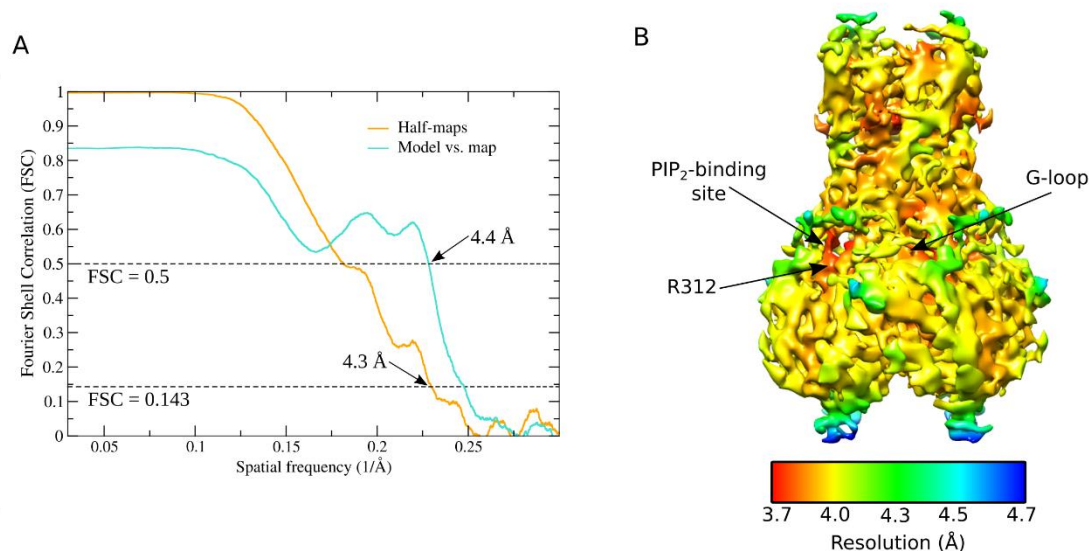


Fig. S3.

Data of human Kir2.1 cryo-EM structure. (A) Fourier shell correlation (FSC) curves. The resolution of the final cryo-EM map was estimated by the half-maps FSC curve (orange curve) using the “gold-standard” cutoff value (0.143). The map vs. model curve is also shown (cyan curve) and the resolution was estimated using the recommended cutoff value (0.5). (B) Local map resolution calculated using Phenix. Some important regions of the protein (PIP₂-binding site, G-loop and the residue R312 and its vicinity) that present a local resolution between 3.7 - 3.8 Å are indicated.

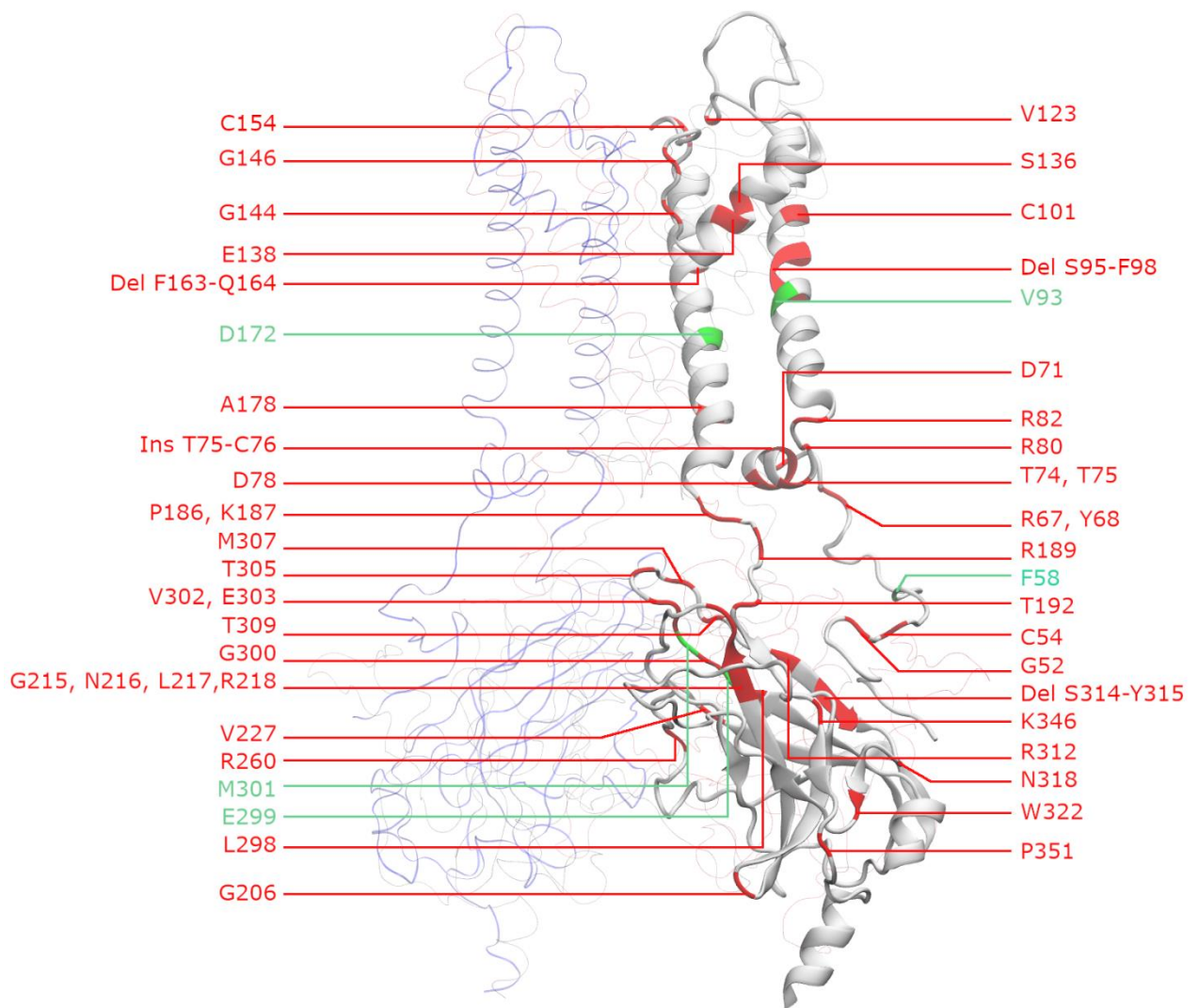


Fig. S4.

Representation of the disease-associated mutations in the structure of the human Kir2.1. Loss-of-function mutations associated with Andersen's syndrome (red) and gain-of-function mutations associated with short QT syndrome, atrial fibrillation, and autism spectrum disorders (green) are highlighted on a single subunit of the structure of the human Kir2.1 protein. Del is for deletion. Mutations R40X, S369X, T400M, and N410S are not represented here because the Kir2.1 structure covers only residues from 42 to 366.

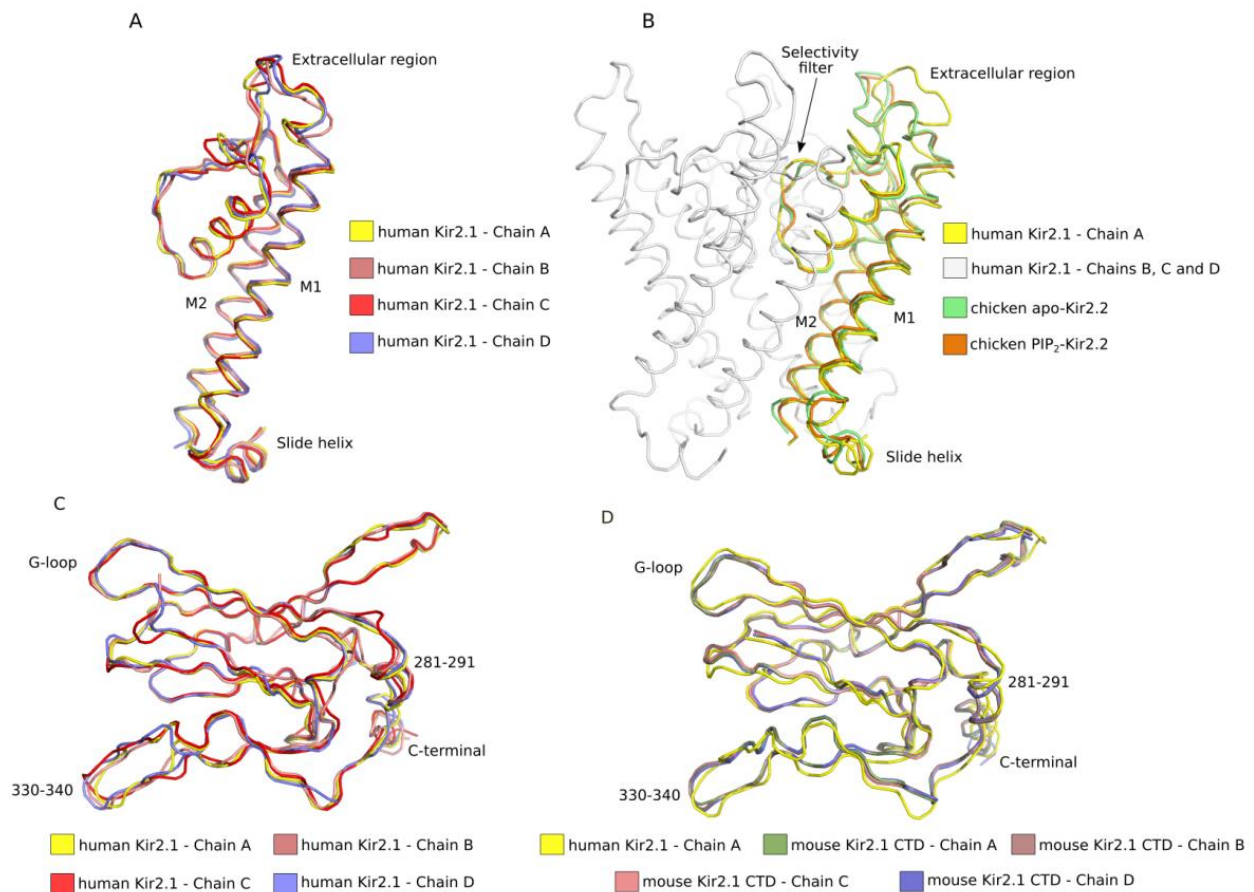


Fig. S5.

Structural comparison between Kir2.1 and Kir2.2 structures. C α atoms superposition between the human Kir2.1 channel cryo-EM structure and crystal structures of mouse Kir2.1 CTD (1U4F) and chicken Kir2.2 (in the absence and presence of PIP₂; 3JYC and 3SPI, respectively). (A) C α atoms superposition of TMD and extracellular region (a.a 72–182) between the four chains of human Kir2.1 channel. (B) C α atoms superposition of TMD and extracellular region (a.a 72–182) between the chain A of human Kir2.1 channel cryo-EM structure and one chain of crystal structures of chicken Kir2.2 in the absence and presence of PIP₂. The chains B, C, and D of the human Kir2.1 channel are also represented. The extracellular region and the typical features of TMD (M1 and M2 helices, selectivity filter and slide helix) are indicated. (C) C α atoms superposition of CTD (a.a 192–364) between the four chains of human Kir2.1 channel. (D) C α atoms superposition of CTD between the chain A of human Kir2.1 channel cryo-EM structure and the four chains of the crystal structure of mouse Kir2.1 CTD. The regions with the highest RMSD are indicated (a.a 281–291, a.a 330–340, and C-terminal end). The G-loop is also indicated.

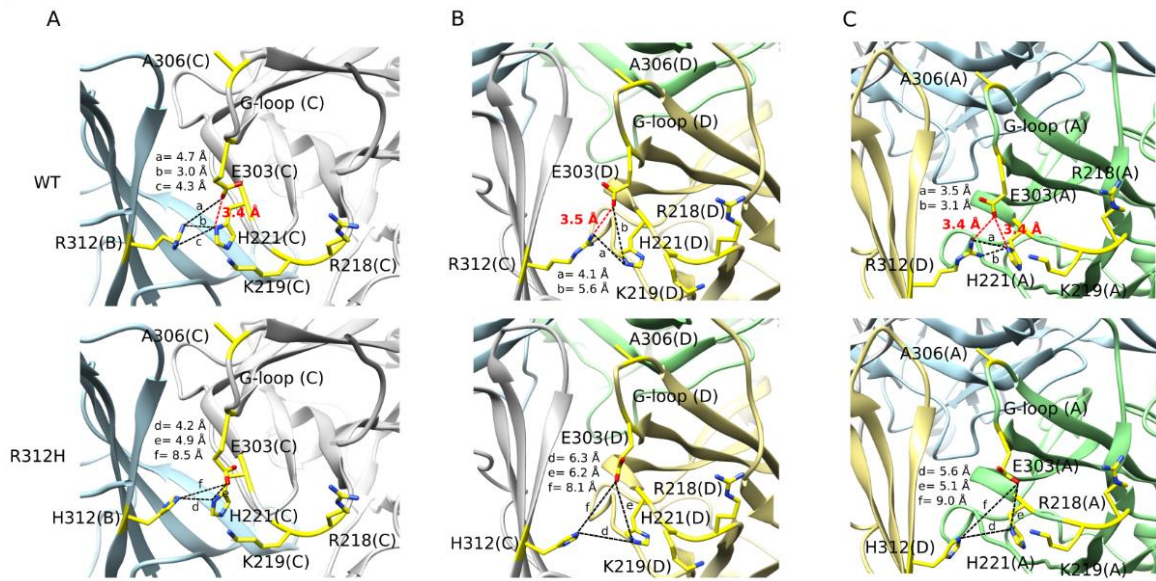


Fig. S6

Impact of the R312H mutation on the human Kir2.1 channel structure. (A) Intersubunit interaction network of R312 in the WT (top) and that of H312 in the R312H mutant (bottom) between chains B and C. (B) idem for chains C and D. (C) idem for chains D and A. The chains A, B, C, and D are shown in green, blue, gray, and yellow, respectively. The chains are indicated in parenthesis. Residues R218, K219, H221, E303, and A306 are represented as yellow sticks. Salt bridge distances are highlighted in red dashes and the other distances in black dashes.

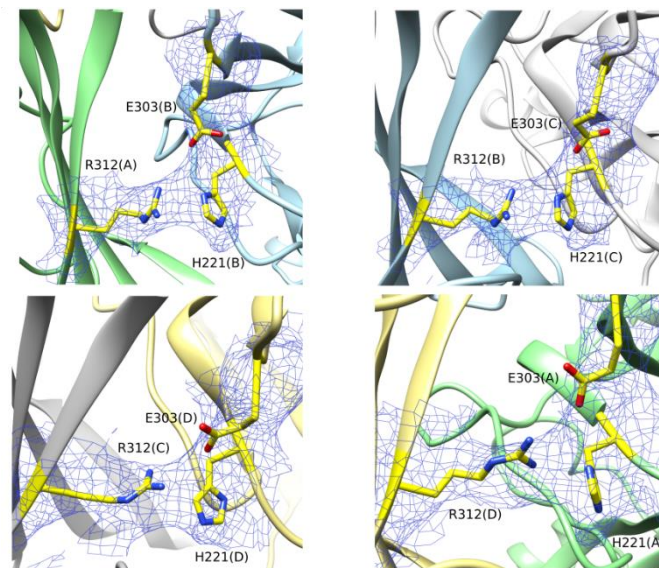


Fig. S7

Electron density maps of the residues R312, E303, and H221 in the human Kir2.1 cryo-EM structure. The residues are shown as yellow sticks, and the chains A, B, C, and D are in green, blue, gray, and yellow cartoons, respectively. The respective chains are indicated in parenthesis. Maps at 4 σ .

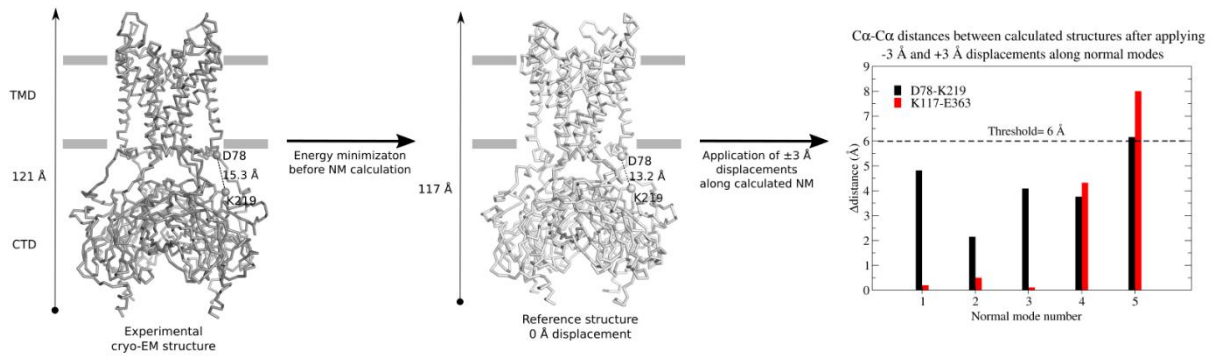


Fig. S8 Contribution of normal modes to extension/compression movements and tethering of the CTD to the TMD. Left panel: human Kir2.1 cryo-EM structure 121 Å long (gray ribbon). Residues D78 and K219 are shown as spheres and the Ca-Ca distance is indicated. Middle panel: reference structure after energy minimization, used for NM calculation. Ca-Ca distance of residues D78 and K219 is indicated. Right panel: Mode 5 was the only NM in which both Ca K117-E363 (red bars) and D78-K219 (black bars) distances were reduced by at least 6 Å (dashed line) between the calculated structures after +3 Å and -3 Å RMSD displacement along the NMs.

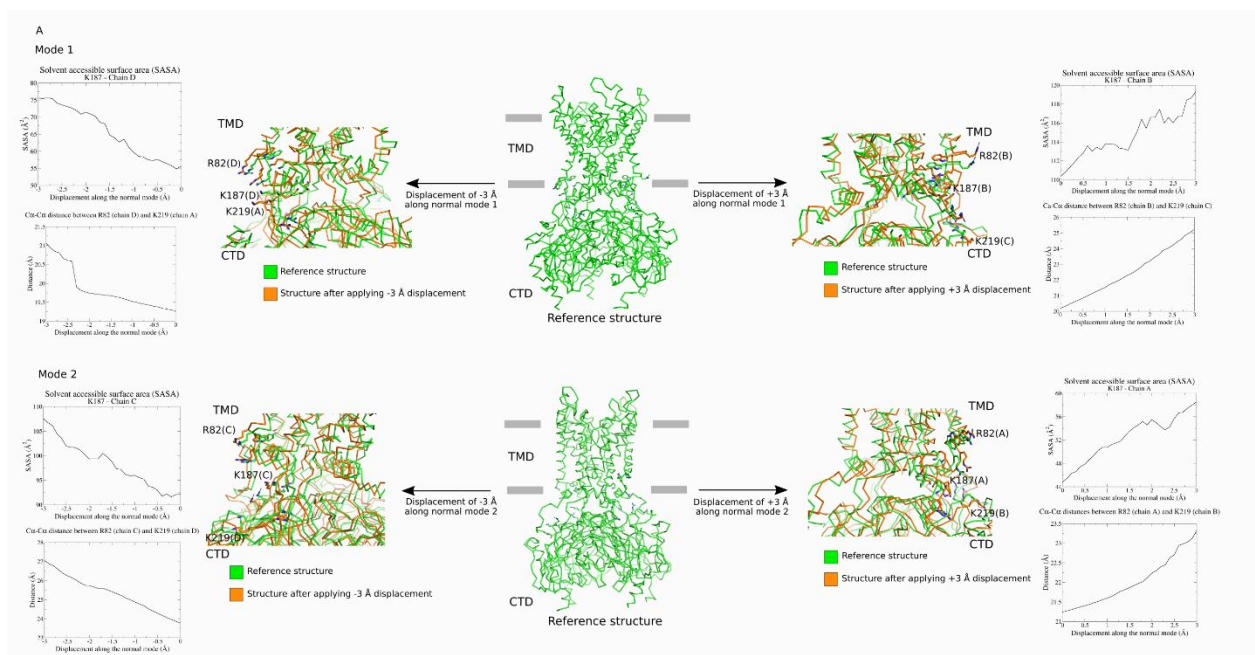


Fig. S9 Contribution of normal modes to opening of the PIP₂ binding site in the human Kir2.1 channel. Ribbon representation of the human Kir2.1 channel cryo-EM structure after ± 3 Å RMSD displacement along the modes number 1 (panel A) and 2 (panel B). The reference and the displaced structures are shown in green and orange, respectively. The residues R82, K187, and K219 are shown in sticks. The lateral graphs display the solvent accessible area (SASA) of K187 and the Ca-Ca distance between R82 and K219 residues from adjacent chains over ± 3 Å RMSD displacement along the modes 1 and 2. Gray horizontal bars indicate plasma membrane boundaries.

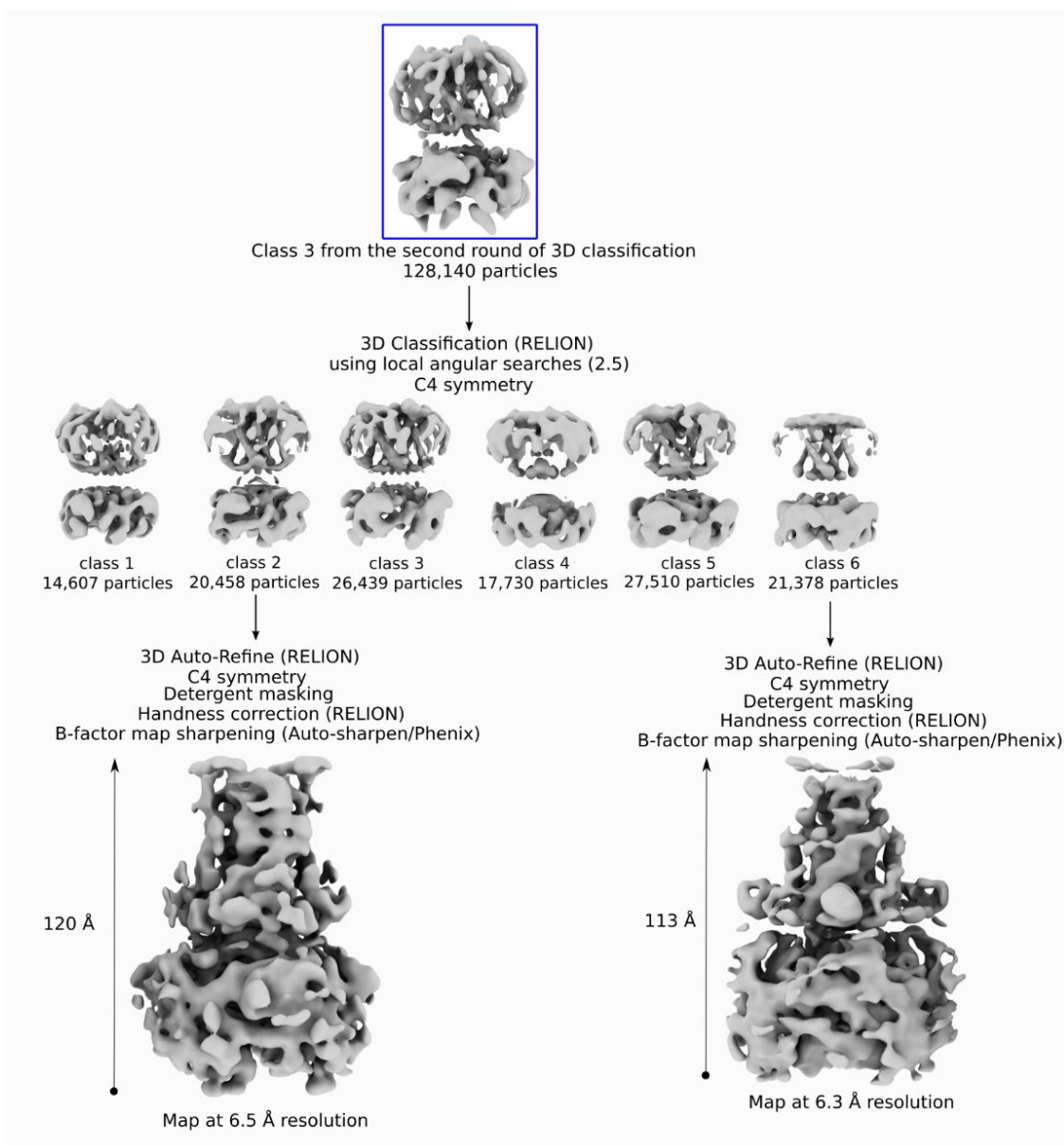


Fig. S10 3D Classification of the particles from the class 3 of the second round of 3D classification (see Fig. S2) using fine angular searches. The maps and the number of particles for the six classes obtained in this 3D classification are shown. The maps of two of these classes were subsequently subjected to 3D Auto-Refine and after detergent masking, handness correction and sharpening provided two different maps that illustrates the compact and the extended conformations of the Kir2.1 channel (size in length of 113 Å and 120 Å, respectively).

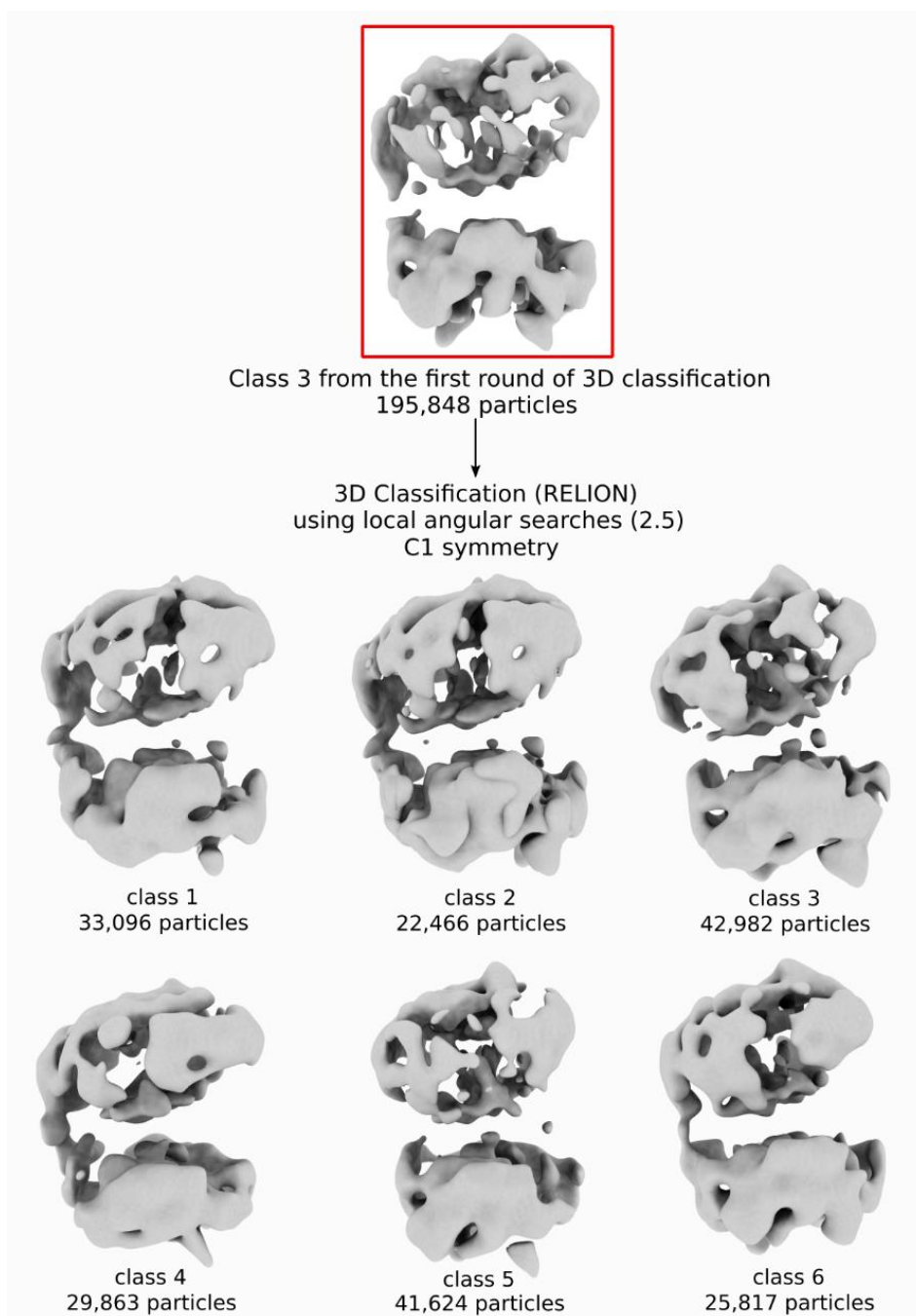


Fig. S11. 3D Classification of the particles from the class 3 of the first round of 3D classification (see Fig. S2) using fine angular searches. The maps and the number of particles for the six classes obtained in this 3D classification are shown.

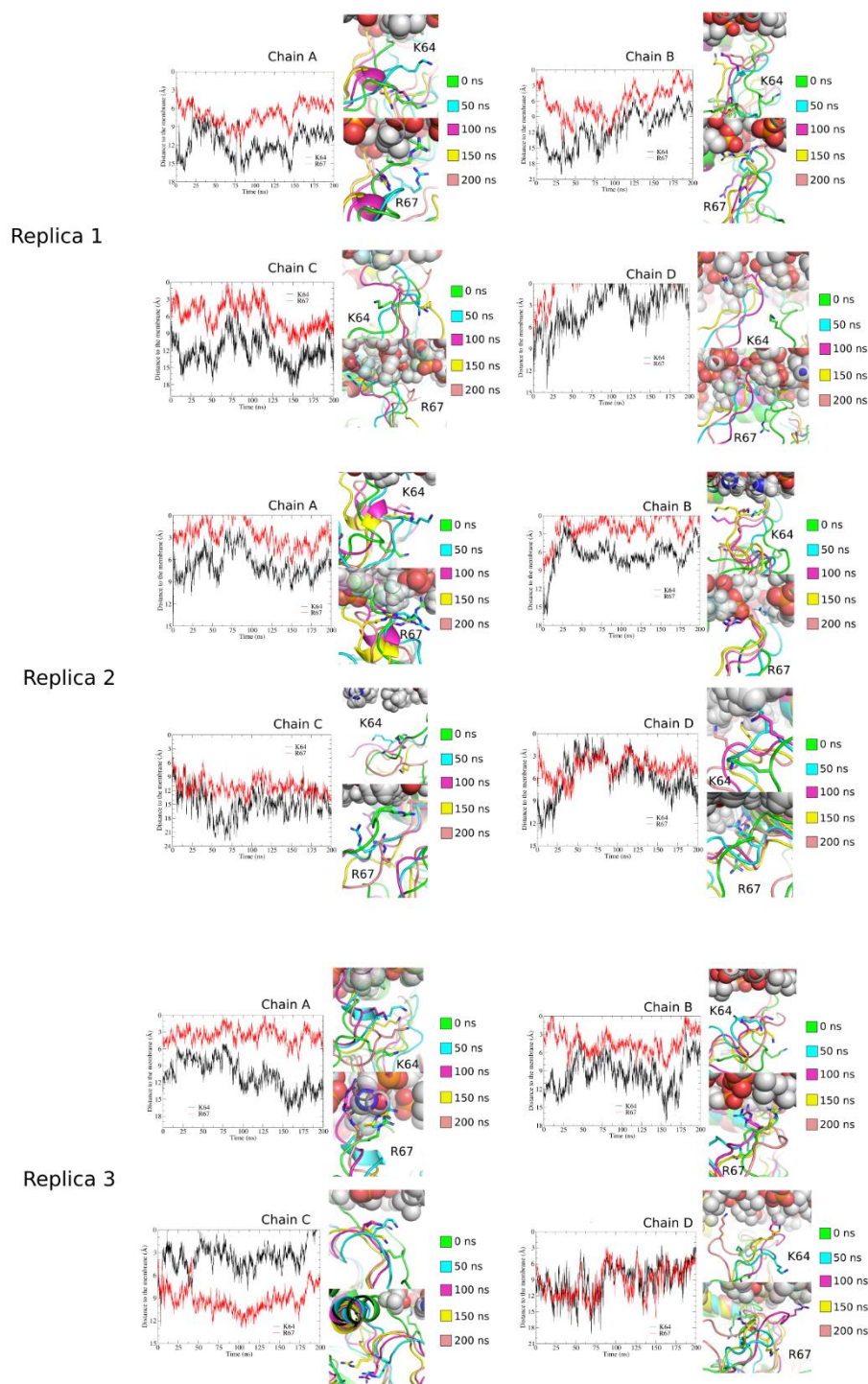


Fig. S12. K64 and R67 tethering to the membrane emerging from molecular dynamics simulations. Analysis of the 200 ns MD trajectories concerning K64 and R67 residues in the four chains in the three replicates. In each of these panels, snapshots at different times along the MD simulations are shown: 0 ns (green), 50 ns (cyan), 100 ns (magenta), 150 ns (yellow), and 200 ns (salmon). K64 and R67 residues are highlighted in sticks. These panels also contain the distances between the K64 and R67 residues to the plane of the phosphate groups from the inner membrane. To calculate these distances, the inner membrane was centered at $Z=0$. The 0 value represents the membrane level.

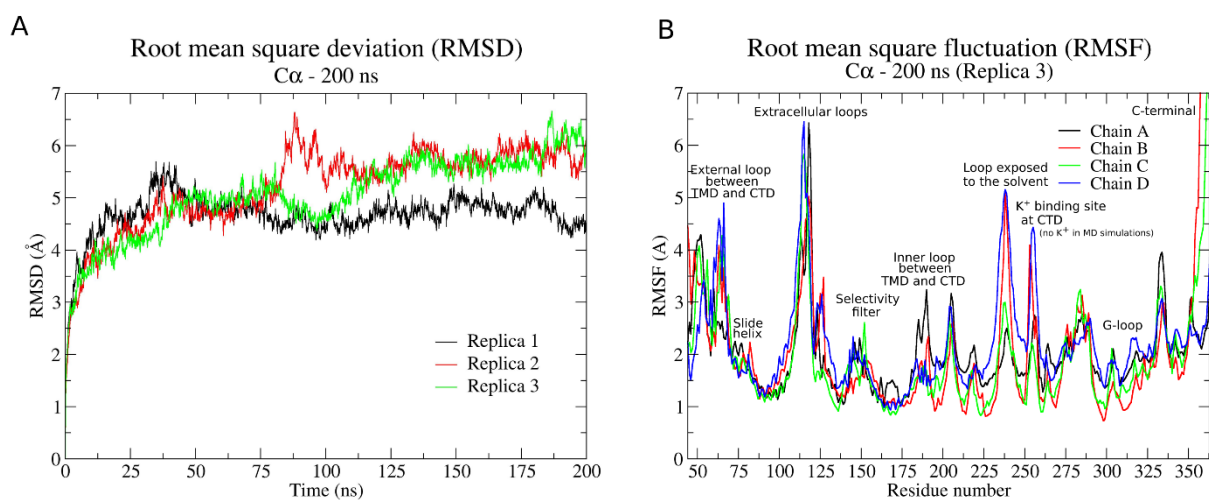


Fig. S13. Root mean square deviation (RMSD) and root mean square fluctuation (RMSF) analysis of MD simulations of the human Kir2.1 cryo-EM structure. (A) C α RMSDs of the protein in the three 200 ns long MD replica trajectories. Replica 1, 2, and 3 are shown in black, red, and green, respectively. (B) C α RMSF of the residues from one representative replica (Replica 3) MD trajectory. Chains A, B, C, and D are shown in black, red, green, and blue, respectively. The most important structural regions, and the regions that present high RMSF values are indicated.

Surface Plasmon Resonance controls and supplementary experiments

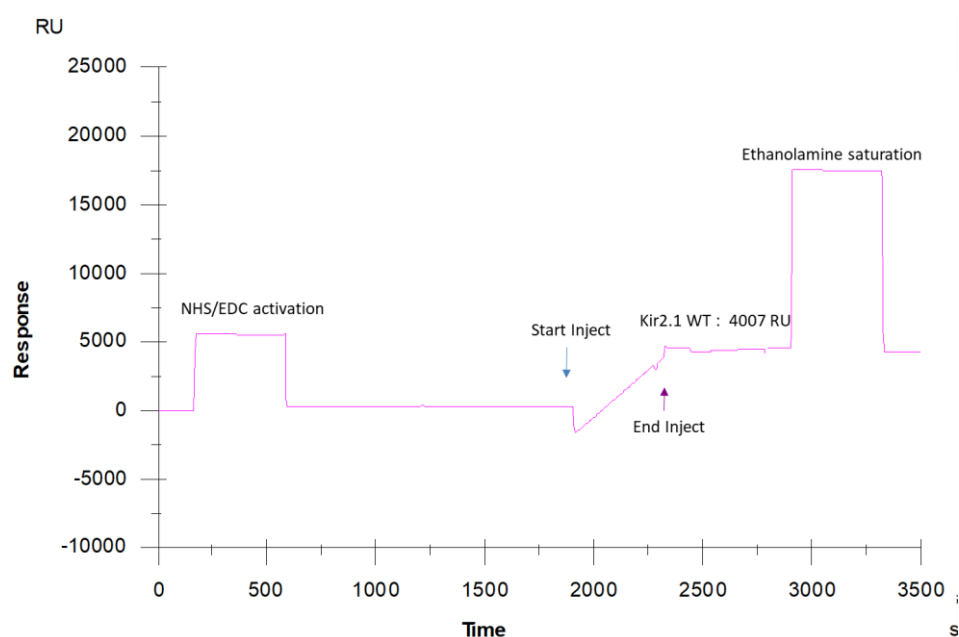


Fig. S14. Activation of CM5 sensor chip with NHS/EDC and immobilization of Kir2.1 WT. 50 mM Kir2.1 (in sodium acetate pH 4.5) was injected at 50 μ L/5 min. The surface chip was saturated with ethanolamine pH 8.

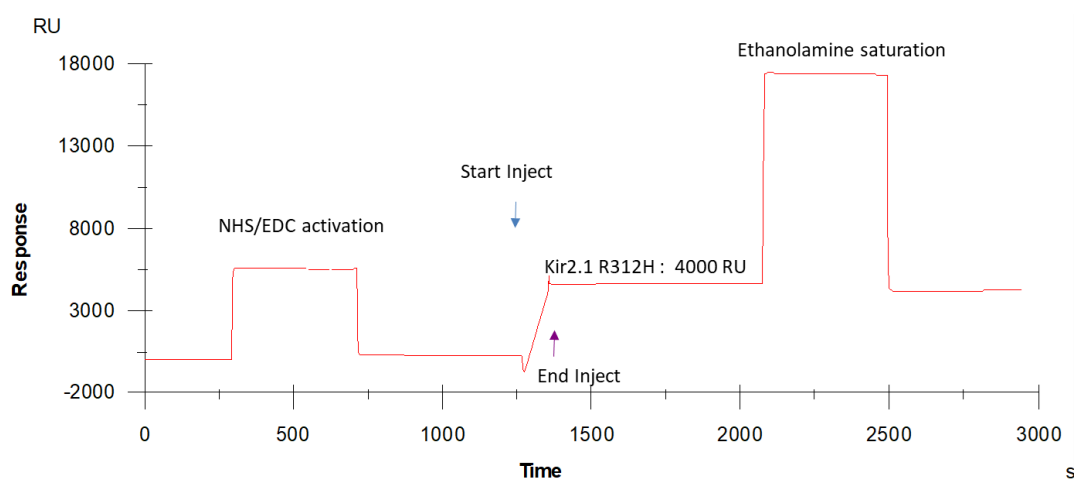


Fig. S15. Activation of CM5 sensor chip with NHS/EDC and immobilization of Kir2.1_R312H. 50 mM Kir2.1 (in sodium acetate pH 4.5) was injected at 50 μ L/5 min. The surface chip was saturated with ethanolamine pH 8.

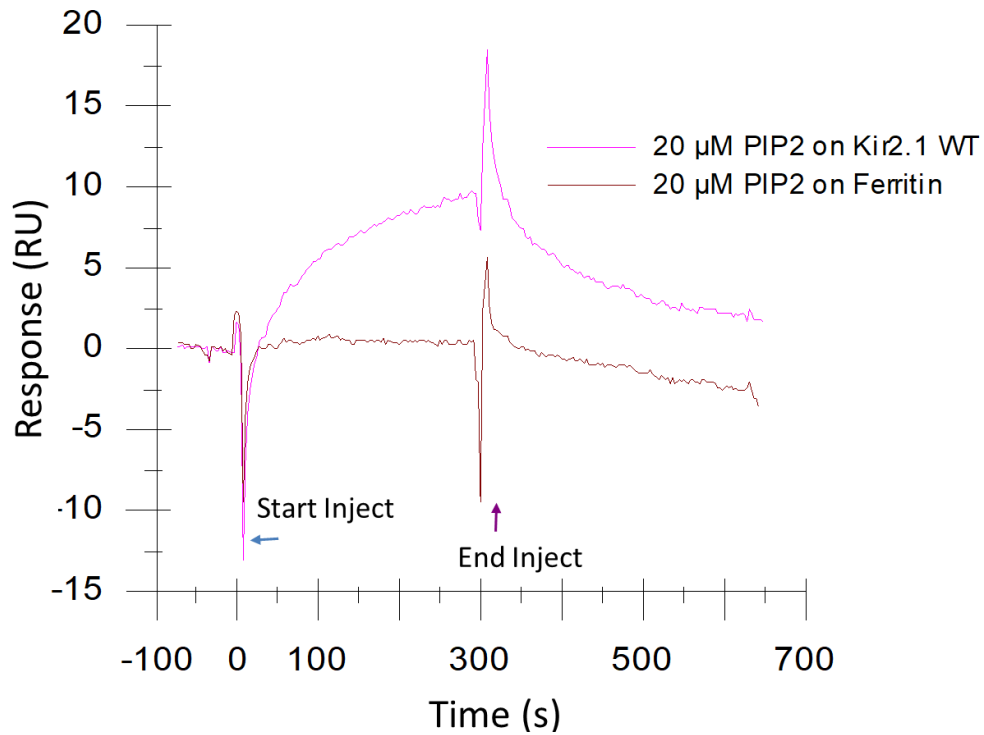


Fig. S16. Negative control: Comparative binding of PIP₂ on Kir2.1 WT and Ferritin on CM5 chip. 20 μM PIP₂ was injected at 25μL/5min. PIP₂ binding is specific to Kir2.1 as no PIP₂ bound to Ferritin.

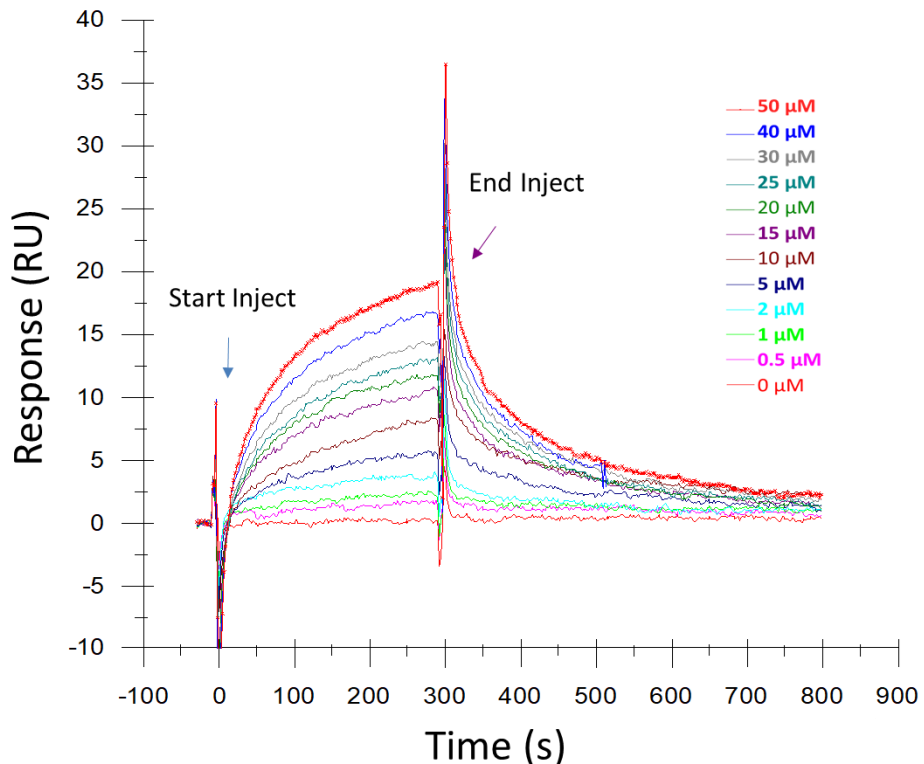


Fig. S17. Comparative binding of PIP₂ on Kir2.1 WT at different concentrations on a CM5 sensor chip.

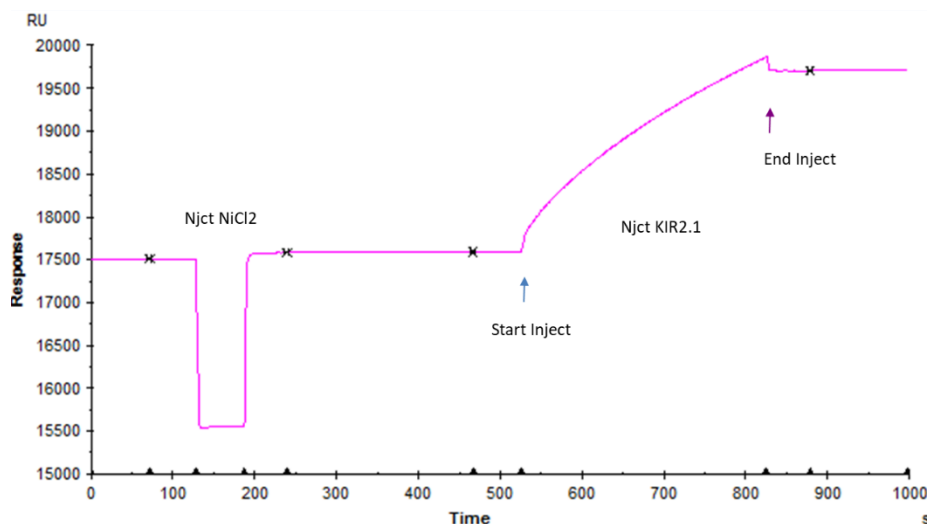


Fig. S18. Activation of NTA sensor chip with NiCl_2 and immobilization of Kir2.1 WT. 50 mM Kir2.1 was injected at 50 $\mu\text{L}/5$ min. The surface chip was saturated with ethanolamine pH 8.

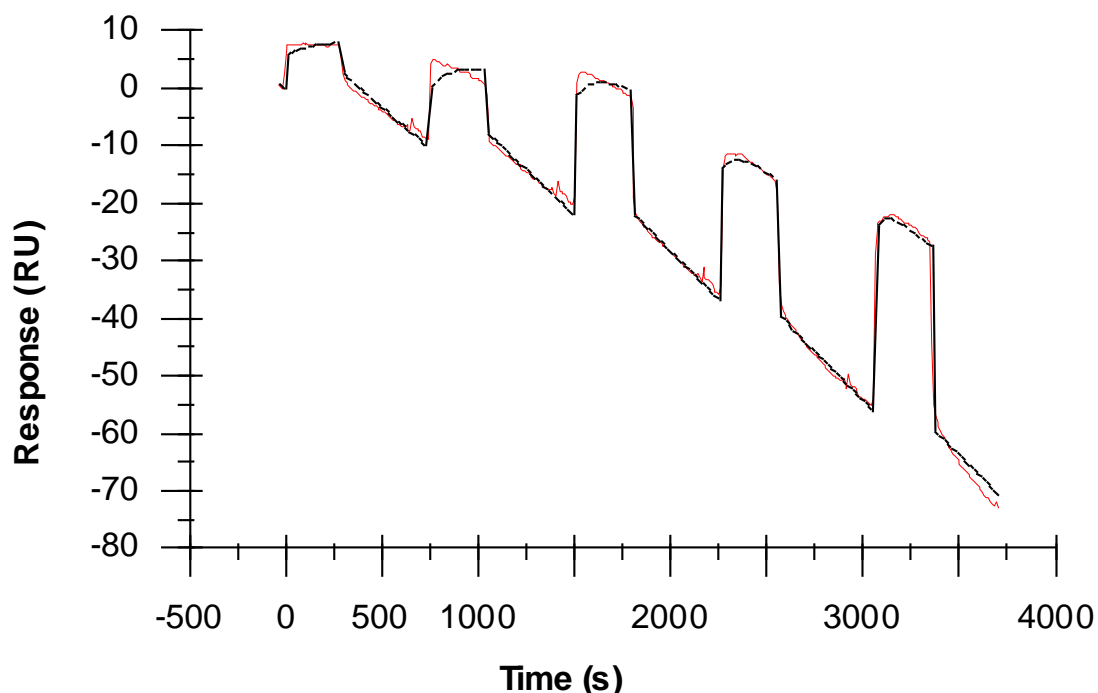


Fig. S19. **Binding kinetics of PIP_2 on Kir2.1 WT on an NTA sensor chip.** Five sequential injections of PIP_2 are shown, 0.312–5 μM , at 25 $\mu\text{L}/5$ min. In color, experimental data; in black, fitted curve. The single-cycle kinetics assays were carried out in duplicate; only one replica is shown. The SPR response is expressed in response units (RU) relative to the time in seconds. The K_D determined 2.54 ± 1.45 μM , consistent with that observed with CM5 surface chip.

Table S1.

 α superposition between various Kir2 channel structures

(A) **Superposition of TMD.** Pairwise superposition of TMD between chains of human Kir2.1 cryo-EM structure, chicken apo-Kir2.2, and PIP₂-Kir2.2 crystal structures (3JYC and 3SPI, respectively). (B) **Superposition of CTD.** Pairwise superposition of CTD between chains of human Kir2.1 cryo-EM structure and mouse CTD Kir2.1 crystal structure (1U4F). (C) **Superposition of G-loop.** Pairwise superposition of G-loop (300-315 region) between chains of human Kir2.1 cryo-EM structure and mouse CTD Kir2.1 crystal structure (1U4F). Root mean square deviation (RMSD, Å) of C α atoms.

A: Superposition TMD

	Human Kir2.1 - Chain A	Human Kir2.1 - Chain B	Human Kir2.1 - Chain C	Human Kir2.1 - Chain D	Chicken apo-Kir2.2 (3JYC)	Chicken PIP ₂ -Kir2.2 (3SPI)
Human Kir2.1 - Chain A	-	1.45	1.20	1.01	4.84	5.01
Human Kir2.1 - Chain B	1.45	-	1.20	1.39	4.75	4.81
Human Kir2.1 - Chain C	1.20	1.20	-	1.28	4.64	4.79
Human Kir2.1 - Chain D	1.01	1.39	1.28	-	4.89	5.04
Chicken apo-Kir2.2 (3JYC)	4.84	4.75	4.64	4.89	-	0.81
Chicken PIP ₂ -Kir2.2 (3SPI)	5.01	4.91	4.79	5.04	0.81	-

B: Superposition CTD

	Human Kir2.1 - Chain A	Human Kir2.1 - Chain B	Human Kir2.1 - Chain C	Human Kir2.1 - Chain D	Mouse Kir2.1 Chain A	Mouse Kir2.1 Chain B	Mouse Kir2.1 Chain C	Mouse Kir2.1 Chain D	Chicken apo-Kir2.2 (3JYC)	Chicken PIP ₂ -Kir2.2 (3SPI)
Human Kir2.1 - Chain A	-	1.47	1.57	0.91	1.30	1.30	1.27	1.27	3.96	3.89
Human Kir2.1 - Chain B	1.47	-	1.30	1.47	1.70	1.75	1.72	1.72	4.19	4.11
Human Kir2.1 - Chain C	1.57	1.30	-	1.48	1.90	1.91	1.92	1.89	4.36	4.29
Human Kir2.1 - Chain D	0.91	1.47	1.48	-	1.38	1.38	1.37	1.36	4.10	4.03
Mouse Kir2.1- Chain A (1U4F)	1.30	1.70	1.90	1.38	-	0.32	0.28	0.35	3.87	3.80
Mouse Kir2.2- Chain B (1U4F)	1.30	1.75	1.91	1.38	0.32	-	0.27	0.30	3.87	3.79
Mouse Kir2.3- Chain C (1U4F)	1.29	1.74	1.92	1.37	0.28	0.27	-	0.29	3.89	3.81
Mouse Kir2.4- Chain D (1U4F)	1.27	1.72	1.89	1.36	0.35	0.30	0.29	-	3.86	3.78
Chicken apo-Kir2.2 (3JYC)	3.96	4.19	4.36	4.10	3.87	3.87	3.89	3.86	-	0.76
Chicken PIP ₂ -Kir2.2 (3SPI)	3.89	4.11	4.29	4.03	3.80	3.79	3.81	3.78	0.76	-

C: Superposition G-loop

	Human Kir2.1 - Chain A	Human Kir2.1 - Chain B	Human Kir2.1 - Chain C	Human Kir2.1 - Chain D	Mouse Kir2.1 Chain A (1U4F)	Mouse Kir2.1 Chain B (1U4F)	Mouse Kir2.1 Chain C (1U4F)	Mouse Kir2.1 Chain D (1U4F)
Human Kir2.1 - Chain A	-	0.66	0.56	0.46	0.68	0.69	0.59	0.65
Human Kir2.1 - Chain B	0.66	-	0.53	0.60	0.61	0.67	0.62	0.60
Human Kir2.1 - Chain C	0.56	0.53	-	0.60	0.61	0.63	0.60	0.58
Human Kir2.1 - Chain D	0.46	0.60	0.60	-	0.62	0.67	0.59	0.64
Mouse Kir2.1- Chain A (1U4F)	0.68	0.61	0.61	0.62	-	0.28	0.24	0.19
Mouse Kir2.2- Chain B (1U4F)	0.69	0.67	0.63	0.67	0.28	-	0.29	0.27
Mouse Kir2.3- Chain C (1U4F)	0.59	0.62	0.60	0.59	0.24	0.29	-	0.22
Mouse Kir2.4- Chain D (1U4F)	0.65	0.60	0.58	0.64	0.19	0.27	0.22	-

Table S2.

Cryo-EM data collection and refinement statistics

	Sample	Human Kir2.1
Data Collection		
	Microscope	Titan Krios
	Detector	K3 Summit
	Voltage (kV)	300
	Pixel size (Å/pixel)	0.86
	Dose/frame (e/(Å ²))	1.71
	Number of frames	36
	Defocus range (μm)	-1.2 to -2.8
	Movies collected	9,895
	Movies used	7,188
Reconstruction		
	Particles extracted	1,031,472
	Particles used for final reconstruction	63,584
	Final Resolution (Å) (FSC = 0.143)	4.3
Map Sharpening B-factor (Autosharpen/Phenix)		
	Overall b_sharpen applied (Å ²)	404.73
	Final b_iso obtained (Å ²)	69.95
Model composition		
		Chain A (42-366; 324/427 residues)
		Chain B (44-364; 320/427 residues)
		Chain C (43-363; 320/427 residues)
		Chain D (41-365; 324/427 residues)
	Model coverage	
	Non-hydrogen atoms	10358
	Ligands	K: 1 Sr: 2
Refinement		
	Model-to-map CC _{mask}	0.70
	Model-to-map CC _{volume}	0.68
	Model-to-map CC _{peaks}	0.50
	Mean CC for ligands	0.81
	d _{model} (Å)	4.30
	d _{FSC_model} (Å) (FSC = 0.5)	4.4
r.m.s deviations		
	Bond length (Å)	0.003
	Bond angles (°)	0.86
Validation		
	MolProbity Score	2.2
	Clash Score	12.57
	Ramachandran Plot Outliers (%)	0.31
	Rotamer outliers (%)	0.35
	Cβ outliers (%)	0
EMDB ID		EMD-14678
PDB ID		7ZDZ

Video S1.

Structural movement of the human Kir2.1 channel between -3 \AA and 3 \AA RMSD structures displaced along mode 5. 0.1 \AA RMSD step size displacement. The longitudinal length of the structure and the D78-K219 C α -C α distances are highlighted. D78 and K219 residues are in red and orange spheres, respectively.

Video S2.

Structural movement of the human Kir2.1 channel between -3 \AA and 3 \AA RMSD structures displaced along mode 1. 0.1 \AA RMSD step size displacement. Chains A, B, C and D are shown in cyan, orange, green, and yellow, respectively. The residues involved in putative PIP₂ binding for Kir2.x (R80, W81, R82, K182, K185, K187, K188, R189, R218, and K219) are highlighted in gray sticks.

Video S3.

Structural movement of the human Kir2.1 channel between -3 \AA and 3 \AA RMSD structures displaced along mode 2. 0.1 \AA RMSD step size displacement. Chains A, B, C and D are shown in cyan, orange, green, and yellow, respectively. The residues involved in putative PIP₂ binding for Kir2.x (R80, W81, R82, K182, K185, K187, K188, R189, R218, and K219) are highlighted in gray sticks.

Video S4.

Structural movement of the human Kir2.1 channel between -3 \AA and 3 \AA RMSD structures displaced along mode 3. 0.1 \AA RMSD step size displacement.

Video S5.

Structural movement of the human Kir2.1 channel between -3 and 3 \AA RMSD structures displaced along mode 4. 0.1 \AA RMSD step size displacement.

Video S6.

K64 and R67 tethering to the membrane displayed by molecular dynamics simulations. 200 ns of MD simulations of the human Kir2.1 channel. The chains B and D of replica 2 were chosen as representative models of the trajectories of the K64 and R67 residues. The protein is represented in cyan cartoon, and residues K64 and R67 are represented in yellow and red sticks, respectively. The membrane is represented as dots (carbon, phosphate, and oxygen atoms are represented in gray, blue, and red dots, respectively). The membrane was kept still for the purpose of visualizing the trajectories of both residues. Step size of 20 ps.

**5 RECONSTITUTION OF KIR2.1 IN
MODEL SYSTEMS: AMPHIPOLS AND
NANODISCS**

5.1 INTRODUCTION

Although proven to be essential in obtaining MPs, detergents have many drawbacks in the structural characterization of MPs. Detergent micelles are in a thermodynamic equilibrium where monomer molecule associates and dissociates. During solubilization, free detergent molecules insert into the phospholipid membrane. When the detergent concentration is high enough, lipid/detergent/protein mixed micelles are formed. The detergent concentration must be high enough so one micelle contains only one protein, meaning that one needs about 10 micelles per protein molecule. The free micelles serve as a “hydrophobic sink” (Popot 2010) for molecules previously linked to the protein. Because they can dissociate essential protein-protein and protein-lipid interactions, they actively contribute to destabilizing the protein over time (Popot 2010). Many of the structures solved in cryo-EM solubilize the protein in a detergent and then exchange it into a non-detergent membrane mimetic (Choy et al. 2021; Le Bon et al. 2021). Therefore, I investigated two different strategies for stabilizing the purified Kir2.1 channel without detergent: Amphipol trapping and reconstitution into nanodiscs.

The first part of this chapter will focus on Amphipols (Apol), amphipathic surfactants developed by J.L. Popot et al. and further developed by M. Zoonens et al. Amphipols bind to the membrane protein’s transmembrane domain by multiple hydrophobic contact points. They form stable complexes with the protein and have slow dissociation rates. Note that amphipols do not associate to form micelles; hence do not have a CMC. Therefore, the detergent can be easily removed without affecting the protein-Apol complex. Apols will be used to stabilize the protein to obtain a structure at a higher resolution.

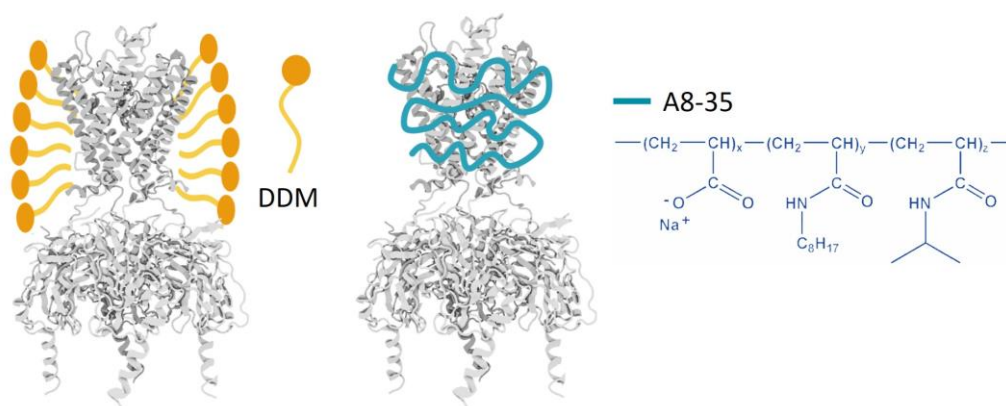


Figure 5-1 Schematic arrangement of DDM (left) vs. Apols (right) around Kir2 TMD. The chemical structure of Apol A8-35 is depicted.

The second part of this chapter will focus on reconstituting Kir2.1 into nanodiscs. It is a section showing the nanodisc reconstitution's optimization process, which is not always straightforward. I have chosen to showcase this trial and error part in the hopes of helping the next struggling Ph.D. student reading this manuscript. Nanodiscs are discoidal lipid bilayers stabilized by membrane scaffolding proteins (MSPs) derived by S.G. Sligar from ApoA-1, a human high-density lipoprotein. They provide a more native environment to membrane proteins. The size of the nanodiscs formed is determined by the length of the MSP and the stoichiometry of lipids chosen for the reconstitution. I decided to test three MSPs of different lengths: MSP1, MSP1D1, and MSP1E1, forming 9.7-9.8, 9.5-9.7, and 10.4-10.6 nm discs, respectively. We will begin with the necessary production and purification of the membrane scaffolding protein (MSP) and lipid preparation and end with the preliminary results and perspectives.

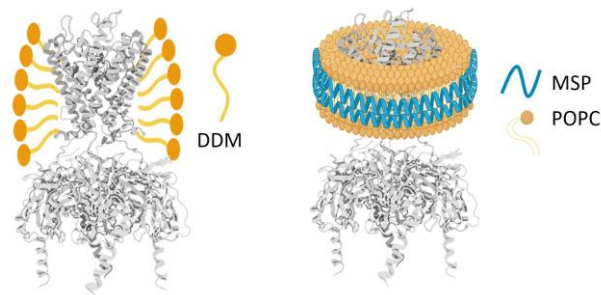


Figure 5-2. Schematic representation of DDM vs. nanodisc around Kir2 channel. The right panel shows MSP and POPC wrapped around the TMD.

5.2 PART I: CHARACTERIZATION OF KIR2.1 IN AMPHIPOLS

5.2.1 Materials and Methods

Amphipols (Apol) are amphipathic surfactants that bind to the membrane protein's transmembrane domain by multiple hydrophobic contact points. Apols form stable complexes with the protein, and the detergent can be easily removed by (1) the addition of bio-beads or (2) by cycles of dilution under the detergent's critical micellar concentration (CMC) and concentration (Popot et al. 2003; Zoonens et al. 2014).

5.2.1.1 Preparing Amphipols

A8-35 amphipol (Apol) powder was dissolved in Milli-Q water at $50 \text{ mg} \cdot \text{mL}^{-1}$ and $5.58 \text{ mg} \cdot \text{mL}^{-1}$. The Apol solution was homogenized with vortex and incubated for 2 h at RT with gentle agitation to ensure proper rehydration.

5.2.1.2 Preparing Bio-Beads

Polystyrene bio-beads (Bio-Rad) were washed with 96% ethanol followed by several washes in milli-Q water, with centrifugation for 2 min at 4700 rpm 4 °C, and then stored in water with some NaN₃.

5.2.1.3 Reconstitution of Kir2.1 in Amphipols

The concentration of purified Kir2.1 was determined by NanoDrop 2000 spectrophotometer, confirmed by the BCA test, and converted into mass units. 6 µg of resuspended Apol were added to each 1 µg of Kir2.1 in solution (Table 5-1) and incubated for 45–60 min at 4 °C with gentle agitation.

5.2.1.4 Detergent removal

Bio-Beads were added at 20 times the mass of DDM detergent initially present in the sample and incubated for 3 h at 4 °C under gentle agitation. The Bio-Beads were discarded after a 5-min centrifugation step was performed to discard.

Table 5-1 Reconstitution of Kir2.1 in Amphipols

Concentration of Kir2.1	Volume of Kir2.1	Mass of Kir2.1	Kir/Apol mass ratio	Mass of Apol	Starting Apol Concentration	Volume of Apol
0.155 µg · mL ⁻¹	900 µL	139.5 µg	1:5.5	767.25 µg	50 mg · mL ⁻¹	15.35 µL

Concentration of DDM	Sample Volume	Mass of DDM	Bio-Beads to add
0.03%	900 µL	0.27 mg	5.4 mg

The structure of Kir2.1 in DDM was solved at 4.3 Å resolution (Chapter 4) using QF 1.2-1.3 copper grids with a thin carbon layer added. Indeed, adding an extra carbon layer was required; otherwise, Kir2.1 would be deposited entirely in the carbon film outside the holes. This extra carbon layer added noise to the images, limiting the cryo-EM map's resolution. Additionally, Kir2.1-DDM showed a slight preferential orientation in cryo-EM grids. The side views were more represented than the top and bottom views. The cryo-EM map has its lowest resolution in this top region consisting of flexible loops.

5.2.2 Results

5.2.2.1 Finding the suitable Kir2.1: Apol ratio

The reconstitution of Kir2.1 in Amphipols was studied by negative staining and cryo-EM. The goal was to determine which ratios were best for obtaining a stable, non-aggregated tetramer that could subsequently be structurally analyzed. Various Kir2.1: Apol ratios were evaluated (n=2) 1:0.5, 1:1, 1:2, 1:3, 1:4, 1:5, and 1:6 (Table 5-2) to identify the ideal Apol mass ratio required to keep Kir2.1 soluble and stable in an aqueous solution without detergent. Once DDM was removed with Bio beads, negative staining grids were made and observed.

Table 5-2 Ratio of Kir2.1 to Apol

Concentration of Kir2.1	Volume of Kir2.1	Mass of Kir2.1	Kir2.1:Apol mass ratio	Mass of Apol
0.083 $\mu\text{g} \cdot \mu\text{L}^{-1}$	40 μL	3.32 μg	1: 0	0
0.083 $\mu\text{g} \cdot \mu\text{L}^{-1}$	40 μL	3.32 μg	1: 0.5	1.66 μg
0.083 $\mu\text{g} \cdot \mu\text{L}^{-1}$	40 μL	3.32 μg	1: 1	3.32 μg
0.087 $\mu\text{g} \cdot \mu\text{L}^{-1}$	40 μL	3.48 μg	1: 2	6.96 μg
0.087 $\mu\text{g} \cdot \mu\text{L}^{-1}$	40 μL	3.48 μg	1: 3	10.44 μg
0.087 $\mu\text{g} \cdot \mu\text{L}^{-1}$	40 μL	3.48 μg	1: 4	13.92 μg
0.087 $\mu\text{g} \cdot \mu\text{L}^{-1}$	40 μL	3.48 μg	1: 5	17.4 μg
0.087 $\mu\text{g} \cdot \mu\text{L}^{-1}$	40 μL	3.48 μg	1: 6	20.88 μg

Two controls were performed, a positive control containing Kir2.1 in DDM, untreated, and negative control where DDM is removed without adding Apols. In negative staining, the positive control showed Kir2.1 as a white particle on a gray background, as expected. The sample is very concentrated, and thus particles are in close contact with each other, with little aggregation.

The negative control (1:0) consisted of enormous aggregates of Kir2.1, which is expected as DDM was removed with bio-beads and no further amphipols treatment was conducted. The 1:0.5 ratio showed that the protein was aggregated, forming small protein clusters with uneven distribution across the carbonated copper grid, indicating insufficient Apols to keep the protein soluble. The 1:1 ratio displayed minor aggregation throughout the grid. It is the minimum ratio sufficient to allow reconstitution into Apols, although it does not provide a homogeneous sample. Ratio 1:2 allowed a good distribution of particles and kept the protein stable, and prevented aggregation. The best ratios were 1:4 and 1:5, showing excellent sample distribution across the grid, different orientations, and little to no aggregation, despite the elevated concentration.

The contrast in ratio 1:6 was not as sharp as 1:4 and 1:5; the particles seemed a little diffuse, perhaps due to an excess of free Apol.

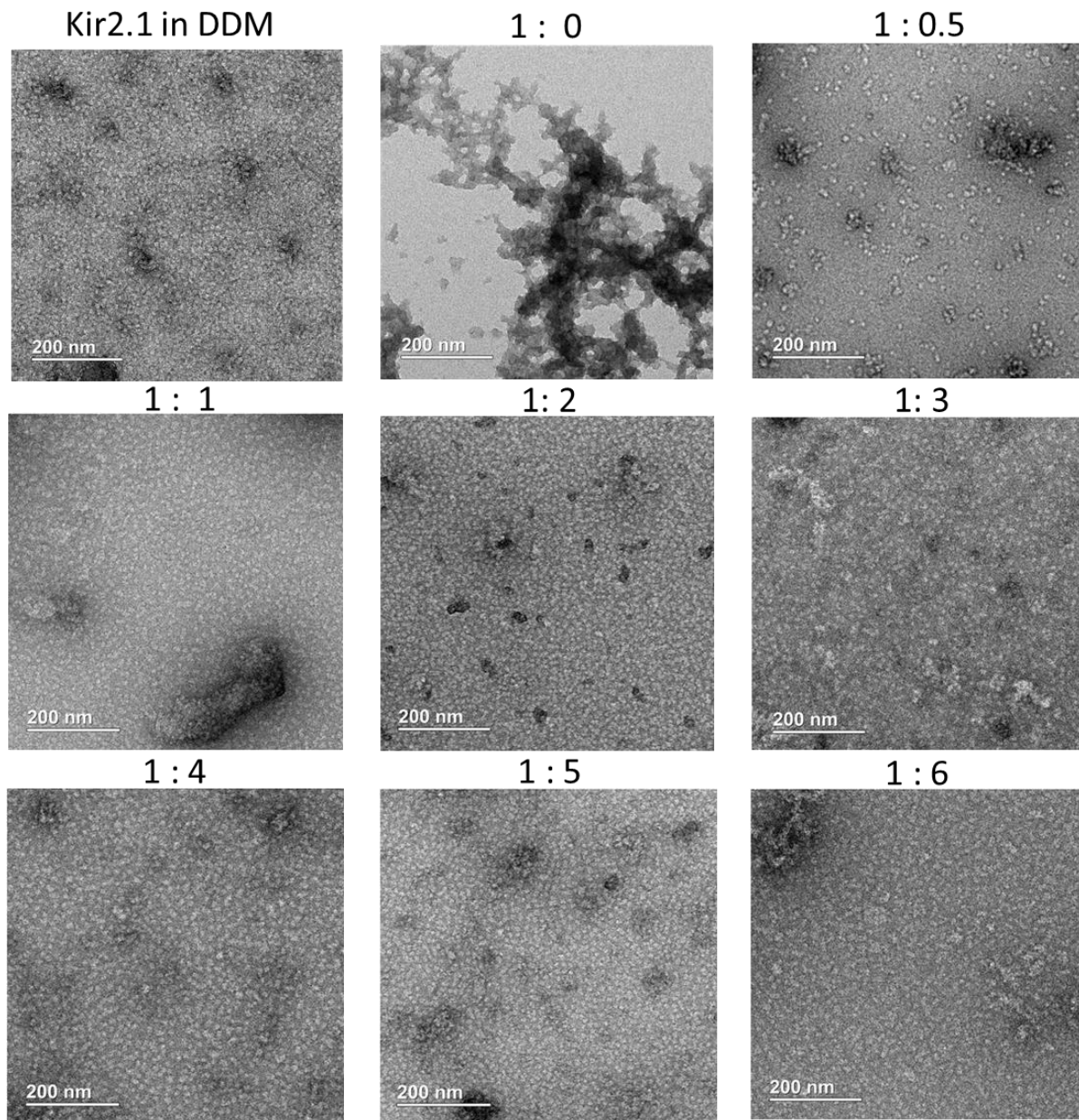


Figure 5-3 Kir2.1 to Apol ratios

A stability test was performed with the ratio of 1:4, where a negative staining image was taken on day zero (Figure 5-4, left), the protein was stored at 4 °C for 7 days, and grids were prepared on day seven (Figure 5-4, right), and observed again by negative staining. The results indicated that Kir2.1 was very stable in Apol, as there was minimal aggregation after a week, the particles showed good distribution on the grid, and the particles retained their usual appearance. Kir2.1 in detergent (DDM) does not show this stability and starts to aggregate after 3 days.

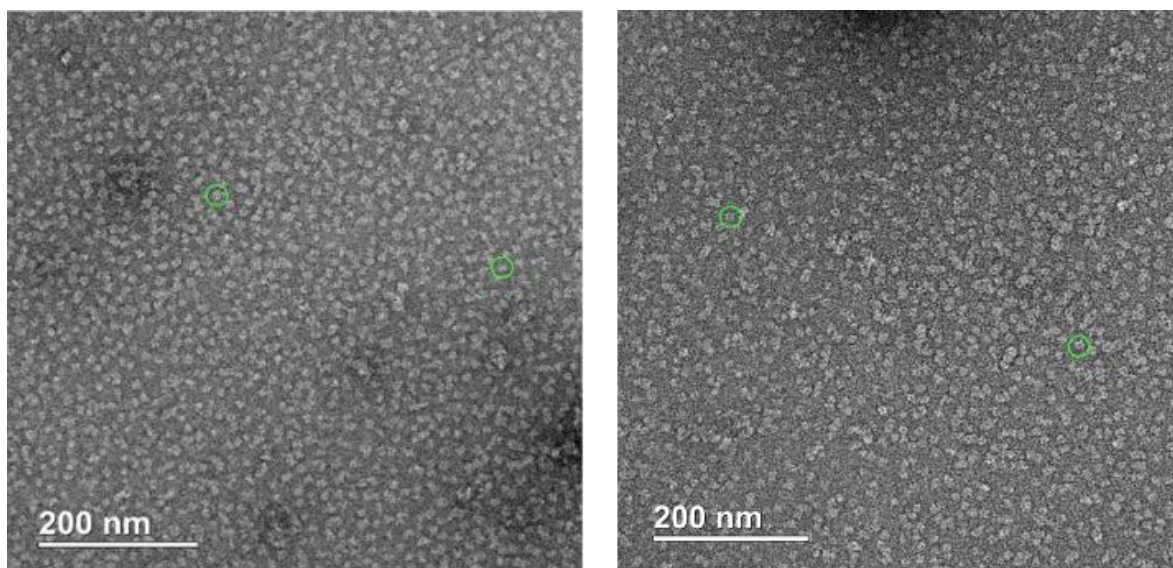


Figure 5-4. Negative staining image of Kir2.1 1:4 Apol. In each image, two Kir2.1 particles are selected (in a green circle) as an example. Left panel: Image taken right after exchange. The particles are homogeneous with an even distribution throughout the grid. Right panel: shows the same sample after one week of storage at 4 °C. The individual particles remain discernible (with some clustering) and well distributed throughout the grid.

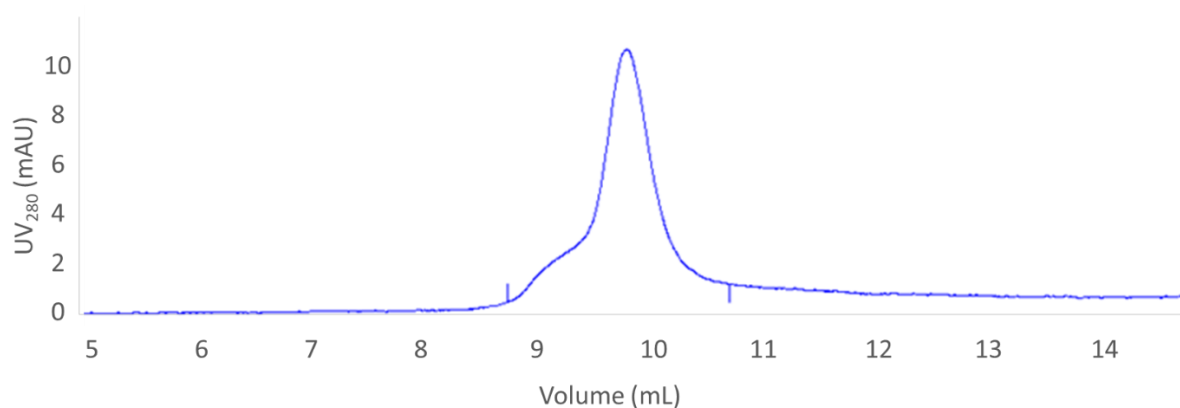


Figure 5-5 SEC profile of Kir2.1-Apol

An SEC was performed after reconstitution into Apols. The elution profile showed no indications of aggregation, and Kir2.1-Apols eluted as a single peak at 9.76 mL with a corresponding R_s of 65 Å (in agreement with 64.7 ± 1.3 Å in Kir2.1-DDM).

5.2.2.2 The cryo-EM grid preparation trials.

Following the encouraging results observed of Kir2.1-Apol on negative staining and SEC profile, I investigated the sample using cryo-EM to determine the potential of obtaining a structure at a higher resolution. For this, I tested two parameters in parallel: eliminating the extra carbon layer from the QF grids (in DDM) and the effect of the exchange into Apol on the distribution of particles on the grid.

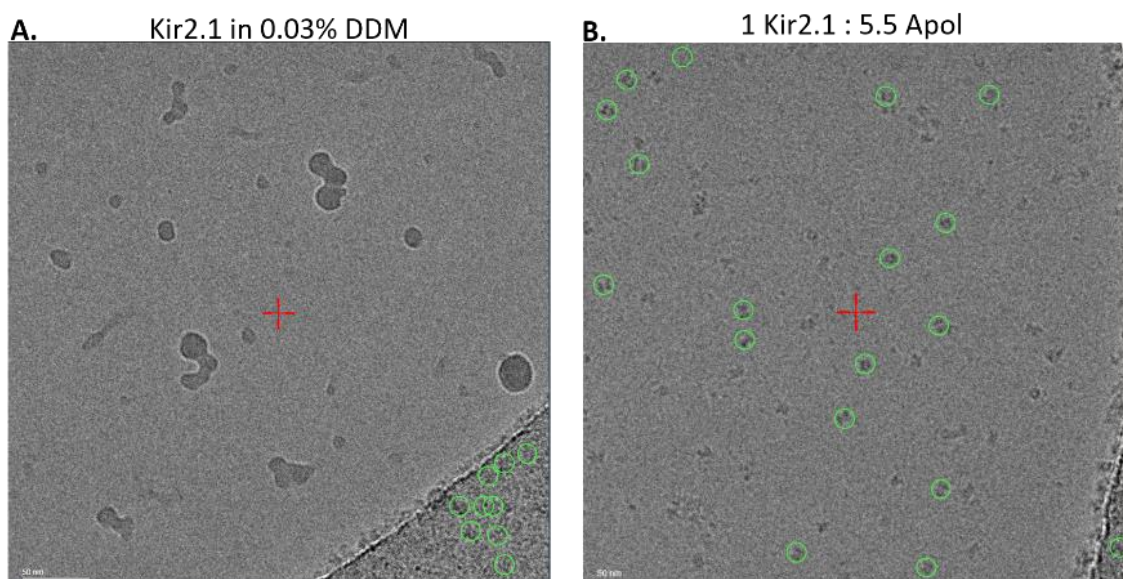


Figure 5-6. Cryo-EM image of Kir2.1 in DDM and in Apol. Kir2.1 appears as a gray particle on a gray background. A) Kir2.1 at $0.4 \text{ mg} \cdot \text{mL}^{-1}$ in 0.03% DDM showed no particles in the foil holes without an extra carbon layer. B) Kir2.1 at $0.4 \text{ mg} \cdot \text{mL}^{-1}$ at 1: 5.5 Apol ratio deposited well in the foil holes without carbon.

The distribution of Kir2.1 was investigated in different types of cryo-EM grids, including QF, Lacey, and UltrAuFoil QF (Table 5-3). Kir2.1-DDM did not deposit into the holes (Figure 5-6 A) unless carbon was present, apart from the UltrAuFoil grids made of a gold support and gold film. The freezing conditions of Kir2.1-DDM in UltrAuFoil grids are currently being explored with essential ligands. On the other hand, Kir2.1 in Apols was deposited into the foil holes (Figure 5-6 B) in all the grids tested using the same blotting conditions.

Table 5-3 Summary of grid distribution of Kir2.1 in DDM vs. in Apols

Grid Type	Grid Support	Grid Film	+ Carbon layer	Kir2.1 distributed in foil holes?	
				DDM	A8-35
QF	Cu	C	No	No	n/a
Lacey	Cu	C	No	No	n/a
QF	Cu	C	Yes	Yes	Yes
QF	Au	C	No	No	Yes
UltrAuFoil	Au	Au	No	Yes	Yes

5.2.2.3 Grid preparation, data collection, and image analysis of Kir2.1 in Apol

3 μL of purified Kir2.1-Apol (1:5.5 ratio) at $0.6 \text{ mg} \cdot \text{mL}^{-1}$ was added to glow discharged QF 1.2-1.3 300 mesh gold grids, using the same blotting conditions as Kir2.1-DDM.

18,826 images were collected at 105,000x magnification on the Krios Titan 300 kV in electron counting mode at identical conditions as section 2.5.5.2 data collection with the following exceptions: exposures of 2.11 s dose-fractionated into 60 frames with a dose rate of $1.02 e^-/\text{\AA}^2$, resulting in a total dose of $58.86 e^-/\text{\AA}$, and the defocus ranged from -0.6 to $-2.4 \mu\text{m}$, with $0.2 \mu\text{m}$ regular intervals. Two acquisitions were made per foil-hole.

After manual inspection, the micrographs containing poor ice quality or too much carbon (outside the foil hole) were discarded, and only 6,961 images were retained for image analysis. The movies were motion-corrected and dose-weighted using MotionCor2 (Zheng et al. 2017). The CTF parameters were estimated using CTFFIND4 (Rohou et Grigorieff 2015). Only the 6,641 images with a resolution below 7\AA were kept. A total of 2,188 particles were picked manually using SHIRE-crYOLO, and a picking model was created using the PhosaurusNet network to train the software. A total of 781,076 particles were picked using SPHIRE-crYOLO and were submitted to 2D classification using RELION. The extracted particles were binned 4 times and subject to one round of 2D classification (100 classes). Forty-six classes containing 720,622 particles were selected for the 3D initial model using a C1 and C4 symmetry (no binning). The C1 initial model was chosen and subject to 3D classification using no applied symmetry. A 3D class containing 223,834 particles was subject to a second round of 3D classification.

Kir2.1 in Apols provided a much better contrast than in DDM. The particles were visible even at a low defocus, $-0.8 \mu\text{m}$, allowing us to set the data collection at a lower defocus than Kir2.1-DDM. More micrographs were estimated to reach a resolution better than 5\AA .

The first round of 2D classification showed many particles in the top and bottom views, which were not as present in Kir2.1-DDM. This sample also revealed many more angles, as shown in Figure 5-7, bottom. In addition, some classes of the 2D classification show that we eliminated the thick layer of detergent around the TMD of the protein. It seems that the density of the Apols around the TMD is much lighter, which is a significant improvement as we suspect that this detergent layer might have limited the resolution of this transmembrane domain of the protein.

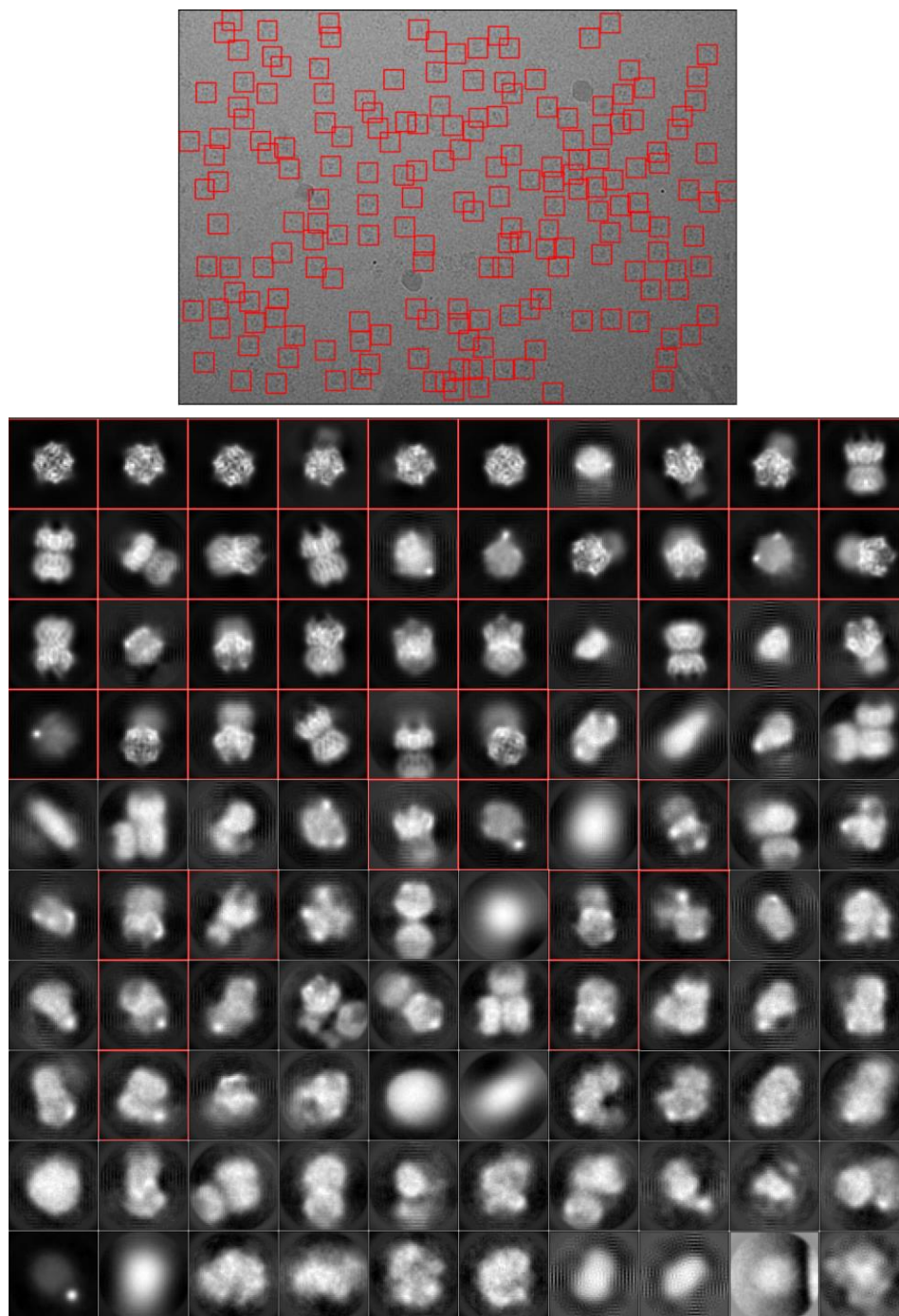


Figure 5-7. Particle picking and 2D classification of Kir2.1-Apol. The particles picked (top) and the 2D classes selected for the 3D initial model (bottom) are contoured by red squares.

Forty-six 2D classes containing 720,622 particles (Figure 5-7) were selected and used for the 3D initial model using a C1 and C4 symmetry. The 3D initial model with no imposed symmetry (C1) was chosen for the first round of 3D classification (Figure 5-8), where one class containing 223,834 particles was selected for a second 3D classification round. The Apol surrounding Kir2.1 was not apparent in these models either, contrary to the large DDM belt around Kir2.1, and the secondary structure was already quite visible at this stage (Chapter 4).

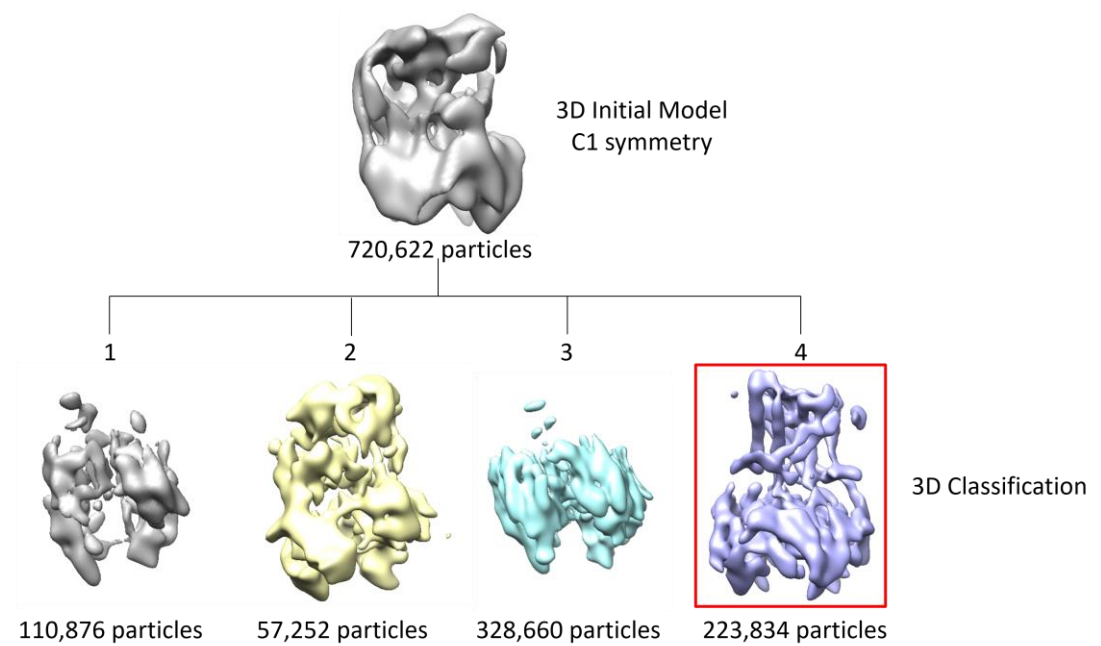


Figure 5-8. 3D initial model and the first round of 3D classification of h_Kir2.1 in Apols

I am currently doing the subsequent analysis on this data set and will be the subject of an upcoming article. However, we can already conclude that exchanging the protein into Apols provided a more stable environment that allowed us to obtain a better distribution of particles in the grids.

5.3 PART II: RECONSTITUTION KIR2.1 IN NANODISCS: INITIAL EXPERIMENTS

Obtaining a structure of Kir2.1 in Apols may allow us to reach a higher resolution and get more insights into the gating mechanisms. Notwithstanding, we search to observe Kir2.1 in a native-like environment associated with ligands. For this reason, I tried reconstituting Kir2.1 into nanodiscs containing POPC. Nanodiscs are discoidal lipid bilayers stabilized by membrane scaffolding proteins (MSPs). MSPs were ‘discovered’ by S. Sligar and are commercially available or can be obtained as plasmids to clone, produce, and purify.

5.3.1 Materials and Methods

5.3.1.1 Production of the Membrane Scaffolding Protein (MSP)

MSPs incorporated onto on pET28a plasmid, respectively, were a gift from S. Sligar and were sent in the form of DH5alpha bacterial stabs. The plasmid contained a kanamycin (Kan) resistance gene and the MSP synthetic gene (either MSP1, MSP1D1,

MSP1E1, or MSP1E3D1) coding for a Tobacco Etch Virus (TEV) cleavage site and a 6x histidine tag. DH5alpha bacteria were streaked onto Luria Broth (LB, Merck) and agar plates and incubated at 37 °C overnight. One single colony was added to a 2 mL LB medium with 50 $\mu\text{g} \cdot \text{mL}^{-1}$ Kan antibiotic and incubated overnight at 37 °C at 230 rpm.

The plasmid was isolated using QIAprep Spin Miniprep Kit (Qiagen) and following the manufacturer’s protocol for low-copy plasmids. The DNA concentration was measured at 350 nm with the Nanodrop 2000. Competent BL21(DE3) cells (Agilent Technologies) were transformed by heat shock following the manufacturer’s instructions. Briefly, 100 μL of competent cells were added to 14-mL BD Falcon polypropylene round-bottom tubes, 25 mM β -ME was added, and the cells were incubated on ice for 10 min. 20 ng of DNA were added and incubated on ice for 30 min, followed by a 45-s heat pulse at 42 °C. After 2-min incubation on ice, 0.9 mL of preheated SOC medium (42 °C, Table 5-4) were added to the transformation reaction and incubated at 37 °C for 1 h at 230 rpm. The transformed cells were spread onto LB-agar plates with 50 $\mu\text{g} \cdot \text{mL}^{-1}$ Kan and incubated overnight at 37 °C.

5.3.1.2 Expression of MSP1D1: culture medium and growth conditions

The MSP was expressed and purified using previously published protocols (Denisov et al. 2004; Ritchie et al. 2009) with modifications for flask cultures instead of fermenters. A 30 mL starter LB culture containing 30 $\mu\text{g} \cdot \text{mL}^{-1}$ Kan was inoculated with a single colony of cells and incubated at 37 °C, 220 rpm until $\text{OD}_{600\text{nm}}$ reached approximately 0.4–0.6 (5–6 h) and stored overnight at 4 °C.

1 L Terrific Broth (TB, Table 5-4) was inoculated with enough starting culture to obtain an $\text{OD}_{600\text{nm}}$ of 0.04. The culture was then separated onto two Erlenmeyer flasks and incubated at 37 °C, 220 rpm, until attaining an $\text{OD}_{600\text{nm}}$ between 0.8–1.2 (about 3 h). 500 μL were aliquoted and labeled pre-induction for SDS PAGE analysis. The cells were induced for 3 h with 1 mM isopropyl β -D-1-thiogalactopyranoside (IPTG) at 37 °C, 220 rpm. The cells were pelleted at 8,000 $\cdot \text{g}$ for 10–15 min at 4 °C, the supernatant was then discarded, and the pellet was either used immediately or stored at -80 °C.

Table 5-4 Composition of MSP1D1 expression buffers

Reagent	LB medium	TB medium	SOC medium
Yeast extract (%)	2	2.4	0.5

Reagent	LB medium	TB medium	SOC medium
Tryptone (%)	2	2	2
Glycerol (%)	0.4	0.4	
Phosphate buffer		0.017 M KH ₂ PO ₄ , 0.072 M K ₂ HPO ₄	
NaCl (mM)	171		10
KCl (mM)			2.5
MgCl ₂ (mM)			10
Glucose (mM)			20

5.3.1.3 MSP1D1 purification

The cell pellet (4–6 g) was resuspended in 20–50 mL of 20 mM phosphate buffer pH 7.4, 1 mM PMSF. Triton X-100 was added to a 1% final concentration once the pellet was resuspended entirely, and some Benzonase (Merck) was added. The cells were lysed by sonication (Table 2-3), and the lysate was clarified by 30-min centrifugation at 30,000 · g, 4 °C.

The lysate was then incubated with 1 mL of pre-equilibrated Ni²⁺ Sepharose Metal Affinity resin (Cytiva) for 2.5 h at 4 °C. The sample was loaded onto a gravity column and washed with 25 CV of Buffer A, Buffer B, and Buffer C (Table 5-5). The MSP was eluted in 20 CV of Buffer D.

Ten 1.5-mL elution fractions were collected and analyzed by SDS-PAGE. The fractions containing the MSP were pooled and dialyzed overnight against Buffer E at 4 °C. The protein sample was filtered using 0.22 µm PES membrane, concentrated to 4–13 mg · mL⁻¹ using Pierce™ Protein Concentrator PES, 10K MWCO, and stored at 4 °C if used directly or –80 °C for later use.

Table 5-5 Composition of buffers for purification of MSP1D1 and MSP1E3D1

Name	Composition
Buffer A	40 mM Tris-HCl, 0.3 M NaCl, 1% Triton X-100, pH 8.0
Buffer B	40 mM Tris-HCl, 0.3 M NaCl, pH 8.0
Buffer C	40 mM Tris-HCl, 0.3 M NaCl, 20 mM imidazole, pH 8.0
Buffer D	40 mM Tris-HCl, 0.3 M NaCl, 0.4 M imidazole
Buffer E	20 mM Tris-HCl, 0.1 M NaCl, 0.5 mM EDTA, pH 7.4, and 0.01% NaN ₃
Nanodisc Buffer	10 mM Tris-HCl pH 7.5, 0.1 M NaCl, 0.05 M KCl, and some NaN ₃

5.3.1.4 Lipid preparation

200 μL of lipid 1-palmitoyl-2-Oleoyl-sn-glycero-3-phosphocholine (POPC, 850457C, Avanti Polar) at $10 \text{ mg} \cdot \text{mL}^{-1}$ in chloroform were aliquoted into glass vials with Teflon caps. The chloroform was evaporated under a stream of argon, and the remainder was evaporated overnight with a vacuum pump.

Buffer containing either sodium cholate or DDM was added to the dried lipid to the desired concentration and vortexed. A stirring bar was added to the tube, and the lipid was left to resuspend overnight. If the lipid was not resuspended properly, a sonication step in an ultrasonic bath was done until the solution became clear and no lipid was visible on the vial walls.

5.3.1.5 Preparation of MSP1D1: POPC empty nanodiscs

MSP1D1 and POPC lipids were added at different molar ratios (1:30, 1:65, 1:75, 1:95, and 1:200, Table 5-6) to an Eppendorf tube on ice for a final volume of 200 μL . Sodium cholate was supplemented to a final concentration of 20 mM. The mixture was incubated for 4 h at 4 $^{\circ}\text{C}$. Bio-beads were added at either 0.5 g per mL or 20 times the amount of detergent present, whichever was more. The mixture was incubated under gentle agitation overnight. Each sample was centrifugated to remove the Bio-Beads, concentrated if needed, and purified by SEC using Nanodisc buffer (Table 5-5). Fractions of 0.5 mL were collected and were investigated by electrophoresis and negative staining to determine the fractions corresponding to empty nanodiscs and proteoliposomes.

Table 5-6 Empty MSP1D1: POPC Nanodisc ratios

	MSP1D1	POPC		MSP1D1		POPC			
$\text{mg} \cdot \text{mL}^{-1}$	4.02	5	Molar ratio	1	30	65	75	95	200
MW	24662	760.076	mM	0.02	0.6	1.3	1.5	1.9	4
mM	0.163	6.58	Volume	25	18.6	40.3	46.5	58.9	123.9

5.3.1.6 Reconstitution of Kir2.1 in MSP1D1: POPC nanodiscs

The reconstitution followed the same protocol as empty nanodiscs (section 5.3.1.5) with the following changes: 400 μL to 600 μL of Kir2.1_R312H (after affinity chromatography) at $0.6 \text{ mg} \cdot \text{mL}^{-1}$ were mixed with MSP1D1 and either cholate-dissolved POPC or DDM-dissolved POPC at 1: 4: 380 and 1: 6: 570 ratios (Table 5-8).

Sodium cholate's final concentration in the mixture was 20 mM, while DDM was kept above 0.05%. The mixture was incubated at 4 °C for 1 h under gentle agitation. Kir2.1_R312H was used simply because I had more stock than Kir2.1_WT at the time. Their elution profiles and biophysical behavior are indistinguishable.

Table 5-7 Reconstitution of Kir2.1_R312H into MSP1D1: POPC Nanodisc

	Kir2.1_R312H	MSP1D1	POPC		Kir2.1_R312H	MSP1D1	POPC
mg · mL ⁻¹	0.6	4.02	5	Molar ratio	1	4	380
MW	206150	24662	760.076	mM	0.00291	0.01164	1.1058
mM	0.00291	0.163	6.58	Molar ratio	1	6	570
				mM	0.00291	0.01746	1.65887

5.3.2 Results

5.3.2.1 Purification of MSP1D1

The production and purification of MSP1D1 went smoothly, and aliquots of 4–13 mg · mL⁻¹ were easily obtained without needing optimization. An extra wash with sodium cholate should be added between Buffer B and Buffer C in the affinity chromatography if purity levels are not satisfactory. All of the MSP is eluted in the first three elution fractions. These three fractions were concentrated to 4–13 mg · mL⁻¹ and used for nanodisc reconstruction, first empty nanodiscs and then reconstruction of Kir2.1.

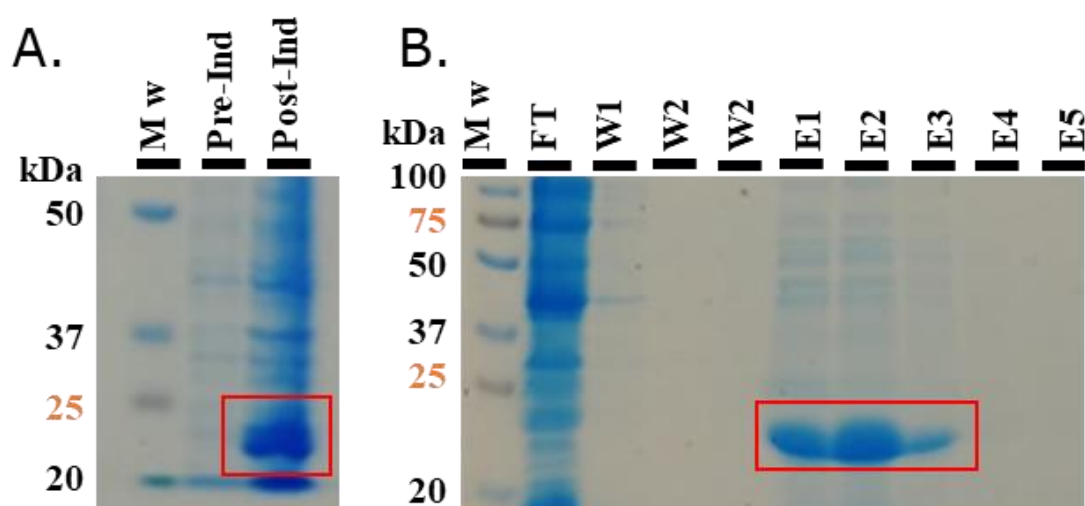


Figure 5-9. SDS PAGE of MSP1D1 production and purification fractions.

5.3.2.2 MSP1D1: POPC empty nanodiscs

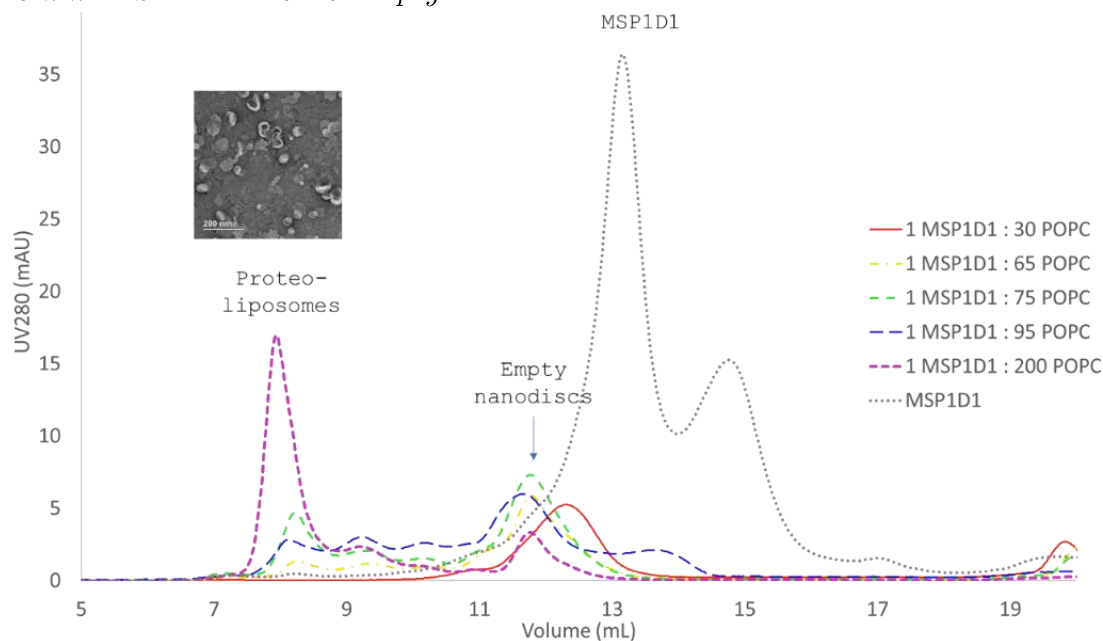


Figure 5-10. Formation of MSP1D1 and POPC empty nanodiscs using the S200 Increase column.

The best experimental MSP1D1: POPC ratio for the empty nanodiscs was 1:65 (Figure 5-10, yellow), in agreement with the literature. It eluted mainly as one peak at 11.8 mL corresponding to $47.2 \text{ \AA} R_H$. Ratio 1:30 eluted with an R_H smaller than the other ratios (12.38 mL) (Figure 5-10, red). Ratio 1:200 showed a significant reduction in the empty nanodisc peak and favored proteoliposomes and liposomes (Figure 5-10, magenta). These empty nanodisc injections allowed calibration of the column with the expected elution volumes for proteoliposomes (8 mL), empty nanodiscs (11.8 mL), and MSP alone (13.2 and 14.8 mL).

Ratio 1:95 (Figure 5-10, blue) provided interesting results; the empty nanodisc peak was slightly shifted to the left from the 11.8 mL elution volume observed in 1:65, 1:75, and 1:200 ratios. Seduced by the temptation of bigger nanodiscs without increasing the proteoliposome peak, we used this starting ratio for the initial reconstitution of Kir into nanodiscs.

5.3.2.3 Reconstitution of Kir2.1 in MSP1D1: POPC nanodiscs

The reconstitution followed the same protocol as empty nanodiscs with the following changes: 400 μL to 600 μL of Kir2.1_R312H (after affinity chromatography) at $0.6 \text{ mg} \cdot \text{mL}^{-1}$ were mixed with MSP1D1 and either cholate-dissolved POPC or DDM-dissolved POPC at 1: 4: 380 and 1: 6: 570 ratios (Table 5-8). Sodium cholate's final

concentration in the mixture was 20 mM, while DDM was kept above 0.05%. The mixture was incubated at 4 °C for 1 h under gentle agitation.

Table 5-8 Reconstitution of Kir2.1_R312H into MSP1D1: POPC Nanodiscs

	Kir2.1_R312H	MSP1D1	POPC		Kir2.1_R312H	MSP1D1	POPC
mg · mL ⁻¹	0.6	4.02	5	Molar ratio	1	4	380
MW	206150	24662	760.076	mM	0.00291	0.01164	1.1058
mM	0.00291	0.163	6.58	Molar ratio	1	6	570
				mM	0.00291	0.01746	1.65887

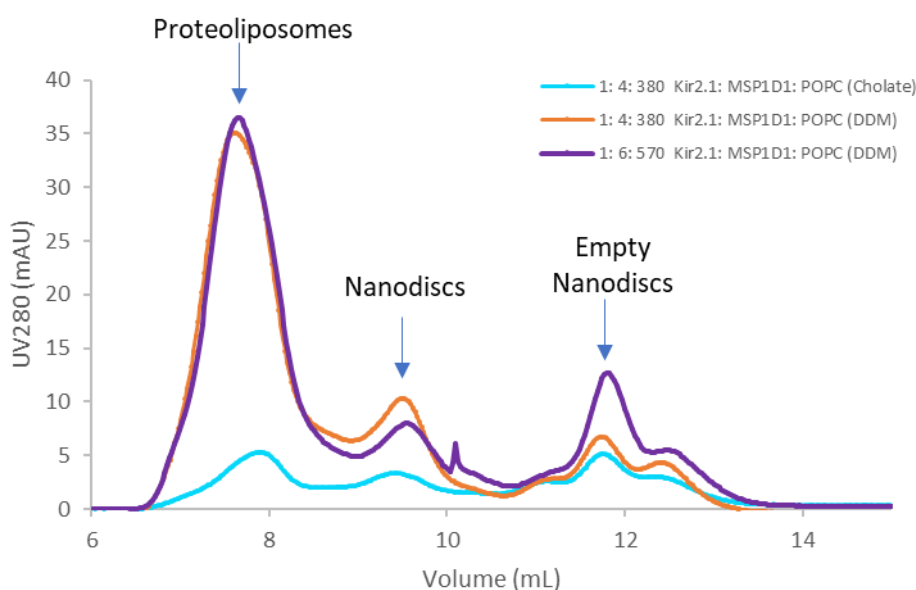


Figure 5-11. SEC elution profile of nanodisc formation using MSP1D1 and POPC using S200 Increase column.

The ratio 1: 6: 570 showed a small percentage of protein reconstituted into nanodiscs, with a vast majority eluting as proteoliposomes and some empty nanodiscs. The ratio 1: 4: 380 showed fewer empty nanodiscs and increased nanodiscs containing Kir2.1_R312H. This suggested that a smaller MSP ratio was to be favored. It also showed that 95 POPC molecules per MSP were too much.

Next, the theoretical expected optimal ratio of MSP to POPC ratio was calculated for Kir2.1. The theoretical cross-sectional area for Kir2.1 by the number of TM segments was 1400 Å². I measured at different points from the cryo-EM structure and obtained a cross-sectional area ranging from 1385 to 1734 Å². The protein is therefore expected to displace 20 to 25 POPC molecules from the nanodisc. The optimal ratios are expected to be close to 1:40 -1:45 MSP: POPC.

Table 5-9 Expected optimal ratio of MSP1D1 to POPC for Kir2.1

	# of POPC	Bilayer area per Nanodisc (\AA^2)	POPC (\AA^2)	Theoretical Cross-sectional area (\AA^2)	Calculated Cross-Sectional area (\AA^2)	POPC displaced by Kir2.1	Expected optimal MSP-POPC ratio
MSP1D1	65	4400	67-69	1400	1385 -1734	20-25	1:40 – 1:45

Ratios 1: 4: 160, 1: 4: 200, and 1: 4: 240 provided fewer proteoliposomes and better results but still yielded a high proteoliposome peak. The lower POPC ratios provided the least proteoliposomes but were still very significant. The following ratio to test would reduce the MSP amount from four to two and one per Kir2.1 tetramer. Notably, ratios 1:1:45 and 1:2:80. These two ratios should provide fewer proteoliposomes and empty nanodiscs. Although optimization of the ratios of Kir2.1 to MSP to POPC lipid is still needed, all the ratios tried yielded nanodiscs containing the protein, which is very encouraging. Ultimately once the yield is improved, these nanodiscs will be used for structural purposes and to characterize the interaction of Kir2.1 and many of the modulators described in the introduction.

5.4 DISCUSSION

5.4.1 Amphipols

The reconstitution into Apols provided a better distribution of Kir2.1 particles in the grid foil holes and a better contrast that allowed acquisition closer to the focal point. It allowed us to avoid using an extra carbon layer that added noise to our data in DDM. However, in many of the images discarded during the visual inspection, the ice was too thick. Perhaps the high Apol ratio contributed to this thickness. Research presented by B. Michon at the APPICOM GDR conference in 2021 pointed to an effect of the concentration of Apol on the ice-thickness and distribution of particles. His presentation showed that below $0.3 \text{ g} \cdot \text{L}^{-1}$ Apol concentration, no particles were distributed inside the hole as the ice was not thick enough. In these experiments, the Apol concentration was at $0.48 \text{ g} \cdot \text{L}^{-1}$. It is then possible that the effect we are observing is not intrinsic to the Apols but rather an effect of ice thickness. However, with DDM, we cannot afford to increase the detergent or protein concentration.

5.4.2 Nanodiscs

Altogether the nanodisc formation was somewhat successful; however, there is much room for improvement as many proteoliposomes were formed and empty nanodiscs, indicating an excess of lipid and MSP. Two areas can be optimized to obtain cleaner

elution profiles. 1) Reduce the amount of MSP per Kir2.1 to 1 and 2, consequently reducing the amount of POPC available to form liposomes. 2) Either produce Kir2.1 and MSP containing different tags to eliminate the empty nanodiscs after affinity chromatography or remove the MSP tag after purification.

MSP1D1 was a good MSP to start; however, the nanodiscs formed will be too small for the subsequent experiments as they can only theoretically host 45 POPC molecules. We want to test lipid mixtures to mimic the lipid bilayer more closely, including PIP₂. A. Zoumpoulakis will carry on this work and optimize the reconstitution using MSP1E3D1 (Ilia G. Denisov et al. 2007), an extended version of MSP1D1, which has already been produced using the same protocol as MSP1D1.

5.5 REFERENCES

- Choy, Brendon C., Rosemary J. Cater, Filippo Mancia, et Edward E. Pryor. 2021. « A 10-Year Meta-Analysis of Membrane Protein Structural Biology: Detergents, Membrane Mimetics, and Structure Determination Techniques ». *Biochimica et Biophysica Acta (BBA) - Biomembranes* 1863 (3): 183533. <https://doi.org/10.1016/j.bbamem.2020.183533>.
- Denisov, I. G., Y. V. Grinkova, A. A. Lazarides, et S. G. Sligar. 2004. « Directed Self-Assembly of Monodisperse Phospholipid Bilayer Nanodiscs with Controlled Size ». *Journal of the American Chemical Society* 126 (11): 3477-87. <https://doi.org/10.1021/ja0393574>.
- Denisov, Ilia G., Bradley J. Baas, Yelena V. Grinkova, et Stephen G. Sligar. 2007. « Cooperativity in Cytochrome P450 3A4 ». *Journal of Biological Chemistry* 282 (10): 7066-76. <https://doi.org/10.1074/jbc.M609589200>.
- Le Bon, Christel, Baptiste Michon, Jean-Luc Popot, et Manuela Zoonens. 2021. « Amphipathic Environments for Determining the Structure of Membrane Proteins by Single-Particle Electron Cryo-Microscopy ». *Quarterly Reviews of Biophysics* 54: e6. <https://doi.org/10.1017/S0033583521000044>.
- Popot, Jean-Luc. 2010. « Amphipols, Nanodiscs, and Fluorinated Surfactants: Three Nonconventional Approaches to Studying Membrane Proteins in Aqueous Solutions ». *Annual Review of Biochemistry* 79 (1): 737-75. <https://doi.org/10.1146/annurev.biochem.052208.114057>.
- Ritchie, T.K., Y.V. Grinkova, T.H. Bayburt, I.G. Denisov, J.K. Zolnerciks, W.M. Atkins, et S.G. Sligar. 2009. « Reconstitution of Membrane Proteins in Phospholipid Bilayer Nanodiscs ». In *Methods in Enzymology*, 464:211-31. Elsevier. [https://doi.org/10.1016/S0076-6879\(09\)64011-8](https://doi.org/10.1016/S0076-6879(09)64011-8).
- Rohou, Alexis, et Nikolaus Grigorieff. 2015. « CTFFIND4: Fast and Accurate Defocus Estimation from Electron Micrographs ». *Journal of Structural Biology* 192 (2): 216-21. <https://doi.org/10.1016/j.jsb.2015.08.008>.
- Zheng, Shawn Q., Eugene Palovcak, Jean-Paul Armache, Kliment A. Verba, Yifan Cheng, et David A. Agard. 2017. « MotionCor2: Anisotropic Correction of Beam-Induced Motion for Improved Cryo-Electron Microscopy ». *Nature Methods* 14 (4): 331-32. <https://doi.org/10.1038/nmeth.4193>.

**6 SIDE PROJECTS: A BACTERIAL
HOMOLOG KIRBAC3.1 AND MUTANTS
W46R AND S129R**

6.1 INTRODUCTION

In our search to understand the gating mechanisms of Kir channels, we evaluated the functional implications of a conserved residue in the TMD and explored the gating behavior of constitutively open channels.

These two side projects aimed to experimentally validate the computational studies on the open and closed populations of KirBac3.1 performed using molecular dynamics and normal modes (C. Fagnen). I expressed two mutants of a bacterial homolog to human Kir2.1, KirBac3.1 (S129R and W46R) in *Escherichia coli* and purified them by affinity chromatography followed by size exclusion chromatography. W46R is the bacterial homologous mutation corresponding to the human Kir6.2 channel W68R mutation that causes hyperinsulinism in humans. KirBac3.1_S129R is the mutant channel containing an engineered mutation in the inner pore-lining helix (TM2) that causes the channel to be trapped in an open conformation. Electrophysiological tests were performed on purified W46R and S129R to obtain channel open probabilities that successfully validated the computational studies. This work resulted in two publications shown here.

Integrative study of the structural and dynamical properties of a KirBac3.1 mutant: functional implication of a highly conserved tryptophan in the transmembrane domain.

Charline Fagnen¹, Ludovic Bannwarth², Iman Oubella³, Dania Zuniga⁴, Ahmed Haouz⁵, Eric Forest⁶, Rosa Scala⁷, Saïd Bendahhou⁸, Rita De Zorzi⁹, David Perahia¹⁰ and Catherine Vénien-Bryan^{11*}

Citation: Fagnen, C.; Bannwarth, L.; Oubella, I.; Zuniga, D.; Haouz, A.; Forest, E.; Scala, R.; Bendahhou, S.; De Zorzi, R.; Perahia, D.; et al. Integrative Study of the Structural and Dynamical Properties of a KirBac3.1 Mutant: Functional Implication of a Highly Conserved Tryptophan in the Transmembrane Domain. *Int. J. Mol. Sci.* **2022**, *23*, 335. <https://doi.org/10.3390/ijms23010335>

Academic Editor: Firstname Lastname

Received: date

Accepted: date

Published: date

Publisher's Note: MDPI stays neutral with regard to jurisdictional claims in published maps and institutional affiliations.



Copyright: © 2021 by the authors. Submitted for possible open access publication under the terms and conditions of the Creative Commons Attribution (CC BY) license (<https://creativecommons.org/licenses/by/4.0/>).

- ¹ Sorbonne Université, UMR 7590, CNRS, Muséum National d'Histoire Naturelle, Institut de Minéralogie, Physique des Matériaux et Cosmochimie, IMPMC, 75005 Paris, France AND Laboratoire de Biologie et Pharmacologie Appliquée, Ecole Normale Supérieure Paris-Saclay, 4 Ave. des Sciences, 91190 Gif-sur-Yvette, France charline.fagnen@unicaen.fr
- ² Sorbonne Université, UMR 7590, CNRS, Muséum National d'Histoire Naturelle, Institut de Minéralogie, Physique des Matériaux et Cosmochimie, IMPMC, 75005 Paris, France L_bannwarth@hotmail.com
- ³ Sorbonne Université, UMR 7590, CNRS, Muséum National d'Histoire Naturelle, Institut de Minéralogie, Physique des Matériaux et Cosmochimie, IMPMC, 75005 Paris, France i.oubella@hotmail.fr
- ⁴ Sorbonne Université, UMR 7590, CNRS, Muséum National d'Histoire Naturelle, Institut de Minéralogie, Physique des Matériaux et Cosmochimie, IMPMC, 75005 Paris, France dania.zuniga@sorbonne.universite.fr
- ⁵ Institut Pasteur, C2RT-Plate-forme de Cristallographie, CNRS-UMR3528, 75724 Paris, France ahmed.haouz@pasteur.fr
- ⁶ University Grenoble Alpes, IBS, F-38044 Grenoble, France, CNRS, IBS, F-38044 Grenoble, France, CEA, IBS, F-38044 Grenoble, France Deceased
- ⁷ University Côte d'Azur, CNRS UMR7370, LP2M, Labex ICST, Faculté de Médecine, Nice, France. rosa.scala@univ-cotedazur.fr
- ⁸ University Côte d'Azur, CNRS UMR7370, LP2M, Labex ICST, Faculté de Médecine, Nice, France said.bendahhou@univ-cotedazur.fr
- ⁹ Department of Chemical and Pharmaceutical Sciences, University of Trieste, Via Licio Giorgerim 1, 34127, Trieste, Italy rdezorzi@units.it
- ¹⁰ Laboratoire de Biologie et Pharmacologie Appliquée, Ecole Normale Supérieure Paris-Saclay, 4 Ave. des Sciences, 91190 Gif-sur-Yvette, France david.perahia@ens-paris-saclay.fr
- ¹¹ Sorbonne Université, UMR 7590, CNRS, Muséum National d'Histoire Naturelle, Institut de Minéralogie, Physique des Matériaux et Cosmochimie, IMPMC, 75005 Paris, France catherine.venien-bryan@sorbonne-universite.fr
- ¹² Correspondence: catherine.venien-bryan@sorbonne-universite.fr

Abstract: ATP-sensitive potassium (K-ATP) channels are ubiquitously expressed on the plasma membrane of cells in several organs, including the heart, pancreas, and brain, and they govern a wide range of physiological processes. In pancreatic β -cells, K-ATP channels composed of Kir6.2 and SUR1 play a key role in coupling blood glucose and insulin secretion. A tryptophan residue located at the cytosolic end of the transmembrane helix is highly conserved in eukaryotes and prokaryote Kir channels. Any mutation on this amino acid causes a gain of function and neonatal diabetes mellitus. In this study, we have investigated the effect of mutation on this highly conserved residue on a KirBac channel (prokaryotic homolog of mammalian Kir6.2). We provide the crystal structure of the mutant KirBac3.1 W46R (equivalent to W68R in Kir6.2) and its conformational flexibility properties using HDX-MS. In addition, the detailed dynamical view of the mutant during the gating was investigated using *in silico* method. Finally, functional assays have been performed. A comparison of important structural determinants for the gating mechanism between the wild type KirBac and the mutant W46R suggests interesting structural and dynamical clues and suggests a mechanism of action of the mutation that leads to the gain of function.

Keywords: crystal structure of KirBac3.1W46R; HDX-Mass Spectrometry; Molecular Dynamics; Normal Modes; electrophysiology; gain of function Kir; neonatal diabetes mellitus

1. Introduction

Inwardly rectifying potassium channel (Kir channel) regulates membrane electrical excitability and K⁺ transport in a wide range of cell types. They control various processes, including vascular tone, heart rate, and insulin secretion. Dysfunctional Kir channels are directly associated with a growing number of diseases [1]. Kir channel activity is controlled by dynamic conformational changes that regulate the flow of K⁺ ions through the central pore of the channel [1, 2]. This process is known as 'gating,' and understanding the molecular mechanism behind these dynamic changes in the structure of Kir channels is essential to understanding how these channels function for both health and disease.

Kir6.1 and Kir6.2 are typical Kir channels; they have two transmembrane helices, TM1 and TM2, linked by a pore loop, and intracellular amino and carboxy termini. When associated with sulfonylurea receptor proteins (SUR1 or SUR2, belonging to the ABC (ATP-Binding Cassette) transporter superfamily), they form the ATP-sensitive potassium (K-ATP) channels. K-ATP channels are primarily expressed in the pancreatic endocrine islets, brain, cardiac myocytes, skeletal muscle, and vascular smooth muscle [3]. K-ATP channels consist of the pore-forming subunits, Kir6.1 and Kir6.2, and a large auxiliary subunit, SUR1, SUR2A, and SUR2B. Four SURs and four Kir6.x form an octameric channel complex. The association of a specific SUR with a particular Kir6.x subunit forms the K-ATP of a particular tissue. They have various physiological roles, including controlling the release of insulin from pancreatic β cells and regulating blood vessel tone and blood pressure [30].

K-ATP channels are so-called because they open when cellular ATP levels fall, thus linking cellular metabolism to membrane excitability. They also respond to Mg-ADP and are regulated by several cell signaling pathways [1, 4, 5]. K-ATP channels detect metabolic changes *via* three classes of ATP/ADP binding sites. One site, located on the Kir subunit, causes inhibition of the channel (close the channel) when ATP is bound. The other two sites, located on the NBDs (nucleotide-binding-domain) of SUR subunit, bind to Mg²⁺-ATP and Mg²⁺-ADP, causing dimerization of the NBDs, which counteracts the inhibitory action of ATP on Kir6.2 and thereby stimulate channel [30].

Blood glucose levels determine ATP and ADP concentrations. When glucose levels rise, the intracellular ATP to ADP ratio increases due to glycolysis, and ATP inhibition dominates suppressing K-ATP channel activity. On the contrary, the ATP to ADP ratio decreases when blood glucose level drops and MgADP stimulation prevails, increasing channel activity. Loss-of-function mutations cause hyperinsulinemic hypoglycemia of infancy, characterized by persistent and unregulated insulin secretion and life-threatening hypoglycemia. Conversely, gain-of-function mutations alter insulin secretion and produce neonatal diabetes mellitus, which manifests within the first six months of life. Because the K-ATP channel is also expressed in the brain, patients with functionally severe mutations can exhibit neurological symptoms in addition to neonatal diabetes mellitus, a condition known as DEND syndrome [6–11].

KirBac3.1, Kir6.2, and Kir6.1 channels are homotetramers of four subunits. Each subunit has a transmembrane domain (TMD), containing an outer transmembrane helix (TM1), a selectivity filter (SF), an inner transmembrane helix (TM2). Besides the TMD, there is a cytoplasmic domain (CTD) composed of N- and C- termini located on the intracellular side of the membrane.

A novel heterozygous dominant mutation, W68R, in the Kir6.2 subunit of the K-ATP channel, in a patient with transient neonatal diabetes, developmental delay, and epilepsy, has been identified [12] [REF]. This tryptophan residue at the cytosolic end of TM1 is very well conserved across the prokaryotic, eukaryotic, and mammalian Kir family and is found at the position W46 in KirBac3.1.

In this paper, we present the crystal structure of KirBac3.1 W46R mutant channel (homologous to the human Kir6.2 channel) at 2.80 Å and provide a structural and functional characterization using a multi-technique approach. The mutation replaces a tryptophan residue that is highly conserved across the Kir family to an arginine, disrupts the contacts between the outer (TM1) and inner (TM2) helices, and creates new contacts shown on our crystallographic data. HDX-MS experiments show differences in the conformational flexibility of the W46R mutant when compared with the KirBac3.1 WT. Besides, *in silico* molecular dynamics studies allow us to investigate in detail the influence of this mutated residue on the molecular mechanism of gating of the channel. Moreover, this mutated channel's open probability (P_o) has been investigated through functional experiments, finally corroborating the *in silico* investigations.

2. Results

2.1. Crystal Structure of KirBac3.1 W46R

The tryptophan at position 46 in KirBac3.1, corresponding to W68 in Kir6.2, located at the cytosolic end of transmembrane helix 1 (TM1) (Figure 1C), is highly conserved within the inward rectifying potassium channel family, suggesting that it has a critical role.

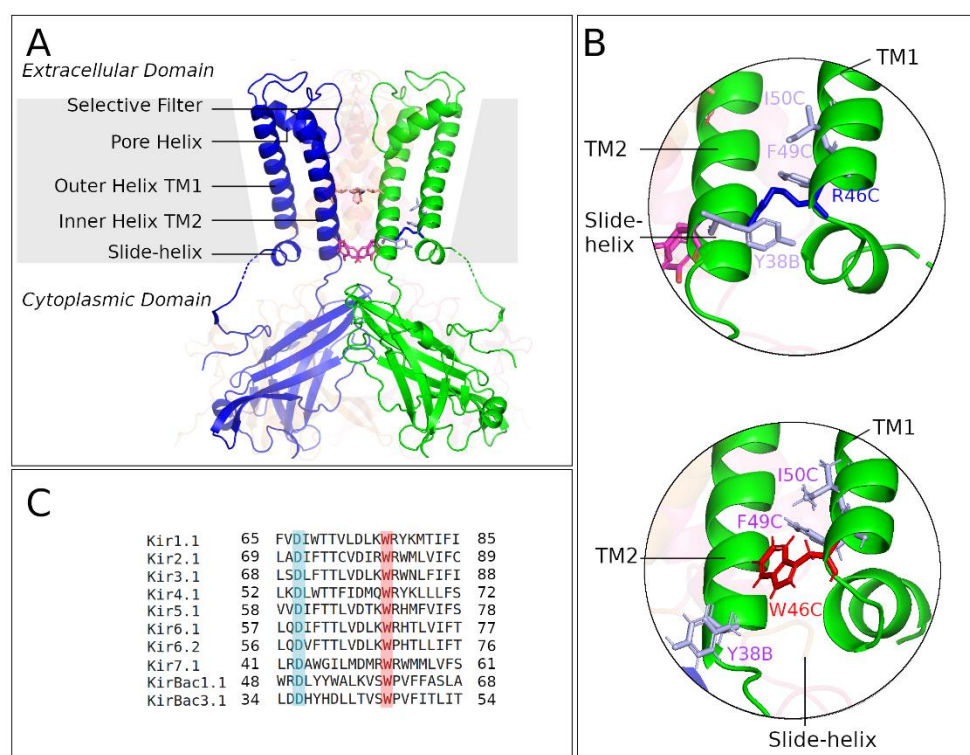


Figure 1. Crystallographic structure of KirBac3.1 W46R. A) Structure of KirBac3.1 W46R showing the location of the mutant R46 at the bottom of TM1. The grey area represents the membrane, and arrows indicate the various domains in the figure. Orange and magenta residues at the center of the channel correspond to the constriction points Leu124 and Tyr132, respectively. For clarity, two subunits out of four are represented. B) Top: Zoom on the area around the mutation R46 (blue) at the bottom of TM1 from chain C (R46-C) interacting with Y38-B on the slide helix of the n-1 chain (chain A counterclockwise neighbor chain). Bottom: Same area as above with KirBac3.1 WT (PDB 2WLJ). W46-C (chain C, in red) in the "flipped-in" conformation packed against the C-terminal end of TM2 (chain B). C) Alignment for Kir channels sequences. The tryptophan residue at the position corresponding to W68 in Kir6.2,

at the bottom of TM2, is absolutely conserved (pink). The aspartate residue at the position corresponding to D58 in Kir6.2, on the slide helix is also highly conserved (cyan); note that the Y38 (KirBac3.1) is equivalent to F61 (Kir6.2).

We expressed the mutant W46R of KirBac3.1, corresponding to pathological forms of the human homologous Kir6.2 channel, and investigated this mutant's high-resolution structure. The R46 mutation replaces the hydrophobic tryptophan and introduces a positively charged residue. The KirBac3.1 W46R mutant channel was expressed, purified, and crystallized, and the structure was solved and refined to 2.80 Å resolution. We grew crystals of the W46R mutant belonging to space group P2₁2₁2. The structure was solved by molecular replacement, and a final model containing 279 out of the 301 residues of the construct was refined to an R-factor of 22.2% and an R-free of 28.7%, with 99.3% of the residues in the final model lying either in the most favorable or in the allowed regions of the Ramachandran plot. The complete data collection and refinement statistics are shown in Table 1, and the crystallographic structure is shown in Figure 1A. A backbone alignment with the structure of the KirBac3.1 WT (PDB 2WLJ) [13] showed that the two structures were very similar (root mean square deviation, rmsd = 0.471 Å). Both structures, WT and W46R, are in a closed state.

Interestingly, despite this overall similarity, significant differences were evident in the vicinity of residue 46 (W or R) (Figures 1A and B). As a consequence of the mutation, a series of changes occur in the inter and intrasubunit interactions at the level of the bundle crossing at the bottom of the transmembrane helix compared with the KirBac3.1 WT (Figure 1B). In most X-ray structures of WT Kir channels, the residue corresponding to W68 in Kir6.2 is in the "flipped-in" conformation tightly packed against the C-terminal end of TM2, as seen in the crystal structure (Figure 1B bottom, residue marked as W46 according to KirBac3.1 numbering). As a result, the W46 side-chain interacts with the F135 and R134 at the bottom of the TM2 (Figure 3). More seldom, the tryptophan side-chain can adopt a different rotameric conformation ("flipped-out"), pointing away from the channel pore and removing the interaction with the bottom end of TM2 (Kir2.2, PDB 3JYC). The atomic structure of the W46R mutant shows that the four R46 side-chains point away from the channel pore and are engaged in intersubunit connections with residues Y38 and D36 on the slide helix of the adjacent subunit (n-1: counterclockwise neighbor chain) (Figure 1B top).

Data Collection	
Space group	P2 ₁ 2 ₁ 2
Cell dimensions (Å)	106.77, 113.98, 89.18
Cell angles	90° 90° 90°
Resolution (Å)	48.34-2.80
Completeness (%)	99.6
I/σ (I)	19.67 (1.31 in the high-resolution shell)
Clashscore	8
Ramachandran outliers	1.7%
Side-chain outliers	9.3%
Refinement with REFMAC 5.8.0258	
R, R free	0.222, 0.287
R free test set	1372 reflections (5%)

Wilson B-factors (\AA^2)	89.3
Total number of atoms	4341
Average B-factors, all atoms (\AA^2)	97.464
RMS of Z score of bond lengths	0.70
RMS of Z score of bond angles	0.89

Table 1 Data collection and structure refinement statistics for KirBac W46R

2.2. HDX-MS measurements

The conformational flexibility of KirBac3.1 W46R mutant was investigated using HDX-MS. This technique is based on the exchange of deuterium atoms at the amide backbone of a protein, reflecting its conformational dynamics, followed by proteolytic digestion and spectrometry analysis [14–16]. HDX has already been extensively used on soluble and membrane proteins [17–19]. HDX was performed on KirBac3.1 W46R mutant in the presence of detergent and compared to KirBac3.1 WT also in detergent and recently reported [17], Figure 2A. In previously published work, we have established that the presence of detergent does not affect the conformational changes of the KirBac3.1 channel [20]. We tested digestion with various proteases to achieve sequence coverage as extensively as possible. The optimized conditions resulted in 86% sequence coverage with nepenthesin. However, this enzyme did not allow coverage of regions 57-87 (second half of the TM1 and the beginning of the pore helix), 143-147 ($\beta 3$), and 195-199 (second half of the $\beta 7$). Deuterium incorporation was monitored as a function of time for each peptide generated from the W46R mutant (Figure S1).

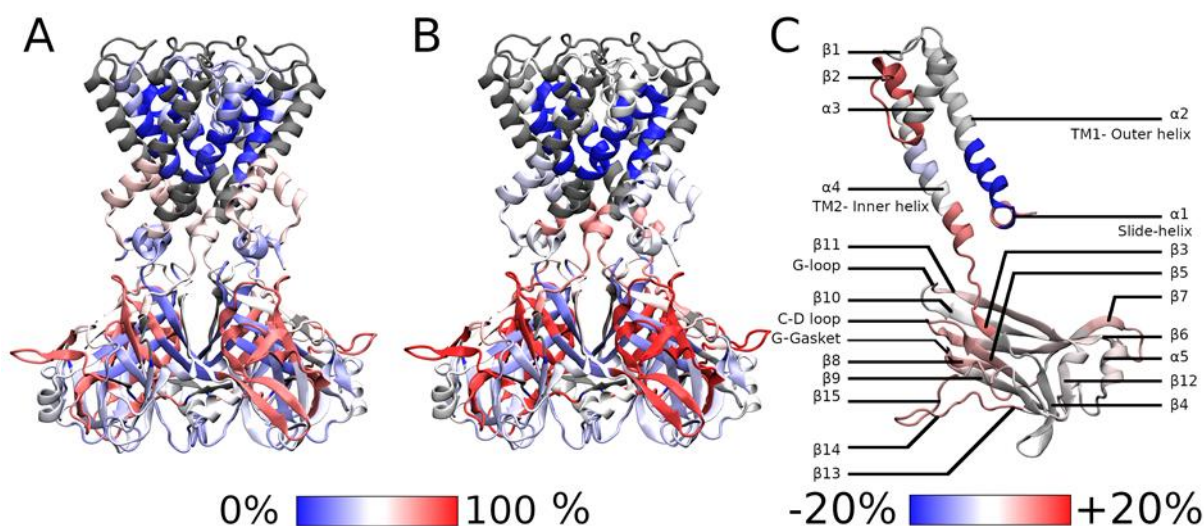


Figure 2. HDX-MS rates. A) HDX-MS rates of peptides reported for the KirBac3.1 WT [17] and B) for the mutant W46R. C) Rate difference between the W46R mutant and KirBac3.1 WT. The scale of the deuterium exchange rate is shown at the bottom of the figures, with blue corresponding to low exchange rate and high rigidity; and red to high exchange rate and high flexibility.

Our data show that the most flexible regions for KirBac3.1 W46R are the loops extending outside the CTD (aa 271-285 between $\beta 14$ et $\beta 15$, in red in Figure 2B, see Figure 2C for the nomenclature) with an HDX rate of 68.0%. The next, more flexible, three domains are: i) at the G-gasket just below the CD-loop and the entire $\beta 8$, (aa 199-210, with HDX rate of 66.0%); ii) the stretch going from the end of the $\beta 5$ and the start of the $\beta 6$ including the CD-loop in the middle (aa 162-174, HDX

rate of 65,7%); and iii) the stretch going from the end of $\beta 6$ and the start of $\beta 7$ including the facing-down loop in the middle (aa 181-194, with HDX rate of 64.1%). On the CTD, the stretch including the end of the G-loop and the following $\beta 11$ also shows some flexibility (aa 250-260, HDX rate of 43.1%).

In the transmembrane domain, the stretch at the bottom of TM2-loop and $\beta 3$, which includes the Y132 restriction point, shows some flexibility (aa 132-143, with an HDX rate of 53.7%). On the contrary, the top of the TM2, is exceptionally stiff, while the slide helix also shows less flexibility (aa 36-42, with an HDX rate of 28.9%).

We compared the conformational dynamics of the W46R mutant with the KirBac3.1 WT (Figure 2C). In the figure, the blue color on the structure indicates a higher rigidity for the W46R mutant than the WT, while red stretches represent regions where the mutant shows increased conformational flexibility. Interestingly, the stretch that includes the very end of the slide helix, R46 mutation, and the bottom half of the TM1 external helix (aa 43-56) is not as flexible as the WT (normalized HDX rate of 37.9% compared with 65.1%). The interactions network around the R46 residue is remarkably stable. This stretch including R46 is also the only part of the mutant protein which is more rigid than the WT. On the contrary, the stretch of aa 36-42 before the mutation and including most of the slide helix (excepted the very end) is more flexible than in the WT (normalized HDX rate of 41.57% compared with 26.92%). This difference is the largest of all the peptides analyzed.

Higher flexibility induced by the presence of the mutation has also been observed for other parts of the protein: i) on the stretch including the bottom of the pore helix, the selectivity filter, and the top of the external helix (aa 93-112, normalized HDX rate of 50.04% for the mutant compared with 30.08% for the WT); ii) on the stretch corresponding to the bottom of the internal helix and a large loop just before the $\beta 3$ (aa 131-143, normalized HDX rate 77.32% compared with 61.26%) where the increased deuterium exchange rate could be interpreted as a higher accessibility surface; iii) on the stretch corresponding to sheets $\beta 5$ and $\beta 6$ in the cytoplasmic domain and CD loop (aa 162-174, normalized HDX rate 94.61% compared with 83.1%); and iv) on the segment that includes the G-loop which is slightly more flexible in the case of the mutant (aa 250-260, normalized HDX rate 62.05% compared with 55.25%).

2.3. Theoretical Results on KirBac3.1 W46R

The theoretical results presented in this section are based on MDeNM simulations, in which a selected set of normal modes (NMs) related to channel gating are excited in molecular dynamics (MD) simulations [21]. Through a combination of MD and NMs, this method is a realistic exploration of the relevant normal mode space for the gating processes taking into account the full environment (water, ions, and membrane) of the protein at a given temperature. These simulations were supplemented by standard MD simulations on a uniformly distributed set of structures obtained from MDeNM that provide a reasonably good estimation of the open/closed (and partially open) states populations as previously reported [17, 22].

2.3.1. Interaction Networks

Interaction network analyses were performed on the crystallographic structures of KirBac3.1 WT (PDB 2WLJ) [13] and on the KirBac3.1 W46R mutant model (see Materials and Methods) to elucidate the impact of the mutation W46R on the structural and dynamical properties of the protein. The residue W46 in KirBac3.1 WT can adopt two alternative conformations, called flipped-in, in the majority of cases (side-chain of W46 oriented towards the channel) and flipped-out (side-chain of W46 oriented towards the outside of the channel) (Figure 3A). Figure 3C presents details on the flipped-in structure. The atomic structure of the W46R mutant shows that the four R46 side-chains point away from the channel pore in the crystal structure of the mutant W46R (Figure 3B). This is also observed in the obtained structures of KirBac3.1 W46R (98.68% of the 25415 relaxed MDeNM structures).

The first analysis focused on the KirBac3.1 WT: we compared the interaction networks (hydrogen bonds, van der Waals interaction, π - π and π -cation interactions) at the W46 residue level in flipped-in and flipped-out configurations. Interaction networks around W46 for these two configurations are shown in Figure 3 D, E, F, G respectively for chains A, B, C, and D, separately (for more details, see Figure S2). W46 is tightly packed against the C-terminal end of TM2 of the same subunit and interacts with R134 and F135 at the bottom of this inner helix in the flipped-in conformation. Conversely, in the flipped-out conformation, these interactions are not possible, confirming the movement of the W46 residue away from the bottom of the inner helix and the center of the channel.

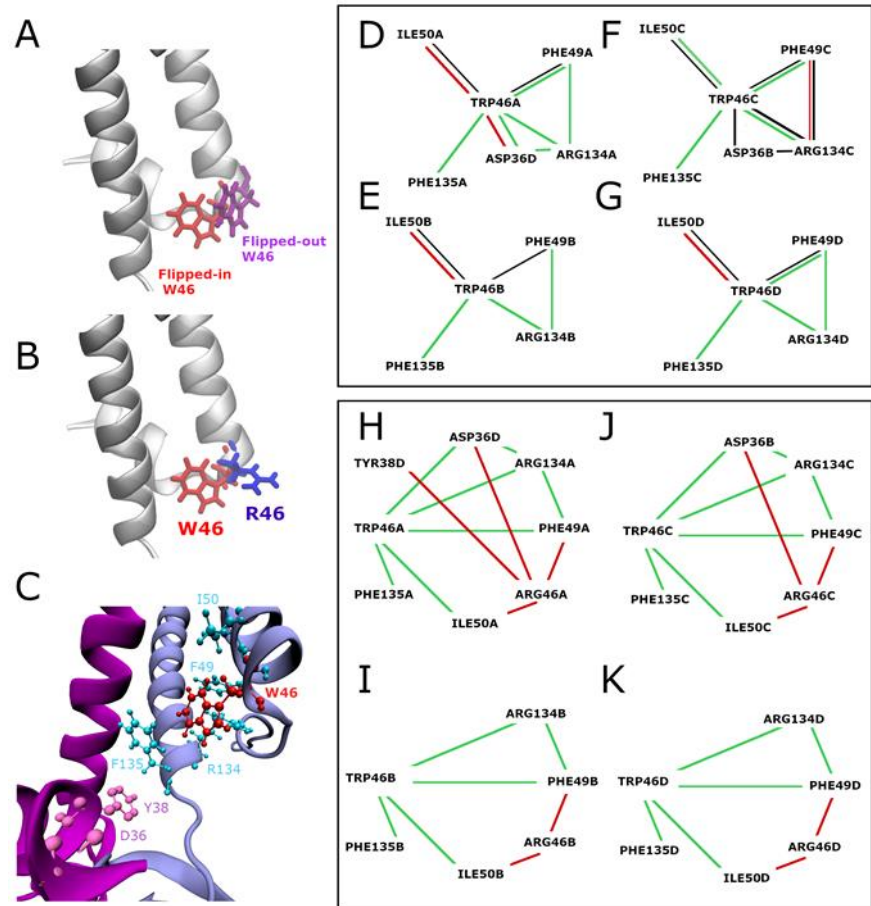


Figure 3. Overview of the network of interactions around W46 (KirBac3.1 WT) and R46 (KirBac3.1 W46R). A) KirBac3.1 WT: representation of the W46 flipped-in (in red, from X-ray structure PDB 2WLJ) and the flipped-out (in purple, from a representative structure issued from MDeNM simulations [17]). B) Superimposition of the residue W46 (flipped-in) in red and the mutation R46 in blue from our crystallographic structure. C) Network of interactions around W46. The chains A and D are colored in blue and magenta, respectively, and the residue W46 (flipped-in) is in red. D, E, F, and G) KirBac3.1 WT: Comparison of the interaction network of residue W46 in flipped-in and flipped-out conformations for the chains A (panel D), B (panel E), C (panel F), D (panel G). The green lines indicate the interactions present in the flipped-in configuration but absent in the flipped-out one, and red lines those present in the flipped-out configuration but absent in the flipped-in one. Black lines are shared between the two conformers. H, I, J, and K) Comparison of the interaction network of residue W46 flipped-in (KirBac3.1 WT) and residue R46 (KirBac3.1 W46R) for the chains A (panel H), B (panel I), C (panel J), D (panel K). The green lines indicate the interactions present in KirBac3.1 WT but absent in W46R mutant, and the red lines the interactions present in the W46R mutant but absent in KirBac3.1 WT. For more details, see Figure S2.

The second analysis focused on comparing the interaction network around the W46 residue, in its flipped-in conformation (the most frequent conformation) in KirBac3.1 WT and the interaction network around R46 in the W46R mutant (Figure 3 H, I, J, K, and Figure S2 for more details). Some similarities are evident, e.g., in all the four subunits, corresponding to chains A, B, C, and D, both residues W46 and the mutated one R46 residue interact with the residues Ile50 and F49 on

the same external helix TM1. However, there are some clear differences. The interactions between the flipped-in W46 residue and the two R134 and F135 residues at the bottom of the TM2 are lost in the case of the W46R due to the orientation of the mutated residue R46 toward the outside of the channel. Along with this loss of interactions, a new network around R46 is established and interestingly new interactions can take place with D36 and/or W38 residues in the slide helix of the adjacent subunit (n-1). It is important to highlight that only R46 residues from opposite chains (A and C) interact with the slide helix. Such contact is not evident for the other two opposite chains (B and D). These observations suggest that the mutation R46 alters the interaction of the outer and inner helices at the level of the bundle crossing, disrupts a hydrophobic cluster (Figure S3), and promotes the interaction of the bottom end of the outer external helix with the slide helix of the adjacent (n-1) subunit. The R46 side-chain points towards the outside of the channel and shows similarities with the flipped-out configuration of W46 residues in the wild type (WT).

2.3.2. Contacts between residues

- Accessible surface of the residues W46 and R46

We calculated the accessible surface areas (ASAs) of residue 46 (W in WT and R in the W46R mutant) on all the 25415 relaxed MDDeNM structures. This value measures the residue's interactions in this position and its degree of exposure to the solvent. The histograms of the ASA values given in Figure 4A show that R46 in the mutant is more exposed than W46 in WT. The corresponding average value is 87.42 \AA^2 with a standard deviation (SD) of 24.87 \AA^2 for the WT and 158.7 \AA^2 (SD = 30.81 \AA^2) for the mutant. These values are in accordance with our crystallographic data showing that the residue R tends to point out of the channel. We should also consider the different hydrophobicity of the two residues. R is more hydrophilic than W and therefore has more favored interactions with the water environment or the polar heads of the phospholipids.

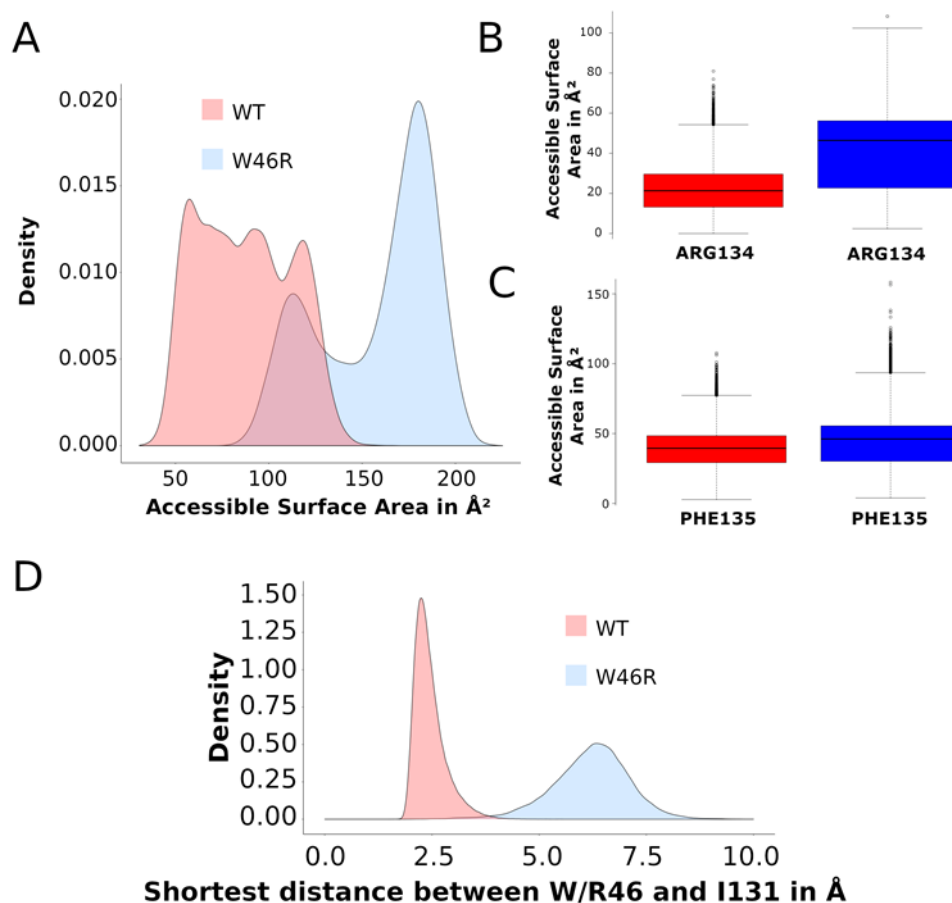


Figure 4. Accessible surface areas and shortest distances on MDeNM structures. A) Histogram of Accessible Surface Area (ASA) values of residue W46 in KirBac3.1 WT (in red) and R46 in KirBac3.1 W46R (in blue) obtained on the set of relaxed MDeNM structures. B) Boxplot of ASA values of R134 in KirBac3.1 WT (in red) and in KirBac3.1 W46R (in blue) over the same set of structures. C) Boxplot of ASA values of F135 in KirBac3.1 WT (in red) and in KirBac3.1 W46R (in blue) over the same set of structures. D) Histogram of the shortest distances on MDeNM structures between residue 46 and I131 in KirBac3.1 WT (in red) and KirBac3.1 W46R (in blue).

- Accessible surface of the residues R134 and F135 and contacts with I131

In the closed flipped-in state, the side-chain of W68 in Kir6.2 (PDB 6JB1) is directed towards the C-terminal end of TM2 and holds hydrophobic contacts with residues I167, K170, and T171 [23, 24]. In the homologous KirBac3.1 channel, W46, corresponding to W68 in Kir6.2, is also directed to the C-terminal end of TM2 (Figure 1B and 2C) and is close to the I131 (corresponding to I167 in Kir6.2), R134 (corresponding to K170 in Kir6.2) and F135 (corresponding to T171 in Kir6.2).

In KirBac3.1, the proximal residues R134 and F135 are more exposed to the solvent in the mutant W46R than in the WT (Figure 4B and C), supporting the suggested loss of interaction with R46 in the mutant protein. It is worth noticing the significant increase in ASA value for R134 compared to F135. R134 shows an ASA average value of 21.77 \AA^2 ($SD=10.96 \text{ \AA}^2$) in the KirBac3.1 WT and 41.05 \AA^2 ($SD=18.19 \text{ \AA}^2$) in the mutant W46R. F135 shows an average value of 38.90 \AA^2 ($SD=13.87 \text{ \AA}^2$) and 44.27 \AA^2 ($SD=17.59 \text{ \AA}^2$) in KirBac3.1 WT and W46R mutant, respectively. These results are explained by the fact that R134 is closer to the bottom end of TM2 and, therefore, more accessible to the solvent. It is also interesting to note that R46 has a higher ASA value than R134, indicating the significant exposure and flexibility of the latter.

The distribution of shortest distances between residues W46/R46 and I131 calculated on the MDeNM set of conformations shows that the shortest distance is higher (for all the chains) in the mutant (Figure 4D). The average values are 2.45 Å (SD=0.37 Å) and 6.20 Å (SD=0.9 Å) for the WT and the W46R mutant, respectively.

All the evidence gathered with this study points to a clear disruption of these crucial interactions between TM1 and TM2 in the case of the W46R mutant, compared to the WT protein.

2.3.3. Impact of the mutation on the gating

In order to investigate the effects of the mutation W46R on various dynamical components of the gating mechanism from the selected normal modes described in Materials and Methods, we carried out MD simulations using MDeNM including the entire environment (water, lipids, ions). Structural and dynamical features taken into account are i) the movement of the slide helix of each chain, ii) the movement of the whole cytoplasmic domain, and iii) the coordinated movement of the transmembrane helices.

- Upward movement of the slide helix

The W46R mutation's impact on the motion of the slide helix was analyzed considering the interaction of the R46 residue with residues of the slide helix of the adjacent protein monomer (n-1). To this end, we calculated the correlations between the upward movement of the slide-helices (definition of the angle in Material and Methods and Figure 5B, in pink) and the shortest distances between R46 at the extremity of TM2 and D36 located at the extremity of the slide helix. This movement has been previously highlighted as important in the gating of the channel [17]. Figure 5A shows the positive correlation between helix movements and inner-residues distances in blue circles, while red circles indicate negative correlations. The diameter and color intensity of each circle are proportional to the strength of the correlation. The shortest distances between R46 and D36 of neighboring chains (n-1) are mainly correlated with the upward movement of slide helices. Therefore, it can be inferred that a smaller distance between these two residues induces a larger upward movement of slide helices.

More precisely, i) the shortest distance d_{46a36d} , d_{46b36a} , and d_{46c36b} (see Figure 6's caption for definitions) are correlated with the upward movement of the chain A (*upa*); ii) distances d_{46c36b} , and d_{46d36c} are correlated with the upward movement of the chain B (*upb*); iii) the distances d_{46d36c} , and d_{46a36b} , are correlated with the upward movement of the chain C (*upc*). Altogether, this evidence points towards a clear correlation in the mutated protein between the upward movement of the slide helices and shortened distances between R46 and D36 residues belonging to the adjacent chain (n+1 or n-1). In the WT protein, which is mostly in flipped-in conformation, (98.68% of the relaxed MDeNM structures), such correlations are still visible but involve the adjacent chain (n+1) (Figure 5C).

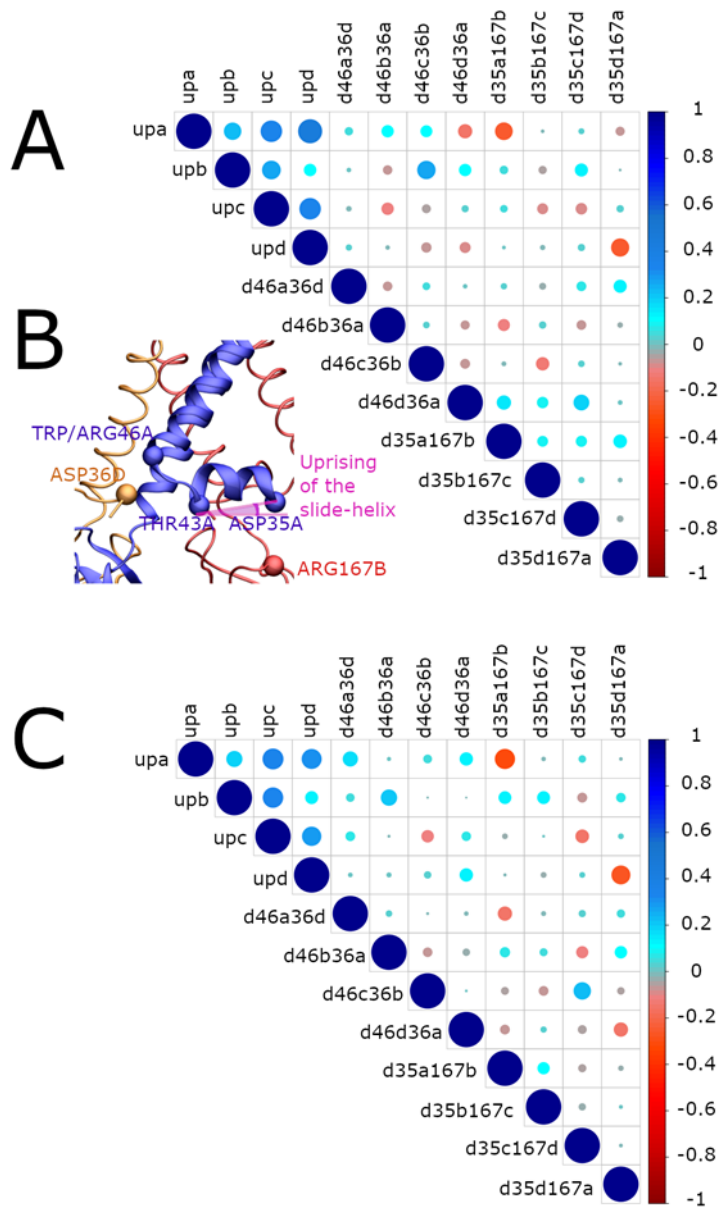


Figure 5. Correlation between the interactions of the slide-helices and their upward movement in KirBac3.1 W46R and WT. A) Correlations in the W46R mutant. The upward movement of the slide-helix for the chains A, B, C, and D is denoted upx, where x is the letter of the chain. D46n36n-1 corresponds to the shortest distance between the R46 residue of the chain n and the D36 residue of the chain n-1, and d35n167n+1 to that between the D35 residue of the chain n and the R167 residue of the chain n+1. The blue circles correspond to positive correlations, while the red ones correspond to negative correlations. The diameter and the color intensity of a circle are proportional to the strength of the correlation. B) Locations of the residues and the slide-helix upward movement angle definition are considered in the correlations in pink. C) Correlations in the case of KirBac3.1 WT.

- Movement of the cytoplasmic domain

We analyze here the movement of the cytoplasmic domain since it has been considered an essential factor in gating [17, 25–28]. To investigate its relation with the upward movement of the slide helices, the shortest distance between D35, the first residue of the slide helix, and R167, located at the top of the cytoplasmic domain on the CD-loop, was taken as a measure of the proximity of these two structural regions. Also, inter-chain distances were taken into account to corroborate the findings. Significant correlations were observed between these distances and the upward movement of the slide helices, as shown in Figure 5A. Furthermore, strong negative correlations are present between inter-chain distances and the upward movement of the slide helices to the membrane. When these distances decrease, the slide helices come closer to the membrane. More

precisely, $d_{35a167b}$ and $d_{35d167a}$ are inversely correlated with the upward movement of the chain A (upa), and $d_{35b167c}$ and $d_{35c167d}$ are inversely correlated with a similar upward movement of the chain C (upc); similarly, $d_{35d167a}$ has an inverse correlation with the upward movement of chain D (upd). Interestingly, the WT protein structure displays the same type of correlations (Figure 5C).

For each monomer of the protein, the comparison of correlations involving the distance between residue 46 and residue 36 ($d_{46n36n-1}$) on the neighboring chain (n-1) and the distance between residue 35 and residue 167 ($d_{35n167n+1}$) on the neighboring monomer (n+1) for KirBac3.1 WT and KirBac W46R reveals clear differences. Indeed, these distances are correlated in the case of KirBac3.1 W46R but not in the case of the KirBac3.1 WT. We hypothesize that this is the consequence of a new interaction present in the W46R mutant but not in the WT protein between R46 and D36 on the slide helix. While in the WT, the residue D35 interacts with R167 on the same polypeptide chain, the mutation at position 46 creates an inter-chain interaction between D36 and R46. The slide-helix is, therefore, held in place by two interactions in different directions. In the case of the WT, the interaction D35-R167 promotes the orientation of the slide-helix towards the cytoplasmic domain, significantly reducing its upward movement. On the contrary, the formation of the new R46-D36 interaction in the W46R favors the movement of the slide-helices toward the transmembrane domain.

- Movement of the transmembrane helices

The correlation between the upward movement of the slide helix and the tilting of the inner and outer transmembrane helices may affect the channel's gating at the constriction points L124 and Y132. Definition of the inner and outer tilts is shown in Figure 6B in red and blue, respectively, and Materials and Methods. The MDDeNM sets for the mutant protein were analyzed to highlight correlations between structural determinants involved in the slide-helix movement and the tilting of the transmembrane helices (Figure 6A). High correlation values indicate the interplay between the inner and outer helices' tilt angles with the movement of the slide helices. Similar correlations were obtained for the WT (Figure 6C).

In the center of the channel, two constriction points corresponding to residues L124 and Y132 are important for the gating as they control the passage of the potassium ions through the channel. In more detail, the gating at L124, represented by inter-chain distances g_{124ac} and g_{124bd} is correlated with the upward movement of the slide-helices (upa,b,c,d). In addition, the g_{124ac} distance is correlated with the tilt of the transmembrane helices (tiltin, tilton). On the contrary, the opening of the gate at the level of the residue Y132 represented by the inter-chain distances g_{132ac} and g_{132bd} has an inverse correlation with the upward movement of the slide-helices (upa,b,c,d) and the tilt of the transmembrane helices (tiltin, tilton). In the case of KirBac3.1 WT, data from the MDDeNM set show no clear correlation between the gating at the level of residue L124, while the opening of the gate at the level of the residue Y132, specifically for chains B and D is mainly correlated with the upward movement of the slide-helices and the tilting of the transmembrane helices (contrarily to KirBac3.1 W46R).

The upward motion of the slide-helix causes the tilt of both transmembrane helices in such a way that the central portions of the transmembrane helices move away from the center of the channel (L124) while their cytoplasmic ends get closer to the bottom of the channel (Y132). This causes the increase of the opening of the channel at the level of L124 but a decrease in the channel's opening at the level of Y132.

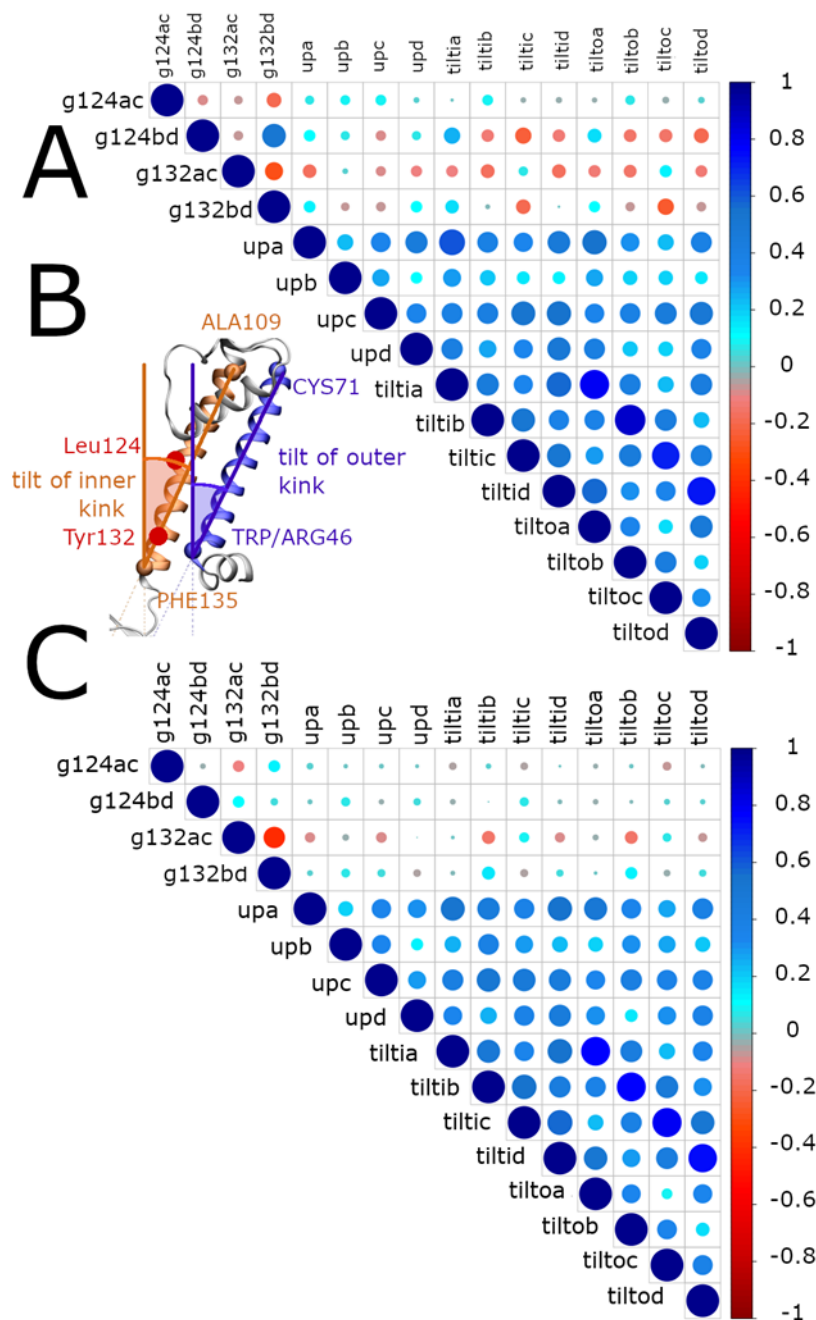


Figure 6. Correlation between the gating and the upward movement of the slide-helices and inclinations of the transmembrane helices in KirBac3.1 W46R. A) Correlations in the W46R mutant. The shortest distance between the residues L124 belonging to the chains A and C defining the gating at this level is denoted g124ac, and similarly, for Y132, it is designated g132ac. The upward movement of the slide-helices of the chains A, B, C and D are denoted upa, upb, upc, upd, respectively. The tilt angle of the axes of the inner and outer helices from the perpendicular line to the membrane plane are denoted tiltin and tiltou, respectively, where n is the name of the chain. Blue and red circles correspond to positive and negative correlations, respectively. The diameter and the color intensity of a circle are proportional to the strength of the correlation. B) Definition of the inner and outer tilts (brown and blue, respectively). The upward movement of the slide-helices is defined as in Figure 5B Constrictions points L124 and Y132 are shown. C) Correlations in the case of KirBac3.1 WT.

2.3.4. Population of open and closed states corresponding to the MDcNM relaxed structures

Note that in this work, a "closed" state is defined by a conduction pathway that is sterically occluded and an "open" state in which the pathway is sufficiently wide to accommodate at least a non-hydrated potassium ion. Four channel-gating states can be defined based on the open or closed conformation of the two main

constriction points (L124 and Y132) as observed in the relaxed structures (for more details, see [17]): 1) Fully open state when the shortest distances at the two constriction points are larger than the ionic diameter of K^+ (diameter of K^+ ion considered 3.53 Å); 2) Fully closed state when both distances are smaller than the ionic diameter of K^+ ; 3) Half-open state 1 when the gate at residue L124 is open and the gate at residue Y132 is closed; 4) Half-open state 2 when the gate at residue Y132 is open and the gate at residue L124 is closed. Interestingly, the fully open state structures constitute about 7.4% of the whole population for the mutant protein, a slightly higher percentage (0.5%) than KirBac3.1 WT (6.8% Table 2). Furthermore, we can notice that the gate at residue Y132, closer to the cytoplasmic domain, is more often closed than the gate at residue L124 (32.5% versus 10.8%, respectively). It follows that the residue Y132 in both protein WT and the W46R mutant protein is the most restrictive point of the ion pathway. A more significant observation is that the 'gate' at L124 is more open in the case of the mutant W46R compared with WT (33% and 29%, respectively). On the contrary, the gate at Y132 is less open in the mutant W46R than WT (11% and 14%, respectively).

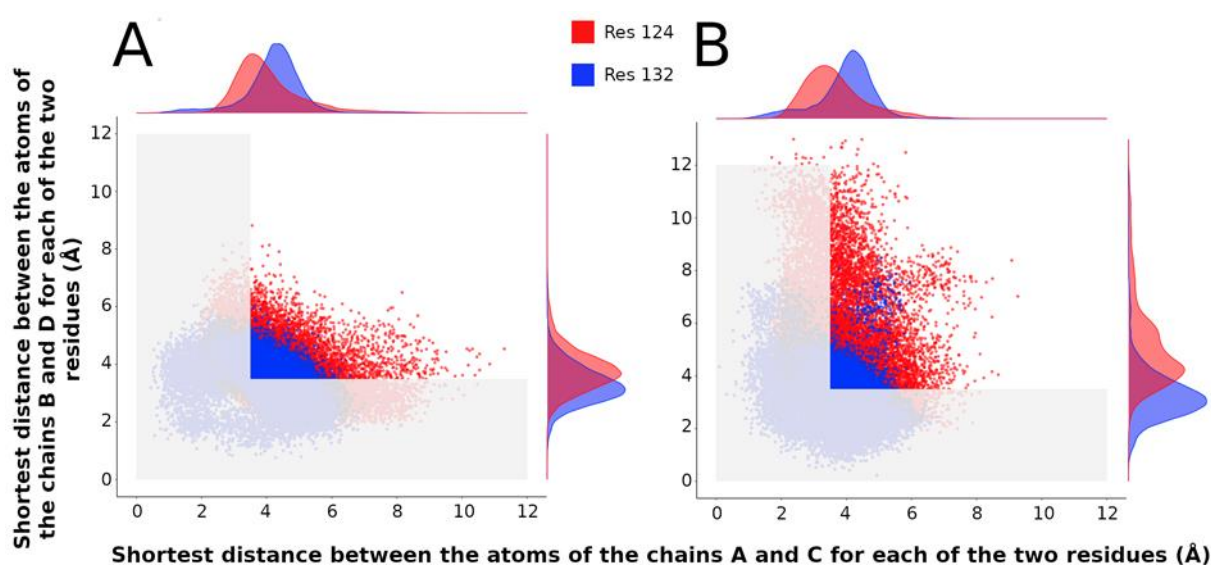


Figure 7. Gating at the two constriction points L124 and Y132 A-B) Scatter plots of distances between $C\alpha$ atoms of the residues 124 (in red) and 132 (in blue) for chains AC and BD. A: for KirBac3.1 WT B: KirBac3.1 W46R.

More details about the amplitude of the channel opening at the gating points on the scatter plots of shortest distances between the opposite chains A and C and those between chains B and D at both constriction points over all the MDeNM relaxed structures are shown in Figure 7A and 7B for the WT and the W46R mutant proteins, respectively. The shortest distance between opposite chains at the level of the two constriction points is always lower than 15 Å for WT protein (Figure 7A) but higher than 15 Å for a small population of the simulated structures of the W46R mutant (Figure 7B). Interestingly, for this population, the opening is more prominent at residue Y132 compared with residue L124.

Table 2. Populations (in percentage) of different opening states in the relaxed structures of KirBac W46R obtained through MDeNM simulations and single-channel recording of the mutant and KirBac3.1WT

Channel states	Kirbac3.1 WT (%) (Ref 16)	KirBac3.1 W46R (%)
Fully open	6.8	7.4
Fully closed	50.2	49.3
Half open 1 (124 open, 132 closed)	28.8	32.5
Half open 2 (132 open, 124 closed)	14.2	10.8
Current recordings of KirBac3.1 in planar lipid bilayers	9.9 (± 1.3 , n= 1803)	7.1

2.4. Functional studies of the W46R protein

Purified W46R was incorporated in a preformed lipid bilayer. Figure 8A shows single-channel traces for a 3-min consecutive recording at +100 mV and channels gating with multiple sub-states as described for the Kirbac3.1 WT channels [17]. Analysis of the amplitude value versus the dwell confirms seven levels during this recording time (Figure 8B inset). Fits of the histogram of all levels versus current amplitude reveal a single-channel conductance value of 36 pS, similar to that recorded for the WT channels (47 pS at -80 mV [17]). From this recording, the open probability (P_o) was 0.071 (Table 2). We performed recordings at other potentials that led to P_o in the same order of magnitude (data not shown).

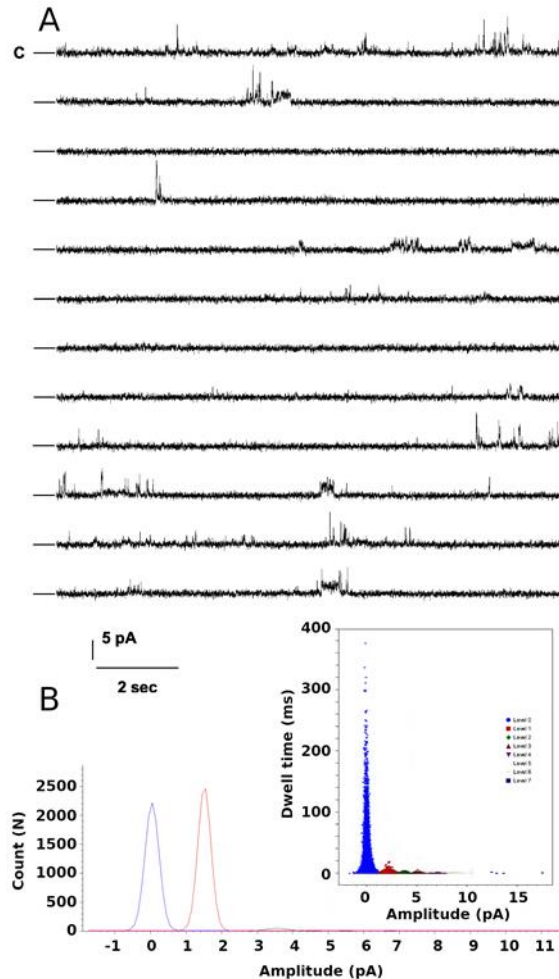


Figure 8. Single-channel recordings of the Kirbac W46R channels A) Current traces from 3-min consecutive recordings at +100 mV test potential. The closed state is labeled as C. B) Amplitude histogram fits of all events for the selected seven levels gating between closed and open states during 3 min. Inset shows current amplitude values versus dwell time for all seven levels.

3. Discussion

3.1. Characteristics of mammalian Kir6.2 channel

Tryptophan at residue 68 of Kir6.2 subunit is critical for correct channel function [12]. Most of the W68 mutants in Kir6.2 cause a gain in channel function. In all Kir crystal structures, the residue corresponding to W68 in Kir6.2 lies at the N-terminal end of TM1, close to the hinge region that leads to the slide helix. As seen in most of the X-ray structures of WT Kir channels, this highly conserved residue is in the flipped-in conformation, tightly packed against the C-terminal end of TM2 in a hydrophobic cluster (Figure S3 and Video S1), with the tryptophan side-chain pointing toward the center of the channel. The residue also interacts with I131, F135, and R134 at the bottom of the TM2. These interactions favor the closed state of the channel. However, it has been suggested that the flipped-out

conformation of W68 is required for the movement of TM2 that leads to an open state [12].

Multiple residues in Kir6.2 (more than 70) are known to cause neonatal diabetes mellitus. They can be divided into three classes: the class of residues that act directly by increasing the opening probability of the channel, the class of residues that participate in ATP binding (including those who lie in close vicinity), and the residues that are acting as a conformational relay by which ATP binding is translated into pore closure [30].

3.2. KirBac3.1 W46R: a good model for studying analogous W68R mutation in mammalian Kir6.2

Here we investigate the effect of one particular mutation on the bacterial homolog KirBac3.1 channel and compare our findings to the mammalian Kir6.2. We support the idea that the KirBac3.1 W46R mutant characterized here may represent a good model for studying the analogous mutation in the human channel and that it can help provide insights into the molecular mechanisms responsible for the gain of function of the channel. Therefore, we solved the structure of KirBac3.1 W46R at 2.8 Å resolution and used this model to investigate the dynamics of the protein. Structural comparison between Kir6.2 and KirBac3.1 is shown in Figure S5.

In the case of the mutant KirBac3.1 W46R, replacing the hydrophobic residue tryptophan with a positively charged arginine in this region is likely to have a destabilizing effect. Analysis of the X-ray structure of KirBac3.1 W46R and the modeled structure from 2WLJ, with an rmsd of 1.712 Å between the two structures, shows that the residue R46 does not point toward the center of the channel but resembles the flipped-out conformation of W46 pointing away from the channel pore. As a consequence, the previously described interaction with the cytoplasmic end of the TM2 helices and the hydrophobic cluster around W46 are disrupted (this hydrophobic cluster is also present in Kir6.1 and Kir6.2 [29]), and the R46 residue forms a new network of interactions with the slide helix of the neighboring subunit (n-1) involving D36 and W38 residues. Note that D36 is also highly conserved among the Kir channels (Figure 1C).

W46R does not appear to increase the opening probability of the KirBac3.1 channel.

Our functional and structural experiments showed no significant difference between the opening probabilities of the WT and mutated channels. The fully open state structures constitute about 7.4% of the whole population, compared to KirBac3.1 WT (6.8%, Table 2). The functional studies confirm these data and show that the open probability (P_o) for the W46R is even slightly smaller than the WT (7.1% compared with 9.9%, respectively). The HDX studies show that the only region that is less flexible compared with the WT structure is at the cytoplasmic bottom end of the TM1, including the R46 mutation, suggesting that the network of interactions formed between the mutated residue R46 and the slide helix increases the rigidity of this protein segment. This suggests that the mutation does not affect the channel's intrinsic open probability, as other neonatal diabetes mutations do with the human isoform [30].

Gating transitions of KirBac3.1 W46R revealed by molecular dynamics simulations

Despite the similar open probabilities between the KirBac3.1 WT and W46R, the mutant describes a different behavior. Indeed, the detailed dynamical view of the entire mutant channel during the gating associated with the open/closed transition was uncovered by *in silico* studies that show a sequence of molecular events that, due to lack of interactions between TM1 and TM2, trigger the opening of the channel. In the WT state, the tryptophan residue at position 46 forms contacts with transmembrane domain 2 (TM2) that hamper its movement and gate opening. In the W46R mutant, the arginine side-chain is flipped away from the channel pore, enabling the movement of TM2 and the establishment of new contacts with the slide helix of the neighboring subunit (n-1) that aid in the gating

mechanism and increased open state stability. The gating mechanism can be summarized as a succession of events: i) R46 interacts with slide helix (D36); ii) The upward movement of the slide helices induces the bending of the TM1 and TM2; ii) this, in turn, causes a larger opening of the channel at the level of the residue L124 but a closer interaction between the sub-units at the level of residue Y132. Interestingly, some of these events can be correlated between the different chains, unlike what happens for the WT [17] where there is no correlation between the different chains. Therefore, these particular synchronized steps could help for the opening of the channel.

To further assess the flexibility of the structures of KirBac3.1 WT and W46R mutant, we compared the rms fluctuations between the two structures. The results are shown in Figure S4 where KirBac3.1 WT seems, in general, more flexible than the mutant KirBac3.1 W46R. However, the stretch that includes the very end of the slide helix, R46 mutation, and the bottom half of the TM1 external helix (aa 43-56) is not as flexible as the WT, as noticed in HDX-MS.

3.3. Suggestions to Kir6.2 by analogy

W68 does not directly participate in ATP binding

The ATP- binding site on Kir6.2 lies at the interface between two Kir6.2 subunits and close to the L0 loop of SUR. While the resolution of the cryo-electron microscopy density does not allow precise determination of atomic-level ATP-protein interactions [31, 32] (see structures PDB 6C3P and PDB 6C03), when combined with the finding of functional studies, it provides an accurate model of the ATP- binding site. The amino acids belonging to the ATP-binding site using Kir6.2 numbering are R50 and N48 for chain A, and I182, K185, Y330, F333, and G334 for chain B. The other residues lying nearby (such as H46, E51, Q52, R201, and G53) are important for stabilizing the interaction with ATP. Even if residue 68 was previously reported as not directly implicated in the interaction with ATP, the introduction of a mutation could lead to a destabilization of the nearby region responsible for ATP binding, as reported for other neonatal diabetes mutations [30]. This destabilization of the closed channel by disrupting the nearby hydrophobic cluster in the closed state (Figure S3) has been reported previously for other mutations such as K170 (K170T) and I167 (I167L) in Kir6.2. These mutations result in neonatal diabetes by reducing inhibition by ATP [33, 34]. Various mutations at residue T171 can also cause a significant increase in the open probability [35]. All these residues are known to interact with W68.

Therefore, it is possible that the substitution of W68 by R may result in a pathogenic reduction of ATP sensitivity (inhibition) by disrupting the normally present interaction between the bottom of TM1 and the slide helix. This is in line with the reduced sensitivity toward ATP inhibition already reported for the corresponding human mutant W68R, which also has been characterized by increased currents [12]. Furthermore, W68 could be necessary for the conformational relay by which ATP binding in mammalian Kir6.2 is translated into pore closure. The mutation could then alleviate the functional inhibition due to ATP binding. Although our results on the KirBac3.1 mutant channel do not allow to conclude on this aspect, they provide structural insights that may be useful for understanding Kir6.2-associated disorders.

In conclusion, W68 represents a highly conserved residue among the Kir channels, also conserved in the human K-ATP channels. Here we show, by analogy with KirBac3.1 W46R mutant, that W68 and its network of interactions are crucial for the healthy activity of this channel, as it is involved in controlling channel gating. In the human channel, mutations of this residue lead to neonatal diabetes. Our findings may represent the basis for further investigations on the homologous human K_{ATP} channel to provide novel insights into the molecular mechanisms responsible for the pathological gain of function of the channel.

4. Materials and Methods

4.1 Experimental Data

4.1.1 Protein expression and purification

The W46R mutation was introduced using site-directed mutagenesis into a synthetic KirBac3.1 gene inserted in pET30a. The open reading frame of this construct had been codon-optimized for expression in *Escherichia coli*. Protein expression and purification of this mutant channel were performed as outlined before [36]. Briefly, after cell disruption by the French press, the protein was directly solubilized with 45 mM DM (Decyl β -D-maltopyranoside), centrifuged, and the supernatant was loaded onto a Co^{2+} affinity column. The protein was promptly purified on a Superdex 200 10/300 column pre-equilibrated with 2 mM TriDM buffer. Concentrated preparations (1-2.5 mg/mL) of purified proteins were stored at -80°C in buffer containing 20 mM Tris, pH 7.4, 150 mM KCl, and 0.2 mM TriDM.

4.1.2 Protein Crystallization

We used the experimental procedures and equipment available in the crystallography core facility at the Institut Pasteur, Paris, [37] to perform the crystallization screening trials. Briefly, with a MosquitoTM nanoliter-dispensing system (TTP Labtech), we set up crystallization sitting drops of 400 nL containing a 1:1 mixture of protein and crystallization solutions (672 different commercially available conditions). The protein drop was equilibrated against a 150 μL reservoir in multiwell plates (Greiner Bio-One). The crystallization plates were stored at 18°C in a RockImager (Formulatrix) automated imaging system to monitor crystal growth. Manual optimization was performed in Linbro plates with the hanging-drop method by mixing 2 μL of KirBac3.1 W46R protein at 10 mg/mL with 2 μL of reservoir solution. The best crystals were obtained under the conditions containing 15% (w/v) PEG- MME 5k, 15% (v/v) glycerol, 1 M LiCl, and 100 mM MES pH 6.5. For data collection, the crystals were flash-cooled in liquid nitrogen using the reservoir solution as cryo-protectant.

- Data collection and structure determination

The X-ray diffraction data were collected at 100K on the PROXIMA-1 beamline (Synchrotron SOLEIL, St Aubin, France) using a Dectris pixel-array PILATUS 6M detector at a wavelength of 1.07114 \AA to a resolution of 2.80 \AA . The diffraction images were integrated with the program XDS [38]. The KirBac3.1 W46R crystals belong to the P2₁2₁2 space group with cell dimensions of 106.77 \AA 113.98 \AA 89.18 \AA . Molecular replacement was carried out with Phaser (CCP4 suite), using a search model derived from the closed structure of KirBac3.1 closed state at 2.85 \AA (PDB 2WLJ). Five percent of the reflections were set aside in the free R set. The asymmetric unit has a solvent content of 69.4% and contains two polypeptide molecules. The model was refined in real space interactively using Coot [39] and refined using BUSTER-TNT [40], which included a final round of translation, vibration, and screw-rotation (TLS) anisotropic refinement, as implemented in BUSTER-TNT. An additional restrained refinement was carried out using REFMACS [41]. The final model contains two polypeptide chains with 276 and 265 residues out of 301, respectively. The model also contains 23 solvent molecules and four ions (three K^+ and one Mg^{2+}). The final model having 99.3% of all residues in the favored or allowed regions of the Ramachandran plot was validated using MolProbity [42]. The crystals parameters, data statistics, and refinement parameters are shown in Table 1. All structural figures were generated with PyMOL (version 1.3r1). The PDB accession code of this structure is 7ADI.

4.1.3 Pepsin Digestion, Hydrogen/Deuterium exchange approach coupled to mass spectrometry (HDX-MS) and HPLC

Peptide Separation of this mutant channel was performed as outlined before [17]. Briefly, all protein digestions in solution were performed in an ice bath at 0°C . Protease solutions were prepared in 500 mM glycine (pH 2.2). KirBac3.1 proteins samples were digested in the same buffer for 2–5 min using a protease/substrate ratio of 1:1 or 1:10 (wt/wt) for pepsin and nepenthesin,

respectively, either in solution or immobilized on a resin. The increase in digestion time did not affect the proteolysis.

HDX-MS reactions were carried out on KirBac3.1 W46R at a protein concentration of about 10 μ M. The reaction was initiated by a 10x dilution of the protein samples (10 μ L) into a deuterated buffer containing 50 mM KCl and 0.2 mM TriDM. The time course of the HDX was followed over a 20-min period by sequential withdrawing 120 μ L of deuterated samples, which were immediately added to 26 μ L of quenching buffer (8 M guanidium chloride, 500 mM glycine HCl, pH 2.2), rapidly mixed, and flash-frozen in liquid nitrogen. After protease digestion in solution or on column in an ice bath at 0 °C, the peptides were loaded onto a peptideMicroTrap (Michrom Bioresources) column and washed with 0.03% TFA in water (HPLC solution A). They were then separated on a reversed-phase C12 column as previously described [19].) during 26 min. The column was connected to the electrospray source of the mass spectrometers until 30% (vol/vol). The valves, trap cartridge, and column were cooled to 0 °C by immersion in an ice bath as outlined before [19]. The tandem MS (mapping) analyzes were performed on an ion trap mass spectrometer (Esquire 3000+; Bruker Daltonics) to identify the peptides after separation on HPLC. Mass measurements and local deuteration kinetics analysis were performed on a time-of-flight (TOF) mass spectrometer (6210; Agilent Technologies) equipped with an electrospray source. Each deuteration experiment was performed in triplicate. Data were processed with MassHunter software (Agilent Technologies). The qualitative analysis, the deconvolution, and calculation of the average masses were carried out in Magtran [43].

4.1.4 Functional studies of the KirBac W46R protein in black lipid membrane

Purified KirBac3.1 W46R (130 μ g/mL) in DM (decylmaltoside) detergent (1.5 mM) was added to the upper chamber (150 μ L) to a preformed bilayer. The Orbit mini apparatus was used (Nanion, Germany, horizontal planar lipid bilayer system), with two chambers separated by a partition with a 100- μ m hole where the lipid bilayer is formed by 1,2-diphytanoyl-sn-glycero-3-phosphocholine (DPhPC, 10–30 pF). The lower chamber contained 150 mM KCl, 10 mM MOPS, pH 7.4. After membrane bilayer formation, the upper chamber solution was changed to 150 mM KCl, 10 mM MOPS pH 8. Currents were recorded using Elements Data Reader (Nanion, Germany) and analyzed using Clampfit (Axon Instrument Inc, USA) software, sampled at 100 μ s, and filtered at 1.25 kHz. The recording was performed at 24 °C using Nanion temperature control unit.

4.2 Theoretical data

4.2.1 Modeling and Dynamics

The X-ray structure of KirBac3.1 with an atomic resolution of 2.6 Å (PDB 2WLJ) [13] was used to model the complete WT structure. As the first 34 residues were missing in the X-ray structure, this segment was excluded from our model, and the missing atoms were constructed using the CHARMM program [44]. Residues 1 to 34 of the protein are not likely to be involved in the gating process. The tetrameric complex was built by applying a two-fold symmetry axis for this structure using the "Protein Interface Surface and Assemblies" software through Pisa [45] at EBI. The W46R mutation was achieved with Chimera [46], considering the modeled WT structure. The ionization states of residues in both structures were established using PROPKA3 [47, 48]. A complete system comprising a DOPC membrane, TIP3P type water molecules [49], and KCl ions at 150 mM concentration within a box of 116.243 Å x 116.243 Å x 133.255 Å was built using the membrane-builder module of Charmm-Gui webserver [50, 51]. This web server uses the "Orientations of Proteins in Membranes" (OPM) [52] software to imbed the protein into the membrane. We used the charmm36 force field [53]. The WT and mutant structures were first energy minimized, then further relaxed by carrying out short molecular dynamics simulations for 600 ps at a constant temperature of 300 K using the Nose-Hoover thermostat and constant pressure of 1 atm using the Langevin piston. Such a structure constituted the starting point for the Normal Mode calculations and MDenM simulations. The Leapfrog Verlet

algorithm was used for propagating the movement. The cut-on and cut-off distances for nonbonded interactions were set at 10 Å and 12 Å, respectively, and between these values, a switching function was applied [17].

4.2.2 Normal Modes

The first 200 lowest frequency normal modes (NMs) of the structure KirBac3.1 W46R structure were calculated with the DIMB method [54] in CHARMM. A switching function was applied to the nonbonded interactions by setting a cut-on distance of 10 Å and a cut-off of 12 Å. A distance-dependent dielectric constant of $2r$ (r being the interatomic distance) was used. The minimization was carried out under harmonic restraints applied to atomic positions, which were gradually reduced and finally continued without restraints by performing 50,000 steps of CG (Conjugate Gradient) followed by ABNR (Adopted Basis Newton Raphson) minimization until reaching an RMS energy gradient of 10^{-5} Kcal mol⁻¹ Å⁻¹. The NMs of this minimized structure were then computed. We selected from these modes those directly involved in the channel gating to be used in MDeNM (Molecular Dynamics using excited Normal Modes) simulations, following the same procedure as for KirBac3.1 WT [17]. 8 contributing modes were selected, with the ranking numbers 85, 86, 106, 150, 153, 154, 166, and 171 ordered in increasing frequencies. We selected these modes according to their contributions to the opening/closing of the channel by following a list of criteria as explained in [17, 22].

4.2.3 Molecular Dynamics using excited Normal Modes

The MDeNM method [21] was applied to explore the large-scale conformational changes in the protein. This method allows an extensive conformational exploration in the normal mode space coupling global and local motions. It consists of propagating the movements by kinetic excitations along the different linear combinations of mode vectors in MD simulations, each one of these simulations constituting a replica. These combined vectors are chosen to point to different regions of the normal mode space allowing an extensive exploration. Substantial conformational changes could then be explored in a series of relatively short MD simulations to obtain a set of structures that would require at least simulations in the range of ms with conventional MD. Our study, considered 130 replicas for KirBac3.1 W46R, which allowed for an extensive conformational sampling (total simulation time = 0,4 ns × 130 replicas = 52 ns). A filtering procedure was used to determine the mode combinations allowing an isotropic distribution of the vectors [17]. We considered for each replica a series of 7 kinetic energy excitations for each replica, each lasting 1.5 ps, and corresponding to an 8 K temperature increase of the protein. These simulations were carried out with the CHARMM program using a dedicated script (available upon request).

- Relaxation of the excited MDeNM structures

MDeNM provided 910 excited structures (7 excitations for every 130 replicas). This set of structures contained a few similar structures despite the rms filtering. Therefore, we proceeded to a clustering of the structures based on the channel rmsd (1.0 Å for KirBac3.1 W46R), carried out with the clustering tool of VMD, yielding 85 clusters. The structure closest to the average structure within each cluster was chosen as the representative of the group. They were then relaxed during 0.4 ns standard molecular dynamics performed with NAMD using the same force field as before. Finally, we considered the last 0.3 ns of the trajectories in which the remaining excitation energy is substantially dissipated, providing 25415 structures used in our analysis.

4.2.4 Interaction networks

The interaction networks around the residue 46 in KirBac3.1 WT (flipped-in and flipped-out configurations) and KirBac3.1 W46R mutant were determined using the Ring Web server of the University of Padova [55] and Cytoscape [56]. The nodes of the network correspond to the residues, and the edges to the

physicochemical interactions, hydrogen bonds, or Van der Waals interactions. In addition, specific sub-networks were established by Cytoscape, which reads the files created by Ring and extracts information related to the residues of interest and their neighbors and the interactions between them.

4.2.5 Structural determinants

Accessible Surface Area (ASA) was calculated with a Tcl script in VMD [57], the shortest distance between residues with the CHARMM program [44], and the Pearson correlation coefficients with the cor module of the R software (<https://www.R-project.org/>)

- Upward angle of the slide-helices

The upward angle of a given chain's slide-helix (residues from T43 to D35) is defined as the angle between its axis and the membrane plane (Figure 5B, in pink). It measures its proximity to the membrane; the higher the value, the closer to the membrane. The upward angles of the A, B, C, and D chains' slide-helices are denoted upa, upb, upc, and upd, respectively.

- Tilt angle of the transmembrane helices

The tilt angle of a transmembrane helix is defined as the angle between its axis and the perpendicular to the membrane plane (Z-axis) (Figure 6B). The inner helix of each chain is delimited from A109 to F135 and the outer helix from the residue 46 (in W/R46 or WT) to Cys71. The tilt angles of the inner transmembrane (TM) helices are named inclia, inclib, inclc, inclid for the chains A, B, C, and D, respectively, and similarly incloa, inclob, incloc, and inclod concerning the outer TM helices.

Supplementary Materials: The following are available online at www.mdpi.com/xxx/s1, **Figure S1** Heat Map of the KirBac3.1 W46R mutant. **Figure S2.** Detailed overview of the network of interactions around W46 (KirBac3.1 WT) and R46 (KirBac3.1 W46R). **Figure S3** Hydrophobic cluster **Figure S4:** Root-Mean Square Fluctuation by residue computed on all relaxed structures from MDeNM in red and blue for KirBac3.1 WT and KirBac3.1 W46R, respectively. **Figure S5:** Structural comparison between the two structures Kir6.2 (red) and KirBac3.1W46R (blue) **Video S1** Hydrophobic Cluster on WT and W46R.

Author Contributions: Conceptualization, DP, EF, and CV-B; methodology, DP, EF, and CV-B; software, DP and CF; validation, DP, EF, SB, AH; and CV-B, LB, IO, and DZ expressed the protein. LB, IO, and EF performed the Hydrogen Deuterium Exchange Mass spectrometry (HDXMS) experiments. CF performed the MDeNM calculations under the supervision of DP. SB and RS performed single-channel investigations. LB and IO performed the crystallization with the help of AH. AH collected the data at the synchrotron. LB and RDZ solved the 3D structure, CF, DP, and CV-B wrote the manuscript with the help and comments from all authors

All authors have read and agreed to the published version of the manuscript

Funding: This research was funded by SERVIER and ANR-CNRS CACSICE (CVB); AFM-téléthon grant (#19928 and #23207, SB and CVB) and PhD research funding, MESRI (CF and DZ). This work was performed using HPC resources from the "Mésocentre" computing center of CentraleSupélec and ENS Paris-Saclay supported by CNRS and Région Île-de-France (<http://mesocentre.centralesupelec.fr/>). It was granted access to the HPC resources of IDRIS under the allocation 100512 made by GENCI/IDRIS (DP).

Institutional Review Board Statement: Not applicable

Informed Consent Statement: Not applicable

Data Availability Statement: Accession codes. The atomic coordinates of the KirBac3.1 W46R structure have been deposited in the Protein Data Bank under the accession code 7ADI.

Acknowledgments: We acknowledge the crystallography facility at the Pasteur Institute, synchrotron SOLEIL (St Aubin, France) for provision of synchrotron beam time and the staff of Proxima-1 for assistance during X-ray data collection;

Conflicts of Interest: The authors declare no conflict of interest.

References

1. Aguilar-Bryan L, Bryan J (1999) Molecular biology of adenosine triphosphate-sensitive potassium channels. *Endocr Rev* 20:101–135. <https://doi.org/10.1210/er.20.2.101>
2. Antcliff J, Haider S, Proks P, et al (2005) Functional analysis of a structural model of the ATP-binding site of the K-ATP channel Kir6.2 subunit. *EMBO J* 24:229–239. <https://doi.org/10.1038/sj.emboj.7600487>
3. Nichols CG, Singh GK, Grange DK (2013) K-ATP Channels and Cardiovascular Disease Suddenly a Syndrome. *Circ Res* 112:1059–1072. <https://doi.org/10.1161/CIRCRESAHA.112.300514>
4. Nichols C (2006) K-ATP channels as molecular sensors of cellular metabolism. *Nature* 440:470–476. <https://doi.org/10.1038/nature04711>
5. Vedovato N, Ashcroft FM, Puljung MC (2015) The Nucleotide-Binding Sites of SUR1: A Mechanistic Model. *Biophys J* 109:2452–2460. <https://doi.org/10.1016/j.bpj.2015.10.026>
6. Ashcroft FM (2007) ATP-sensitive K⁺ channels and disease: from molecule to malady. *Am J Physiol-Endocrinol Metab* 293:E880–E889. <https://doi.org/10.1152/ajpendo.00348.2007>
7. Babenko AP, Polak M, Cave H, et al (2006) Activating mutations in the ABCC8 gene in neonatal diabetes mellitus. *N Engl J Med* 355:456–466. <https://doi.org/10.1056/NEJMoa055068>
8. Gloyn A, Pearson E, Antcliff J, et al (2004) Activating mutations in the gene encoding the ATP-sensitive potassium-channel subunit Kir6.2 and permanent neonatal diabetes. *N Engl J Med* 350:1838–1849. <https://doi.org/10.1056/NEJMoa032922>
9. Hattersley A, Ashcroft F (2005) Activating mutations in Kir6.2 and neonatal diabetes - New clinical syndromes, new scientific insights, and new therapy. *Diabetes* 54:2503–2513. <https://doi.org/10.2337/diabetes.54.9.2503>
10. Proks P, Antcliff J, Gloyn A, et al (2005) Molecular basis of Kir6.2 mutations causing neonatal diabetes and neonatal diabetes with neurological features. *Biophys J* 88:181A
11. Ashcroft F (1988) Adenosine 5'-triphosphate-sensitive potassium channels *Annu Rev Neurosci* 11:97–118. <https://doi.org/10.1146/annurev.ne.11.030188.000525>
12. Maennikoe R, Stansfeld PJ, Ashcroft AS, et al (2011) A conserved tryptophan at the membrane-water interface acts as a gatekeeper for Kir6.2/SUR1 channels and causes neonatal diabetes when mutated. *J Physiol-Lond* 589:3071–3083. <https://doi.org/10.1113/jphysiol.2011.209700>
13. Clarke OB, Caputo A, Hills AP, et al (2010) Domain reorientation and rotation of an intracellular assembly regulate conduction in Kir Potassium Channels. *Cell* 141:1018–1029
14. Forest E, Man P (2016) Conformational Dynamics and Interactions of Membrane Proteins by Hydrogen/Deuterium Mass Spectrometry. In: MusVeteau, I (ed) *Heterologous expression of membrane proteins: Methods and Protocols*, 2nd edition. pp 269–279
15. Oganesyan I, Lento C, Wilson DJ (2018) Contemporary hydrogen deuterium exchange mass spectrometry. *Methods* 144:27–42. <https://doi.org/10.1016/j.ymeth.2018.04.023>
16. Vadas O, Jenkins ML, Dornan GL, Burke JE (2017) Using Hydrogen-Deuterium Exchange Mass Spectrometry to Examine Protein-Membrane Interactions. In: Gelb, MH (ed) *Enzymology at the membrane interface: Interfacial enzymology and protein-membrane binding*. pp 143–172
17. Fagnen C, Bannwarth L, Oubella I, et al (2020) New Structural insights into Kir channel gating from molecular simulations, HDX-MS and functional studies. *Sci Rep* 10:8392. <https://doi.org/10.1038/s41598-020-65246-z>
18. Giladi M, Almagor L, van Dijk L, et al (2016) Asymmetric Preorganization of Inverted Pair Residues in the Sodium-Calcium Exchanger. *Sci Rep* 6:. <https://doi.org/10.1038/srep20753>
19. Mehmood S, Domene C, Forest E, Jault J-M (2012) Dynamics of a bacterial multidrug ABC transporter in the inward- and outward-facing conformations. *Proc Natl Acad Sci U S A* 109:10832–10836. <https://doi.org/10.1073/pnas.1204067109>
20. Gupta S, Bavro VN, D'Mello R, et al (2010) Conformational changes during the gating of a potassium channel revealed by structural mass spectrometry. *Struct Lond Engl* 1993 18:839–846. <https://doi.org/10.1016/j.str.2010.04.012>
21. Costa MGS, Batista PR, Bisch PM, Perahia D (2015) Exploring Free Energy Landscapes of Large Conformational Changes: Molecular Dynamics with Excited Normal Modes. *J Chem Theory Comput* 11:2755–2767. <https://doi.org/10.1021/acs.jctc.5b00003>
22. Fagnen C, Bannwarth L, Zuniga D, et al (2021) Unexpected Gating Behaviour of an Engineered Potassium Channel Kir. *Front Mol Biosci* 8:. <https://doi.org/10.3389/fmolb.2021.691901>
23. Ashcroft FM (2000) *Ion channels and diseases*. Academic press, New-York
24. Ding D, Wang M, Wu J-X, et al (2019) The Structural Basis for the Binding of Repaglinide to the Pancreatic K-ATP Channel. *Cell Rep* 27:1848+. <https://doi.org/10.1016/j.celrep.2019.04.050>
25. Bavro VN, De Zorzi R, Schmidt MR, et al (2012) Structure of a KirBac potassium channel with an open bundle crossing indicates a mechanism of channel gating. *Nat Struct Mol Biol* 19:158–163. <https://doi.org/10.1038/nsmb.2208>
26. Bernsteiner H, Zangerl-Plessl E-M, Chen X, Stary-Weinzinger A (2019) Conduction through a narrow inward-rectifier K⁺ channel pore. *J Gen Physiol* 151:1231–1246. <https://doi.org/10.1085/jgp.201912359>
27. Li D, Jin T, Gazgalis D, et al (2019) On the mechanism of GIRK2 channel gating by phosphatidylinositol bisphosphate, sodium, and the G $\beta\gamma$ dimer. *J Biol Chem* 294:18934–18948. <https://doi.org/10.1074/jbc.RA119.010047>
28. Whorton MR, MacKinnon R (2011) Crystal Structure of the Mammalian GIRK2 K(+) Channel and Gating Regulation by G Proteins, PIP(2), and Sodium. *Cell* 147:199–208. <https://doi.org/10.1016/j.cell.2011.07.046>
29. Cooper PE, McClenaghan C, Chen X, et al (2017) Conserved functional consequences of disease-associated mutations in the slide helix of Kir6.1 and Kir6.2 subunits of the ATP-sensitive potassium channel. *J Biol Chem* 292:17387–17398. <https://doi.org/10.1074/jbc.M117.804971>

30. Pipatpolkai T, Usher S, Stansfeld PJ, Ashcroft FM (2020) New insights into KATP channel gene mutations and neonatal diabetes mellitus. *Nat Rev Endocrinol* 16:378–393. <https://doi.org/10.1038/s41574-020-0351-y>
31. Puljung MC (2018) Cryo-electron microscopy structures and progress toward a dynamic understanding of KATP channels. *J Gen Physiol* 150:653–669. <https://doi.org/10.1085/jgp.201711978>
32. Lee KPK, Chen J, MacKinnon R (2017) Molecular structure of human KATP in complex with ATP and ADP. *eLife* 6:e32481. <https://doi.org/10.7554/eLife.32481>
33. Shimomura K, Hoerster F, de Wet H, et al (2007) A novel mutation causing DEND syndrome - A treatable channelopathy of pancreas and brain. *Neurology* 69:1342–1349. <https://doi.org/10.1212/01.wnl.0000268488.51776.53>
34. Tarasov AI, Girard CA, Larkin B, et al (2007) Functional analysis of two Kir6.2 (KCNJ11) mutations, K170T and E322K, causing neonatal diabetes. *Diabetes Obes Metab* 9:46–55. <https://doi.org/10.1111/j.1463-1326.2007.00777.x>
35. Drain P, Geng X, Li L (2004) Concerted gating mechanism underlying K-ATP channel inhibition by ATP. *Biophys J* 86:2101–2112. [https://doi.org/10.1016/S0006-3495\(04\)74269-1](https://doi.org/10.1016/S0006-3495(04)74269-1)
36. De Zorzi R, Nicholson WV, Guigner J-M, et al (2013) Growth of large and highly ordered 2D crystals of a K⁺ channel, structural role of lipidic environment. *Biophys J* 105:398–408. <https://doi.org/10.1016/j.bpj.2013.05.054>
37. Weber P, Pissis C, Navaza R, et al (2019) High-Throughput Crystallization Pipeline at the Crystallography Core Facility of the Institut Pasteur. *Mol Basel Switz* 24. <https://doi.org/10.3390/molecules24244451>
38. Kabsch W (2010) Integration, scaling, space-group assignment and post-refinement. *Acta Crystallogr D Biol Crystallogr* 66:133–144. <https://doi.org/10.1107/S0907444909047374>
39. Emsley P (2004) Coot: model-building tools for molecular graphics. *Acta Crystallogr Sect -Biol Crystallogr* 60:2126–2132. <https://doi.org/10.1107/s0907444904019158jissn>
40. Blanc E, Roversi P, Vornrhein C, et al (2004) Refinement of severely incomplete structures with maximum likelihood in BUSTER-TNT. *Acta Crystallogr S Section -Struct Biol* 60:2210–2221. <https://doi.org/10.1107/S0907444904016427>
41. Murshudov GN, Skubák P, Lebedev AA, et al (2011) REFMAC5 for the refinement of macromolecular crystal structures. *Acta Crystallogr D Biol Crystallogr* 67:355–367. <https://doi.org/10.1107/S0907444911001314>
42. Chen VB, Arendall WB III, Headd JJ, et al (2010) MolProbity: all-atom structure validation for macromolecular crystallography. *Acta Crystallogr Sect -Struct Biol* 66:12–21. <https://doi.org/10.1107/S0907444909042073>
43. Zhang Z, Marshall A (1998) A universal algorithm for fast and automated charge state deconvolution of electrospray mass-to-charge ratio spectra. *J Am Soc Mass Spectrom* 9:225–233. [https://doi.org/10.1016/S1044-0305\(97\)00284-5](https://doi.org/10.1016/S1044-0305(97)00284-5)
44. Brooks B, Bruccoleri R, Olafson B, et al (1983) CHARMM - A program for macromolecular energy, minimization, and dynamics calculations. *J Comput Chem* 4:187–217. <https://doi.org/10.1002/jcc.540040211>
45. Krissinel E, Henrick K (2007) Inference of macromolecular assemblies from crystalline state. *J Mol Biol* 372:774–797. <https://doi.org/10.1016/j.jmb.2007.05.022>
46. Pettersen EF, Goddard TD, Huang CC, et al (2004) UCSF chimera - A visualization system for exploratory research and analysis. *J Comput Chem* 25:1605–1612
47. Olsson MHM, Sondergaard CR, Rostkowski M, Jensen JH (2011) PROPKA3: Consistent Treatment of Internal and Surface Residues in Empirical pK(a) Predictions. *J Chem Theory Comput* 7:525–537. <https://doi.org/10.1021/ct100578z>
48. Sondergaard CR, Olsson MHM, Rostkowski M, Jensen JH (2011) Improved Treatment of Ligands and Coupling Effects in Empirical Calculation and Rationalization of pK(a) Values. *J Chem Theory Comput* 7:2284–2295. <https://doi.org/10.1021/ct200133y>
49. Jorgensen W, Chandrasekhar J, Madura J, et al (1983) Comparison of simple potential functions for simulating liquid water. *J Chem Phys* 79:926–935. <https://doi.org/10.1063/1.445869>
50. Jo S, Kim T, Iyer VG, Im W (2008) Software news and updates - CHARNIM-GUI: A web-based graphical user interface for CHARMM. *J Comput Chem* 29:1859–1865. <https://doi.org/10.1002/jcc.20945>
51. Lee J, Cheng X, Swails JM, et al (2016) CHARMM-GUI Input Generator for NAMD, GROMACS, AMBER, OpenMM, and CHARMM/OpenMM Simulations Using the CHARMM36 Additive Force Field. *J Chem THEORY Comput* 12:405–413. <https://doi.org/10.1021/acs.jctc.5b00935>
52. Lomize MA, Pogozheva ID, Joo H, et al (2012) OPM database and PPM web server: resources for positioning of proteins in membranes. *Nucleic Acids Res* 40:D370–D376. <https://doi.org/10.1093/nar/gkr703>
53. Huang J, MacKerell AD Jr (2013) CHARMM36 all-atom additive protein force field: Validation based on comparison to NMR data. *J Comput Chem* 34:2135–2145. <https://doi.org/10.1002/jcc.23354>
54. Mouawad L, Perahia D (1993) Diagonalization in a mixed basis: A method to compute low-frequency normal modes for large macromolecules. *Biopolymers* 33:599–611. <https://doi.org/10.1002/bip.360330409>
55. Piovesan D, Minervini G, Tosatto SCE (2016) The RING 2.0 web server for high quality residue interaction networks. *Nucleic Acid Res* 44:W367–W374. <https://doi.org/10.1093/nar/gkw315>
56. Shannon P, Markiel A, Ozier O, et al (2003) Cytoscape: A software environment for integrated models of biomolecular interaction networks. *Genome Res* 13:2498–2504. <https://doi.org/10.1101/gr.1239303>
57. Humphrey W, Dalke A, Schulten K (1996) VMD: Visual molecular dynamics. *J Mol Graph Model* 14:33–38. [https://doi.org/10.1016/0263-7855\(96\)00018-5](https://doi.org/10.1016/0263-7855(96)00018-5)

This next article focuses on the S129R mutation, engineered to trap the KirBac3.1 channel in an open conformation.

Article

Unexpected Gating Behaviour of an Engineered Potassium Channel Kir

Charline Fagnen^{1,2}, Ludovic Bannwarth¹, Dania Zuniga¹, Iman Oubella¹, Rita de Zorzi³, Eric Forest⁴, Rosa Scala⁵, Samuel Guilbault⁵, Saïd Bendahhou⁵, David Perahia² and Catherine Vénien-Bryan¹

¹Sorbonne Université, UMR 7590, CNRS, Muséum National d'Histoire Naturelle, Institut de Minéralogie, Physique des Matériaux et Cosmochimie, IMPMC, 75005 Paris, France.

²Laboratoire de Biologie et de Pharmacologie Appliquée, Ecole Normale Supérieure Paris-Saclay, Centre National de la Recherche Scientifique, Gif-sur-Yvette, France.

³Department of Chemical and Pharmaceutical Sciences, University of Trieste, Via Licio Giorgeri 1, 34127, Trieste, Italy

⁴University Grenoble Alpes, IBS, F-38044 Grenoble, France, CNRS, IBS, F-38044 Grenoble, France, CEA, IBS, F-38044 Grenoble, France.

⁵University Côte d'Azur, CNRS UMR7370, LP2M, Labex ICST, Faculté de Médecine, 06107 Nice, France.

CONDENSED RUNNING TITLE: engineered protein Kir channel gating

KEYWORDS: Potassium Channel KirBac3.1; Molecular Dynamics and Normal Modes; HDX-Mass Spectrometry; single channel recording

Fagnen C, Bannwarth L, Zuniga D, Oubella I, De Zorzi R, Forest E, Scala R, Guilbault S, Bendahhou S, Perahia D and Vénien-Bryan C (2021) Unexpected Gating Behaviour of an Engineered Potassium Channel Kir. *Front. Mol. Biosci.* 8:691901. doi: 10.3389/fmolb.2021.691901

KEYWORDS: Potassium Channel KirBac3.1; Molecular Dynamics and Normal Modes; HDX-Mass Spectrometry; single channel recording

Abstract

In this study, we investigated the dynamics and functional characteristics of the KirBac3.1 S129R, a mutated bacterial potassium channel for which the inner pore-lining helix (TM2) was engineered so that the bundle crossing is trapped in an open conformation. The structure of this channel has been previously determined at high atomic resolution. We explored the dynamical characteristics of this open state channel using an *in silico* method MDeNM that combines molecular dynamics simulations and normal modes. We captured the global and local motions at the mutation level and compared these data with HDX-MS experiments. MDeNM provided also an estimation of the probability of the different opening states that are in agreement with our electrophysiological experiments. In the S129R mutant, the Arg129 mutation releases the two constriction points in the channel that existed in the wild type but interestingly creates another restriction point.

Introduction

A detailed study of function requires careful dissection of the mechanistic steps. Protein engineering can provide a powerful tool for studying the relationships between structure and function. The design of various potassium channels with carefully chosen replacement residues has helped describe the gating mechanism of these channels. For instance, we can mention mutations close to the selectivity filter [1], on the wall of the cytoplasmic pore [2], on the cytoplasmic domain [3], at the end of the cytoplasmic pore [4], at the extracellular domain of Kir2.2 [5], at the bottom of the bundle crossing [6], or at the level of the cytoplasmic domain subunit interfaces [7]. All these investigations, either *in silico* or experimental (NMR, FRET, etc.) provided valuable information.

A few years ago, the open state kir channel's crystal structure was revealed by KirBac3.1 S129R [8, 9], which was designed so that the channel was trapped in an open conformation. Indeed, before the publication of this structure, most structures were known in the closed state, with the conduction pathway occluded. The use of an engineered protein made it possible to observe for the first time at high resolution the KirBac channel with the bundle-crossing gate in an open conformation, where the constriction points (Leu124 and Tyr132) are released [8] as shown in **Figure 1**. This structure allowed proposing a mechanism for opening the channel. In this structure, we noticed that the mutated residue Arg was facing the channel's center and therefore could create the condition for another unexpected constriction point. However, this channel is functionally open [10] and we did not notice any toxic effect of this engineered protein on the host cell [11]. We then decided to investigate further this mutated channel's function and dynamics using an experimental and *in silico* study, allowing us to explain its particular behavior, which, despite unexpected characteristics, provided valuable information on the open state structure.

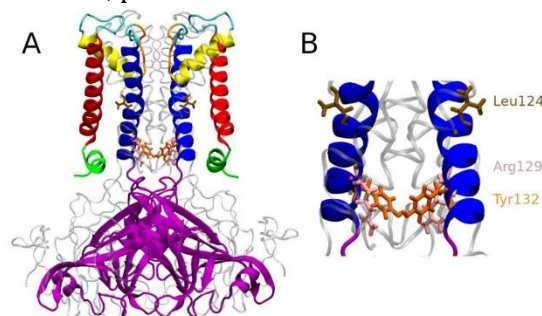


Figure 1. Anatomy of KirBac3.1 S129R from the modelled KirBac3.1 S129R. A) The transmembrane portion of each monomer of KirBac1.1 is composed of four helices: slide helix (green), transmembrane helix 1 (red), pore helix (yellow), and transmembrane helix 2 (blue). The mutation S129R is situated at the level of the helix bundle (pink), at the bottom of the inner helix. B) Leu124 and Tyr132 are shown in color brown and orange respectively. Arg129 is shown in pink.

Results and discussion

1 Hydrogen/Deuterium exchange approach coupled to mass spectrometry (HDX-MS)

We investigated the protein conformational flexibility of the S129R mutant protein (open state) using HDX-MS. This technique is based on the exchange of deuterium atoms at the amide backbone of a protein, reflecting its conformational dynamics, followed by proteolytic digestion and spectrometry analysis. HDX has been widely used on soluble and membrane proteins [12]. HDX was performed on the purified KirBac3.1 S129R mutant protein in the presence of detergent (**Figure 2B**). We have established in previous work that the presence of detergent does not affect conformational changes of the KirBac channel [13, 14]. The results were compared to those of WT for which the same detergent was used ([14] and **Figure 2A**), the comparison is shown in **Figure**

2C where red shows a S129R segment more flexible compared with the same segment in WT. The Optimized conditions resulted in sequence coverage of 86% with nepenthesin [14]. However, this enzyme did not allow covering the regions 57-87 (top half of the TM1 and the beginning of the pore helix), 143-147 (β 3) and 195-203 (second half of the β 7) for nomenclature see **Figure 2C**. Deuterium incorporation was monitored as a function of time for each peptide generated from the S129R mutant (Figure S1).

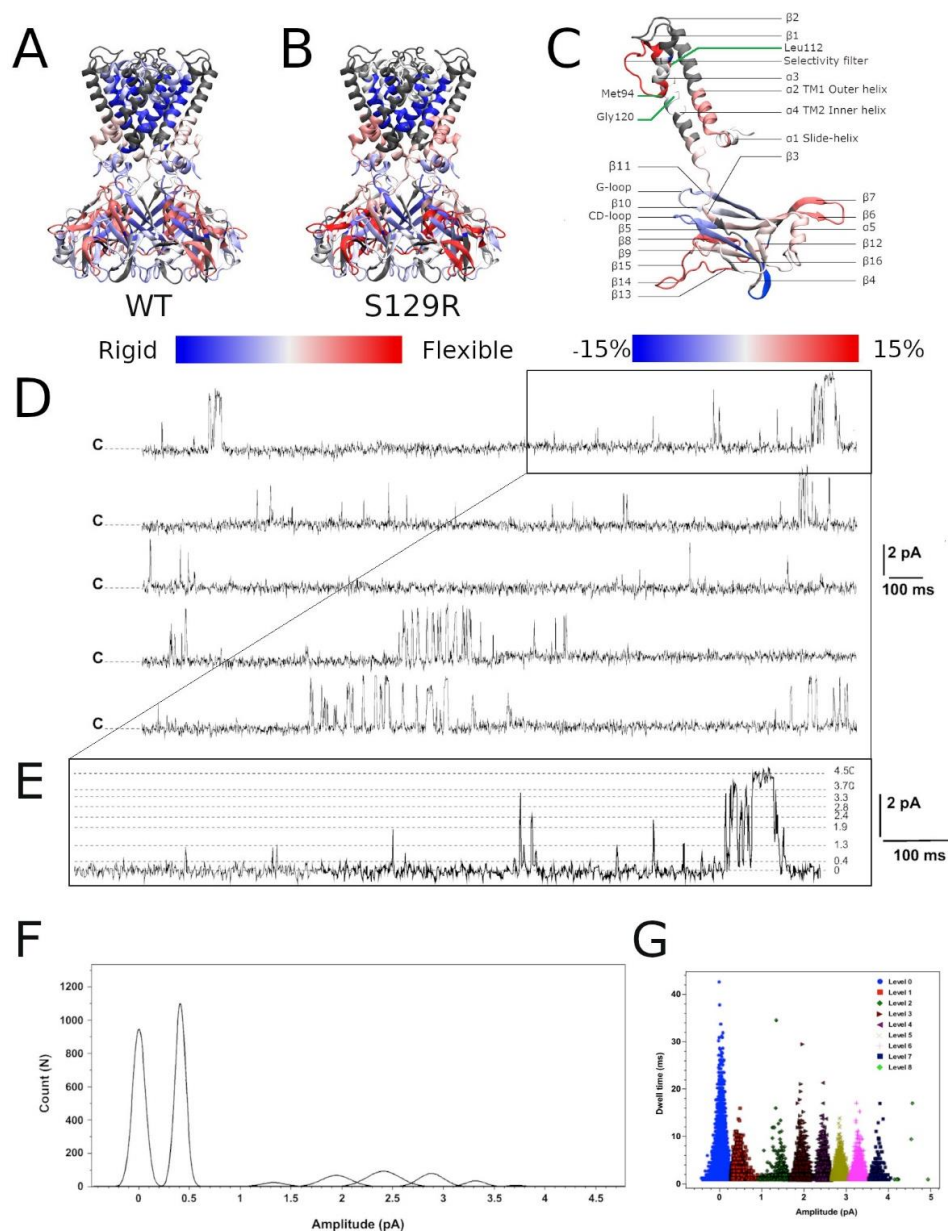


Figure 2. HDX-MS and single channel recordings HDX-MS rates of peptides reported for **A**) KirBac3.1 WT [12] and **B**) the mutant S129R. Identified peptides are drawn with blue (low exchange and low flexibility) to red (high exchange and high flexibility) color according to their percentage of deuterium exchange after 1,200 s (scale of exchange shown at the bottom of the figures). **C**) Nomenclature of secondary structures and rate of exchanges between the mutant S129R and KirBac3.1 WT. Scale of deuterium exchange rate is shown at the bottom of the figures, same color code as for A and B. Red appears when S129R is more flexible than WT and blue when S129R is more rigid than WT. **D**) Single channel recordings from KirBac3.1 S129R channels, traces obtained from 6 min consecutive recordings at +150 mV holding potential. Closed state is labelled C. E, an enhancement of the upper trace to show the multiple sub states induced by the S129R mutant. F, amplitude histogram fits (gaussian) of all events for the selected levels gating between closed and open states during 6 min. G: S129R channels gate with multiple subconductance states. Dwell time for all events at 150 mV test potential is plotted for all current levels.

1.1 Comparison between the KirBac3.1 WT (closed conformation) and S129R mutant (open state).

Our data shows that the most flexible regions for KirBac3.1 S129R are the loops extending outside the CTD (aa 271-285 between β 14 and β 15, in red **Figure 2B**; see also **Figure 2C** for the nomenclature). This external loop is subjected to the swinging movement during the gating [14]. If we compare the closed state of KirBac3.1 and the open state of KirBac3.1 S129R, the latter shows slightly more pronounced flexibility with a maximum value for the HDX of $68\% \pm 2.2$ (Mean \pm S.D n=3) against $59.1\% \pm 2.5$ for the closed state as shown in **Figure 2C**.

1.2 Structural flexibility of the transmembrane domain during the gating:

The largest change in the deuteration exchange percentage in the **S129R mutant** (35% versus 21%, compared with WT) is observed for the Thr93-Leu112 peptides (end of α 3 (pore helix), selectivity filter and top of α 4, (TM2)) , a feature described previously [13]. This includes the Met94 which is located towards the base of the pore-loop helix and packs closely with the Gly120 in TM2. Based on deuterium exchange percentages, the inner helix in the mutant S129R appears more flexible than in WT. At the TM1 level, there is an increase in deuteration, particularly at the bottom of the external helix, of $53.7\% \pm 2.2$ against $45.2\% \pm 1.3$ (**Figure 2C**).

1.3 Cytoplasmic domain:

These domains do not remain static during gating, and conformational changes should occur as the channel opens and closes. For both closed and open states, the greatest flexibility is found at the external loop. The KirBac3.1 cytoplasmic domain consists of two major β -sheets, one (which we refer to as β I, includes the large β 6, β 10 and β 11), that is tilted about 45° to the membrane plane, and a second referred to as β II (which includes the shorter β 3, β 5 and β 9) is approximately parallel to the pore axis as described in [15]. Our flexibility measure shows that the main β I sheet is more rigid than the other major β II sheet for both the WT (closed) and S129R mutant (open). The cytoplasmic domain's interior is more rigid than the exterior, with the highest values of flexibility for the open state.

On the contrary, the G-loop, located next to the CD loop is slightly less flexible in the S129R mutant (open state) ($9\% \pm 1.2$ against $12\% \pm 0.8$ in the close state). The G-loop has been described as very flexible [4, 11, 16, 17]. The five amino acids, 162 to 174 of the CD-loop, are also more rigid in the S129R mutant (open state) than in the WT (closed state) ($49\% \pm 2.3$ vs. $58\% \pm 2.5$). The decrease in deuteration in these two loops shows that they are involved in a network of interactions with neighboring amino acids, which are therefore less flexible. This was also found in [13].

1.4 To further assess the structural deviations of these two states, we compared the root mean square displacements (rmsd) of the residues (equation given in Materials and Methods) calculated over the MDeNM relaxed structures of KirBac3.1 WT (closed) and KirBacS129R (open). The results are shown in Figure S2. Minor rmsd values were observed in the closed state, particularly in the transmembrane region. For both structures, the smallest rmsd values (less than 2.8\AA) are in the transmembrane region. The open state shows slightly higher values, particularly in the region of TM1, the pore helix, and the bottom of TM2 with a high value at the position of the S129R mutation. The cytoplasmic domain exhibits higher rmsd values particularly the external loop, which reaches 5.8\AA and 5.2\AA , for the open and closed states, respectively. This is in agreement with HDX-MS data, for which the highest flexibility is in this region.

2 Current recordings of KirBac3.1 in planar lipid bilayers.

When reconstituted into black lipid membranes, the KirBac3.1 S129R channels exhibit significant gating activity as shown by current recordings for 6 min at +150 mV (**Figure 2D**). As reported for the KirBac3.1 WT and KirBac 1.1, the KirBac 3.1 S129R gates with multiple subconductance states [18, 19]. The amplitude values for these levels are 0.40 ± 0.001 pA, 1.32 ± 0.002 pA, 1.94 ± 0.003 pA, 2.41 ± 0.001 pA, 2.88 ± 0.002 pA, 3.31 ± 0.001 pA, 3.71 ± 0.002 pA, and 4.50 ± 0.007 pA (**Figure 2E**). Fits of Gaussian distributions of amplitude histograms resulted in a single channel current level of 4.5 ± 0.007 pA, corresponding to a conductance value of 30 pS (**Figure 2F**). A value similar to that has been obtained for KirBac 3.1 WT (47 pS) [14]. KirBac S129R gates with subconductance level activity that increases the P_o to levels as high as 44.05 ± 2.6 % (Mean \pm S.D. $n = 16107$, number of events). Plotting dwell time *versus* current amplitude of all the events shows that the S129R mutant gates with more subconductance levels, than the WT, that are contributing to the overall P_o as follow: 7%, 3%, 11%, 9%, 5%, 6%, 4%, and 1%, respectively (**Figure 2G**). We have already shown that WT channels gate with only 2 subconductance levels (1 pA and 2 pA current amplitude) [14].

3 Theoretical Results

The theoretical results presented in this section are based on MDeNM (Molecular Dynamics with excited Normal Modes) simulations in which different linear combinations of a selected set of normal modes (NMs) related to the opening/closing of the channel are excited in molecular dynamics (MD) simulations [20]. Through such a combined use of both methods, MDeNM allows a realistic exploration of the normal mode space relevant for the opening/closing mechanism taking into account the full environment (membrane, water, ions) of the protein at the ambient temperature. Standard MD simulations were thereafter carried out on a uniformly distributed set of structures obtained from MDeNM, which provided a reasonably good estimate of the populations of open/closed (and partially open) states. MDeNM is based on covering uniformly without any bias the whole normal mode space defined by a selected set of low frequency modes. In our study the normal modes that were chosen are all those that are involved in the opening/closing motion of the channel. Therefore, the open and closed states were equally and uniformly sampled. The tests that were done in the original article [20] has shown an extensive not biased sampling, giving a good estimation of the probabilities of different states.

3.1 Constriction points along the channel in the KirBac3.1 WT and the S129R mutant

In this work, a 'closed' state is defined by a conduction pathway which is sterically occluded and an 'open' state in which the pathway is sufficiently wide to accommodate at least a non hydrated potassium ion. The channel encompasses the region between residues 121 and 133. The constriction points in this region for the WT are located at the levels of Leu124 and Tyr132 (**Figure 1B**). To have a dynamical view of the relaxed structures obtained in the MD simulations (that follow the MDeNM), we calculated the shortest atom-atom distance (including hydrogens) between the same residues that are at the opposite chains at a given constriction level (Tyr132 or S/R129). The distances were calculated on KirBac3.1WT (closed state) and the KirBac3.1 S129R (open state) (**Figure 3A** and **Figure 3B**, respectively). The average shortest distance at the level of Ser129 in KirBac3.1 WT is 9.53\AA (SD=0.47 \AA) (**Figure 3A** in red) and that at the level of Arg129 in S129R mutant is narrower with a value of 4.46\AA (SD=1.28 \AA) (**Figure 3A** in blue). This is a

marked decrease in the channel diameter at the level of the mutation. Interestingly, the mutation at residue 129 introduces another constriction point in the channel which should not allow the K^+ ion to pass easily. **Figure 3** shows a set of distances situated in the gray zone which is indicative of a closed state.

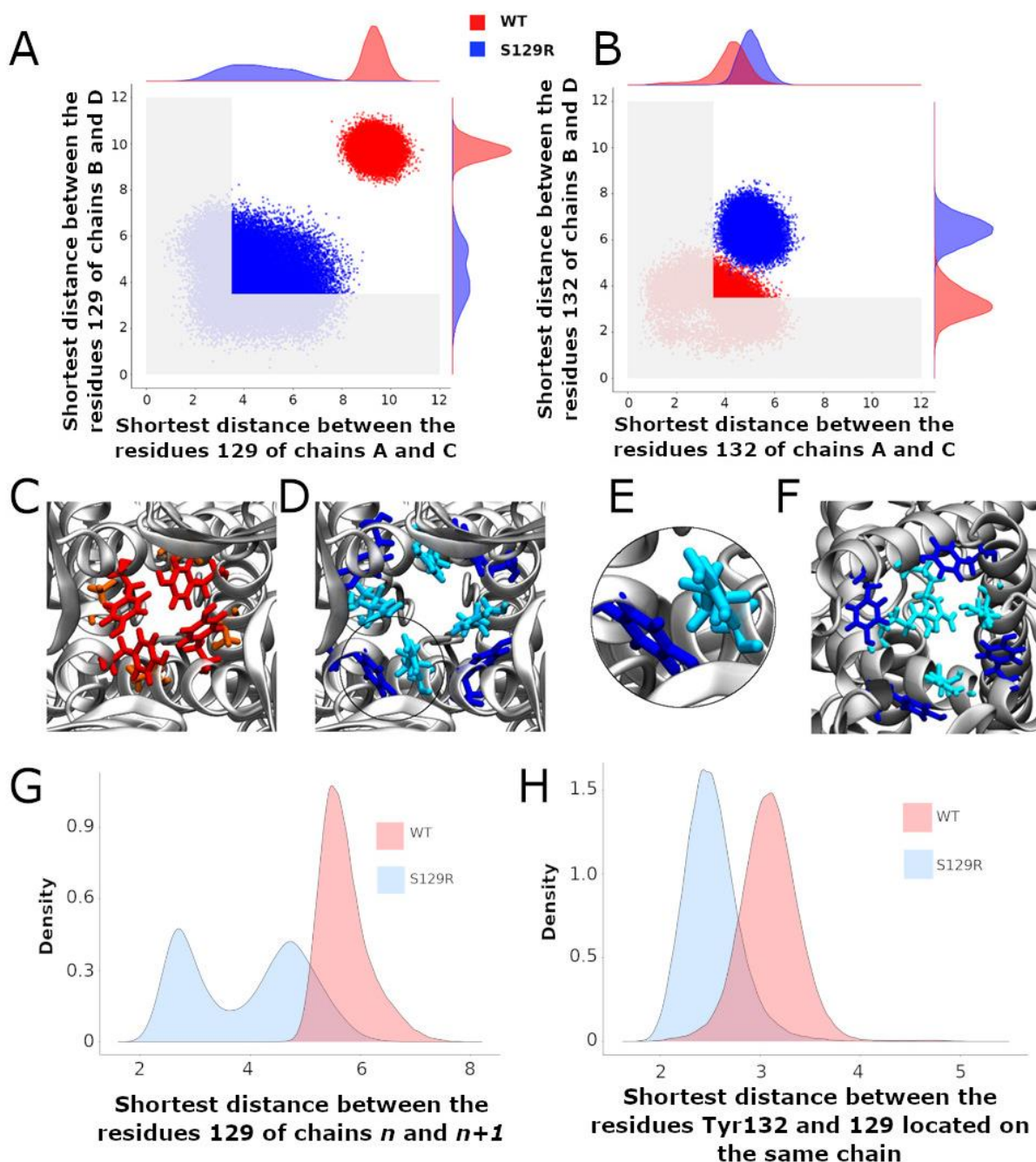


Figure 3. Gating at the mutation S129R and at the constriction point Tyr132 **A)** Scatter plots of the shortest distances between the chains B and D and between A and C at the level of the residue 129. The shortest distance between two residues is that between their respective atoms including the hydrogens; **B)** Scatter plots of the shortest distances between the chains B and D and between A and C at the level of the residue Tyr132. A-B) Red and blue points correspond to the KirBac3.1 WT and KirBac3.1 S129R, respectively. The gray area delimits the region where the channel is closed. **C-E):** representation of the relaxed structures; **C)** Locations of the residues Tyr132 (red) and Ser129 (orange) in KirBac3.1 WT; **D)** Locations of the residues Tyr132 (dark blue) and Arg129 (cyan) in KirBac3.1 S129R; **E)** Zoom on the Van der Waals between Tyr132 and Arg129 in KirBac3.1 S129R; **F)** Locations of the residues Tyr132 (dark blue) and Arg129 (cyan) pointing toward the center of the channel in KirBac3.1 S129R; **G)** Histograms of the shortest distance between residue 129 of the chain n and the residue 129 of the chain $n+1$; **H)** Histograms of the values of the shortest

distances between the residues 129 and Tyr132 from the same chain. The histograms in panels G and H were established by taking into account all the chains.

Tyr132 has been described as a constriction point in KirBac3.1 WT confirmed with an average shortest distance obtained of 3.72Å (SD= 0.87Å)[14] In the KirBac3.1 S129R mutant, the average shortest distance, at this constriction point is larger with a value of 5.75Å (SD 0.87Å) (**Figure 3B** points in blue and **Figure 1B** in orange). This point of constriction is therefore released. The Leu124 constriction point is also in an open configuration in the KirBac3.1 S129R mutant (**Figure 1B** in brown). We provided in Table S1 the radius values of the pore (computed with the HOLE program) at the constriction levels, as well as the kink angle values of the TM1 for the KirBac3.1 WT and KirBac3.1 S129R crystallographic structures, and KirBac3.1 S129R simulated structures in one of their closed or open conformations. It is worth to notice that the pore at the level of the mutation can adopt a narrower radius in a representative MDeNM structure comparatively to its X-ray structure. We also notice that at the level of the residue 132 we have a larger pore radius for the simulated closed structure than in the X-ray structure. The kink angles of TM1 in three chains out of four are also larger in the chosen simulated open structure than in the closed one, but their mean values (**Figure 4**) are all larger in the mutant than in the WT, a trend similar to what is observed when comparing both X-ray structures.

3.2 Interactions of the residue 129

We investigated the interactions of residue 129 with its neighboring residues and the changes in the interaction network caused by the mutation in all the relaxed MDeNM structures[14].

The probability density of the distances between two adjacent Ser129 in WT showed a single peak around 5.9Å, the two residues being quite distant (**Figure 3G**, in red). Note that higher density of probability means more favorable interactions. For the mutant, the distances between two adjacent Arg129 are distributed into two populations centered around 2.7Å and 4.8 Å (**Figure 3G**, in blue). The first peak corresponds to a close interaction between the two arginine heads which point towards the center of the channel and therefore obstructing it (**Figure 3F** in cyan), the second representing more distant residues similar to KirBac3.1 WT. The interaction energy computed between pairs of Arg shows that those belonging to opposite chains can interact favorably as shown in the scatter plot of the interaction energy *versus* the shortest distance in Figure S3 computed for the ensemble of the MDeNM relaxed structures. It is seen that interaction energies can reach values close to -4 kcal/mole. The representative structure corresponding to the lowest interaction energy is also displayed in this figure. Although Arg has a positive charge it was shown that they can interact favorably between them adopting different orientations [21].

Note that the distribution of shortest distances depend on which chains are considered. Indeed, the crystallographic structures of KirBac can exhibit four-fold symmetry, but more often two-fold symmetry or even no symmetry[8,11,19]. Moreover, the side chains in these crystallographic structures are slightly asymmetric.

We investigated the interaction between the mutated residue and Tyr132 which constitutes a region of constriction along the channel in WT (**Figure 3H**). The most populated shortest distance is greater for WT (3.3Å) than for mutant (2.5Å). The contact between the two residues for the mutant is shown in **Figures 3D-E**.

In the closed state, residue 132 points towards the center of the channel and obstructs the passage of the K⁺ ion (**Figure 3C** in red). In the mutant, Tyr132 is displaced from the channel's center coming in contact with Arg129, as shown in **Figure 3D** (See also Figure S4 for details).

The interaction energies between the Arg129 and Tyr132 as a scatter plot are given in Figures S5 and S6 with the molecular graphics of the most favorable structures. They show that they can interact strongly with an interaction energy around -10 kcal/mol in the case of Arg129B and Tyr132C forming a hydrogen bond between them (Figure S6), and around -5 kcal/mol between Arg129B and Tyr132B. Interestingly, the Arg129 residues in all four chains point either to the center of the channel and thus block the passage of K⁺ ion (**Figure 3F**) or interact with the aromatic ring of Tyr132 residues (**Figure 3D**).

3.3 Open and closed state populations

Four channel-gating states can be defined based on the open or closed conformation of the two main constriction points (Leu124 and Tyr132) as observed in relaxed structures (for more details, see [14] Figure S7): 1) Fully open state, sufficiently wide to accommodate at least a non-hydrated K⁺ ion, that is, when the shortest diametrically opposed inter-chain atomic distances at the two constriction points are greater than the ionic diameter of K⁺ (diameter of K⁺ ion considered 3.5275 Å [22]); 2) fully closed state, when both distances are less than the ionic diameter of the potassium ion; 3) partially open state 1, when the gate at residue Leu124 is open, and the gate at residue Tyr132 is closed; 4) partially open state 2 when the gate at residue Tyr132 is open, and the gate at residue Leu124 is closed. Considering the previous observation showing that the side chain of the mutant Arg129 can point towards the center of the channel and constitutes another constriction point, we therefore added another partially closed configuration at the level of Arg129.

We analyzed 34086 relaxed structures issued from MDeNM simulations for KirBac3.1 WT and 29600 for KirBac3.1 S129R to have important information on these states' populations. The populations of the different WT and mutant states are shown in Table 1, indicating that the fully open state in KirBac3.1 WT is only populated by about 6.8%. Such a low value is consistent with the population obtained by previous electrophysiological experiments [14]. In contrast, the S129R mutant is mostly open by about 53%, the Arg129 keeping the two Leu124 and Tyr132 restriction points, always open. Interestingly, the Arg can adopt two conformations: one in which it interacts directly with Tyr132, and the other where it points to the channel's center obstructing it. Therefore, the closed state of the mutant depends only on the conformation of Arg. Ironically, the mutated residue, which was introduced in the protein to force the channel to open, by trapping the bundle crossing in an open conformation, causes some obstruction to the potassium ion's passage.

Table 1. Populations (in percentage) of different opening states in the relaxed structures of KirBac S129R obtained through MDeNM simulations and single channel recording; comparison with KirBac3.1 WT is shown.

Opening Types	KirBac3.1 WT (%)	KirBac3.1 S129R (%)
Fully open	6.8	52.8

Fully closed	50.2	0.0
Gating 124 open, Gating 132 closed	28.8	0.0
Gating 132 open, Gating 124 closed	14.2	0.0
Gating 129 closed	0.0	47.2
Current recordings of KirBac3.1 in planar lipid bilayers	9.9 (± 1.3, n = 1803) (ref 14)	44.05 (± 2.6 % Mean \pm S.D. n= 16107)

3.4 Structural modifications between the closed (KirBac3.1 WT) and open (KirBac3.1 S129R) states.

3.4.1 Kink of the outer helix TM1

The TM1 outer helices' kink angles were calculated to determine the extent to which their bending is involved in the channel's opening. We compared the kink angles for the TM1s for KirBac3.1 WT and S129R, which are given in **Figure 4**.

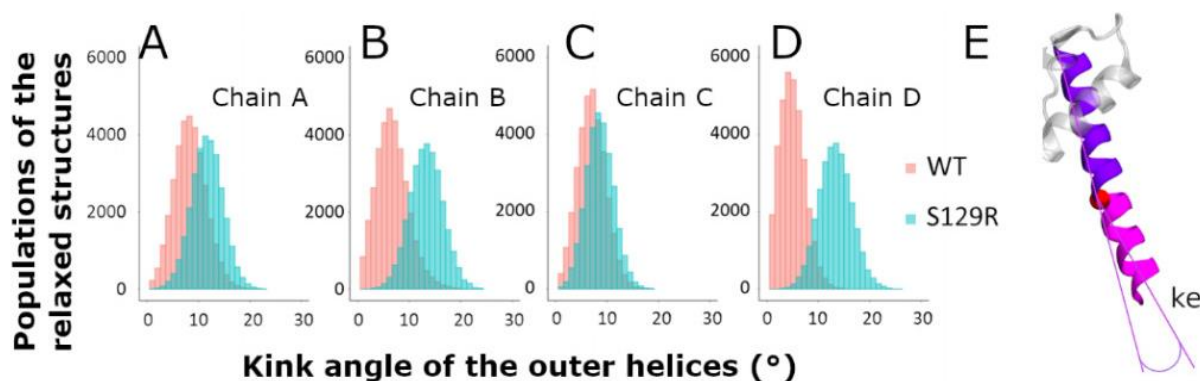


Figure 4. Kink of the outer helices, TM1. Histograms of the values of the kink of the external helices during the relaxed simulations of molecular dynamics after MDeNM. The structures populations of KirBac3.1 WT are represented in red and the structures of KirBac3.1 S129R in blue. **A)** Kink of the outer helix of the chain A. **B)** Kink of the outer helix of the chain B. **C)** Kink of the outer helix of the chain C. **D)** Kink of the outer helix of the chain D. **E)** Representation of the outer kink angle (ke).

We calculated the kink of the outer helix on all the relaxed structures. The mean values of the kink of TM1 for the chains A, B, C and D of KirBac3.1 WT are respectively of 8.39° (SD=3.09°), 6.51° (SD=3.12°), 7.04° (SD =2.70°) and 4.97° (SD=2.39°) while the mean values for KirBac3.1 S129R are 11.70° (SD = 3.03°), 13.33° (SD =3.18°) , 8.59° (SD=2.66°) and 13.308° (SD=3.18°). These results highlight that the presence of the mutation S129R on TM2 has a knock-on effect on TM1, triggering a greater kink of this outer helix as noticed in the cryo-EM analysis [10].

3.4.2 Rotation of the cytoplasmic domain

Motions of the cytoplasmic domain that couple ligand binding to the gating of the channel have been thoroughly investigated and various models have been proposed. From the KirBac3.1 S129R mutant's crystallographic data, a model described as "twist to open" has been proposed, on which a rotation of about 25° of the CTD around the central axis of the channel perpendicular to the membrane is crucial to allow gating. This is why we performed a thorough examination of the

angle of rotation of each chain's cytoplasmic domain around the central axis on all the relaxed structures (See the definition of the rotation angle **Figure 5A**).

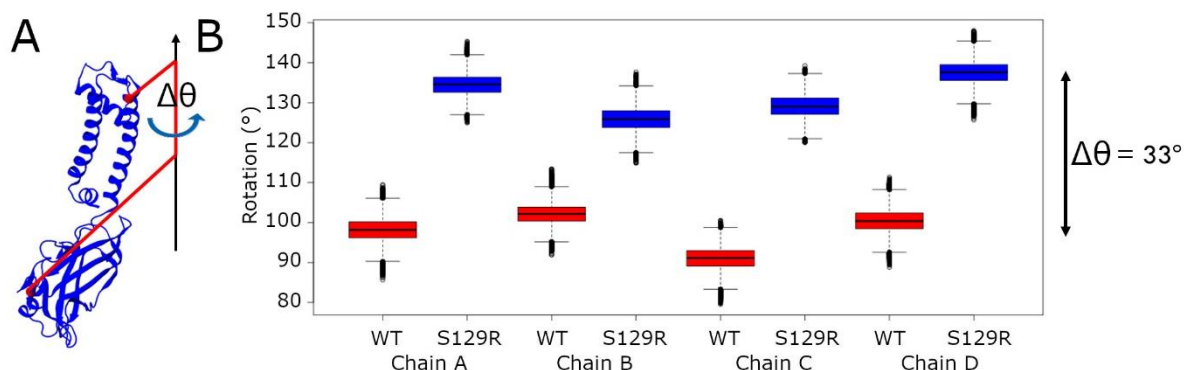


Figure 5. Rotation of the cytoplasmic domain. **A)** Definition of the cytoplasmic domain rotation angle of a given chain; **B)** Boxplots of the rotation angle's values of the cytoplasmic domain for each chain for KirBac3.1 WT and KirBac3.1 S129R. The angles were computed on all the relaxed structures of KirBac3.1 WT (red) and KirBac3.1 S129R (blue). The middle line of each box corresponds to the median values. The variation of the 33° between the WT and mutant were obtained from these average values.

We compared the rotation angles of the cytoplasmic domain of the KirBac3.1 WT and KirBac3.1 S129R, they are given in **Figure 5B**. The mean cytoplasmic domain rotation values are 97.95° (SD = 5.13°) and 131.78° (SD=5.41°) for WT and mutant, respectively. An average difference of 33° is observed between the two systems. This is to be compared with the data obtained from crystallographic structures, which show a difference of the cytoplasmic domain rotation angle of 30° between the KirBac3.1 WT (closed state) and KirBac3.1 S129R (open state) [8]. It can be observed that both experimental and *in silico* studies are very comparable. The structures obtained by MDeNM appear very stable with very small variations.

To study the S129R mutation effect on the interaction between the cytoplasmic domain and the membrane interface, we calculated two distances: i) between His35 on the slide helices and Arg167 (CD-loop on the CTD); ii) between Pro138 (the linker between the transmembrane and the cytoplasmic domain) and Phe250 (G-loop on the CTD). The G-loop has been described as being mobile during gating in molecular dynamics studies[23, 24] and X-ray data[4]. The location of residues is indicated in **Figure 6C**.

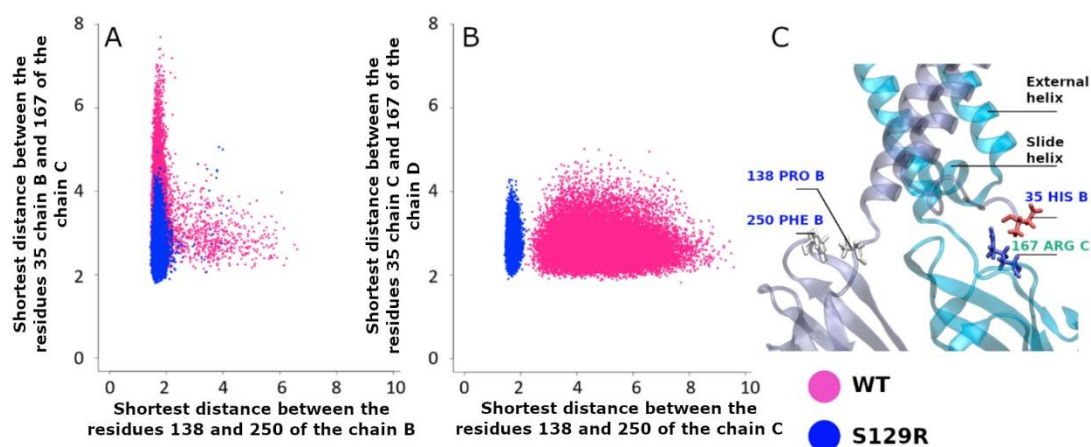


Figure 6. Interaction between the cytoplasmic and the membrane interface. Pink points are for KirBac3.1 WT, blue points for the S129R mutant. **A)** Shortest distance between the slide-helix (residue Asp35 Chain B and the CD-loop (residue Arg167 Chain C) versus the shortest distance between the linker (residue Pro138 Chain B) and the G-Loop (residue Phe250 Chain B); **B)** Shortest distance between the slide-helix (residue Asp35 Chain C) and the CD-loop

(residue Arg167 Chain D) versus the distances between the linker (residue Pro138 Chain C) and the G-Loop (residue Phe250 Chain C); **C**) Location of the interactions.

The structures resulting from the dynamics highlight the differences between WT and the mutant. **Figure 6A** shows that the interaction between Pro138 and Phe250 (chain B) is stronger in S129R compared to WT. The distances between the amino acids are from 1.91 Å to 5.06 Å in the S129R mutant (in blue) and from 1.82Å to 7.70Å in KirBac3.1 WT (in red) predominantly closed (93.2% of the structures). The same trend is observed for the chain C, shown in **Figure 6C**, as they do not exceed 2.34 Å while the range of values for WT extends over 9.58 Å (**Figure. 6B**). The distances between the residues His35 Chain B and Phe167 Chain C are also lower in S129R

The S129R mutant shows a stronger interaction between the cytoplasmic domain (G-loop and C loop) and the membrane interface (slide helix and linker) and a greater stability.

Conclusion

Our MDeNM simulations on S129R show clearly that the mutation leads to a greater opening probability of about 52.8 % compared to 6.8% in the WT, which is corroborated by functional data from single channel recordings 44.05 (± 2.6 % Mean \pm S.D. n= 16107) compared with 9.9 (± 1.3 , n = 1803) in the WT. In this study, we observed the opening of the constriction points in the channel and the inherent motions of KirBac3.1 S129R associated with the gating in the absence of K⁺ inside the pore. Our *in silico* results, in the estimation of open state population, carried out in the absence of K⁺ ions, are very similar with experimental electrophysiological accounting of these ions. The gating is therefore mainly linked to the intrinsic dynamical properties of the channel and not dependent only on the presence of the K⁺ ions. The presence of the Arg mutation triggers the release of the two constriction points that existed in WT protein, but at the same time, this residue can block the passage of the K⁺ ion through the channel. Indeed, Arg can adopt two conformations, pointing either towards the channel's center or standing parallels to the channel and interacting with Tyr132. This explains why the opening probability is only 52.8% and not 100%. Also, the transmembrane external helices (TM1) show a more pronounced kink and flexibility in the case of the S129R mutant in agreement with our HDX-MS experiments. In addition, the contacts between Pro138 and Phe250 (G-loop), and the inter-chain contact between His35 (slide-helix) and Arg167 (CD-loop) are stabilized, and the mutant shows a greater stability.

One of the conclusions of this study is that care must also be taken when selecting replacement residues since this could affect importantly the structural and dynamical behaviour of the system under consideration as it is the case here.

Materials and Methods

This article focuses on understanding the structural behavior of KirBac3.1 S129R, making the comparison with the KirBac3.1 WT necessary to detect its specific aspects. The data and details concerning the latter were described in our previous article [14].

1 Protein expression and purification

Same construct as for the protein used for the structure determination was used [8]. Protein expression and purification of this mutant channel were performed as outlined before [11].

Briefly, after cell disruption by French press, the protein was solubilized with 45 mM DM (Decyl β -D-maltopyranoside), centrifuged, and the supernatant was loaded onto a Co²⁺ affinity column. The protein was promptly purified on a Superdex 200 column pre-equilibrated with 2mM TriDM buffer. Concentrated preparations (1-2.5 mg/ml) of purified proteins (>95% purity, judged by SDS-PAGE) were stored at -80°C in a buffer containing 20 mM Tris, pH 7.4, 150 mM KCl and 0.2 mM TriDM.

2 Pepsin Digestion, Hydrogen/Deuterium exchange approach coupled to mass spectrometry (HDX-MS) and HPLC Peptide Separation and Mass spectrometry of peptides.

These experiments were performed as outlined before [14]. Briefly, all protein digestions in solution were performed in an ice bath at 0 °C. Protease solutions were prepared in 500 mM glycine (pH 2.2). KirBac3.1 S129R protein samples were digested in the same buffer for 2–5 min using a protease/substrate ratio of 1:1 or 1:10 (wt/wt) for pepsin and nepenthesin, respectively, either in solution or immobilized on a resin. The increase in digestion time did not affect the proteolysis. HDX-MS reactions were carried out on KirBac3.1 S129R at a protein concentration of about 10 μ M. The reaction was initiated by a 10x dilution of the protein samples (10 μ L) into a deuterated buffer containing 50 mM KCl and 0.2 mM TriDM. The time course of the HDX was followed over a 20-min period by sequential withdrawing 120 μ L of deuterated samples, which were immediately added to 26 μ L of quenching buffer (8 M guanidium chloride, 500 mM glycine HCl, pH 2.2), rapidly mixed, and flash-frozen in liquid nitrogen. After protease digestion in solution or on column in an ice bath at 0 °C, the peptides were loaded onto a peptideMicroTrap (Michrom Bioresources) column and washed with 0.03 % TFA in water (HPLC). They were then separated on a reversed-phase C12 column (1 \times 50 mm, Jupiter; Phenomenex) using a linear gradient of 15–45 % (vol/vol) of solution B (CH₃CN 95 % and TFA 0.03 %) during 26 min. The tandem MS (mapping) analyzes were performed on an ion trap mass spectrometer (Esquire 3000+; Bruker Daltonics) to identify the peptides after their separation on HPLC. Accurate mass measurements and local deuteration kinetics analysis were performed on a time-of-flight (TOF) mass spectrometer (6210; Agilent Technologies) equipped with an electrospray source. Each deuteration experiment was performed in triplicate. Data were processed as described in [14]

3 Electrophysiology

An Orbit mini was used (Nanion, Germany, horizontal planar lipid bilayer system), where two aqueous chambers (150 μ L) are separated by a partition with a 150- μ m hole where the lipid bilayer is formed by 1,2-diphytanoyl-sn-glycero-3-phosphocholine (DPhPC, 15–50 pF). The lower chamber contained 150 mM KCl, 10 mM MOPS, pH 7.4. After membrane bilayer formation, the upper chamber solution was changed to 150 mM KCl, 10 mM MOPS pH 8. 1 μ L of purified KirBac3.1 S129R (90 μ g/mL) in DDM (n-DoDecyl- β -D-maltoside) detergent (0.015%) was added to the upper chamber to a preformed bilayer. Currents were recorded using Elements Data Reader (Nanion, Germany) and analyzed using Clampfit (Axon Instrument Inc, USA) software, sampled at 100 μ s and filtered at 1.25 kHz. Recordings were performed at 24 °C.

4 Molecular Modelling

KirBac3.1 was modelled in two different states, the closed one, modeled from the PDB structure of the wild type, 2WLJ (at 2.60Å atomic resolution) described also previously [14], and the open one, modeled from the PDB structure 3ZRS (KirBac3.1 S129R at 3.05Å resolution). KirBac3.1

S129R had missing C and N-terminal fragments, so the modeled structure describes the protein from residue 35 to 295; other missing atoms were rebuilt using the CHARMM program. We applied the P42₁2 symmetry to the 3ZRS PDB structure using the Protein Interface Surface and Assemblies software[25] to build the tetramer. We applied the “Orientation of Proteins in Membranes” (OPM) software [26] and the protein was then included into a 114.566 x 114.566 x 128.572 Å³ water box containing 36 629 water molecules with 150 mM KCl, and an 1,2-dioleoyl-sn-glycero-3-phosphocholine (DOPC) membrane using CHARMM-GUI [27, 28] .

5 Normal Modes.

Structures were minimized using the steepest descent (SD) and conjugate-gradient (CG) methods followed by Adopted Basis Newton Raphson (ABNR) algorithm. Harmonic restraints were applied during SD minimization, which were gradually reduced. Then the system was subjected to 50000 CG steps without restraints followed by ABNR minimization until a convergence of 10⁻⁵ Kcal mol⁻¹ Å⁻¹ RMS energy gradient was reached. The first 200 lowest frequency normal modes, ranged in ascending order of frequencies, with all the atoms taken into account were computed using the iterative DIMB method [29, 30] in CHARMM.

It was necessary to select the modes that contribute the most to the channel's conformational changes to proceed with the MDeNM calculations. The channel was defined from residues 121 to 133. For each normal mode, the minimized energy structure was first globally displaced by 2Å of RMSD. To select them, a process similar to the one used for the KirBac3.1 WT was applied[14]. Firstly, the ten normal modes showing the highest variations at the level of the channel were retained. To evaluate these variations, the distances between the residues 125 of opposite chains were considered. Secondly, only the normal modes describing spherical and elliptical opening of the channel were taken into account. Redundant modes were excluded keeping only the lowest frequency normal modes. This protocol allowed us to select 4 modes that affect the most the gating of the S129R.

6 Molecular Dynamics using Excited Normal Modes

The Molecular Dynamics using excited Normal Modes (MDeNM) method [20], promotes large conformational changes while taking into account the coupling with local fluctuations. This method allows a larger exploration of the conformational space and the generation of a wide variety of different structures at a lower computation time, which would not have been possible using only the standard MD. The method consists first to achieve different linear combinations of the selected normal mode vectors such that the combined vectors describe different movements of a given region (here the channel region). They are chosen such that the displaced structures along them up to a given distance (1 Å) display a uniform distribution of local RMSDs between them (see ref [20]for more details).

In a second stage these directions are used in MD simulations for defining additional velocities oriented along these very directions, and corresponding to a given kinetic energy, that are added to the current MD velocities. Such a kinetic excitation was periodically repeated at a given period of time (called the relaxation time) for propagating the movement to larger distances and allowing the coupling with local motions. A sufficient number of excitations were applied to reach an energetically acceptable large displacement. The simulations were carried out independently for every NM combined vector, each of these simulations being called a replica simulation. For each replica 10 successive excitations were applied, each one corresponding to a 4K rise of the overall

temperature; the relaxation time between two excitations was 1 ps. The numbers of replica used are 62 and 66 for KirBac3.1 WT and KirBac3.1 S129R, respectively.

6.1 Relaxation of the MDeNM structures

Free MD simulations were carried out on MDeNM structures to relax them further energetically and release the excess kinetic energy that would have been accumulated during the excitations. These relaxation simulations were carried out on a limited number of representative structures obtained by clustering the MDeNM structures to save simulation time. The VMD clustering tool [31] was used to find at least 100 different clusters separated by a distance greater than an RMS threshold of 0.9Å on the channel (from Met121 to Ala133). A representative structure was chosen for each cluster, which was the closest to the cluster's average structure. Unique structures not belonging to any cluster were also selected. Overall, 114 and 99 clusters were obtained for KirBac3.1 WT and KirBac3.1 S129R, respectively. Each representative structure was subjected to a free MD simulation of 0.4 ns to release the excess kinetic energy and allow local movements to occur, amounting to a total of 39.6 ns for all the KirBac3.1 S129R's structures considered. The simulations were carried out with NAMD v2.10[32] at constant temperature of 300K and constant pressure of 1 atm using Langevin piston. Periodic Boundary Conditions and the Particle Mesh Ewald method were used for the electrostatic interactions. The motion propagation is driven by the Leapfrog Verlet algorithm. Concerning the non-bonded interactions, the cut-on and the cut-off were 10 and 12Å, respectively. Charmm36 force field was used for the simulations. The parameters used were the same for the MDeNM simulations.

6.2 Analysis of Molecular Dynamics simulations.

The results presented in this article are based on the relaxed structures from free MD simulations in which only the last three-quarters of the trajectories were kept, that represents 29 600 structures.

The shortest distance between two residues was calculated considering the distances between all their respective atoms including the hydrogens with the CHARMM software. The shortest distances calculated at the different levels of the channel and different pairs of residues were used to define the various open/closed states. Six shortest distances were considered: i) between Leu124 of chain A and Leu124 of chain C, ii) between Leu 124 of chain B and Leu124 of chain D, iii) between Tyr132 of chain A and Tyr132 of chain C, iv) between Tyr132 of chain B and Tyr132 of chain D, v) between Arg129 of chain A and Arg of chain C, iv) between Arg129 of chain B and Arg129 of chain D.

The kink of each of the outer helices is defined by the angle between the axis of the first part of the helix going from Trp46 to Leu56 and that of the second part going from Leu56 to Asp80.

The cytoplasmic domain rotation for each of the chains was calculated as the pseudo bonds' dihedral angle defined by four successive points defined by Leu108, its projection on the central Z-axis passing through the channel, the projection of Ile266 on the same axis, and Ile 266 itself.

The kink and the dihedral angles were calculated using the CHARMM software.

The Root-Mean-Square Deviation of a given atom i (RMSD_i) was computed over the ensemble of all the MDeNM relaxed structures for KirBac3.1 WT (34086 structures) and KirBac3.1 S129R, (29600 structures), respectively. The RMSD_i is defined by the equation

$$RMSD_i = \sqrt{\frac{1}{N} \sum_{n=1}^N |r_i(n) - r_i^{ref}|^2}$$

where i is the atom number, N the total number of structures considered, $r_i(n)$ the position of the atom i in the structure n , r_i^{ref} the position of the atom i in the reference structure. The RMSD of a given residue was calculated by averaging the $RMSD_i$ of atoms belonging to the given residue.

Acknowledgments

We would like to thank financial supports from SERVIER and ANR CACSICE (#11-EQPX-0008) (CVB); AFM grant (#23207) (SB and CVB) and PhD research funding, MRT (CF). This work was performed using HPC resources from the “Mésocentre” computing center of CentraleSupélec and ENS Paris-Saclay supported by CNRS and Région Île-de-France (<http://mesocentre.centralesupelec.fr/>). It was granted access to the HPC resources of IDRIS under the allocation 100512 made by GENCI/IDRIS (DP).

Author Contributions: DP, EF and CVB conceived and designed the research. CF performed the MDeNM calculations under the supervision of DP; RDZ, DZ, LB and IO expressed the protein. LB, IO and EF performed the Hydrogen Deuterium Exchange Mass spectrometry (HDX-MS) experiments. SB, SG and RS performed single channel investigations. CF, DP and CVB wrote the manuscript with the help of comments from all authors.

Competing Interests: All authors declare no competing interests.

References

1. Capener CE, Proks P, Ashcroft FM, Sansom MSP (2003) Filter flexibility in a mammalian K channel: models and simulations of Kir6.2 mutants. *Biophys J* 84:2345–2356. [https://doi.org/10.1016/S0006-3495\(03\)75040-1](https://doi.org/10.1016/S0006-3495(03)75040-1)
2. Fujiwara Y, Kubo Y (2006) Functional roles of charged amino acid residues on the wall of the cytoplasmic pore of Kir2.1. *J Gen Physiol* 127:401–419. <https://doi.org/10.1085/jgp.200509434>
3. Inanobe A, Nakagawa A, Kurachi Y (2013) Conformational changes underlying pore dilation in the cytoplasmic domain of mammalian inward rectifier K⁺ channels. *PloS One* 8:e79844. <https://doi.org/10.1371/journal.pone.0079844>
4. Pegan S, Arrabit C, Zhou W, et al (2005) Cytoplasmic domain structures of Kir2.1 and Kir3.1 show sites for modulating gating and rectification. *Nat Neurosci* 8:279–287. <https://doi.org/10.1038/nn1411>
5. Li J, Xie X, Liu J, et al (2014) Lack of negatively charged residues at the external mouth of Kir2.2 channels enable the voltage-dependent block by external Mg²⁺. *PloS One* 9:e111372. <https://doi.org/10.1371/journal.pone.0111372>
6. Linder T, Wang S, Zangerl-Plessl E-M, et al (2015) Molecular Dynamics Simulations of KirBac1.1 Mutants Reveal Global Gating Changes of Kir Channels. *J Chem Inf Model* 55:814–822. <https://doi.org/10.1021/acs.jcim.5b00010>
7. Wang S, Borschel WF, Heyman S, et al (2017) Conformational changes at cytoplasmic intersubunit interactions control Kir channel gating. *J Biol Chem* 292:10087–10096. <https://doi.org/10.1074/jbc.M117.785154>
8. Bavro VN, De Zorzi R, Schmidt MR, et al (2012) Structure of a KirBac potassium channel with an open bundle crossing indicates a mechanism of channel gating. *Nat Struct Mol Biol* 19:158–163. <https://doi.org/10.1038/nsmb.2208>
9. Zubcevic L, Bavro VN, Muniz JRC, et al (2014) Control of KirBac3.1 Potassium Channel Gating at the Interface between Cytoplasmic Domains. *J Biol Chem* 289:143–151. <https://doi.org/10.1074/jbc.M113.501833>
10. Paynter JJ, Andres-Enguix I, Fowler PW, et al (2010) Functional Complementation and Genetic Deletion Studies of KirBac Channels activatory mutations highlight gating -sensitive domains. *J Biol Chem* 285:40754–40761. <https://doi.org/10.1074/jbc.M110.175687>
11. De Zorzi R, Nicholson WV, Guigner J-M, et al (2013) Growth of large and highly ordered 2D crystals of a K⁺ channel, structural role of lipidic environment. *Biophys J* 105:398–408. <https://doi.org/10.1016/j.bpj.2013.05.054>
12. Forest E, Man P (2016) Conformational Dynamics and Interactions of Membrane Proteins by Hydrogen/Deuterium Mass Spectrometry. In: MusVeteau, I (ed) *Heterologous expression of membrane proteins: Methods and Protocoles*, 2nd edition. pp 269–279
13. Gupta S, Bavro VN, D’Mello R, et al (2010) Conformational changes during the gating of a potassium channel revealed by structural mass spectrometry. *Struct Lond Engl* 1993 18:839–846. <https://doi.org/10.1016/j.str.2010.04.012>
14. Fagnen C, Bannwarth L, Oubella I, et al (2020) New Structural insights into Kir channel gating from molecular simulations, HDX-MS and functional studies. *Sci Rep* 10:8392. <https://doi.org/10.1038/s41598-020-65246-z>
15. Wang S, Lee S-J, Heyman S, et al (2012) Structural rearrangements underlying ligand-gating in Kir channels. *Nat Commun* 3:. <https://doi.org/10.1038/ncomms1625>
16. Bichet D, Haass FA, Jan LY (2003) Merging functional studies with structures of inward-rectifier K⁺ channels. *Nat Rev Neurosci* 4:957–967
17. Nishida M, Cadene M, Chait B, Mackinnon R (2007) Crystals structure of a Kir3.1-prokaryotic Kir channel chimera. *Embo J* 26:4005–4015
18. Cheng W W ,L, Enkvetchakul D, Nichols CG (2009) KirBac1.1: It’s an Inward Rectifying Potassium Channel. *J Gen Physiol* 133:295–305
19. Clarke OB, Caputo A, Hills AP, et al (2010) Domain reorientation and rotation of an intracellular assembly regulate conduction in Kir Potassium Channels. *Cell* 141:1018–1029
20. Costa MGS, Batista PR, Bisch PM, Perahia D (2015) Exploring Free Energy Landscapes of Large Conformational Changes: Molecular Dynamics with Excited Normal Modes. *J Chem Theory Comput* 11:2755–2767. <https://doi.org/10.1021/acs.jctc.5b00003>
21. Pednekar D, Tendulkar A, Durani S (2009) Electrostatics-defying interaction between arginine termini as a thermodynamic driving force in protein-protein interaction. *Proteins* 74:155–163. <https://doi.org/10.1002/prot.22142>
22. Huang J, MacKerell AD Jr (2013) CHARMM36 all-atom additive protein force field: Validation based on comparison to NMR data. *J Comput Chem* 34:2135–2145. <https://doi.org/10.1002/jcc.23354>
23. Bernsteiner H, Zangerl-Plessl E-M, Chen X, Stary-Weinzinger A (2019) Conduction through a narrow inward-rectifier K⁺ channel pore. *J Gen Physiol* 151:1231–1246. <https://doi.org/10.1085/jgp.201912359>

24. Li D, Jin T, Gazgalis D, et al (2019) On the mechanism of GIRK2 channel gating by phosphatidylinositol bisphosphate, sodium, and the G β dimer. *J Biol Chem* 294:18934–18948. <https://doi.org/10.1074/jbc.RA119.010047>
25. Krissinel E, Henrick K (2007) Inference of macromolecular assemblies from crystalline state. *J Mol Biol* 372:774–797. <https://doi.org/10.1016/j.jmb.2007.05.022>
26. Lomize MA, Pogozheva ID, Joo H, et al (2012) OPM database and PPM web server: resources for positioning of proteins in membranes. *Nucleic Acids Res* 40:D370–D376. <https://doi.org/10.1093/nar/gkr703>
27. Jo S, Kim T, Iyer VG, Im W (2008) Software news and updates - CHARNIM-GUI: A web-based graphical user interface for CHARMM. *J Comput Chem* 29:1859–1865. <https://doi.org/10.1002/jcc.20945>
28. Lee J, Cheng X, Swails JM, et al (2016) CHARMM-GUI Input Generator for NAMD, GROMACS, AMBER, OpenMM, and CHARMM/OpenMM Simulations Using the CHARMM36 Additive Force Field. *J Chem THEORY Comput* 12:405–413. <https://doi.org/10.1021/acs.jctc.5b00935>
29. Mouawad L, Perahia D (1993) Diagonalization in a mixed basis: A method to compute low-frequency normal modes for large macromolecules. *Biopolymers* 33:599–611. <https://doi.org/10.1002/bip.360330409>
30. Perahia D, Mouawad L (1995) Computation of low-frequency normal modes in macromolecules: improvements to the method of diagonalization in a mixed basis and application to hemoglobin. *Comput Chem* 19:241–246. [https://doi.org/10.1016/0097-8485\(95\)00011-g](https://doi.org/10.1016/0097-8485(95)00011-g)
31. Humphrey W, Dalke A, Schulten K (1996) VMD: Visual molecular dynamics. *J Mol Graph Model* 14:33–38. [https://doi.org/10.1016/0263-7855\(96\)00018-5](https://doi.org/10.1016/0263-7855(96)00018-5)
32. Phillips J, Braun R, Wang W, et al (2005) Scalable molecular dynamics with NAMD. *J Comput Chem* 26:1781–1802. <https://doi.org/10.1002/jcc.20289>

7 CONCLUSION AND PERSPECTIVES

7.1 CONCLUSION

This work aimed to acquire insights into the structure-function relation of Kir2.1 and determine the structure of h_Kir2.1 at high resolution. When I began my Ph.D., no structure of human Kir2.1 had been solved, and only the CTD domain of a mouse Kir2.1 homolog and the crystal structures of c_Kir2.2 with and without PIP₂ were available. Given the lack of Kir structures, we set to provide a structural basis for the study of h_Kir2.1. The emphasis of this thesis was thus to understand the impact of two clinically-relevant AS-causing mutations on the structure and function of Kir2.1 and provide a structural base for the potential development of pharmaceutical correctors later.

During this Ph.D., I was able to achieve all of the goals that were set at the beginning:

1) Establishing a robust protocol to obtain pure and homogenous human Kir2.1 recombinantly expressed in *Pichia pastoris* yeast.

Here I've presented the successful expression in *Pichia pastoris* and purification of human Kir2.1 using DDM. as a perfectly homogeneous tetramer. The protein's quality, monodispersity, and oligomerization state have been evaluated using primarily SEC-MALLS and some DLS (Chapter 3). In this thesis, I show that *P. pastoris* is an excellent organism for producing h_Kir2.1 and that DDM is a suitable detergent for extracting Kir2.1 from the membranes without compromising its quality.

Furthermore, the production and purification protocol established during this thesis results in high-quality protein that can be used for structure determination and biophysical and functional assays.

2) To characterize human Kir2.1 and two naturally-occurring mutations responsible for AS: R312H and C154Y.

The two mutants have been characterized biochemically in Chapter 3, and R312H was explored further in Chapter 4. R312H and C154Y have different biochemical profiles, but both are loss-of-function mutations resulting in a defective channel that is stable in a closed conformation. Studying these two channels allowed me to propose explanations for their lack of function. By combining SEC-MALLS, SPR, electrophysiological recordings, *in silico* studies, and cryo-EM structure analysis, we could propose an explanation for the loss of

function due to the R312H mutation and a hypothesis for the gating of the Kir2.1 channel.

3) To characterize the interaction between the Kir2.1 channel (WT and mutants) and the lipid PIP₂.

The interaction between PIP₂ and Kir2.1 (WT and mutants) is explored briefly in Chapter 3 for C154Y and in more detail in Chapter 4. All three channels were able to interact with the lipid PIP₂, although the dissociation constants differed. The PIP₂-Kir interaction is specific as PIP₂ only bound to Kir2.1 and not the control (Ferritin). It is reversible, at least in detergent, as observed by the spontaneous dissociation at the end of the PIP₂ injections. It would be interesting to investigate the interaction in a more native environment where PIP₂ could become anchored to a lipid bilayer (nanodiscs).

4) To determine the structure of human Kir2.1 at high resolution using cryo-EM.

The resolution of h_Kir2.1 was determined at 4.3 Å resolution using cryo-EM, with local resolutions of 3.7 Å. The resolved structure contains no modulators and is in a closed state. Only one apparent K⁺ ion is found in the structure, in the cytoplasm (not hydrated) in contact with D-255. This finding confirms that the pore extends beyond the TMD, all the way to the cytoplasm. Four constriction points were identified I-176, M-180, A-306, and D-255. Since A-306 is part of the G-loop domain, the G-loop in Kir2.1 acts as a gating point. This structure showed structural features different from c_Kir2.2, which highlights the importance of using this structure as a basis for future computational experiments, functional assays, and drug design.

The resolution of Kir2.1 was limited mainly by the large detergent belt surrounding the TMD domain and because a carbon layer needed to be added to the grids, adding noise to the images. I have investigated different strategies for stabilizing the purified Kir2.1 channel without detergents, such as exchanging detergent with amphipols and reconstitution into nanodiscs to obtain increased resolution and a native-like environment. The ongoing data processing of Kir2.1 reconstituted in Apol indicates that a higher resolution can be attained.

Additionally, during my Ph.D. I collaborated with C. Fagnen, a former Ph.D. student in the lab, to study the bacterial homolog. I produced and purified two KirBac3.1

mutants to evaluate the functional implications of a conserved residue in the TMD and explore the gating behavior of constitutively open channels.

The *in silico* studies performed on the h_Kir2.1 structure we solved suggested that Kir2.1 can go from an extended conformation to a compressed conformation in the absence of PIP₂. This was confirmed by the presence of particles in the compressed state in our cryoEM dataset collected without PIP₂. This leaves a burning question: if PIP₂ does not prompt the compression of the channel simultaneously opening it as previously believed, what is its role in the activation of the channel? I have allowed myself to speculate given my data and current literature and here's what I humbly propose: the gating mechanism of Kir2.1, and perhaps other Kir channels, consists of a series of small sequential movements (rather than simultaneous large motions) that lead to an open and conductive channel (Figure 7-1). Stage I: Kir2.1 is closed, elongated, and blocked. Stage II: Kir2.1 compresses in the absence of PIP₂ and the blockers are liberated through either a voltage-dependent or voltage-independent step. Stage III: The compressed state is stabilized by PIP₂. PIP₂-binding upon the binding site close to residues R218 and K219, which, in turn, transduce the binding signal through H221-R312 and R312-E303 in the G-loop and then causes the A306 constriction point to be released by simply changing the sidechains into an alternate conformation. Stage IV: As the PIP₂-stabilized channel opens, K⁺ ions rush through rendering the SF in a conductive state. Of course, this hypothetical mechanism requires investigation.

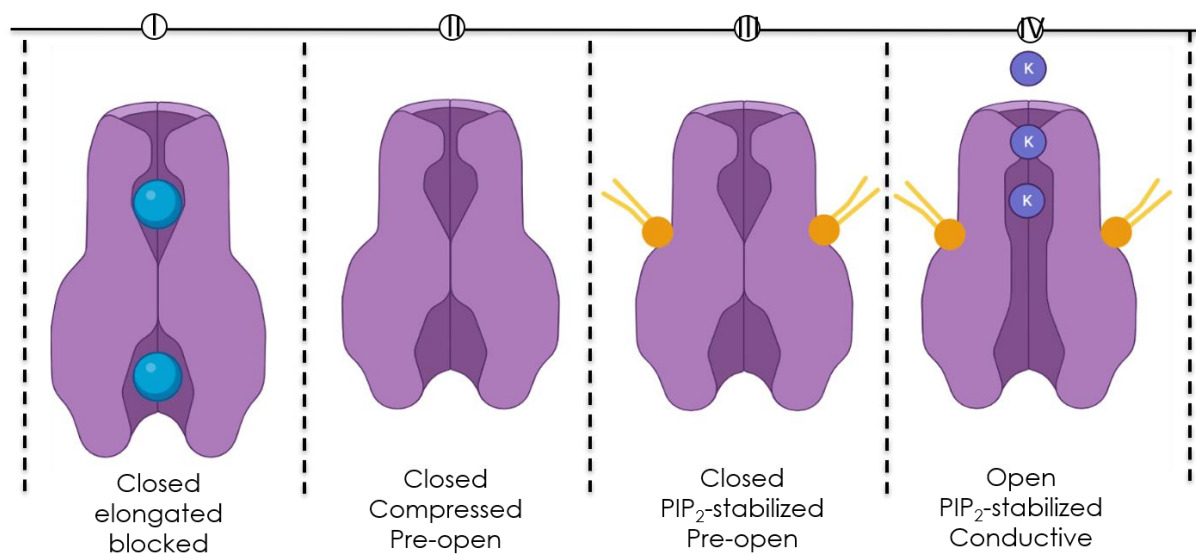


Figure 7-1 Hypothetical mechanism of PIP₂-stabilized channel activation

7.2 PERSPECTIVES

Now that the structure of human Kir2.1 is known, this opens the way for many experiments, particularly concerning the interaction of this channel with PIP₂. The next logical step is to determine the structure of Kir2.1 with PIP₂. This is ongoing work; the appropriate Kir2.1:PIP₂ ratios and blotting conditions have been determined, and the preliminary results using UltraUfoil grids are promising. New grids will be prepared on July 27th, and the data acquisition is scheduled for July 29th, 2022. This will allow us to establish whether the compressed structure predicted by the *in silico* studies in the apo state is the same obtained with PIP₂ docked. We will be able to compare the changes from the apo state to PIP₂-docked structures with those of available c_Kir2.2 homolog to better understand the differences between the two channels. In addition, this study will hopefully allow us to understand the gating with the other conformational changes allowing the opening of the pore at different constriction points.

Human Kir2.1 structures in distinct closed, intermediate, and open states are crucial for understanding the mechanisms involved in channel gating and how PIP₂ induces or stabilizes the compressed state, which can be extremely difficult to produce. Consequently, the experimental data will be supplemented with *in silico* analyses, notably NM analysis, classical MD simulations, and coarse-grained MD (CGMD) simulations. CGMD will make it possible to understand how and where PIP₂ will bind to Kir2.1 and its impact on the channel.

The ongoing Kir2.1-Apol results are promising. I will continue refining the 3D maps and determine the structure of Kir2.1 in the apo state to obtain a better resolution than that obtained in DDM. In this new structure, I will explore the conformational heterogeneity of the samples in the hopes of capturing Kir2.1 in different conformational states.

Several agonists and regulators will be explored structurally and functionally, including secondary anionic lipids, cholesterol, polyamines, and the PDZ domain. In addition, we hope to know the interactions between miRNAs and Kir2.1, so crucial in cardiology, in collaboration with the team of Dr. Jidong Fu in the United States. For this, the reconstitution of Kir2.1 into nanodiscs will continue to be optimized.

Once the nanodisc reconstitution is perfected, Förster resonance energy transfer (FRET) will be performed to investigate the effect of ligand binding on the

conformational features of Kir2.1. Much work is planned for the AS-causing mutants, C154Y and R312H. Electrophysiological recording of Kir2.1 WT in oocytes will be performed and compared with the mutants under varying conditions, as well as FRET. The effect of the C154Y mutation in cell trafficking will be explored using different constructs. The experimental perspectives will be preceded by *in silico* studies currently being launched. For R312H, determining the structures with and without PIP₂ at high resolution will allow the validation of the hypotheses established in Chapter 4.

Finally, once the different structures of h_Kir2.1 are determined and an understanding of the mechanism is achieved, a long-term perspective is to collaborate with pharmaceutical companies to develop possible allosteric correctors to stabilize the open conformation in defective channels.

Table of Figures

FIGURE 1-1. TOPOLOGY OF THE FOUR K^+ CHANNEL FAMILIES.....	15
FIGURE 1-2. SCHEMATIC VOLTAGE VS. CURRENT RELATIONSHIP OF KIR CHANNELS	18
FIGURE 1-3. KIR CHANNEL PHYLOGENETIC TREE.....	19
FIGURE 1-4. SEQUENCE ALIGNMENT OF EUKARYOTIC KIR CHANNELS AND KIRBAC HOMOLOGS WITH STRUCTURAL ANNOTATIONS.....	21
FIGURE 1-5. THE AMINO ACID SEQUENCE PERCENT IDENTITY BETWEEN VARIOUS KIRBAC, HUMAN, MOUSE, CHICKEN KIR CHANNELS, AND KCSA.	22
FIGURE 1-6. STRUCTURE OF H_KIR2.1 (PDB 7ZDZ) WITH STRUCTURAL FEATURES ANNOTATED (RESULT FROM CHAPTER 4).	23
FIGURE 1-7. SUMMARY OF SOME KIR AND KIRBAC CHANNEL STRUCTURES. THE SEQUENCE IDENTITY REFERS TO THE UNIPROT SEQUENCE COMPARED TO HUMAN KIR2.1. THE STRUCTURE COVERAGE DENOTES THE PERCENTAGE OF AMINO ACID SEQUENCE INCLUDED IN THE PROTEIN CONSTRUCT....	24
FIGURE 1-8 HYPOTHETICAL PIP_2 ACTIVATION MECHANISM IN EUKARYOTIC KIR CHANNELS AND DEACTIVATION IN KIRBAC CHANNELS.	27
FIGURE 2-1: pPIC9K EXPRESSION VECTOR.	43
FIGURE 2-2: SUMMARY OF KIR2.1 EXPRESSION PROTOCOL.....	44
FIGURE 2-3: EFFECT OF IONIC STRENGTH ON THE SAMPLE.....	51
FIGURE 2-4. SEC-MALLS CONFIGURATION	54
FIGURE 2-5. NORMALIZATION OF DETECTORS AT DIFFERENT ANGLES IS NECESSARY BECAUSE THE LIGHT INTENSITY CAN BE ANISOTROPIC.....	58
FIGURE 2-6: SPR PHENOMENON	60
FIGURE 2-7: BASIC SPR PROTOCOL. A CM5 SENSOR CHIP IS ACTIVATED WITH EDC/NHS, FOLLOWED BY LIGAND INJECTION (KIR2.1) IN ACIDIC pH AND THEN ANALYTE BINDING (PIP_2).....	61
FIGURE 2-8: BASIC ANATOMY OF A TRANSMISSION ELECTRON MICROSCOPE (FROM PASTEUR INSTITUTE).	65
FIGURE 2-9: AMPLITUDE AND PHASE CONTRAST.....	67
FIGURE 2-10. CTF AND ITS ENVELOPE FUNCTION ARE DEPICTED. UNPUBLISHED LECTURE MATERIAL FROM N. BOISSET.	68
FIGURE 2-11: DEMONSTRATION OF WIENER FILTERING AND PHASE FLIPPING (FROM N. BOISSET, UNPUBLISHED LECTURE MATERIAL).....	69
FIGURE 2-12 SINGLE-PARTICLE ANALYSIS FLOWCHART.....	70
FIGURE 2-13 EXAMPLE OF NOISE REDUCTION BY AVERAGING AND 2D CLASSIFICATION (DATA FROM N. BOISSET)	72
FIGURE 2-14. CENTRAL SECTION THEOREM. (DATA FROM N. BOISSET).....	72
FIGURE 2-15: VITROBOT MARK IV FOR THE PREPARATION OF FROZEN-HYDRATED SPECIMENS.	76
FIGURE 2-16: LACEY VS. QF GRID	77
FIGURE 3-1. CELL GROWTH AND EXPRESSION OF KIR2.1 AND MUTANTS IN <i>P.PASTORIS</i>	90
FIGURE 3-2. DETERGENT SCREEN FOR OPTIMAL SOLUBILIZATION OF HUMAN KIR2.1 EXPRESSED IN <i>PICHIA PASTORIS</i>	92

FIGURE 3-3. WESTERN BLOT OF KIR2.1 SOLUBILIZATION TEST USING DIFFERENT DETERGENTS WITH OR WITHOUT ADDED LIPIDS.....	94
FIGURE 3-4. TWO-STEP PURIFICATION OF KIR2.1.	94
FIGURE 3-5. KIR2.1 SEQUENCE WITH SEGMENTS IDENTIFIED BY MASS SPECTROMETRY.	95
FIGURE 3-6. DETERMINATION OF KIR2.1 STOKES RADIUS BASED ON SEC ELUTION PROFILE.....	96
FIGURE 3-7. DLS MEASUREMENTS SHOWING R_s VALUES FOR KIR2.1 COMPLEX AND DDM MICELLES. ...	97
FIGURE 3-8. A) KIR2.1 SEC-MALLS ELUTION PROFILE IN 20 mM TRIS-HCL, pH 8, 200 mM KCL, 1 mM EDTA, 0.018% DDM (0.018% DDM SEC BUFFER) USING SUPERDEX 200 COLUMN (S200).....	99
FIGURE 3-9. A) SEC-MALLS PROFILE OF KIR2.1 IN 20 mM TRIS-HCL pH 7.4, 150 mM KCL, 1 mM EDTA, 0.03% DDM. LS, UV, AND Δ RI ARE SHOWN IN RED, GREEN, AND BLUE, RESPECTIVELY.....	101
FIGURE 3-10. SEC PROFILE OF KIR2.1 EXTRACTED IN 0.5% FC14.....	102
FIGURE 3-11. SEC-MALLS PROFILE OF KIR2.1-WT FC14-DDM IN 0.03% DDM SEC BUFFER.	103
FIGURE 3-12. A) SEC-MALLS PROFILE OF FC14-PCC-MALT KIR2.1 IN 0.03% PCC-MALT SEC BUFFER.	105
FIGURE 3-13. MICROGRAPH OF KIR2.1 FC14-DDM AND 2D CLASSIFICATION.	106
FIGURE 3-14. 3D INITIAL MODELS OF KIR2.1-FC14-DDM IN NEGATIVE STAINING.....	107
FIGURE 3-15. 3D MAP FROM KIR2.1 FC14-DDM OBTAINED BY NEGATIVE STAINING AT 18.4 Å RESOLUTION USING EMAN2.....	107
FIGURE 3-16. COMPARISON OF SEC PURIFICATION OF KIR2.1 WT AND R312H AND C154Y MUTANTS.	108
FIGURE 3-17. SEC-MALLS PROFILE OF KIR2.1_R312H IN 20 mM TRIS-HCL pH 7.4, 150 mM KCL, 1 mM EDTA, 0.03% DDM.....	109
FIGURE 3-18 C154Y ELUTION PROFILES AND NATIVE PAGE B) NATIVE PAGE COMPARING KIR2.1 WT AND C154Y.....	111
FIGURE 3-19. SPR SENSORGRAM OF KIR2.1_C154Y (5844 RU LEVEL) IMMOBILIZED ONTO A CM5 CHIP.	111
FIGURE 3-20. DISULFIDE BONDS IN CRYO-EM H_KIR2.1 STRUCTURE AT 4.3 Å RESOLUTION AND ALIGNMENT OF AMINO ACIDS IN DIFFERENT KIR CHANNELS.....	112
FIGURE 3-21. <i>PICHIA PASTORIS</i> CELL CULTURE AT 0.5 OD _{600NM} IN A MALASSEZ CHAMBER FOR COUNTING CELLS.	117
FIGURE 3-22. EFFECT OF pH AND AGITATION SPEED ON THE GROWTH OF <i>PICHIA PASTORIS</i> CULTURE..	118
FIGURE 3-23. WESTERN BLOT OF CLONES EXPRESSING KIR2.1_WT.	118
FIGURE 3-24. DETERMINATION OF THE DDM'S CRITICAL MICELLAR CONCENTRATION USING FLUORESCENCE SPECTROSCOPY.....	120
FIGURE 3-25. LYSIS TESTS OF <i>P. PASTORIS</i> USING 2.4, 2.5, AND 2.5 KBAR PRESSURE.	121
FIGURE 3-26. WESTERN BLOT OF KIR2.1 SOLUBILIZATION TEST USING DIFFERENT MEMBRANE PROTEINS (MP) TO DDM DETERGENT CONCENTRATION RATIOS FOLLOWING POOR LYSIS.....	122
FIGURE 3-27. OPTICAL MICROSCOPY AND WESTERN BLOT ANALYSIS OF LYSIS AT 2.7 KBAR.....	122
FIGURE 3-28. COMPARISON OF SEC ELUTION PROFILES AFTER MECHANICAL LYSIS VS. DIRECT EXTRACTION.....	124
FIGURE 3-29. COMPARISON OF LYSIS IN KIR2.1. P1 (PELLET) AND SN1 (SUPERNATANT).....	124
FIGURE 3-30 WESTERN BLOTS OF SOLUBILIZATION OF KIR2.1 AFTER LYSIS WITH CELL D, PROTOPLASTS, AND PROTOPLAST PLUS CELL D.....	125

FIGURE 3-31. LYSIS OF <i>P. PASTORIS</i> CELLS USING GLASS BEADS AND WB ANALYSIS OF KIR2.1 SOLUBILIZATION.....	126
FIGURE 5-1 SCHEMATIC ARRANGEMENT OF DDM (LEFT) VS. APOLS (RIGHT) AROUND KIR2 TMD.....	174
FIGURE 5-2. SCHEMATIC REPRESENTATION OF DDM VS. NANODISC AROUND KIR2 CHANNEL..	175
FIGURE 5-3 KIR2.1 TO APOL RATIOS.....	178
FIGURE 5-4. NEGATIVE STAINING IMAGE OF KIR2.1 1:4 APOL.....	179
FIGURE 5-5 SEC PROFILE OF KIR2.1-APOL.....	179
FIGURE 5-6. CRYO-EM IMAGE OF KIR2.1 IN DDM AND IN APOL.....	180
FIGURE 5-7. PARTICLE PICKING AND 2D CLASSIFICATION OF KIR2.1-APOL.....	182
FIGURE 5-8. 3D INITIAL MODEL AND THE FIRST ROUND OF 3D CLASSIFICATION OF H_KIR2.1 IN APOLS	183
FIGURE 5-9. SDS PAGE OF MSP1D1 PRODUCTION AND PURIFICATION FRACTIONS.....	187
FIGURE 5-10. FORMATION OF MSP1D1 AND POPC EMPTY NANODISCS.....	188
FIGURE 5-11. SEC ELUTION PROFILE OF NANODISC FORMATION USING MSP1D1 AND POPC.....	189
FIGURE 7-1 HYPOTHETICAL MECHANISM OF PIP ₂ -STABILIZED CHANNEL ACTIVATION.....	238